# *Environment related surface phenomena and their influence on properties of Ti-6Al-4V and Ti-6Al-2Sn-4Zr-2Mo : oxidation at elevated temperature and corrosion during chemical treatment*

**Birhan Sefer**

DOCTORAL THESIS

# Environment Related Surface Phenomena and their Influence on Properties of Ti-6Al-4V and Ti-6Al-2Sn-4Zr-2Mo:

## *Oxidation at Elevated Temperature and Corrosion During Chemical Treatment*

Birhan Sefer

Engineering Materials

This thesis is the result of a collaboration between Luleå University of Technology and Universitat Politècnica de Catalunya that aims toward a double degree

UNIVERSITAT POLITÈCNICA DE CATALUNYA

LULEÅ UNIVERSITY OF TECHNOLOGY

This thesis is the result of a collaboration between Luleå University of Technology and Universitat Politècnica de Catalunya that aims toward a double degree

# Environment Related Surface Phenomena and their Influence on Properties of Ti-6Al-4V and Ti-6Al-2Sn-4Zr-2Mo:

*Oxidation at Elevated Temperature and Corrosion during Chemical Treatment*

A thesis submitted to Luleå University of Technology and Universitat Politècnica de Catalunya for the double degree of Doctor of Philosophy by


**Birhan Sefer**

Department of Engineering Sciences and Mathematics
Luleå University of Technology

Department of Materials Science and Metallurgical Engineering
Universitat Politècnica de Catalunya


UNIVERSITAT POLITÈCNICA DE CATALUNYA BARCELONATECH

LULEÅ UNIVERSITY OF TECHNOLOGY

Luleå, August 2016

Engineering Materials

Division of Materials Science

Department of Engineering Sciences and Mathematics

Luleå University of Technology

SE-971 87

The cover image include; The left side shows a picture of TRENT XWB-ICC (Intermediate Compressor Casing) fabricated from Ti-6Al-4V and Ti-6Al-2Sn-4Zr-2Mo alloys and several different forms of materials (sheet, cast, wrought and additive manufactured material). Courtesy of GKN. The right side shows sketch of the TRENT XWB engine that will power the Airbus A350 XWB, and the location of the ICC is indicated.

Printed by Luleå University of Technology, Graphic Production 2016

ISSN 1402-1544
ISBN 978-91-7583-668-3 (print)
ISBN 978-91-7583-669-0 (pdf)

Luleå 2016

www.ltu.se

*To my family*

*without whom my success would not be possible*

*In loving memory of my grandparents*

# ABSTRACT

This doctoral thesis covers investigation of the surface phenomena of Ti-6Al-4V and Ti-6Al-2Sn-4Zr-2Mo alloys related with oxidation at elevated temperature and corrosion during chemical treatment in hydrofluoric-nitric acid ($HF/HNO_3$) solutions. The explored phenomena are related to manufacturing and service conditions of aero-engine components. During manufacturing and operation, the alloys are running at elevated temperatures in oxygen containing environment. Under these conditions there are formations of an oxide on the surface and an oxygen enriched layer below the oxide, commonly referred as alpha-case. The alpha-case is a hard and brittle layer that is detrimental to the mechanical properties and must therefore be minimized or completely eliminated. A conventional method for elimination of alpha-case is chemical processing in $HF/HNO_3$ solutions, known as chemical milling.

Isothermal oxidation treatments in air at 500, 593 and 700 ºC for up to 500 hours were carried out in this study. Both alloys developed rutile type of oxide structure and Ti-6Al-2Sn-4Zr-2Mo exhibited stronger oxidation resistance than Ti-6Al-4V. Transition from parabolic to linear oxidation rate was observed at 700 ºC and $\geq$ 200 hours for both alloys. The difference in the oxidation kinetics of the two alloys is suggested to be related with the chemical composition of the alloys. The oxygen enriched layer, i.e. alpha-case layer, was characterised and its thickness was measured using conventional metallographic and microscopic techniques. Parabolic relationship of the alpha-case layer growth rate with time was observed for both alloys. The oxygen diffusion parameters and activation energies were estimated in the temperature range of 500-700 ºC. Additionally, the oxidation at 700 ºC for 500 hours resulted in microstructural changes and element re-distribution. The bulk and alpha-case layer hardness at micro- and nano-scale were measured using microhardness and nanoindentation techniques. The alpha-case layer had higher hardness due to the solid solution strengthening effect of the diffused oxygen.

The effect of chemical milling in 1:11 $HF/HNO_3$ solution on the surface integrity, and the influence on low cycle fatigue (LCF) strength of cast Ti-6Al-2Sn-4Zr-2Mo alloy was investigated. Short and long chemical processing times (5 and 60 minutes) and three imposed total strain ranges in fatigue tests were evaluated. Significant drop in fatigue life was observed for the samples etched before LCF testing, as compared to the non-etched samples. The influence from etching was found to be most detrimental for fatigue samples tested at the lowest strain ranges. The fatigue life reduction was correlated with the number of crack initiation sites. Multiple crack initiation sites were observed for the etched samples, whereas only one crack initiation site was discerned in the non-etched samples. Inspection of the surface of the etched samples revealed selective and severely etched prior β grain boundaries and pit formation at the triple joints of the prior β grain boundaries. These surface defects were considered as stress raisers promoting an earlier fatigue crack initiation.

The influence of two different molar concentration ratios (1:3 and 1:11) of HF and $HNO_3$ acids on the corrosion behaviour of cast Ti-6Al-4V and Ti-6Al-2Sn-4Zr-2Mo were investigated using electrochemical and atomic force microscopy (AFM) techniques. The corrosion of the two alloys was a function of the $HF/HNO_3$ concentration ratio and also of the alloys' chemical compositions. The AFM measurements revealed selective and faster dissolution rate of the α-phase than the β-phase in the Widmanstätten microstructure. It was considered that the reason for selective dissolution was the formation of local micro-galvanic cells between the α-phase and the β-phase. Moreover, the Volta-potential was measured using scanning Kelvin probe force microscopy (SKPFM) and the obtained maps revealed difference in the Volta-potential between

the α-laths and the β-laths in both alloys. This observation strengthened the likelihood for formation and operation of micro-galvanic cells between the α-phase and the β-phase when the alloys were in contact with $HF/HNO_3$ solution.

**Keywords:** Titanium alloys, oxidation, oxide, alpha-case, chemical milling, corrosion.

# RESUMEN

En esta tesis doctoral se estudian los fenómenos superficiales relacionados con la oxidación a alta temperatura y la corrosión producidos durante el tratamiento químico en soluciones de ácido fluorhídrico-nítrico ($HF/HNO_3$) en las aleaciones Ti-6Al-4V y Ti-6Al-2Sn-4Zr-2Mo. Estos fenómenos se producen durante la fabricación y el servicio de componentes para motores aeronáuticos, pues se dan condiciones de elevada temperatura en un ambiente rico en oxígeno, las cuales favorecen la formación de óxido en la superficie y también de una capa enriquecida en oxígeno debajo del óxido, comúnmente conocida como *alpha-case* o capa alfa. La *alpha-case* es una capa dura y frágil, perjudicial para las propiedades mecánicas, por lo que debe ser minimizada o totalmente eliminada. Un método convencional para eliminar la capa alfa es el procesado químico en soluciones de ácido fluorhídrico-nítrico, conocido como *chemical milling*.

En este estudio se han efectuado tratamientos isotérmicos en aire a 500, 593 y 700 ºC, con duración máxima de 500 horas. Ambas aleaciones desarrollaron óxido tipo rutilo, en tanto que la Ti-6Al-2Sn-4Zr-2Mo mostró mejor resistencia a la oxidación que la Ti-6Al-4V. Se observó una transición de la velocidad de oxidación de parabólica a lineal a 700 ºC y tiempos $\geq$ 200 horas, para ambas aleaciones. Las diferencias en la cinética de oxidación entre ambas aleaciones se han relacionado con su composición química. La capa rica en oxígeno, i.e. *alpha-case*, fue caracterizada y su espesor medido mediante técnicas metalográficas. Se observó que la velocidad de crecimiento de la capa alfa seguía una relación parabólica con el tiempo para ambas aleaciones. La difusión del oxígeno y la energía de activación se estimaron en el rango de temperaturas de 500-700 ºC. Adicionalmente, se comprobé que el tratamiento isotérmico a 700 ºC durante 500 horas dio lugar a cambios microestructurales y a la redistribución de elementos. Las durezas del interior y de la capa alfa se midieron a escalas micro- y nano- mediante técnicas de microdureza y nanoindentación. La capa alfa mostró mayor dureza debido al efecto de endurecimiento por solución sólida debido al oxígeno difundido.

El efecto de la solución 1:11 $HF/HNO_3$ en la integridad superficial y en la resistencia a fatiga en el régimen de oligofatiga (LCF = *Low Cycle Fatigue*) de la aleación Ti-6Al-2Sn-4Zr-2Mo fue investigado. Se evaluaron tiempos de procesado químico cortos y largos (5 y 60 minutos) y tres valores de amplitud de deformación total. Se observó una significativa disminución de la vida a fatiga para las muestras atacadas antes de los ensayos LCF, en comparación con las muestras no atacadas. La influencia del ataque se mostró más perjudicial a bajos valores de deformación impuesta. La reducción en la vida a fatiga se correlacionó con el número de zonas de iniciación de grietas. Múltiples zonas se observaron para las muestras atacadas, mientras que solo un lugar de nucleación de grieta se detectó para las no atacadas. La inspección de las superficies de las muestras atacadas reveló un ataque selectivo y severo en los bordes de grano *prior beta* y la formación de picaduras en los puntos triples de los bordes de grano *prior beta*. Estos defectos superficiales fueron considerados como exaltadores de tensiones que promueven la temprana nucleación de las grietas de fatiga.

Se investigó la influencia en el comportamiento a corrosión de Ti-6Al-4V y Ti-6Al-2Sn-4Zr-2Mo de dos diferentes relaciones de concentración (1:3 y 1:11) de los ácidos HF y $HNO_3$. Se emplearon para ello técnicas electroquímicas y microscopía de fuerza atómica (AFM). La corrosión de las dos aleaciones depende de la concentración de $HF/HNO_3$ y posiblemente también de sus composiciones químicas. Las medidas de AFM revelaron una velocidad de disolución mayor de la fase alfa que de la beta en la microestructura tipo Widmanstätten. Se considera que la razón de esta disolución selectiva es la formación de celdas micro-galvánicas

locales entre ambas fases. Además, el potencial Volta se midió a través de SKPFM (*Scanning kelvin probe force microscopy*) y se obtuvieron mapas que revelaron las diferencias en potencial Volta entre la fase alfa y las agujas beta en ambas aleaciones. Esta observación refuerza la probable formación y operación de celdas micro-galvánicas entres las fases alfa y beta cuando las aleaciones están en contacto con la solución de $HF/HNO_3$.

**Palabras clave:** Aleaciones de titanio, oxidación, óxido, capa alfa, fresado químico, corrosión.

# PREFACE

This thesis is the result of a joint PhD project in the *European School of Materials* (EUSMAT) through the *Joint European Doctoral Programme in Materials Science and Engineering* (DocMASE) between March 2012 and August 2016.

In this PhD project three collaborators were involved; two university partners and one industrial partner. The university partners through the EUSMAT graduate school were Luleå University of Technology (LTU) in Luleå, Sweden and Universitat Politècnica de Catalunya (UPC) in Barcelona, Spain. The industrial partner was GKN Aerospace Engine Systems in Trollhättan, Sweden.

The work described in the thesis has been carried out under supervision of Prof. Dr. Marta-Lena Antti, Division of Materials Science, Luleå University of Technology, Prof. Dr. Robert Pederson, Division of Materials Science, Luleå University of Technology and GKN Aerospace Engine Systems, Prof. Dr. Antonio Mateo, Department of Materials Science, Universitat Politècnica de Catalunya and Prof. Ragnar Tegman, Division of Materials Science, Luleå University of Technology.

The results acquired in the thesis have been presented at international conferences and published in peer-reviewed scientific journals.

The thesis contains two parts.

The first part consists of six chapters that are covering topics as follows:

*Chapter 1:* Introduction to the investigated scientific/industrial problem, the motivation, the aim and objectives of the thesis.

*Chapter 2:* Background to the titanium field with main focus on the metallurgical aspects of titanium and its alloys, the manufacturing process, and the application of titanium alloys in aerospace.

*Chapter 3:* Literature review on oxidation and corrosion during chemical milling of titanium and its alloys.

*Chapter 4:* Experimental part, where the applied experimental methods and instrumental techniques used in the present work are described in a generalised manner.

*Chapter 5:* Short summary of the appended papers.

*Chapter 6:* Conclusions and future work.

Part two of the thesis comprises compilation of six appended papers.

# ACKNOWLEDGMENTS

The work described and presented in this doctoral thesis would not have been possible to accomplish without assistance, guidance, motivation, support, knowledge and encouragement of many people.

In the very beginning, I would like to express generous gratitude to my supervisors, Marta-Lena Antti and Robert Pederson for guiding me through the PhD studies, being patient, providing me with support, understanding and sharing their knowledge with me. I would also like to acknowledge very much both of them for providing me with strong motivation and not losing faith in me. Thanks Marta-Lena and Robert for believing in me!

I would also like to sincerely acknowledge Ragnar Tegman, my never tired advisor and discussion associate for being very kind, patient and always open for long and fruitful discussions. Thanks Ragnar, I have learned a lot from you!

I express my enormous gratitude to my supervisor Antonio Mateo from Spain for showing hospitality during my stay at UPC in Barcelona and for being kind, helpful and always very professional.

I would also like to acknowledge all the co-authors of the appended papers in this thesis, Raghuveer Gaddam, Joan Josep Roa, Illia Dobryden and Nils Almqvist. The work presented in the papers of this thesis would not have been possible without these wonderful people (scientists/researchers).

Special thanks go to the research engineers, Johnny Grahn and Lars Frisk from LTU for always being helpful and sharing their experience in the labs by assisting me with the experimental and the instrumental work. Big thanks also to the technicians from UPC, Isaac López Insa, Trifon Trifonov and Montserrat Domínguez Escalante for helping me in the experimental and instrumental work during the six months stay at UPC, Barcelona.

I sincerely acknowledge Christina Heimdahl for her guidance and support in my personal and professional development.

I am very thankful to all my former and present PhD colleagues and all staff members of Division of Materials Science at LTU for creating pleasant working environment.

Special thanks to the boss of the Department of Engineering Sciences and Mathematics Prof. Elisabet Kassfeldt and to the boss of the Materials Science Division Prof. Lennart Wallström for their support to accomplish this doctoral thesis. Sincere thanks also go to Prof. Lennart Wallström for taking care and sorting out all raised questions and issues of the DocMASE PhD students.

I would like to acknowledge the Joint European Doctoral Programme in Materials Science and Engineering (DocMASE) for providing me with financial support for my first three years of studies. Special thanks go to the managers of the European School of Materials (EUSMAT) and the Joint European Doctoral Programme in Materials Science and Engineering (DocMASE), Prof. Frank Mücklich and Dr. Flavio Soldera for providing me with the chance to be part of the DocMASE family.

I would also like to acknowledge the Wallenberg foundation for providing me with travel grant for participation in the biggest Titanium conference in San Diego, USA.

Thanks to GKN Aerospace Systems for giving me the possibility to be part of their team and take part in their project(s).

Big thanks go to all my friends in Macedonia and Luleå, for their support, motivation and encouragement.

I would also like to express enormous gratitude to my parents and to my brother for always being with me, supporting me constantly through the years and providing me with encouragement, inspiration and motivation. My success would not be possible without having them!

I am also very thankful to the family of my wife Elma for their support and belief in me.

At last, I am very thankful to my wife Elma for her endless love, understanding, encouragement, motivation and support that made me stronger in hard times.

Birhan Sefer

August 2016
Luleå

Ја користам оваа прилика за да искажам благодарност и на македонски јазик до сите оние коишто ми помогнаа, мотивираа и придонесоа на било каков начин во реализацијата на овој докторат.

На почетокот сакам да искажам неизмерна благодарност на моето семејство, на моите родители Зумбер и Наазан и на мојот брат Сенат за моралната и финансиска подршка и силната мотивација во текот на целиот живот. Без нив и нивната подршка не би можел да стигнам до ова што сум денес.

Се заблагодарувам на сите мои пријатели, колеги и поранешни професори од Македонија и пошироко кои безрезервно ме подржуваа и сеуште ме подржуваат. Помеѓу нив посебна почит заслужува мојот ментор Професор Валентин Мирчески, кој уште во моите студентските денови на Институтот за Хемија при Природно Математичкиот Факултет во Скопје ја потикна желбата и љубота во мене кон научно-истражувачката работа.

На крајот сакам да и се заблагодарам на мојата сопруга Елма, за нејзината безконечна љубов, разбирање и безрезервна подршка во текот на годините додека траеа докторските студии.

Бирхан Сефер

Август 2016
Лулео

# LIST OF APPENDED PAPERS

## PAPER I

Raghuveer Gaddam, **Birhan Sefer**, Robert Pederson, Marta-Lena Antti, *Study of alpha-case depth in Ti-6Al-2Sn-4Zr-2Mo and Ti-6Al-4V*. IOP Conf. Series: Materials Science and Engineering 48 (2013) 012002.

## PAPER II

Raghuveer Gaddam, **Birhan Sefer**, Robert Pederson, Marta-Lena Antti, *Oxidation and alpha-case formation in Ti-6Al-2Sn-4Zr-2Mo alloy*. Materials Characterisation 99 (2015) 166-174.

## PAPER III

**Birhan Sefer**, Raghuveer Gaddam, Robert Pederson, Antonio Mateo, Ragnar Tegman, Marta-Lena Antti, *Oxidation behaviour of Ti-6Al-4V and Ti-6Al-2Sn-4Zr-2Mo alloys exposed to air at elevated temperatures*. Submitted to Journal of Corrosion Science.

## PAPER IV

**Birhan Sefer**, Joan Josep Roa, Antonio Mateo, Robert Pederson, Marta-Lena Antti, *Evaluation of the bulk and alpha-case layer properties in Ti-6Al-4V at micro- and nano-metric length scale,* in: V. Venkatesh, A.L. Pilchak, J.E. Allison, S. Ankem, R. Boyer, J. Christodoulou, H.L. Fraser, M.A. Imam, J. Kosaka, H.J. Rack, A. Chatterjee, A. Woodfield (Eds.). Proceedings of the 13$^{th}$ World Conference on Titanium, John Wiley & Sons Inc., Hoboken, New Jersey, 2016, pp. 1619-1624.

## PAPER V

**Birhan Sefer**, Raghuveer Gaddam, Joan Josep Roa, Antonio Mateo, Marta-Lena Antti, Robert Pederson, *Chemical milling effect on the low cycle fatigue properties of cast Ti-6Al-2Sn-4Zr-2Mo alloy*. International Journal of Fatigue 92 (2016) 193-202.

## PAPER VI

**Birhan Sefer**, Illia Dobryden, Nils Almqvist, Robert Pederson, Marta-Lena Antti, *Corrosion behaviour of cast Ti-6Al-4V and Ti-6Al-2Sn-4Zr-2Mo alloys in hydrofluoric-nitric acid solutions*. Submitted for publication.

## Conference contributions/presentations

1. Raghuveer Gaddam, **Birhan Sefer**, Robert Pederson, Marta-Lena Antti, *Study of alpha-case depth in Ti-6Al-2Sn-4Zr-2Mo and Ti-6Al-4V*. Oral presentation at the 7th EEIGM (École Européenne d'Ingénieurs en Génie des Matériaux) conference in Luleå, Sweden, March 2013.

2. **Birhan Sefer**, Raghuveer Gaddam, Robert Pederson, Marta-Lena Antti, *Study of the Alpha-Case Layer in Ti-6Al-2Sn-4Zr-2Mo and Ti-6Al-4V by Electron Probe Micro Analysis*. Poster presentation at the MSE 2014 (Materials Science and Engineering) Congress in Darmstadt, Germany, September 2014.

3. **Birhan Sefer**, Joan Josep Roa, Antonio Mateo, Robert Pederson, Marta-Lena Antti, *Evaluation of the bulk and alpha-case layer properties in Ti-6Al-4V at micro and nano-metric length scale*. Oral presentation at the Ti-2015: 13th World Conference on Titanium in San Diego, California, USA, August 2015.

# LIST OF TABLES

# LIST OF FIGURES

# CONTENTS

# Part I

# 1 INTRODUCTION

This chapter briefly describes the investigated scientific/industrial problem and the motivation for performing this work together with the aim and objectives of the thesis.

## 1.1 Problem formulation and motivation

The work presented in this thesis was performed in collaboration with GKN Aerospace Engine Systems that is developing and manufacturing large aero-engine components for commercial aircrafts. It is important to highlight that the aero-engine designers are working continuously towards improvement of the efficiency of future generations of aero-engines. Important challenges that the aerospace industry is facing include reducing the environmental and economic impact from burning fossil fuels. One way to improve the efficiency of the aero-engines is to increase the working pressure in the engine, which in turn results in increased working temperature. Another way to reduce fuel consumption is to manufacture the aero-engines from lighter and more advanced materials. To be able to meet these challenges materials research today focuses on understanding the limitations of currently existing titanium alloys in order to extend their applicability. At the same time development of titanium alloys with improved customised properties is an on-going strive by industry. Introduction of new materials normally needs long term research efforts and therefore it seems that the best starting point is to increase the knowledge and understanding of the oxidation behaviour and thermal stability of already existing conventional titanium alloys.

Titanium alloys have a long tradition in manufacturing of airframe and aero-engine components. The outstanding properties of titanium alloys, such as high strength, low density and excellent corrosion resistance compared to other engineering metallic materials, make them attractive candidates for aerospace applications [1-3]. Ti-6Al-4V and Ti-6Al-2Sn-4Zr-2Mo are two of the most common commercial titanium alloys that are used for manufacturing critical static and rotating aero-engine components such as blades, disks and rotors [4]. Ti-6Al-4V is featured with good fatigue strength up to 300 ºC, whereas Ti-6Al-2Sn-4Zr-2Mo is known as high temperature alloy and is characterised with excellent fatigue and creep resistance properties up to 450 ºC [5]. The service temperature limitation for titanium alloys in load bearing applications is mainly limited by their high reactivity with oxygen at elevated temperatures, i.e. $\geq$ 480 ºC. During such conditions, titanium alloys are oxidising readily. The oxidation results in oxide scale formation on the surface of the alloys and oxygen diffusion into the bulk, i.e. formation of subsurface oxygen enriched layer. This subsurface layer is hard and brittle and it is commonly referred to as alpha-case [1-3]. The alpha-case layer is known to impair important mechanical properties such as tensile ductility, facture toughness and especially the fatigue strength [6-11].

The alpha-case development is unavoidable during manufacturing of titanium aero-engine components as result of the various thermo-mechanical processing steps that are normally carried out at high temperatures and in presence of oxygen. However, alpha-case could potentially also develop locally on the titanium alloy components during operation of the engines. Hence, the

aerospace industry is highly precautious and has strict policies for how to minimise or completely eliminate this layer on highly loaded and critical aero-engine components. In industrial practice the alpha-case is removed either mechanically by machining or chemically by immersion of the titanium aero-engine components into chemical baths consisting of mixtures of hydrofluoric (HF) and nitric ($HNO_3$) acids. The chemical treatment of the components is known as chemical milling and it is convenient for handling components with complex geometry [1-3]. Removal of the oxide scale and alpha-case layer using chemical milling treatment is not trivial. Even though this treatment shows positive outcome in removing the oxide scale and alpha-case layer, it adds potential threat to the surface integrity and therefore also on the mechanical performance of the components, especially under dynamic loading conditions.

Research aiming towards increased understanding of the behaviour of the commonly used Ti-6Al-4V and Ti-6Al-2Sn-4Zr-2Mo alloys, at conditions related to the manufacturing process and how to fulfil the requirements for next generation of aero-engines is of great importance for the aerospace industry. In particular, better understanding of the surface phenomena taking place during oxidation at elevated temperature and during chemical milling treatment, and the influence of these surface phenomena on the properties of the titanium alloys would result in better performance and decreased manufacturing costs of aero-engine components. Thus, the above needs and challenges were the motivation for performing the work presented in this thesis.

## 1.2 Aim and objectives of the thesis

The aim of the work was to understand the behaviour and properties of Ti-6Al-4V and Ti-6Al-2Sn-4Zr-2Mo alloys when subjected to conditions similar to the ones during manufacturing and service of aero-engine components. These conditions involve exposure of the alloys to elevated temperature and oxygen containing environment (i.e. oxidation phenomena) and chemical treatment in $HF/HNO_3$ acid solutions (i.e. corrosion phenomena).

The following research questions were formulated:

*What is the behaviour of Ti-6Al-4V and Ti-6Al-2Sn-4Zr-2Mo alloys when exposed to elevated temperature in air and in $HF/HNO_3$ solutions, respectively?*

*Is there a difference in the oxidation and corrosion behaviour of the two alloys, and if yes why do they behave differently when exposed to the same environment and/or conditions? What are the parameters responsible for such a difference?*

*How do oxidation and corrosion influence some of the important properties, such as hardness and low cycle fatigue (LCF)?*

In order to provide answers to the research questions stated above, certain objectives were defined. The objectives of the present work could be classified in two groups with respect to the investigated phenomena, oxidation and corrosion, respectively. They were as follows:

*Oxidation*

- Evaluate and compare the thermal stability of Ti-6Al-4V and Ti-6Al-2Sn-4Zr-2Mo at long term isothermal exposure at elevated temperature and oxygen containing environment, such as:
  - Understand and compare the oxidation behaviour in the temperature range of 500-700 ºC up to 500 hours exposure time.
  - Characterise and compare the oxide scales and oxygen enriched layers (alpha-case).
  - Estimate and compare the oxygen diffusion parameters.
- Develop an understanding for and compare the influence of the alloying elements on the oxide scale and alpha-case layer formation for the two alloys.

*Corrosion*

- Understand the influence of the chemical milling treatment on the low cycle fatigue (LCF) properties in Ti-6Al-2Sn-4Zr-2Mo alloy.
- Compare and understand the corrosion behaviour of Ti-6Al-4V and Ti-6Al-2Sn-4Zr-2Mo in $HF/HNO_3$ acid solutions and the influence of different molar concentration ratios between HF and $HNO_3$ acids.

# 2 BACKGROUND

This chapter covers basic introduction for the metallurgical and manufacturing aspects of titanium and its alloys. In addition, the application of Ti-6Al-4V and Ti-6Al-2Sn-4Zr-2Mo for manufacturing aero-engine components is also addressed.

## 2.1 Crystal structure and metallurgical aspects of titanium

Pure titanium (Ti) exists in two crystalline forms, α-Ti (α-phase) with hexagonal close-packed (HCP) crystal structure and β-Ti (β-phase) with body-centred cubic (BCC) crystal structure, see Figure 2.1 [3].

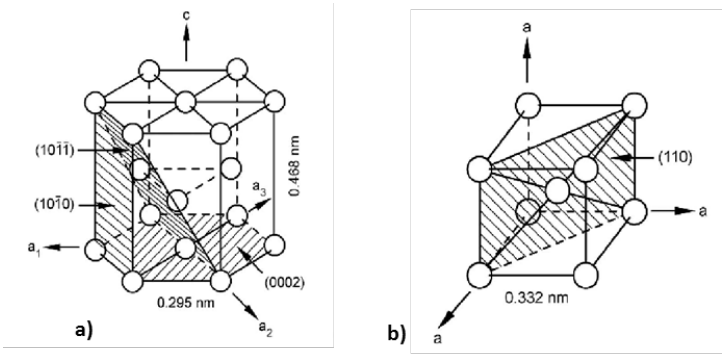


**Figure 2.1** Crystal structures of titanium, a) hexagonal close-packed (α-phase) and b) body centred-cubic (β-phase) [3]

The stability of the two crystalline forms of titanium is dependent on the temperature. At room temperature and temperatures up to 882 ± 2 ºC the α-phase is stable, whereas at temperatures above 882 ± 2 ºC the β-phase stability prevails. The temperature at which α-phase transforms to β-phase is known as the β-transus temperature. The β-transus temperature of titanium is strongly dependent on the purity of the titanium metal, and by adding different alloying elements the β-transus temperature can be changed and adjusted. In general, the existence of titanium in two phases and the feasibility to control the stability of the phases at room temperature is of particular importance for the processing metallurgy of titanium and its alloys, providing excellent basis for adjustment and achievement of outstanding mechanical properties [3].

Alloying elements are divided into three main groups and two subgroups, with respect to their stabilisation effect on the α-phase and the β-phase. Figure 2.2 illustrates the division of the alloying elements and their particular effect on the β-transus temperature.

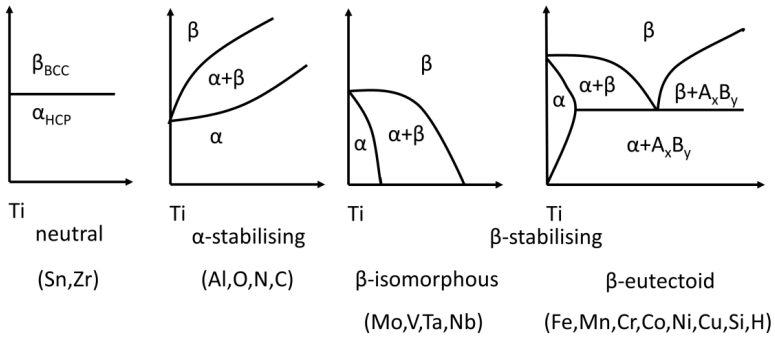


**Figure 2.2** Effect of alloying elements on phase diagrams of titanium alloys [3]

As seen from Figure 2.2, α-stabilising elements like aluminium (Al), oxygen (O), nitrogen (N) and carbon (C) increase the β-transus temperature and stabilise the α-phase. Elements such as molybdenum (Mo), vanadium (V), tantalum (Ta), niobium (Nb), iron (Fe), manganese (Mn), chromium (Cr), cobalt (Co), nickel (Ni), copper (Cu), silicon (Si) and hydrogen (H) stabilise the β-phase and are therefore known as β-stabilisers, decreasing the β-transus temperature. Moreover, the β-stabilizing elements are divided into two subgroups, β-isomorphous and β-eutectoid elements. The elements with high solubility in titanium belong to the group of β-isomorphous elements, whereas the elements that have limited solubility and form intermetallics belong to the β-eutectoid group of elements. Finally, the third group of elements does not affect the β-transus temperature and they are known as neutral elements. Their additions contribute to the solid solution strengthening of titanium alloys [3].

## 2.2 Titanium alloy classification

Titanium alloys are divided into three main classes: α, α+β and β alloys. To which class a titanium alloy belongs to depends on the phase dominating the alloy at room temperature that in turn depends on the type and amount of alloying elements added [2]. Furthermore, the α and β titanium alloys are divided into two subclasses named near-α and metastable or near-β titanium alloys. Figure 2.3 shows an example of a schematic three dimensional phase diagram describing the classification of titanium alloys.

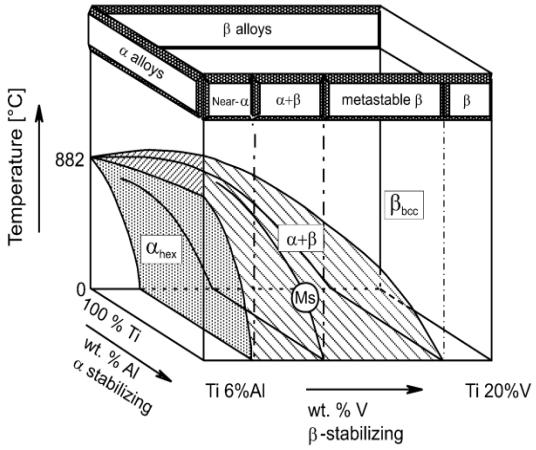


**Figure 2.3** Schematic three-dimensional phase diagram for classification of titanium alloys [2]

### 2.2.1 α and near-α titanium alloys

To this class belong commercially pure titanium (CP-Ti) and titanium alloys that contain either α-stabilising and/or neutral alloying elements such as O, Al and Sn. The different CP-Ti grades differ only in the content of O. The O content drastically increases the strength, but at the same time reduces the ductility [1]. This class of titanium alloys is characterised by high corrosion resistance and good workability and their primary use is in the chemical and petrochemical industries. The near-α titanium alloys contain minor fractions of β-stabilising elements, for example Mo and V. These alloys are used in high temperature applications, i.e.500-550 ºC, since they have high strength and excellent creep resistance. The excellent creep properties are partly due to small additions of Si which form Ti-Si precipitates in the prior beta grain boundaries, thus preventing dislocation climb and deformation [3].

### 2.2.2 α+β titanium alloys

The α+β class of alloys contains α (Al) and β (Mo or V) stabilising elements in larger amounts than in near-α alloys. This class is known to have a good combination of high strength and ductility when compared with the other two main classes of titanium alloys [4]. Ti-6Al-4V is the most utilised titanium alloy because of its good balance of properties such as good castability, plastic workability, heat treatability and weldability [4]. Its production comprises more than 50 % of the total production of titanium alloys in the world.

### 2.2.3 β and near-β titanium alloys

This class is known as metastable β titanium alloys, because it is located in the two phase (α+β) region (see Figure 2.3). β alloys do not form martensite upon fast cooling and usually contains more than 15 wt. % β-stabilising elements. Alloys belonging to this class possess a good combination of properties including the highest tensile strength of all titanium alloys, low Young's modulus, high toughness and fatigue strength [1]. Some drawbacks compared to the α+β class of alloys are increased density, small processing window and high cost. In Table 2.1 some important commercially available titanium alloys are listed along with their characteristic β-transus temperatures and typical tensile and yield strength values [1,3].

**Table 2.1** Important commercial titanium alloys [1,3]

| Commercial name | Composition (wt. %) | $T_\beta$(°C) | $\sigma_{ts}$(MPa)[3] | $\sigma_{ys}$(MPa)[1] |
|---|---|---|---|---|
| **α alloys** | | | | |
| Grade 1 | CP-Ti (0.2Fe, 0.18O) | 890 | 240 | 170 |
| Grade 2 | CP-Ti (0.3Fe, 0.25O) | 915 | 340 | 280 |
| Grade 3 | CP-Ti (0.2Fe, 0.35O) | 920 | 450 | 380 |
| Grade 4 | CP-Ti (0.5Fe, 0.4O) | 950 | 550 | 480 |
| Grade 12 | Ti-0.3Mo-0.8Ni | 880 | 480 | 380 |
| Ti-8-2.5 | Ti-5Al-2.5Sn | 1040 | 790 | 760 |
| **α+β alloys** | | | | |
| Ti-811 | Ti-8Al-1V-1Mo | 1040 | 900 | 830 |
| TIMET 834 | Ti-5.8Al-4Sn-3.5Zr-0.5Mo-0.7Nb-0.35Si-0.06C | 1045 | 1030 | 910 |
| Ti-6Al-2Sn-4Zr-2Mo | Ti-6Al-2Sn-4Zr-2Mo-0.1Si | 995 | 900 | 830 |
| Ti-6Al-4V | Ti-6Al-4V (0.20O) | 995 | 900 | 830 |
| Ti-6Al-4V ELI | Ti-6Al-4V (0.13O) | 975 | 830 | 760 |
| Ti-662 | Ti-6Al-6V-2Sn | 945 | 1030 | 970 |
| Ti-550 | Ti-4Al-2Sn-4Mo-0.5Si | 975 | 1100 | 960 |
| **β alloys** | | | | |
| Ti-10-2-3 | Ti-10V-2Fe-3Al | 800 | 1170 | 1100 |
| Beta 21S | Ti-15Mo-2.7Nb-3Al-0.2Si | 810 | 862 | 793 |
| Ti-15-3 | Ti-15V-3Cr-3Al-3Sn | 760 | 1000 | 965 |
| Beta C | Ti-3Al-8V-6Cr-4Mo-4Zr | 730 | 900 | 830 |
| B120VCA | Ti-13V-11Cr-3Al | 700 | 1170 | 1100 |

## 2.3 Manufacturing of titanium alloys

The manufacturing of titanium alloys is a complex and expensive process that in a simplified manner can be described through the following processing steps [1]:

1) Extraction of titanium sponge by reduction of rutile ($TiO_2$) or ilmenite ($TiFeO_3$) using Kroll's process
2) Purification of the sponge by vacuum distilling process to remove magnesium chloride formed during the Kroll's process
3) Melting the purified sponge with or without addition of alloying elements by vacuum arc re-melting technology (VAR) obtaining ingots

4) Processing of the ingots using different thermal and forming methods to obtain mill products such as bar, plate sheet, strip, wire etc.

Titanium alloys are commercially available in many mill product forms such as: billet, bar, plate, sheet, strip, foil, extrusion, wires and tubing. In order to obtain all these type of mill products various processing operations are applied. Most of these operations are performed above the β-transus temperature, but some of them in later stages are performed below the β-transus. More details about the manufacturing processing steps of titanium alloys can be found elsewhere [1,12].

Among the most common forming methods applied for manufacturing titanium aero-engine components are forging and ring rolling, sheet forming, machining and casting [1,13]. Precision forging is a method used for manufacturing the complex shaped blades in the front and compressor section of aero-engines. This method enables near to net geometrical shape of the blades. Hot forging is used to manufacture titanium rings and engine casings. Large section rings and casings are made from billets by pressing using different tools. Smaller sections are usually made by ring rolling. Large percentage of the aero-engine components are produced by casting. Different types of casting methods are applied such as sand and die casting and investment casting. The investment casting method is the most used because it results in production of components that require no further machining. The production of some aero-engine components requires application of joining techniques, such as welding, in order to assemble sub components into larger structures. Some important welding techniques used for fabrication of aero-engine components are resistance welding by spot and seam, tungsten inert gas (TIG) welding, laser welding and electron beam welding [1].

After a number of conventional thermal and/or thermo-mechanical processing operations, post processing heat treatments are often applied in order to reduce residual stresses as well as to optimise mechanical properties. Conventional heat treatments for titanium alloys include stress relieving, annealing and solution treatment and aging (STA) treatments. Temperatures in the range of 450-800 ºC are commonly used for stress relief of the near-α and α+β Ti alloys.

Annealing is similar to stress relief heat treatment except that it is performed at higher temperature. The main role of annealing treatment is to remove all of the residual stresses and stresses caused by cold and hot working.

Solution treatment and aging (STA) are used to obtain high strength and consists of two steps. During solution treatment the β-to-α-phase ratio is increased and maintained by quenching. During the second step, aging, the α-phase precipitates from the retained β. To avoid contamination with oxygen, hydrogen and nitrogen, all types of heat treatments are preferably performed in vacuum atmosphere.

### 2.3.1 Microstructure, thermo-mechanical processing and mechanical properties

The two phase titanium alloys such as near-α and α+β alloys exhibit several different types of microstructures, such as lamellar, equiaxed and bimodal types. These microstructures can be

obtained through different thermo-mechanical processes. In principle, the thermo-mechanical process for achieving a desired microstructure involves four steps: 1) homogenisation, 2) deformation, 3) recrystallization and 4) annealing [3].

Lamellar microstructures can be obtained through cooling from the β-phase field. Once the temperature falls below the β-transus temperature, for moderate cooling rates β-phase starts to transform to α-phase by nucleating at the prior β grain boundaries and then grow as lamellae's into the prior β grains as shown schematically in Figure 2.4.

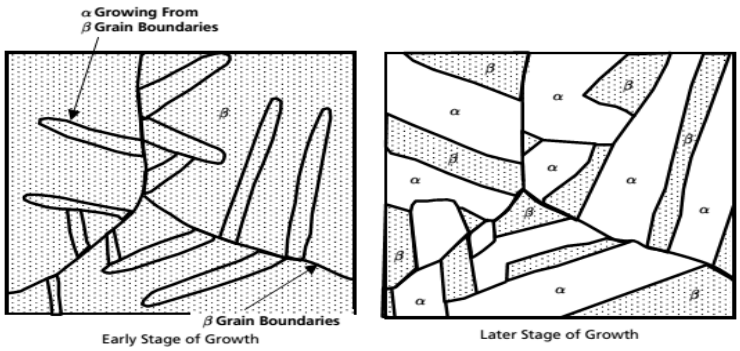


**Figure 2.4** Formation of lamellar microstructure in titanium alloys [14]

The most important processing parameter for obtaining lamellar microstructure is the cooling rate from the β-phase field during the recrystallization step. The cooling rate determines the size of the α-lamellae, the size of the α-colony and the thickness of the grain boundary α layer. Figure 2.5 shows the effect of three different cooling rates on the microstructural features in fully lamellar microstructure known as "basket weave" or Widmanstätten microstructure.

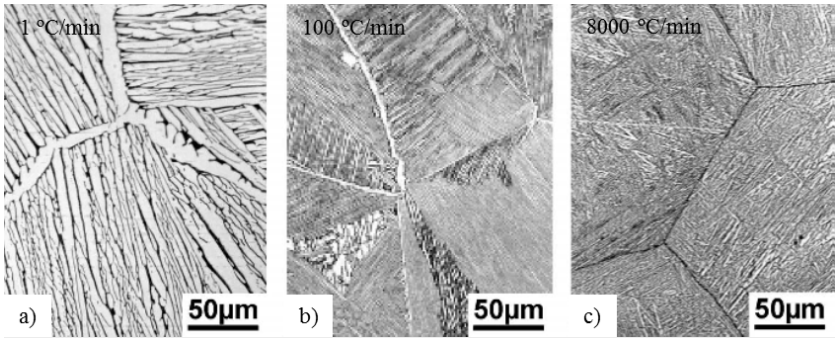


**Figure 2.5** Cooling rate effect on the lamellar microstructure of Ti-6Al-2Sn-4Zr-2Mo after cooling from a temperature above the β-transus, a) at 1 ºC/min, b) 100 ºC/min and c) 8000 ºC/min [3]

One way to obtain equiaxed microstructure is through sufficiently low cooling rate from a temperature slightly lower than the β-transus. This will result in formation of primary α grains and no α-lamellae within the β grains. Another route is through inducing enough plastic deformation followed by a recrystallization treatment at sufficiently low temperatures, at which the equilibrium volume fraction of α-phase is high enough to form equiaxed microstructure directly from the deformed lamellar structure.

Figure 2.6 shows equiaxed microstructure of Ti-6Al-4V alloy with two different grain sizes after recrystallization. The grain size of the equiaxed microstructure can be adjusted through shorter or longer annealing. Moreover, the annealing temperature will define the primary α volume fraction.

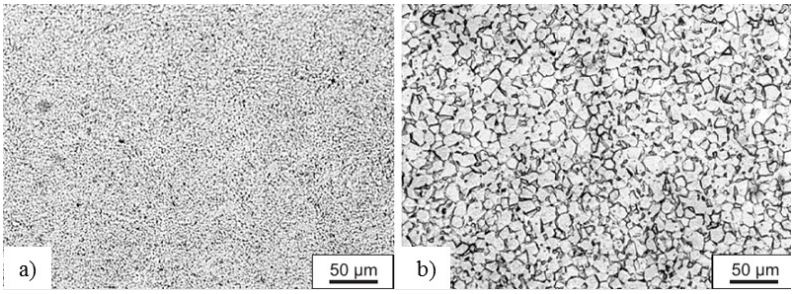


**Figure 2.6** Equiaxed microstructures of Ti-6Al-4V after recrystallization, a) fine and b) coarse [2]

A typical bimodal microstructure can be seen in Figure 2.7. The microstructure consists of primary α grains dispersed in a transformed β matrix, consisting of α and β lamellas. Therefore, the bimodal microstructure is considered as a combination of lamellar and equiaxed microstructure. Obtaining bimodal microstructure involves homogenisation above the β-transus temperature followed by plastic deformation in the α+β phase field, a recrystallization treatment and aging and/or stress relief treatment at temperatures in the α+β phase field.

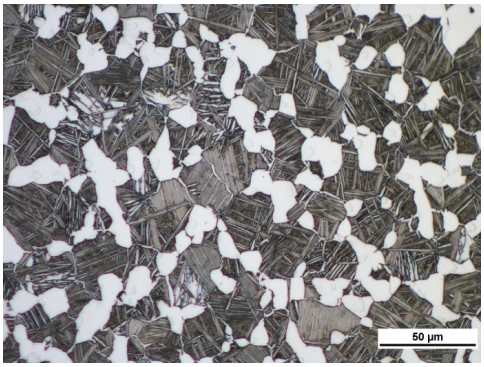


**Figure 2.7** Bimodal microstructure of Ti-6Al-2Sn-4Zr-2Mo alloy

The mechanical properties of titanium alloys depend on the alloying elements and on different processing steps such as various forming- and thermo-mechanical treatments.

*Alloying* is used to adjust the properties through adding and/or changing the chemical composition of the alloy. Different elements are used to modify the strength via precipitation and/or solid solution hardening mechanisms. Alloying also specifies the physical properties of titanium alloys such as density, Young's modulus and thermal expansion coefficient. Moreover, the alloying also determines the chemical resistance of the alloy such as oxidation and corrosion resistance [2].

*Processing* balances the mechanical properties of titanium alloys, by obtaining the desired type of microstructure that fulfils specific properties required by the final application [2].

In general, the properties of different titanium alloy classes are specified by the arrangement, volume faction and individual properties of the α-phase and the β-phase [1-3]. The α+β and β alloys have higher density than α titanium alloys. This is due to the alloying with heavy elements such as V and Mo. In terms of strength, α titanium alloys show moderate strength, because they consist only of α-phase. On the contrary, the α+β and β titanium alloys consist of a mixture of both phases (α and β) and can therefore be strengthened to higher strength levels. However, because of the high strength, the β alloys are featured with low ductility [2]. Moreover, the ductility and the fracture toughness are strongly dependent on the microstructure type (i.e fine, coarse, lamellar or equiaxed). The excellent creep resistance of the near-α alloys is because of the limited ability of atoms to diffuse and to deform the hexagonal closed-packed crystal structure in comparison with the body centred-cubic crystal structure. Thus, increase of the volume fraction of β-phase in titanium alloys results in lower creep resistance. The excellent corrosion resistance of titanium alloys is because of the naturally present thin, dense and highly protective oxide layer ($TiO_2$), forming at room temperature. In general, α alloys are more corrosion resistant than β alloys. Titanium alloys exhibit poor oxidation resistance because of the high reactivity of titanium with oxygen, which is more favourable at higher temperatures and β alloys are more susceptible than α alloys. Welding of titanium alloys is difficult due to the high reactivity with oxygen and hydrogen and therefore welding has to be performed in vacuum or inert gas environments [1].

The microstructure specifies the mechanical properties and hence the mechanical performance of the titanium alloys. Table 2.2 quantitatively shows how the fine, coarse, lamellar and equiaxed microstructures influence selected mechanical properties. For example, the fine grain microstructure is featured with more pronounced tensile strength, higher ductility, fatigue strength and oxidation resistance than the coarse grained microstructures [2]. In contrast, the coarse grain microstructure has considerably better creep resistance than the fine grained microstructures. The equiaxed microstructures deliver high ductility and high fatigue resistance; whereas the lamellar microstructures have high fracture toughness, excellent creep resistance and fatigue crack growth resistance. The high fracture toughness of the lamellar microstructures can be explained by the ability to more easily deflect propagating cracks along the differently oriented α-lamella colonies. The bimodal microstructure combines the good mechanical properties of the lamellar and equiaxed microstructures, respectively, and therefore exhibits well balanced overall mechanical properties.

**Table 2.2** Influence of microstructure on selected mechanical properties for titanium alloys [2]

| Property | Lamellar | Equiaxed | Fine | Coarse |
|---|---|---|---|---|
| **Young's Modulus** | No effect | Positive/negative (texture) | No effect | No effect |
| **Tensile Strength** | Negative | Positive | Positive | Negative |
| **Ductility** | Negative | Positive | Positive | Negative |
| **Fracture Toughness** | Positive | Negative | Negative | Positive |
| **Fracture Crack Initiation** | Negative | Positive | Positive | Negative |
| **Fracture Crack Propagation** | Positive | Negative | Negative | Positive |
| **Creep Strength** | Positive | Negative | Negative | Positive |
| **Oxidation rate** | Positive | Negative | Positive | Negative |

For fully lamellar microstructures the most important microstructure parameters are the prior β grain size, α-colony size, α-lamellae thickness and the morphology and distribution of the inter-lamellar interface, i.e. β-phase. In Figure 2.8 these microstructure parameters are indicated [15].

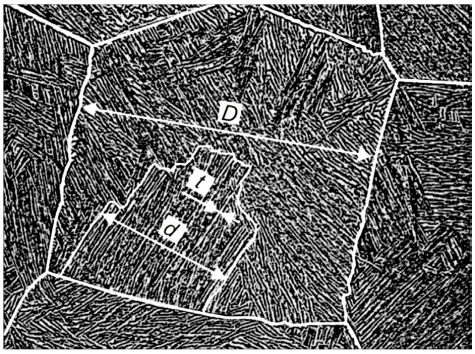


**Figure 2.8** Important microstructural parameters influencing the mechanical properties of lamellar microstructure: D-prior β grain size, d-size of the colony of parallel α-lamellae and t-thickness of α-lamellae [15]

The α-colony size is determined by the cooling rate from the β-phase field and its maximum size is limited by the size of the prior β grain size. Faster cooling rate from the β-phase field results in reduction of the α-colony size, i.e. decreasing of the effective slip length and consequently increase of the yield strength. In addition, faster cooling rate (between 100-1000 ºC/min) also results in increase of the tensile ductility. For even higher cooling rates the ductility decreases significantly [3].

The change of ductility as a function of cooling rate is reflected by changes in fracture mode. Slow cooling rates results in a ductile trans-crystalline dimple type of fracture, whereas a ductile inter-crystalline dimple type of fracture occurs along the continuous α layers at the β grain boundaries for fast cooling rates [3]. Figure 2.9 shows the change of the fracture mode for Ti-6Al-2Sn-4Zr-2Mo when cooled down from the β-phase field with slow and fast cooling rates, respectively.

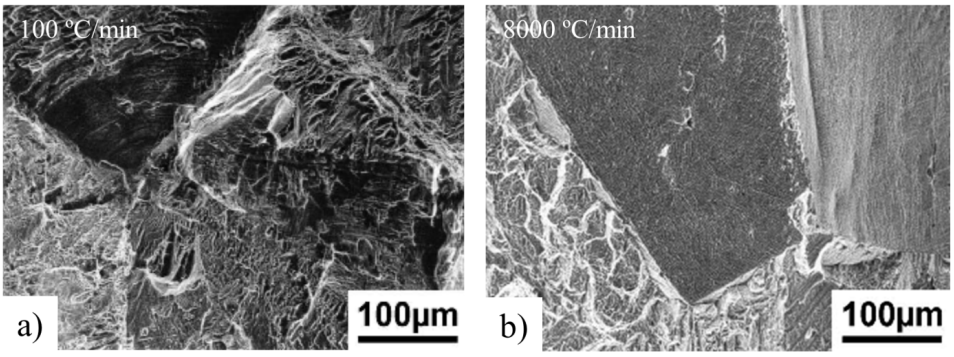


**Figure 2.9** Change of the fracture mode for tensile fracture surfaces of lamellar microstructure of Ti-6Al-2Sn-4Zr-2Mo as function of the cooling rate from the β-phase filed a) 100 ºC/min and b) 8000 ºC/min [3]

For fully lamellar microstructures, the continuous α layers in the prior beta grain boundaries are known to be preferential regions for plastic deformation and therefore premature crack initiation can occur in these regions. As discussed before, this affects the ductility. To what extent the ductility will be affected depends on the strength difference between the continuous α layers and the lamellar matrix. In addition, the ductility is also dependent on the prior β grain sizes. For example, a decrease of the prior β grain size from 600 to 100 µm results in significant increase of the tensile ductility [3].

The high cycle fatigue (HCF) strength of titanium alloys is mainly dependent on the resistance to dislocation movement and therefore usually on the yield stress [3]. In general, the HCF strength for lamellar microstructures is also related to the microstructural parameters (colony size i.e. slip length) and shows similar dependence as the yield strength. For low cycle fatigue (LCF) strength the resistance to crack initiation and propagation of small surface cracks (i.e. micro-cracks) are most important.

Crack nucleation and the first stages of crack propagation occur in a very selective manner at the weakest regions in the microstructure. The micro-crack propagation behaviour depends on the slip length. By increasing the slip length the micro-crack propagation rate is also increasing. In lamellar microstructures the α-colony boundaries (and to some extent also the individual α-lamellas) act as strong obstacles for micro-crack propagation. Decreasing α-colony size results in decreasing of the micro-crack propagation rate. Therefore, the LCF strength of titanium alloys with lamellar microstructure is always improved by increasing the cooling rate from the β-phase field. Figure 2.10 shows a diagram that describes the micro- and macro-crack propagation rate of Ti-6Al-4V alloy as function of coarse and fine lamellar microstructure for a wide stress intensity factor range ($\Delta K = K_{max} - K_{min}$). From the diagram it can be observed that the micro-cracks propagate and grow much faster at low ΔK values than the macro-cracks and this growth rate is more pronounced in the coarse lamellar microstructure than in the fine lamellar microstructure [3].

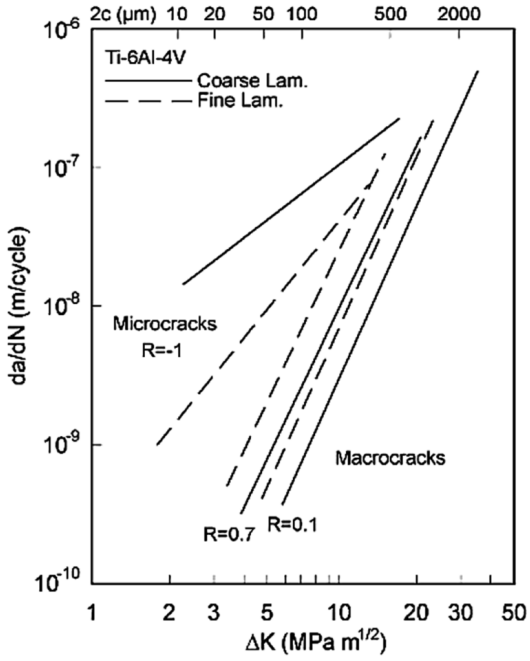


**Figure 2.10** Fatigue crack propagation of coarse and fine lamellar microstructures of Ti-6Al-4V [3]

As mentioned before, the α-colony boundaries, the α-lamellae and the β grain boundaries are strong obstacles for the dislocation movement and consequently for micro-crack propagation.

When micro-crack reaches one of these obstacles it changes the growth direction causing lowering of the micro-crack propagation rate. Therefore, in the case of fine lamellar microstructures, the micro-cracks are initially nucleating at the thickest α-lamellae and then propagate along the interface. Later the micro-cracks are departing from the interface and propagate through the matrix with slow micro-crack propagation rate.

### 2.3.2 Chemical milling and/or pickling

The manufacturing processing routes of titanium alloy components involve different thermo-mechanical processes and heat treatments which may contaminate the titanium surface. One such surface contaminant is oxygen. Titanium is highly reactive with oxygen and even though some of the thermo-mechanical processes and heat treatments are carried out in vacuum and/or inert environments, surface oxygen contamination occurs. Oxygen is an interstitial element that diffuses preferably in the α-phase and it significantly increases the strength through solid solution strengthening. Because oxygen is strong α-stabiliser, increased oxygen concentration elevates the β-transus temperature. When oxygen diffuses into the surface of titanium, a hard and brittle subsurface layer is formed. This oxygen enriched layer is normally referred to as alpha-case and may drastically degrade the mechanical performance of titanium alloy components. Therefore, its presence is strictly controlled and its removal mandatory. The hard and brittle layer of alpha-case is either mechanically machined away or chemically treated using chemical milling and/or pickling treatments by dissolving, i.e. etching, away the surface of the alloys in baths that contain mixtures of strong acids. Chemical milling and/or pickling are suitable processing methods to remove surface oxygen contamination because of their possibility to handle components with complex geometry. It is interesting to note that chemical milling and pickling are conventional treatments that are adopted from the steel industry for removal of surface oxygen contaminations. Both treatments are based on the same principle which involves immersion of the component into a solution containing hydrofluoric (HF) and nitric acid ($HNO_3$) for a controlled period of time. The difference between pickling and chemical milling is in which stage in the manufacturing-processing route they are applied. Pickling is applied in between forming and heat treatment steps during thermo-mechanical manufacturing of mill products, whereas chemical milling is used after the last thermo-mechanical step in order to remove the alpha-case layer and to achieve a surface finish with acceptable roughness.

Chemical milling treatment is also used as method for cutting off material to produce various features on the surface of different titanium alloys components [16]. Figure 2.12 shows one example where chemical milling treatment is used to produce features on the surface of a compressor casing which is fabricated from Ti-6Al-4V. When the chemical milling treatment is used for manufacturing components, like the one shown in Figure 2.11, the process is performed under strictly controlled conditions and in accordance with aerospace standardised specifications [17].

The milling process normally involves five steps consisting of cleaning, masking, scribing, etching and de-masking [16]. The cleaning step is one of the most important steps and must

therefore be carried out thoroughly in order to remove any type of surface contamination that might compromise the uniform adhesion of the mask that is applied in the next step. Masking involves application of a protective chemical resistant coating on the surface of the component. The mask must be cured and cooled at room temperature prior to the next step which is scribing or cutting through the masked area with a tool. This process is used to remove the chemical resistant coating on regions of the component surface where attack of the acid solution is desired.

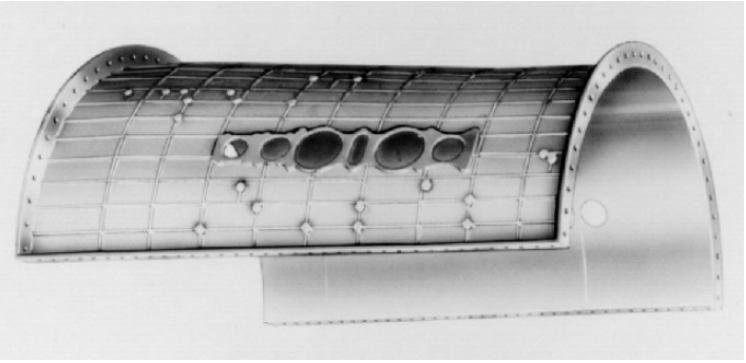

**Figure 2.11** Chemical milling treatment used for making the feature lines on an upper half compressor casing fabricated from Ti-6Al-4V [3]

The following step is etching, i.e. immersion of the cleaned, masked and scribed component into the tank that contains the acid solutions. The immersion time is estimated with respect to the desired removal depth of material by using test samples from the same material with the same thermo-mechanical history as the real component. The removal rate, i.e. the etching rate of material, is a function of the chemical activity which depends on the chemical composition ratio of the acids, temperature of the bath, immersion time and aging of the chemical milling solution. Immediately after the etching step, the component is either washed and/or immersed into a tank of cold water, in order to stop the material removal action by the acids. Before removal of the mask a de-oxidising bath is used to remove deposits on the surface from the etching process such as, oxide film and smut deposits (i.e. metal oxides, chemical compounds or unreacted finely divided particles of the base alloy). This is followed by additional rinse in cold water and now the component is ready for the de-masking step. Removal of the well adherent protective coating can be performed either manually or by using chemicals. Chemical removal softens and swells the mask in order to reduce its adhesion and the mask is removing either by air or water pressure. A final spray-rinse with cold water is done to remove any trapped residuals from the de-masking solution, thereafter the component is left to dry.

One of the major problems related with chemical milling and pickling of titanium alloys is hydrogen absorption as result of a chemical reaction of titanium with the HF acid. Hydrogen is an interstitial element that has the ability to diffuse into the bulk titanium metal and cause

hydrogen embrittlement. Titanium alloys that contain higher volume fractions of β-phase are more susceptible. Hydrogen embrittlement is known to be detrimental for important mechanical properties and could lead to premature failure. In order to prevent hydrogen formation a strong oxidising agent, $HNO_3$ acid, in combination with HF acid is used. The $HNO_3$ acid lowers the hydrogen pick-up significantly as result of oxidising the hydrogen into water and gaseous mixtures of nitric monoxide (NO) and nitric dioxide ($NO_2$), i.e. $NO_x$ mixture.

The recommended chemical composition in weight percentage for chemical milling and/or pickling is between 1-5 wt. % HF and up to 20 wt. % $HNO_3$ [18]. Because the etching rate and hydrogen pick-up is dependent on the exact material composition and its thermo-mechanical and heat treatment history, different titanium alloys will etch differently and adjustments of the chemical composition of the bath is required. In addition, it is common in industrial practice to use various chemical additives such as surfactants in combination with the HF and $HNO_3$ acids, in order to provide better final surface finish of the components. Proper amount of commercially pure titanium sponge is also added to the bath providing moderate activity of the acid solution and preventing vigorous chemical reactions. The dissolution of titanium in HF acid is an exothermic reaction resulting in release of energy in form of heat (6338 cal/g) [16] and therefore the acid bath tanks are equipped with cooling systems. The temperature of the bath is an important parameter that contributes to the efficiency of the milling process controlling the etching rate and therefore special attention on the temperature of the acidic bath is required. Normally it is considered that the bath temperature should never exceed 55 ºC, because at higher temperatures excessive red fuming gas of nitric oxides ($NO_x$) are generated. This gas is highly toxic and reduces the activity of $HNO_3$ acid in the bath.

## 2.4 Titanium alloys in aerospace applications

Aerospace industry is a large user of titanium [19] and Figure 2.12 illustrates the weight percentage of different structural materials used in commercial aircrafts, differentiated between airframe and aero-engine.

The main reasons for using titanium alloys in aerospace applications can be summarised with the following: 1) weight savings (replacement of heavier Fe-based and Ni-based alloys); 2) space savings (replacement of Al alloys); 3) operating, i.e. service temperature (replacement of Al alloys); 4) corrosion resistance (replacement of Fe-based and Al-based alloys); and 5) compatibility with polymer matrix composites (replacement of Al-based alloys and low carbon Fe-based alloys) [4].

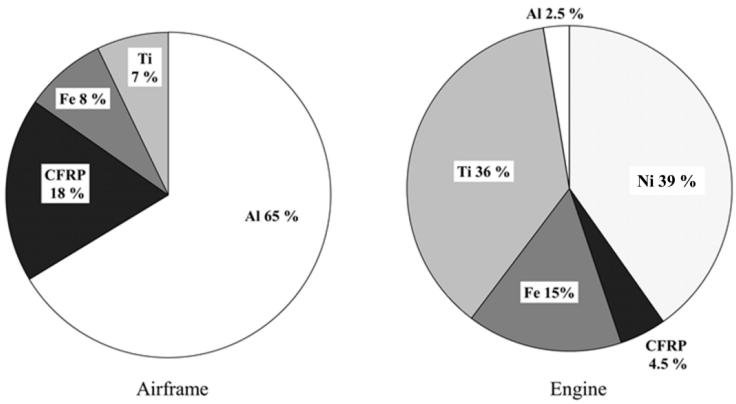


**Figure 2.12** Weight percentages of composites, Al-based, Ti-based and Fe-based alloys used in commercial aircrafts in the airframe and the engine as structural materials [19]

The weight savings are due to the lower density of titanium (4.5 g/cm$^3$) compared with Fe (7.9 g/cm$^3$) and Ni (8.9 g/cm$^3$) based structural materials [3]. The higher specific strength for titanium alloys makes them suitable for substitution of the Al alloys which also results in weight savings. Moreover, titanium alloys have advantages over Al alloys when the service temperature exceeds 130 ºC [4]. The corrosion resistance of titanium alloys is higher compared to Fe-based and Al-based alloys. Furthermore, titanium alloys are galvanically more compatible with polymer matrix composites than Al alloys and low carbon Fe-based alloys. All above mentioned reasons makes titanium alloys to be the second most abundant material used in commercial aero-engines (36 %), after Ni-based super alloys (39 %).

Aero-engine components can be subjected to high mechanical and/or thermal stresses during service. Such demanding service conditions require selection of materials that possess high strength and high thermal tolerance, which titanium alloys do. There are various types of titanium alloys used in aerospace applications, but for aero-engine components mainly two alloys are significantly important, Ti-6Al-4V and Ti-6Al-2Sn-4Zr-2Mo.

Ti-6Al-4V is used for static and rotating aero-engine components [4,19-21]. Castings of Ti-6Al-4V are used for large static components with complex geometry. Ti-6Al-4V is also used for manufacturing fan blades, disks in the low pressure compressor and blades where the operating temperatures are not exceeding 315 ºC [4,22].

Ti-6Al-2Sn-4Zr-2Mo is the main alloy used in gas turbine aero-engines because of its extraordinary creep resistance properties and thermal resistance up to 540 ºC [4,20]. This alloy is used in the compressor for rotating components such as blades, disks and rotors where the operating temperature is too high for Ti-6Al-4V to be used.

It should be pointed out that “maximum working temperature” is a very broad term. In reality the maximum temperature depends on the working condition for each specific aero-engine

component. All commercially used titanium alloys, when exposed to temperatures exceeding 480-500 ºC and ambient atmosphere, will start to form hard and brittle alpha-case layer unless they are protected with high thermal protective coating. For dynamically loaded highly stressed aero-engine components, critical for the engine performance, no alpha-case is allowed to be formed, even after long time in service. Therefore, the use of Ti-6Al-2Sn-4Zr-2Mo in such applications is limited to working conditions where the maximum temperature does not exceed 480 ºC.

# 3 LITERATURE REVIEW

The present chapter consists of two sections that are providing literature review for oxidation and corrosion during chemical milling of titanium and its alloys. Section 3.1 refers to the oxidation in air at elevated temperature, thereby highlighting the oxidation of Ti-6Al-4V and Ti-6Al-2Sn-4Zr-2Mo. Section 3.2 considers the corrosion processes taking place during chemical milling treatment in $HF/HNO_3$ acid solution used for removal of the oxide scale and oxygen enriched layer, i.e. alpha-case.

## 3.1 High temperature oxidation of titanium and its alloys

### 3.1.1 Fundamental principles of metal oxidation

Metal oxidation is a special type of degradation of metals which occurs when the metal is subjected to oxygen and/or other oxidising environment. Most metals in ambient conditions are thermodynamically unstable [23,24]. The metal's instability may be of little or no practical meaning at room temperature because of the slow reaction rate, but at elevated temperatures the instability of the metal increases rapidly. High temperature oxidation of metals is a broad field that is important from scientific and technological point of view [23-27]. It is of high importance to know the oxidation reaction and which the oxidation products are, as well as the kinetics and the mechanisms of the oxidation process and on what they are dependent on. The oxidation of metals usually results in oxide scale formation and it sometimes also involves dissolution of the gas species (i.e. oxygen) into the metal substrate causing embrittlement.

The reaction of a metal (Me) and oxygen gas ($O_2$) could be described through the following chemical equation:

$$\mathrm{aMe\,(s)} + \left(\mathrm{b}/2\right)\mathrm{O_2\,(g)} = \mathrm{Me_aO_b\,(s)} \qquad (3.1)$$

Although reaction (3.1) seems to be simple, the metal oxidation is dependent on many factors and therefore the oxidation mechanisms are complex [24]. Driving force for oxidation and oxide scale formation is the free energy change associated with the formation of the oxide. The oxide will form only if the ambient oxygen pressure is larger than the dissociation pressure of the oxide in an equilibrium state with the metal. This can be described with the expression (3.2) for the chemical reaction (3.1) [24].

$$p\mathrm{O_2} \geq \exp\left\{-\frac{2\Delta G^{\circ}(\mathrm{Me_aO_b})}{bRT}\right\} \qquad (3.2)$$

The standard free energy of oxide formations is a function of temperature. The corresponding dissociation pressures of oxides for some important metal oxides are summarized in the form of Ellingham/Richardson diagrams and Figure 3.1 shows a diagram for some oxides important in high temperature oxidation [24]. The Ellingham/Richardson diagrams can be used for qualitative measurements of the oxide stability at different temperatures and oxygen partial pressures. The diagrams can also be used qualitatively to determine the relative ease of reduction for a particular

oxide to metal and to determine the equilibrium oxygen partial pressure of an oxide at a certain temperature. In addition, they are also used to determine the ratio of $CO/CO_2$ and $H_2/H_2O$ required for reducing the oxide. As seen from the diagram shown in Figure 3.1, the stability of the oxides is increasing going from $Cu_2O$ to CaO and the most stable oxides have large negative $\Delta G^o$ values. However, the drawback of the Ellingham/Richardson diagram is that it does not provide any information about the oxidation kinetics.

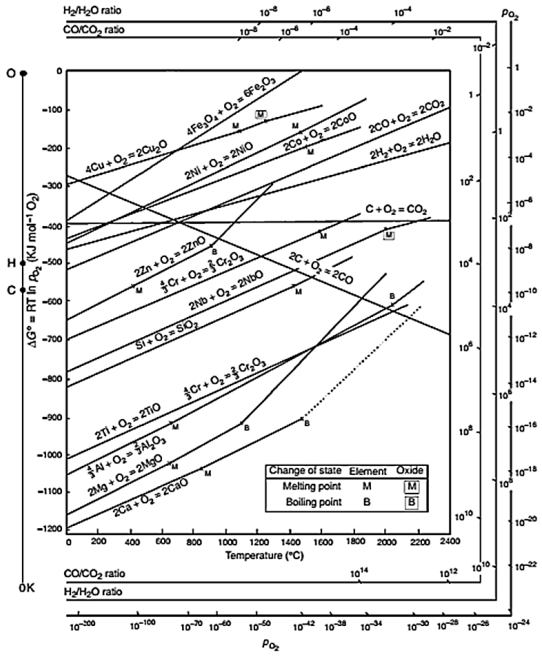


**Figure 3.1** Ellingham/Richardson diagram for some important oxides in high temperature oxidation [24]

Knowledge of the reaction rates and kinetics for metal oxidation is important for elucidation of the oxidation mechanisms. The reaction rates and corresponding rate equations are dependent on a number of factors such as temperature, oxygen pressure, time of the reaction, surface preparation and pre-treatment of the metal. The following rate laws are commonly encountered in oxidation of metals: logarithmic, parabolic and linear [23-27]. These rate laws represent only ideal cases and deviations and intermediate rate equations are also encountered. In continuation, the three ideal rate laws will be presented.

**Logarithmic law**

The logarithmic rate law applies for many metals at temperatures below 400 ºC. This rate is characterised by fast initial rate that slows down to low or negligible rates with respect to time. The logarithmic rate law is described through the following rate equations [24]:

$$\text{Direct: } x = k_{\log} \log(t + t_0) + A \tag{3.3}$$

$$\text{Inverse: } \frac{1}{x} = B - k_{il} \log t \tag{3.4}$$

where $x$ refers to the oxide scale thickness, the amount of oxygen consumed per unit surface area of the metal or the amount of metal transformed to oxide, $t$ represents the oxidation time, $k_{\log}$ and $k_{il}$ are rate constants and $A$ and $B$ are constants.

Commonly the logarithmic rate law is described as oxide film formation that does not involve dissolution of the oxidising gas species into the bulk metal [24]. The model developed by Mott and Cabrera [28] explain the logarithmic rate law for metal oxidation. The authors have described this rate law by formation of electric field effects across very thin oxide films (~ 50 Å) where the rate determining reaction is the transfer of electrons across the thin oxide film itself.

**Parabolic law**

At temperatures above 400 ºC many metals obey parabolic rate law with respect to time. The parabolic rate law is featured with continuous increase of oxide thickness with time and it can be described by the following rate equations [24]:

$$\text{Differential: } \frac{dx}{dt} = \frac{k_p^{'}}{x} \tag{3.5}$$

$$\text{Integrated: } x^2 = 2k_p^{'}t + C = k_p t + C \tag{3.6}$$

where $k_p^{'}$ and $k_p$ are the parabolic rate constants and $C$ is the integration constant. The parabolic rate law indicates that uniform diffusion of one or both reactants through the oxide scale is the rate determining process [24].

The parabolic rate law may be interpreted by the Wagner's [29] oxidation mechanism model. This model applies for high temperature oxidation of metals and considers that the rate determining process is diffusion of ion species (cations and/or anions) across the oxide scale.

**Linear law**

The linear law of oxidation may be described by the following rate equations [24]:

$$\frac{dx}{dt} = k_l t \tag{3.7}$$

$$x = k_l t + C \tag{3.8}$$

where $k_l$ is the linear rate constant and $C$ the integration constant. Contrary to the parabolic and logarithmic rate laws, the linear rate law is constant with time and therefore independent of the amount of gas or metal. In principle, the linear rate law occurs due to formation of cracks and pores in the oxide scale as result of the stress development during oxide growth [30]. Moreover, the linear oxidation rate is strongly dependent on the oxygen pressure in the oxide scale and therefore it is considered that the rate determining processes are phase boundary reactions at the metal/oxide interface [30].

Figure 3.2 illustrates the different oxidation rate laws in the form of change of the oxide scale thickness with respect to oxidation time.

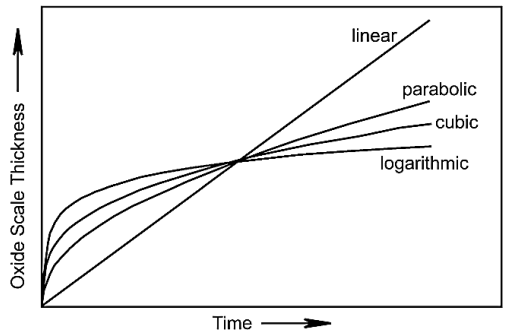


**Figure 3.2** Schematic representation of variation of oxide thickness with respect to oxidation time for different oxidation rate laws [24]

As mentioned before, the oxidation of metals is a complex process and seldom obeys only one rate law. It has been commonly reported for various metals that the oxidation obeys a combination of the rate laws described above [25]. Cubic rate is a law that comprises a combination of logarithmic and parabolic rate laws and it was found for many metals at intermediate temperatures [26]. Another rate law known as para-linear rate law includes a combination of parabolic and linear rate. The parabolic rate is obeyed at initial time of the oxidation and at prolonged oxidation times the parabolic rate changes to linear.

Thermogravimetry is a conventional method used for evaluation of oxidation rate laws and the behaviour of metals. This method involves monitoring of the mass change during time of a

metal with specified surface area. The mass change is manifested as weight gain per surface area and it is occurring because of oxide scale formation and simultaneous diffusion of oxygen into the metal. Measuring the weight gain per surface area of the metal with respect to oxidation time will result in one of the curves shown in Figure 3.2. The obtained curves can be analytically treated with the following equation that comprises all the rate laws presented above [24]:

$$\left(\frac{\Delta W}{A}\right)^n = k_n \cdot t \tag{3.9}$$

where $\Delta W$ is the weight gain, $A$ is the surface area, $k_n$ is the rate constant, $t$ is the exposure time and $n$ is the reaction index. At constant temperature, $\Delta W$ is linear if $n = 1$, parabolic if $n = 2$, cubic if $n = 3$ and quartic if $n = 4$ [24]. The $n$ values could be obtained by regression analysis of log-log plots of $\Delta W$ vs. $t$.

The temperature dependence of the reaction constant $k$ is described with the Arrhenius law [24]:

$$k = k_0 \cdot \exp\left(-\frac{Q}{RT}\right) \tag{3.10}$$

where $k_0$ is the temperature independent pre-exponential factor, $Q$ is the activation energy, $R$ is the universal gas constant and $T$ the absolute temperature in Kelvins. Arrhenius plot of the log $k$ values versus $1/T$ enables comparison of the oxidation resistance of different metals and alloys over broad temperature range and allows computation of the activation energy for the oxidation.

### 3.1.2 Oxide scale and subsurface oxygen enriched layer (alpha-case) formation

The oxidation of metals at elevated temperatures involves formation of uniform oxide scale that covers the metal surface and simultaneous dissolution of oxygen into the bulk metal below the oxide scale. This oxide scale and subsurface oxygen enriched layer formation can be described by the Wagner's model for high-temperature oxidation of metals [29].

Figure 3.3 schematically shows the oxygen concentration profile during oxide scale and oxygen enriched layer formation as suggested by Wagner's model. In the case of titanium, the later process is known as the responsible one for formation of alpha-case. Alpha-case is defined as a continuous hard and brittle layer that forms because of oxygen diffusion into the hexagonal closed-packed crystal structure of α-Ti. The name alpha-case originates from the fact that oxygen is a strong α-stabilising element and its elevated content in titanium and its alloys promotes increase of the β-transus temperature and triggers phase transformation of the retained β-phase to α-phase. Thus, this result in increase of the α/β phase ratio in two phase titanium alloys.

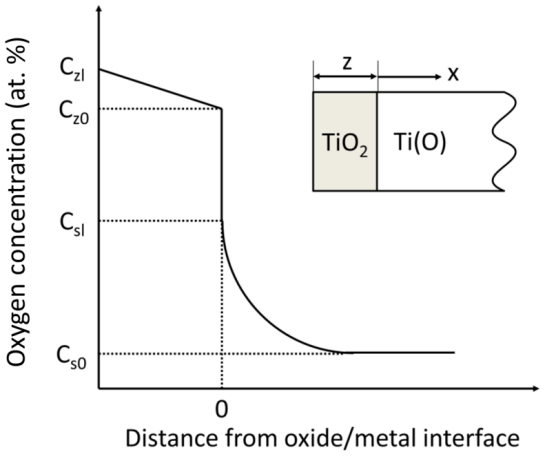


**Figure 3.3** Oxygen concentration profile of oxidised titanium according to Wagner's model [31]

As seen in Figure 3.3 the oxygen concentration profile consists of two individual concentration profiles, one for the oxide scale ($TiO_2$) and the other one for the oxygen enriched layer, i.e. the alpha-case layer. Both profiles are characterised by particular thickness; $TiO_2$ has thickness $z$, whereas the oxygen enriched layer has thickness $x$. The oxygen enriched layer has elevated oxygen content compared to the base metal and its highest oxygen concentration is at the oxide/metal interface, i.e. the $C_{sl}$ point. Further into the base metal, the oxygen concentration gradually decreases and reaches the oxygen bulk concentration at distance $C_{s0}$. The oxygen concentration at the oxide/metal interface ($C_{sl}$) is dependent on temperature and time and it may reach a maximum value of 33 at. %, see the Ti-O phase diagram in Figure 3.4 [32].

The oxide scale formation could be described through a sequence of steps that include oxygen adsorption, nucleation of the oxide, lateral growth of the oxide and formation of compact oxide scale [2]. The first step in oxidation, oxygen adsorption, involves attachment of oxygen on the metal surface through chemisorption or physical adsorption [24]. The difference between the two types of adsorption lies in the bonding between the gas molecules and the metal surface. In physical adsorption gases are bound to the metal surface through week van der Waals forces, whereas in chemisorption stable chemical bonds are formed. Once the oxygen molecules are adsorbed they dissociate and start being adsorbed as atoms. When the metal surface is saturated with adsorbed oxygen atoms oxide nuclei are formed that grow laterally. This lateral growth of the nuclei results in formation of a compact oxide scale that covers the surface of the metal and continued growth of the oxide scale is mainly controlled by mass transport though the scale itself. The mass transport in metal oxides involves transport of electrons and/or ionic species (i.e. cations and anions) through the oxide scale which allows the oxides to behave as semiconductors

[33]. The large number of imperfections in the metal oxides consequently contributes to the mass transport properties [34]. Most common imperfections in metal oxides are metal ions located at the interstitial positions, non-metal ion vacancies, metal ion vacancies and non-metal ions located in the interstitial positions [34]. Based on the conductivity of the metal oxides and the type of imperfections present, the oxides are classified into n and p-type. In general, the n-type oxides grow inwards, whereas the p-type oxides grow outwards with respect to the metal/oxide interface. For example, during oxidation of titanium the formed product is an n-type anion defective $TiO_2$ through which oxygen ions diffuse and react further with the titanium metal [35]. The reaction front is the metal/oxide interface and the oxide scale grows inwards. Except the ionic nature and the conductivity of the oxide scale, the mass transport through the oxide scale can also be affected by grain boundary diffusion at low temperatures and lattice diffusion at high temperatures. In addition, the formation of porous oxide structures, spallation and cracking of the oxide could contribute to the mass transport through the oxide scale and consequently change of the oxide growth rate [23,24].

Titanium and its alloys are highly reactive with oxygen when they are subjected to oxidising environments. This can be described by the Ti-O bond energy (2.12 eV) [36], that is comparable to the Ti-Ti bond energy (2.56 eV) [37]. At room temperature, titanium reacts with oxygen and this reaction leads to formation of a thin, dense, well adherent and passive $TiO_2$ layer. The $TiO_2$ layer has a significant role in protection of the metal from further oxidation and also provides corrosion resistance of the metal in different corrosive environments. Different types of stable titanium oxides can be formed depending on temperature and oxygen pressure. Some of the stable forms of oxides are $Ti_2O$, TiO, $Ti_2O_3$, $Ti_3O_5$, $Ti_nO_{2n-1}$ ($4 < n < 38$) and $TiO_2$. However, for Ti oxidation at temperatures below 1000 ºC and at near-atmospheric pressures only $TiO_2$ rutile type has been detected in the oxide scales [24]. At elevated temperatures ($\geq$ 480 ºC) the $TiO_2$ layer loses its protectiveness and oxygen dissolves into the Ti bulk metal. The dissolution of oxygen in the bulk metal is mainly related to the relatively high solubility of oxygen in α-Ti (~ 33 at. %) [32]. In addition, for oxygen it is well known that it has strong stabilisation effect and hardens the α-phase. From the Ti-O phase diagram in Figure 3.4 it can be seen that the variation of oxygen solubility in α-phase is very small with regard to temperature, whereas the solubility in β-Ti increases with increasing temperature and at 1700 ºC reaches maximum solubility of about 8 at. % [32].

Oxygen diffuses in α-Ti interstitially and preferably occupies the free octahedral interstitial positions in the hexagonal closed-packed crystal lattice. However, a theoretical study by Wu and Trinkle [38] shows that the hexahedral and crowdion interstitial positions are also available for diffusion of the oxygen atoms. The authors points out that all three interstitial positions (i.e. octahedral, hexahedral and crowdion) in the hexagonal closed-packed crystal lattice of α-Ti cooperate and form a network of diffusion pathways where the oxygen atoms could move and that the movement of the oxygen atoms across this interstitial network contributes to the diffusion.

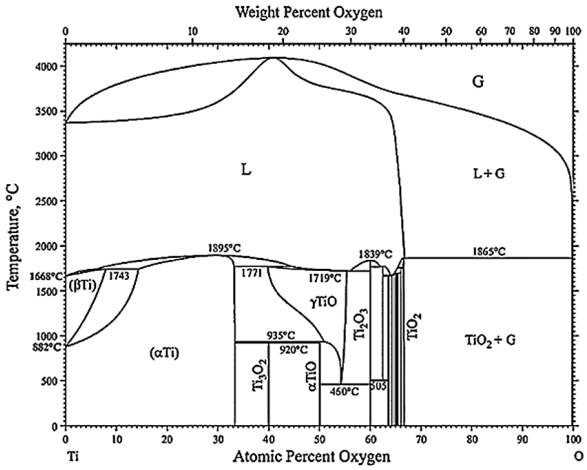


**Figure 3.4** Ti-O phase diagram [32]

The diffusion rate of oxygen in titanium and different alloys has been investigated by many authors. A comprehensive review by Liu and Welsch [39] describes the diffusivity of oxygen, aluminium and vanadium in α- and β-Ti, and in rutile $TiO_2$. The authors showed that the scatter in values obtained by various authors for the pre-exponential factors $D_0$ and the values of the activation energies $Q$ for oxygen diffusion are due to different methods used for obtaining the oxygen concentration gradient and different techniques used for measuring the oxygen concentration.

Numerous methods for measuring the oxygen diffusion can be used, for example internal friction, evaluation of the oxygen concentration using metallographic or other methods such as microprobe analysis, X-ray analysis, tracer analysis etc. [24]. The simplest conventional method used to measure the oxygen diffusivity in titanium and its alloys is the microhardness method. The microhardness method allows an estimation of the oxygen gradient, i.e. the oxygen diffusive zone thickness, through measuring the hardness of the metal since the increase of oxygen concentration in the metal corresponds to an increase of the hardness [40].

Rosa [41] has proposed a dimensionless correlation between the hardness and the oxygen concentration through the following expression:

$$\frac{H - H_{s0}}{H_{sl} - H_{s0}} \infty \frac{C - C_{s0}}{C_{sl} - C_{s0}} \tag{3.11}$$

where $H$ refers to measured hardness, $H_{s0}$ to hardness measured at infinity, i.e. bulk metal hardness and $H_{sl}$ refers to the hardness at the metal/oxide interface. As mentioned above, this simple correlation provides an estimation of the oxygen diffusivity through the use of non-expensive method and avoiding application of complicated and expensive techniques for probing the oxygen concentration.

Furthermore, by estimating the oxygen diffusion coefficient at different temperatures, the pre-exponential factor $D_0$ and the activation energy $Q$ for certain temperature ranges can be obtained using the following Arrhenius equation [42]:

$$D = D_0 \exp\left(-\frac{Q}{RT}\right) \tag{3.12}$$

Table 3.1 shows values for the pre-exponential constants $D_0$ and activation energies $Q$ obtained for diffusion of oxygen in α- and β-Ti estimated by various authors.

**Table 3.1** Pre-exponential constants $D_0$ and activation energies $Q$ for oxygen diffusion in α-Ti, β-Ti and Ti-6Al-2Sn-4Zr-2Mo [39]

| | Temperature (°C) | $D_0$ ($m^2/s$) | $Q$ (kJ/mol) | Method | Reference |
|---|---|---|---|---|---|
| **α-Ti** | | | | | |
| Ti | 700-850 | $5.08 \times 10^{-7}$ | 140 | conc. grad., MG[1]&MH[2] | [43] |
| Ti | 450-550 | $4.97 \times 10^{-11}$ | 102 | conc. grad., AES[3] | [44] |
| Ti-6Al-2Sn-4Zr-2Mo | 538-816 | $6.20 \times 10^{-5}$ | 203 | oxid. | [6] |
| Ti | 700-950 | $4.50 \times 10^{-5}$ | 201 | oxid. | [45] |
| Ti | 650-875 | $4.08 \times 10^{-5}$ | 197 | oxid. | [46] |
| Ti | 250-900 | $4.50 \times 10^{-5}$ | 200 | oxid. | [47] |
| **β-Ti** | | | | | |
| Ti | 1127-1347 | $8.30 \times 10^{-6}$ | 131 | conc. grad. | [48] |
| Ti | 900-1150 | 3.14 | 288 | conc. grad. | [43] |
| Ti | 950-1150 | $6.30 \times 10^{-5}$ | 155 | conc. grad., XSA[4] | [49] |
| Ti | 1335-1575 | $2.00 \times 10^{-6}$ | 115 | conc. grad. | [50] |
| Ti | 932-1142 | $3.30 \times 10^{-2}$ | 246 | oxid. | [41] |

[1]MG-Metallography, [2]MH-Microhardness, [3]AES-Auger electron spectroscopy, [4]XSA-X-ray structure analysis

### 3.1.3 Factors that influence the oxidation

As mentioned before, the oxidation of titanium and its alloys is complicated surface phenomena since it depends on a variety of factors which influence and determine the oxidation kinetics and mechanisms. Oxidation temperature and time are among the strait forward factors that influence the oxidation. Moreover, the oxidation is also strongly dependent on the type of alloy, i.e. alloying elements present in the particular alloy and its microstructure. In continuation, all above factors that influence the oxidation of titanium and its alloys will be briefly addressed by providing general literature overview on the oxidation behaviour, kinetics and mechanism for commercially pure titanium (CP-Ti), Ti-6Al-2Sn-4Zr-2Mo, Ti-6Al-4V and other important alloys used in aerospace applications.

The oxidation of CP-Ti and titanium with small amount of impurities in different environments (i.e. air and pure oxygen at various pressures) at wide temperature ranges have been extensively investigated by many authors [23,24,30,31,51-58]. The most notable studies of titanium oxidation in air at atmospheric pressure at broad temperature ranges have been performed by Kofstad et al. [23,24,30,52,53]. In these studies different oxidation behaviour and kinetics of titanium is reported, which is mainly dependent on the oxidation temperature and

time. Figure 3.5 shows a schematic representation of the oxidation behaviour for titanium at a wide temperature range as a function of the oxidation time.

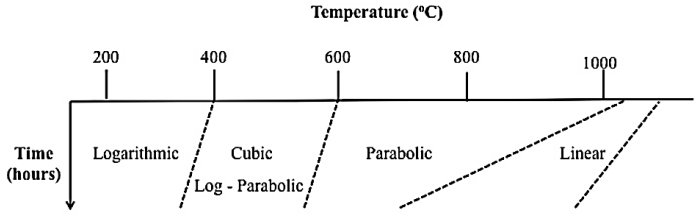


**Figure 3.5** Schematic diagram for the titanium oxidation behaviour at broad temperature range as function of the oxidation time [24]

As seen in Figure 3.5, the titanium oxidation at temperatures below 400 ºC mainly follows logarithmic behaviour with respect to oxidation time. However, for prolonged oxidation times and at temperatures beyond 400 ºC the logarithmic behaviour is changing to cubic. The cubic behaviour is a mixed rate law that consists of logarithmic and parabolic oxidation behaviour and for titanium it was found to occur in the temperature range of 400-600 ºC. At temperatures above 600 ºC, up to 700 ºC, the oxidation behaviour changes to parabolic. After prolonged oxidation times the parabolic oxidation is changing to approximately linear behaviour. In addition, at temperatures higher than 900 ºC, the observed oxidation rate was linear, followed by slower rates after longer times. With respect to the oxide scale formation and oxygen diffusion it was observed that the logarithmic oxidation only results in formation of a thin oxide scale of $TiO_2$. The cubic and the parabolic rates were associated with formation of an oxide scale and oxygen diffusion into the titanium metal responsible for formation of hard and brittle layer known as alpha-case. The linear rate of oxidation it was considered to occur as a result of porosity and cracking of the oxide scale because of stresses developed in the oxide and in the oxygen enriched layer [30].

For titanium alloys more complex oxidation behaviour than for CP-Ti was noticed, mainly because of presence of β-phase, presence and effect of different alloying elements, and also because of different arrangement of the two phases, i.e. different microstructures. The oxidation of different titanium alloys has been investigated by a number of authors and in continuation a short overview of the oxidation in air at elevated temperatures of Ti-6Al-4V and Ti-6Al-2Sn-4Zr-2Mo alloys is presented.

The oxidation of Ti-6Al-4V has been investigated in different oxidising conditions at different temperature ranges and times by a number of researchers [59-73]. The most relevant studies with respect to the work in the present thesis are the studies in [59-61,63-65,68-70,72]. The oxidation behaviour of Ti-6Al-4V alloy in air and in the temperature range of 600-700 ºC was investigated by Frangini et al. [60] for times up to 300 hours. The authors have reported that the oxidation kinetics in this temperature range mainly follows parabolic behaviour, but changes to linear at

700 ºC after 50 hours exposure time. It was considered that the change of the oxidation behaviour from parabolic to linear is because of faster oxide scale growth with increasing temperature. Similar observations were reported by Du et al. [59] and Guleryuz and Cimenoglu [68] at 700 ºC for oxidation times longer than 36 hours. The reason for the change in oxidation behaviour from parabolic to linear is considered to be due to the changes in the morphology of the formed oxide scale. At lower temperatures the formed oxide scale was dense and compact, whereas at higher temperatures it became porous and spalled off which led to an increase of the oxidation rate. Multi-layered structure of the oxide scale was observed consisting of $Al_2O_3$ and $TiO_2$ layers. In the study of Du et al. [61], the air oxidation of CP-Ti was compared with the Ti-6Al-4V alloy. The authors reported faster oxidation of Ti-6Al-4V than of CP-Ti at 750 ºC for exposure up to 240 hours. In context of this work, it was also reported that the additions of Al and V in Ti-6Al-4V have beneficial effect on reducing the oxygen diffusion into the bulk titanium metal [60]. Again, multi-layered structure of the oxide scale formed after oxidation was observed for both materials, where CP-Ti exhibited multi layers of only rutile $TiO_2$ while for Ti-6Al-4V layers of $Al_2O_3$ and $TiO_2$ were discerned. In the work of Mungole et al. [63] the oxidation behaviour of Ti-6Al-4V was investigated in the temperature range of 770-1070 ºC for exposure times up to 12 hours. The authors reported that the oxidation follows parabolic behaviour at all tested temperatures and they estimated the parabolic rate constants ($k_p$/kg$^2$m$^{-4}$s$^{-1}$). In their work they also reported that the oxidation of Ti-6Al-4V is faster in pure oxygen gas environment as compared with in air. In the study of Sugiura [64] the formation of the oxygen enriched layer beneath the oxide scale, i.e. alpha-case, at the temperature range 525-700 ºC was studied. The author reported that the alpha-case growth obeys parabolic behaviour at the tested temperatures. Guleryuz and Cimenoglu [68] have investigated the air oxidation behaviour of Ti-6Al-4V in the temperature range of 600-800 ºC for times between 30 minutes up to 72 hours. The authors reported formation of dense and porous types of oxide scales as a result of the oxidation at different temperatures. In their study it was reported that the oxide scale consists of anatase and rutile type of oxide. In addition, the authors reported that the oxygen dissolution into the alloys resulted in an increase of the lattice parameters of the α-Ti. The oxidation of Ti-6Al-4V in the temperature range of 400-600 ºC between 24 and 60 hours was investigated by Biswas et al. [69]. The authors presented that the oxide scale adherence to the titanium alloy substrate is decreased with increase of the oxide scale thickness and that it occurs due to thermal stresses developed as a result of the oxide scale growth. Kumar et al. [70] have investigated the oxidation behaviour of Ti-6Al-4V in the temperature range of 500-800 ºC and found that the oxide scale spalls off after 8 hours at 800 ºC. As seen by this literature survey about the oxidation behaviour of Ti-6Al-4V, a wide temperature range was covered in the works of others. However, in most of the studies only short oxidation times were considered. As mentioned before, the oxidation behaviour is strongly dependent on temperature but also on the exposure time. In our studies we are covering the oxidation behaviour of Ti-6Al-4V and Ti-6Al-2Sn-4Zr-2Mo for long exposure times of up to 500 hours.

As mentioned earlier, many authors have observed a formation of multi-layered oxide structure during oxidation of Ti-6Al-4V, which consists of $TiO_2$ and $Al_2O_3$ layers. In the study of Du et al. [59] it is shown that the formation of multi-layers in the oxide scale is temperature and time dependent phenomena and the number of $Al_2O_3$ layers increases with increasing either temperature or time. In addition, the authors have presented a mechanism of formation of the multi-layered oxide scale structure that involves the activity of titanium and aluminium and the oxygen partial pressure present in the oxide scale. They communicated that once the $TiO_2$ is formed, the alloy is separated from its environment by the oxide scale. Moreover, the partial oxygen pressure in the oxide decreases moving from the gas/oxide interface towards the oxide/metal interface to a value close to that of the dissociation pressure of $TiO_2$. At such low oxygen partial pressures the minimum activities required to form $Al_2O_3$ at different temperatures are high. However, due to the strong reduction of the Al activity by V it is unlikely to form $Al_2O_3$ at the oxide/metal interface. On the other hand, the oxygen partial pressure at the gas/oxide interface is relatively high which allows formation of $Al_2O_3$ on top of the already formed $TiO_2$. This indicates that oxygen is diffusing inward to the oxide/metal interface, reacting to form $TiO_2$. Hence, the $TiO_2$ thickness is increasing continuously. Contrary, aluminium diffuses outward towards the gas/oxide interface where it reacts with oxygen and forms an outer layer of $Al_2O_3$. Once the double oxide layer of $TiO_2$ and $Al_2O_3$ is formed the consequent grow of the oxide scale causes cracks at the oxide/metal interface when some critical thickness of the oxide scale is reached. The cracking is a result of developed stresses formed by the oxide scale growth and the different thermal expansion coefficients of the oxide scale and the metal substrate. The cracking initially starts at the edges and expands progressively through the entire surface of the oxide. The detachment of the oxide scale from the metal substrate increases the oxygen partial pressure close to the oxide/metal interface fulfilling conditions favourable for formation of the second $TiO_2$ layer. As the oxidation continues, these processes will repeat consequently resulting in formation of multi-layered structures of $TiO_2$ and $Al_2O_3$ layers on the oxide scale in Ti-6Al-4V. The oxidation mechanism of formation of multi-layered oxide scale on Ti-6Al-4V according Du et al. [59] is schematically shown in Figure 3.6.

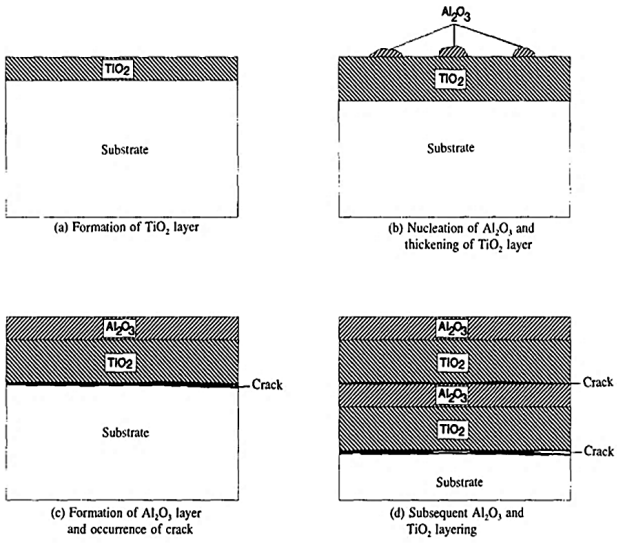


**Figure 3.6** Schematic illustration of the formation of multi-layered structure of the oxide scale in Ti-6Al-4V by Du et al. [59]

For changes in oxidation kinetics is not responsible only the multi-layered structure of the oxide scale. The work of Pitt and Ramulu [65] showed that also the microstructure has an influence on the oxidation kinetics. In their study they were investigating the effect of coarse and fine microstructures in Ti-6Al-4V on the oxidation kinetics and the oxygen diffusion. They showed that a fine microstructure exhibits faster oxidation kinetics and thicker alpha-case layer compared with a coarser microstructure.

There are less studies available on the oxidation of Ti-6Al-2Sn-4Zr-2Mo [6,7,71,74-77] compared with Ti-6Al-4V. Shamblen and Redden [6] have investigated the oxidation of Ti-6Al-2Sn-4Zr-2Mo in the temperature range of 318-871 ºC for 12000 hours. The authors succeeded to establish a relationship between the diffused oxygen concentration and hardness. In addition, they also investigated the effect of oxidation on the ductility noticing considerable loss of ductility as a result of subsurface oxygen contamination and embrittlement. One of the most notable studies on Ti-6Al-2Sn-4Zr-2Mo is the work of Shenoy et al. [7], were they presented the oxidation behaviour of Ti-6Al-2Sn-4Zr-2Mo alloy in the temperature range of 593-760 ºC for times up 332 hours using thermogravimetric analysis. Similar as for Ti-6Al-4V, parabolic oxidation behaviour up to 650 ºC was observed, which at higher temperatures deviated from parabolic behaviour at particular time intervals. The authors observed two parabolic stages during oxidation of Ti-6Al-2Sn-4Zr-2Mo separated by a transient region. They measured the oxygen concentration at the oxide/metal interface using microhardness experiments and revealed

that the oxygen concentration during the first stage of parabolic oxidation was 7 at.% and in the second parabolic stage it was 18 at. %. The authors associated the change in the oxidation behaviour at higher temperatures with the formation of a porous oxide scale. They reported that the higher oxygen concentration measured at the oxide/metal interface for the second parabolic stage was due to formation of the porous oxide scale. The porosity of the oxide allowed oxygen to diffuse faster close to the oxide/metal interface and consequently to diffuse into the base alloy. The oxidation of Ti-6Al-2Sn-4Zr-2Mo in the temperature range 450-750 ºC was studied by Peters et al. [74] based on weight gain measurements up to 100 hours. Moreover, the authors were focused on the mechanical behaviour of the alloy using four and three-point bending experiments and reported that premature cracking occurred due to subsurface oxygen embrittlement. The activation energy for oxygen diffusion in Ti-6Al-2Sn-4Zr-2Mo with bimodal microstructure and in the temperature range of 538-649 ºC was estimated based on metallographic measurements of the oxygen enriched layer thickness using oxalic etchant by McReynolds [75] (244 kJ/mol) and Shamblen and Redden [6] (203 kJ/mol). Study by Tiley et al. [76] showed that the lath crystallographic orientation in the lamellar microstructure of the Ti-6Al-2Sn-4Zr-2MoSi alloy also has effect on the oxygen diffusion rate. The authors suggested that the β-phase and the α/β interfaces between the neighbouring α-laths in the colony microstructure have contributed to the deeper oxygen ingress in the alloy due to the faster diffusion rate in comparison with the α- phase.

Other high temperature titanium alloys used in aerospace applications such as TIMET 834 (Ti-5.8Al-4Sn-3.5Zr-0.5Mo-0.7Nb-0.35Si-0.06C) [9,78-81], Ti60 (Ti-5.8Al-4.0Sn-3.5Zr-0.4Mo-0.4Nb-1.0Ta-0.4Si-0.06C) [82] and Ti-6Al-2Sn-4Zr-6Mo [83] have also been studied. The oxidation behaviour of these alloys is similar to the Ti-6Al-2Sn-4Zr-2Mo, with the exception that no significant change in the oxidation kinetics occurs at higher temperatures and/or after longer exposure times. One notable difference between Ti-6Al-2Sn-4Zr-2Mo and TIMET 834 alloy is that in TIMET 834 presence of $Ti_3AlN$ phase in the formed oxide scale was found [78-81,84].

As mentioned before the oxidation of titanium alloys is also dependent on the alloying elements. The influence of aluminium content on the oxidation of titanium in the temperature range of 550-750 ºC was investigated by Chaze and Coddet [85]. The authors have reported significant decrease of the solubility of oxygen in the bulk by addition of Al (from 34 to 0.3 at. %). The beneficial influence of Al on the oxidation behaviour of Ti-Al alloys is attributed to the decrease of the oxygen diffusion rate in rutile as result of doping the rutile oxide with Al interstitials and/or dispersion of $Al_2O_3$ in the rutile scale. Becker et al. [86] showed that additions of 1.4 wt. % of V in Ti-Al alloys prevent formation of $Al_2O_3$ in the oxide scale which results in increase of the oxidation kinetics. Thus, it seems that V additions reduce the oxidation resistance of titanium alloys. According to Perkins et al. [87] additions of V is detrimental to the oxidation in titanium alloys that do not contain sufficient amount of β-phase because of the high possibility for V to form transient oxides. A comprehensive work about the influence of selected elements on the oxidation of Ti-Al alloys was performed by Shnida and Anada [88,89]. The authors have investigated the effect of twenty-four elements and classified them into three subgroups: 1)

detrimental (Cu, Y, V, Cr, Pd, Pt and Mn); 2) neutral (Sn, Zr, Hf, Ta, Ni, Ag, Au, O and Co); and 3) beneficial (Al, Si, Nb, Mo, C, B and W). They investigated the oxidation of Ti-Al alloys in air in the temperature range of 800-1000 ºC and by monitoring the weight gain the authors resolved the effect of different amount of element additions on the oxidation resistance. In their work they highlighted the beneficial effect of Mo and W on the oxidation resistance. These two elements form enriched layers just beneath the oxide scale and prevent oxygen to diffuse into the metal substrate. The effect of Mo is considered to be complex since it has impact on the stability of the oxide phases and the Al diffusion in the oxide. On other hand, the presence of Al is also beneficial for the oxidation resistance and this element tends to form stable and dense $Al_2O_3$ layer that prevents oxygen to diffuse into the metal. According to the authors V additions makes the oxide scale more porous and is therefore detrimental for the oxidation resistance. In general, they claim that the doping effect of the alloying elements in the oxide scale has significant influence on the oxidation behaviour of the Ti-Al alloys. Doping with elements that have lower valence than titanium in $TiO_2$ is considered to increase the number of oxygen vacancies in the oxide that in turn results in faster oxide growth and reduced oxidation resistance. The effect of Si additions was also beneficial for the oxidation resistance. The authors reported that this is due to formation of a stable thin layer of $SiO_2$ on the oxide/metal interface which decreases the oxidation rate. Lausma [90] used X-ray photoelectron spectroscopy (XPS) to study the chemical composition of the oxide scale developed as a result of oxidation in air in the temperature range of 150-450 ºC for 1 hour. The author has reported that the oxide scale that forms is mainly rutile type $TiO_2$ with thicknesses ranging between 6-40 nm. However, the oxide scale formed after oxidation was contaminated, i.e. doped, with significant amounts of the alloying elements present in the Ti-6Al-4V. Al was detected in the outermost surface in the oxide scale, whereas V content was insignificant at the surface but present in larger amount inside the oxide.

As mentioned a few times earlier, the oxidation of titanium and its alloys results in formation of a rutile type of oxide scale. Rutile has tetragonal crystal structure and its ideal chemical formula is $TiO_2$. However, at elevated temperatures and/or low partial pressures of oxygen rutile exhibits significant non-stoichiometry $TiO_{2-x}$, where $x$ could vary up to ~ 0.008 depending on temperature and oxygen partial pressure. The oxygen deficiency of non-stoichiometric rutile is compensated with point defects in the oxide structure such as oxygen vacancies and titanium interstitials [91]. At elevated temperatures and oxidizing conditions the dominating defects in rutile are oxygen vacancies, whereas titanium interstitials prevails at low temperatures and more reducing conditions [34,92]. The presence of defects in the non-stoichiometric rutile can alter the diffusion of oxygen and ions (anions and cations) and thereby affect the overall oxidation kinetics. Another possible reason for the complex oxidation kinetics can be related to the anisotropic diffusion properties of the rutile tetragonal crystal structure. This applies in particular for small monovalent ($M^{+}$), divalent ($M^{+2}$) and trivalent ($M^{+3}$) cations that can exhibit several orders of magnitude faster diffusion when diffusing in parallel direction to the c-axis of rutile compared to the perpendicular direction [91].

### 3.1.4 Influence of oxidation on the mechanical properties

Elements such as oxygen, nitrogen and carbon are known as interstitial elements because they diffuse into the bulk titanium metal and occupy the free interstitial lattice positions in the α-phase. The diffusion of these elements results in solid solution strengthening effect that affects the mechanical properties and thereby the mechanical performance of titanium and its alloys. Several studies can be found concerning the influence of the interstitial elements on various mechanical properties [36,93]. Finlay and Snyder [93] have studied the influence of oxygen, nitrogen and carbon contents on the tensile and yield strength, hardness and ductility of commercially pure titanium (CP-Ti). Figure 3.7 shows plots that summarise the effect of the content of these three interstitial elements on the ultimate tensile and yield strengths, hardness and ductility of CP-Ti.

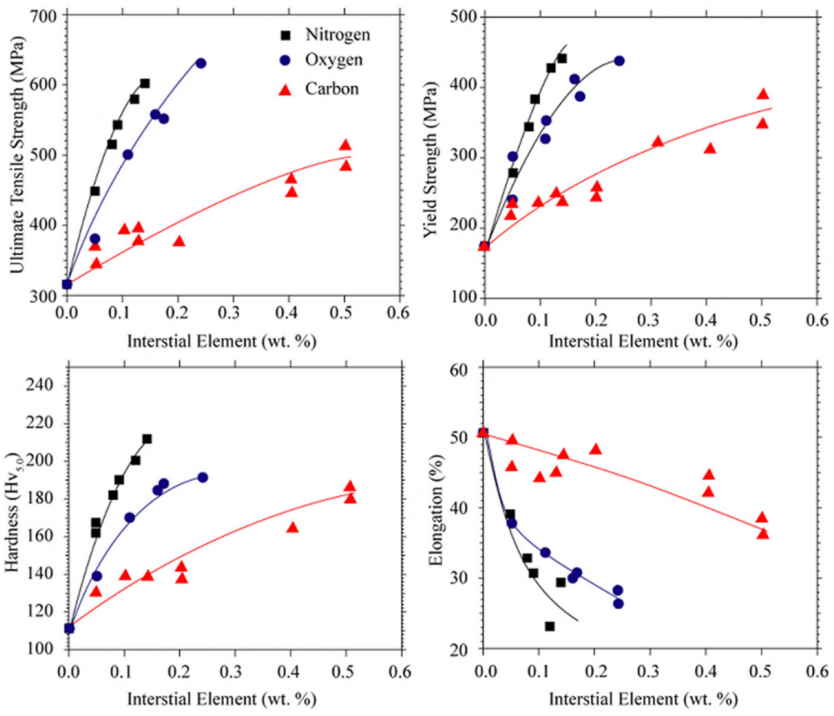


**Figure 3.7** Effect of nitrogen, oxygen and carbon interstitial elements on the mechanical properties of CP-Ti [93]

The plots show that the strength (tensile and yield) and the hardness of CP-Ti is a function of the content of interstitial element and increase notably with increasing content of the interstitial

elements. On the other hand, the increase of the tensile and yield strength results in substantial decrease of the ductility. Although all interstitial elements exhibit similar effect of increasing the tensile and yield strength of CP-Ti, yet their individual effect on selected properties is different. Nitrogen has the largest effect and is followed by oxygen and carbon.

The effect of the interstitial elements on mechanical properties of titanium and some titanium alloys was also reported by Ogden and Jaffe [94]. They showed that the effect of the interstitials in titanium alloys is similar to the effect in CP-Ti thereby highlighting that the magnitude of the effect is dependent on the amount and type of alloying elements. Another important property studied by these authors was the effect of interstitial elements on the thermal stability at elevated temperatures. It is well known that the dissolved interstitial elements increase the rate of formation of α- from β-phase, causing detrimental effect on the thermal stability of titanium alloys and thereby reducing important mechanical properties such as ductility, strength, fracture toughness and fatigue life. The authors reported that the effect of the interstitial elements on the stability of two phase titanium alloys is directly related to their effects on the β-decomposition kinetics.

Among the interstitial elements, oxygen is of particular interest because of the high chemical reactivity with titanium at elevated temperatures and the relatively high solubility in α-Ti (~33 at. %) [32]. Kahveci and Welsch [95,96] investigated the effect of oxygen concentration on the hardness and the α/β phase ratio in Ti-6Al-4V. They showed that increase of oxygen concentrations significantly increases the hardness and the volume fraction of α-phase at given temperatures. A large number of studies can be found for different alloys providing insight on the detrimental effect of oxygen uptake on several mechanical properties, such as ductility, tensile strength, fatigue life and fracture toughness [6-8,10,11,62,97-105]. Shamblen and Redden [6] found a correlation between the increase of the oxygen contamination depth and the subsequent loss of ductility in Ti-6Al-2Sn-4Zr-2Mo. This was also confirmed by Shenoy et al. [7] for the same alloy, reporting reduction of the tensile elongation from 12.7 to 2.5 % dependent on the oxygen concentration and contamination depth. Liu and Welsch [98] studied the influence of the oxygen concentrations and the different heat treatment conditions on the hardness and the ductility in Ti-6Al-2V and Ti-2Al-16V. They reported that the hardness is a function of the square root of the oxygen concentration and that it is increasing in similar manner in the two alloys regardless of the differences in chemical composition. The heat treatment conditions also affect the strength but in different ways in the two alloys. The strength of Ti-6Al-2V was not affected during aging, whereas it was doubled in Ti-2Al-16V. Additionally, aging in combination with increased oxygen concentrations caused precipitation of $Ti_3Al$ particles in the α alloy, whereas α and omega (ω) or only α precipitates were formed in the β alloy depending on the aging temperature. Moreover, they reported that the ductility is strongly decreasing by increase of oxygen concentration in Ti-6Al-2V leading to total brittleness at oxygen concentration of 0.65 wt. %. On the other hand, they reported that the ductility in the Ti-2Al-16V alloy was also decreased with increasing oxygen concentration, without embrittlling the alloy even at 0.59 wt. % oxygen concentrations. Studies for Ti-6Al-4V by Dong and Li [62] and for

Ti-6Al-2V by Ebrahimi et al. [101] showed reduction of the fatigue limit with 27 % and 18 %, respectively, which was mainly due to the thermal oxidation and oxygen embrittlement of the alloys. The dependency of tensile properties on the oxidation in TIMETAL 1100 and Ti60 was studied by Leyens et al. [8] and Jia et al. [82]. Both studies reported that the oxidation has significant effect on the tensile properties of the alloys, featured by decreasing strength and ductility. The influence of different microstructures, interstitial impurity and temperature on the fracture toughness was investigated by Horiya and Kishi [105]. The author reported a general decrease of the fracture toughness for all three classes of titanium alloys (α, α+β and β alloys) with increasing the strength as function of the different type of microstructure (α + retained β, equiaxed α + transformed β, fine acicular α, primary α + precipitated α+β, β, β+fine α and β+coarse α), interstitial impurity content (oxygen), and temperature (0 to -196 ºC). The fracture toughness of titanium alloys is dependent on the initiation and propagation resistance of micro-cracks generated by the pre-crack tip before maximum load and does not depend on the alloy type and test temperature. The influence of oxidation and oxygen enriched layer formation (i.e. alpha-case) of Ti-6Al-2Sn-4Zr-2Mo on the low cycle fatigue (LCF) properties was studied by Gaddam et al. [11]. The authors have reported significant decrease in LCF strength as a function of thickness of oxygen enriched layer. In this work it was reported that as little as 2 μm of alpha-case reduced the fatigue life with as much as 50 %, and with 10 μm thick alpha-case the fatigue life was decreased with 90 %. The authors showed that the hard and brittle oxygen enriched layer beneath the oxide scale (i.e. alpha-case) resulted in multiple crack initiation sites and consequent tremendous decrease of the fatigue life.

## 3.2 Corrosion during chemical milling processing

As demonstrated in the previous section the oxidation and oxygen diffusion into titanium alloys (oxygen enriched layer, i.e. alpha-case formation) has detrimental effect on important mechanical properties of titanium alloys. The conventional treatment for removal of any oxygen surface and subsurface contamination (alpha-case) involves using chemical milling or pickling [1-3]. An aqueous solution containing mixture of HF and $HNO_3$ acids in proper molar concentration ratios is used. The combination of acids (HF and $HNO_3$) used for the chemical milling treatment is highly corrosive resulting in dissolution, i.e. etching away material from the surface.

In order to have insight and understand the processes and phenomena taking place during chemical milling (etching) of titanium and its alloys it is essential to have basic knowledge of the corrosion behaviour. Therefore in this section, a general overview of metal corrosion, the corrosion behaviour of titanium and its alloys and a short literature review on the corrosion studies in HF/$HNO_3$ acids solution and other environments is presented.

### 3.2.1 Fundamental principles of metal corrosion

Corrosion of metals in solutions is defined as simultaneous transfer of mass and charge across the metal/solution interface and refers to the degradation of a metal by its environment. When a

metal is immersed in a solution it could be immune, active or passive [106]. Metals that behave inert are noble metals such as gold (Au), silver (Ag) and platinum (Pt) and they stay thermodynamically stable for a long time and there is no weight loss of the metal. However, if the metal is active, then the metal corrodes, i.e. dissolves into the solution by forming soluble, non-protective corrosion products. The active behaviour of metals in solution is characterised by metal weight loss with time. Finally, passive metals are those metals that corrode with a very slow corrosion rate through formation of stable thin film of oxide as protective corrosion product. Among these metals are chromium, titanium, aluminium, nickel, and alloys based on these metals.

Corrosion of metals in chemical solutions is an electrochemical process where the chemical and electrochemical reactions are coupled [107]. The electrochemical reaction involves change of the valence of the reactants (by gaining or losing an electron/s) and takes place through two half-cell reactions, i.e. oxidation and reduction. The half-reaction of metal oxidation is also known as anodic reaction and involves electron/s loss and increase of the oxidation number of the metal. The metal oxidation reaction, i.e. anodic reaction, can be described by the following half-reaction:

$$\mathrm{Me\,(s)} \rightarrow \mathrm{Me}^{n+}\mathrm{(aq)} + ne^{-} \tag{3.13}$$

where Me is metal in solid phase and $\mathrm{Me}^{n+}$ is the metal in oxidised state present in the aqueous solution. However, the anodic reaction is always coupled with a cathodic reaction (i.e. reduction) during which the reducing species gain electrons. Common cathodic reactions during corrosion of metals are the following:

$$2\mathrm{H}^{+}\mathrm{(aq)} + 2e^{-} \rightarrow \mathrm{H_2(g)} \tag{3.14}$$

$$\mathrm{O_2(g)} + 2\mathrm{H_2O} + 4e^{-} \rightarrow 4\mathrm{OH}^{-}\mathrm{(aq)} \tag{3.15}$$

Reaction (3.14) is the predominant cathodic reaction in acidic solutions (pH $\leq$ 7), whereas reaction (3.15) is common in neutral or alkaline solutions (pH $\geq$ 7). On a corroding metal surface the anodic and cathodic reactions occur in coupled manner at different places on the metal surface. The reason for the occurrence of these reactions on the same metal surface is because of the heterogeneous nature of the metal surfaces such as different crystallographic orientation of the grains, grain boundaries and other defects such as edge, step, kinks, screw dislocations and point defects.

In general, two major types of corrosion are recognised; uniform and localised corrosion. During uniform corrosion the metal is attacked, i.e. corrodes, uniformly all over its entire surface, and during localised corrosion local anodes and cathodes on the same metal surface exist. The three most common localised corrosion types are pitting, crevice and stress-corrosion cracking. In pitting corrosion the metal passive film is locally attacked, usually due to effect of chloride ions or any other halogen elements ($F^{-}$, $Br^{-}$ and $I^{-}$), whereas stress-corrosion cracking occurs during combined action of applied stress and corrosive chemical solution. Fontana and Greene [108] have classified the different types of metals corrosion into eight forms: uniform

(general) corrosion, crevice corrosion, pitting, stress-corrosion cracking, galvanic corrosion, intergranular corrosion, selective leaching, and erosion corrosion.

### 3.2.2 Corrosion behaviour of titanium and its alloys

The excellent corrosion resistance of titanium and its alloys in various chemical solutions is mainly attributed to the spontaneous formation of a chemically inert, well adherent, thin and passive film of $TiO_2$ [109,110] with typical thickness of about 6-10 nm that protects the titanium metal from active dissolution (i.e. corrosion) in different environments. The oxide film can be amorphous or crystalline and if crystalline then is either anatase type or the more stable rutile type. An interesting effect of the thin oxide film is that it can instantaneously re-heal itself if damaged, by traces of oxygen and/or water (moisture) present in the environment. In general, titanium and its alloys are chemically resistant to various chemical environments and only few chemicals can destroy the passivity and cause titanium to corrode. Table 3.2 shows a general overview of the corrosion resistance of titanium in different chemical environments.

**Table 3.2** Corrosion resistance of titanium in different chemical environments [111]

| Resistant | Not resistant |
|---|---|
| ***Acid solutions*** | |
| $HNO_3$, all concentrations up to boiling temperature | $H_2SO_4$, HCl ≥ 10 %, HF |
| Aqua regia, (25 ºC) | Fuming nitric acid, high temperature |
| $H_2SO_4$, HCl ≤ 10 %, (25 ºC) | $H_3PO_4$ ≥ 30 %, (35 ºC) |
| $H_3PO_4$ ≤ 30 %, (35 ºC) | Trichloracetic acid, boiling |
| $H_3PO_4$ ≤ 5 %, (boiling) | Oxalic acid, boiling |
| $H_2CrO_4$ , acetic, oxalic, lactic and formic acids, (25 ºC) | Forming acid, boling |
| ***Alkaline solutions*** | |
| Diluted, room temperature solutions | Hot NaOH concentrated solutions |
| NaClO | Most of the concentrated hot alkaline solutions |

The potential-pH diagram (*Pourbaix diagram*) for the Ti-$H_2O$ system at 25 ºC is shown in Figure 3.8 [112]. Titanium is an active metal and its immune region is nearly at the bottom of the potential-pH diagram. As seen, the passive region of titanium extends over the entire pH range, starting at very acidic to very alkaline, under moderate reducing to highly oxidising conditions. Titanium corrodes under reducing and highly acidic conditions.

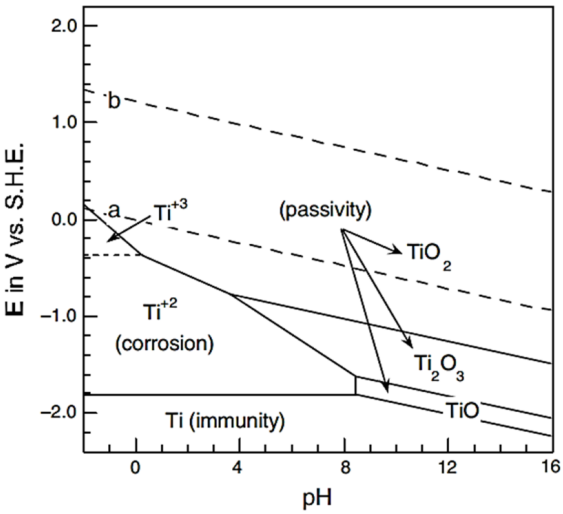


**Figure 3.8** Pourbaix diagram for the Ti-$H_2O$ system at 25 ºC [112]

Even though titanium and its alloys are considered resistant to corrosion, still under certain circumstances corrosion does occur. The following forms of corrosion have been noted on titanium and its alloys; general corrosion, crevice corrosion, pitting corrosion, hydrogen embrittlement, and stress-corrosion cracking [106]. It has been noted that additions of certain alloying elements such as palladium (Pd) and ruthenium (Ru) significantly improve the corrosion resistance [113]. Additions of V and especially Mo result in improvement of the corrosion resistance in reducing aqueous solutions, whereas an addition of Al was noted to be detrimental for the corrosion resistance [114]. When the corrosion resistance is important for certain applications the α and near-α class of titanium alloys are preferable choice because they have shown better corrosion resistance than α+β and β class of alloys in various environments [110].

It is well known that hydrofluoric acid, i.e. the fluoride ($F^-$) ions, easily destroys the passivity in aqueous solutions resulting in uniform corrosion. Conditions suitable for loss of passivity part from the presence of $F^-$ ions a low pH, i.e. acidic environment must be present [110,115]. A common problem under active conditions where corrosion occurs by proton ($H^+$) reduction is hydrogen evolution and absorption of hydrogen by the titanium metal with risk for hydrogen embrittlement. Hydrogen embrittlement is detrimental to the mechanical properties since it causes hydrogen induced cracking due to the formation of brittle hydrides. Pitting corrosion has been noted in solutions that contain bromide ($Br^-$) ions because of adsorption of the $Br^-$ ions on impurity inclusion sites that contain Al, Si or Fe [110]. In alkaline solutions the corrosion rate increases significantly due to the higher solubility of the passive film. As an example, in hydrogen peroxide solutions at pH > 12, commonly used in the pulp and paper industry, the

corrosion rates are extremely high and related to the aggressiveness of the $HO_2^-$ anion. Compilations of tables with corrosion rate data for commercial pure titanium in various chemical environments are available in the literature [1].

The presence of two phases in titanium alloys, i.e. the α-phase and the β-phase, raises the question of how these phases, arranged in particular manner for a specific type of microstructure, will behave and respond when subjected to different types of corrosive environments. Moreover, the presence of various alloying elements and their distribution in certain phases also opens the question if titanium alloys are susceptible to localised corrosion such as pitting, crevice and/ or intergranular type of corrosion. There are numerous publications available concerned with the corrosion behaviour of titanium alloys and their susceptibility to localised corrosion in various chemical environments [116-121]. Gurrappa [117] investigated the susceptibility of Ti-6Al-4V to pitting and crevice corrosion in three different environments (chemical, marine and industrial) at low and high temperatures. He reports that Ti-6Al-4V is resistant to localised corrosion in chemical and marine environments, but susceptible to pitting and crevice corrosion in industrial environments.

More insight about the influence of the microstructure and the phase volume fractions (i.e. α and β vol. %) on the corrosion behaviour and susceptibility to localised corrosion of Ti-6Al-4V and Ti-6Al-2Sn-4Zr-Mo can be found in the studies performed by Atapour et al. [118] and Raja et al. [116], respectively. The work of Atapour et al. [118] compares the corrosion behaviour of Ti-6Al-4V in NaCl and HCl as a function of three different microstructures (equiaxed, bimodal and lamellar) with different volume fractions of primary α (0 %, 10-20 %, 40-50 % and 90 %). All three microstructures revealed passive behaviour in NaCl, while in HCl showing an active to passive transition. The fully lamellar microstructure with 0 % primary α showed the lowest corrosion resistance and the α/β interface was preferentially more attacked by HCl than the α-phase. This is because of partitioning and more pronounced difference in chemical composition of the main stabilising elements (Al and V) between the α-phase and the β-phase, leading to possible formation of galvanic cells and preferential corrosion of the β-phase. However, the authors also showed that by using heat treatments and modifying the microstructure, the partitioning of the main alloying elements could be adjusted affecting the corrosion resistance. Raja et al. [116] studied the tendency for pitting corrosion as a function of different heat treatments of Ti-6Al-2Sn-4Zr-2Mo and three types of microstructures (Widmanstätten, acicular martensite and α-plates) in 1 M NaBr solution using electrochemical polarisation technique. The authors show that the electrochemical pitting parameters such as pitting potential $E_{pit}$ and protection potential $E_{pp}$ are strongly affected by the heat treatment condition. The Widmanstätten microstructure exhibited the lowest protection potential as compared to the other types of microstructures. The pitting corrosion manifested as selective attack and faster dissolution of the α-plates, i.e. α-phase, compared to the β-phase. The reason for such behaviour was attributed to the inherent variations of the main stabilising elements (Al and Mo) content rendering in formation of galvanic cells between the two phases. The studies of Chen and Tsai [119] and Nakhaie et al. [122] are of significant importance for increasing the understanding of the

corrosion behaviour of the individual α- and β-phases of Ti-6Al-4V in $H_2SO_4$/HCl and HF/$HNO_3$ acid mixtures, respectively. The authors used advanced techniques such as Atomic Force Microscopy (AFM) and Scanning Kelvin Probe Force Microscopy (SKPFM) to investigate the corrosion behaviour of the individual phases when in contact with corrosive solutions. Both studies showed that the α-phase corrodes at a faster rate compared to the β-phase and the main reason is due to partitioning of the main alloying elements (Al and V) between the phases that leads to formation of micro-galvanic cells.

As seen the corrosion of titanium alloys is dependent on many parameters such as type of corrosive environment, presence of the α-phase and the β-phase, each with their own individual characteristics, chemical composition of the alloys, microstructure type as well as, thermal history of the materials.

### 3.2.3 Chemical milling mechanisms and factors that control the dissolution rate in hydrofluoric-nitric acids

As mentioned earlier, chemical milling is a common process used in the steps of manufacturing of titanium alloy components for various applications. In aerospace industry it is used for etching away, i.e. remove, surface and subsurface oxygen contaminations of aero-engine components, i.e. oxide scale and alpha-case layer, formed after thermo-mechanical treatments at elevated temperature and in oxygen containing environments. The removal rate of the metal depends on several processing parameters such as molar concentration ratio between the two acids, temperature, agitation, i.e. stirring of the bath, age of the bath, etc. By maintaining strict control over all these processing parameters a constant and strictly controlled removal rate can be obtained. Chemical milling is advantageous for processing components with complex net geometry compared to conventional mechanical machining technology. The expected outcomes from using chemical milling treatment are effective removal of the entire alpha-case layer while obtaining acceptable surface finish, i.e. surface roughness that does not require additional processing operations.

The chemical milling treatment in HF/$HNO_3$ solutions is a complicated process that involves a combination of chemical and electrochemical reactions occurring at the metal/acid solution interface. HF acid has the ability to dissolve the naturally present passive film of $TiO_2$ and the chemical reaction of $TiO_2$ with HF acid can be represented by the following equation [123-129]:

$$TiO_2(s) + 6HF(aq) \rightarrow [TiF_6]^{2-}(aq) + 2H_3O^+(aq) \qquad (3.16)$$

The reaction (3.16) results in dissolution of the passive film of $TiO_2$ and leads to formation of soluble titanium hexafluoro complexes. Once the protective $TiO_2$ film is entirely dissolved the titanium metal is exposed to the HF acid. In such conditions the metal will start to react with the HF acid according the following chemical equation [123-129]:

$$Ti(s) + 6HF(aq) \rightarrow H_2TiF_6(aq) + 2H_2(g) \qquad (3.17)$$

Similar as in reaction (3.16), the reaction (3.17) results in titanium hexafluoro complex formation and hydrogen gas formation. Other authors [130] have proposed that the reaction of Ti

with HF acid might result in oxidation of titanium to its three-valence state according the following chemical reaction:

$$2\mathrm{Ti\,(s)} + 6\mathrm{HF(aq)} \rightarrow 2\mathrm{TiF_3(aq)} + 3\mathrm{H_2(g)} \qquad (3.18)$$

However, because of instability of the $Ti^{3+}$ ions, it is expected that they will be slowly oxidised to $Ti^{4+}$ ions either by the oxygen present in the aqueous solution or by the HF acid. Again, the reaction of titanium with HF is resulting in titanium hexafluoro complexes and hydrogen gas formation as shown in reaction (3.17). The hydrogen gas formed during this reaction may result in hydrogen embrittlement by hydride formation, which might deteriorate the mechanical properties. Therefore, in order to resist the hydrogen gas formation, a strong oxidising acid is used in combination with HF, such as $HNO_3$. The role of the $HNO_3$ acid is to oxidise the hydrogen gas, which reaction can be described as follows [124-126,129]:

$$3\mathrm{H_2\,(g)} + 2\mathrm{HNO_3(aq)} \rightarrow 2\mathrm{NO\,(g)} + 4\mathrm{H_2O\,(l)} \qquad (3.19)$$

During this reaction (3.19) the hydrogen gas is oxidised to water and NO gas, which can be a mixture of NO and $NO_2$ gases (i.e. $NO_x$ mixture). However, besides oxidising the hydrogen gas and minimising hydrogen embrittlement, the $HNO_3$ acid also oxidises the metal surface and forms passive films of $TiO_2$. The process of oxidising the titanium metal surface with help of $HNO_3$ acid to form passive $TiO_2$ film can be represented by the following chemical equation [124-126,129]:

$$3\mathrm{Ti\,(s)} + 10\mathrm{HNO_3(aq)} \rightarrow 3\mathrm{TiO\left(NO_3\right)_2(aq)} + 5\mathrm{H_2O\,(l)} + 4\mathrm{NO\,(g)} \qquad (3.20)$$

As noted by reaction (3.20), the oxidising of the titanium metal surface results in formation of a passive film that is contaminated by nitric groups. Panagopoulos [131] has investigated the surface chemical composition of titanium after chemical etching in a mixture of HF, $HNO_3$ and $H_2SO_4$ acids, by using X-ray photoelectron spectroscopy. The author has reported presence of Ti, O and contamination of fluoride through the thickness of the oxide layer. Moreover, N and S were also detected, but only at the titanium metal surface. The passive film formed according to reaction (3.20) will further react with the HF acid resulting in dissolution of the $TiO(NO_3)_2$ film as shown by reaction (3.16). Again, the dissolution of the passive film will result in formation of soluble titanium hexafluoro complexes and $NO_x$ gas will be released.

The reactions (3.16) to (3.20) will take place on the metal surface providing continuous progress of the corrosion process, i.e. metal dissolution. This can be described by the following overall chemical reaction [123-129]:

$$\mathrm{Ti} + n\mathrm{HF} + \mathrm{HNO_3} \rightarrow \mathrm{TiF_n^{(4-n)}(aq)} + \frac{1}{2}\mathrm{N_2O} + 2\frac{1}{2}\mathrm{H_2O} + \left(n-4\right)\mathrm{H^+} \qquad (3.21)$$

The factors that control the dissolution rate are: activity, i.e. concentration of the HF and $HNO_3$ acids, their ratios, temperature of the HF/$HNO_3$ solution, and agitation (stirring) of the HF/$HNO_3$ solution. The temperature increase of the acid mixture leads to faster dissolution rates [132], but as mentioned earlier, temperatures above 55 ºC might be detrimental because of excessive toxic $NO_x$ gas formation and consequent increase of the surface roughness [133]. Agitation of the acid solution is important for the dissolution rate because it provides uniform attack on the metal surface followed by better surface finish. Biljmer [123] have determined the

dissolution rates of titanium by weight and thickness loss measurements before and after 10 minutes immersion in $HF/HNO_3$ solutions with different concentration ratios between the acids. The author reported that the maximum dissolution rate is in 10-20 wt. % of $HNO_3$ acid regardless of the HF acid content. Moreover, a HF content increase up to 20 wt. % resulted in higher dissolution rates, whereas a $HNO_3$ content increase resulted in decreased surface roughness. Numerous studies can be found devoted to the influence of $HF/HNO_3$ on the corrosion behaviour of titanium and Ti-6Al-4V [123,125-129,132-135]. Studies of the corrosion behaviour of Ti-6Al-2Sn-4Zr-2Mo in HF and $HNO_3$ acid solution were not found. Notable reports on the corrosion behaviour of titanium in $HF/HNO_3$ solutions are the studies of Sutter et al. [127-129]. The authors have investigated the behaviour of Ti in $HF/HNO_3$ solutions with different concentration ratios between the acids using electrochemical and spectroscopy techniques. In general, the authors have shown that titanium behaves passive in $HF/HNO_3$ solutions. They posed emphasis on the depletion and/or aging of the $HF/HNO_3$ solution due to the HF consumption as a result of the reaction with titanium and formation of soluble titanium hexafluoro complexes (i.e. $[TiF_6]^{2-}$ ions). The formation of complexes by continuous consumption of HF reduces the activity of the $HF/HNO_3$ solution leading to hydrolysis of the $[TiF_6]^{2-}$ ions and formation of oxofluoro or hydroxofluoro complexes (see Figure 3.9).

These complexes are not reactive with titanium and tend to accumulate on the metal surface which leads to lowering of the overall dissolution rate. The authors have corroborated the presence of the oxo- and hydroxofluoro complexes by Raman spectroscopy and have observed restored activity of the $HF/HNO_3$ acid mixtures by adding new portion of HF. Moreover, Sutter et al. [127,128] have reported that the critical parameter controlling the dissolution rate and the activity of the $HF/HNO_3$ acid solution is the concentration ratio between the HF acid and dissolved titanium (i.e. $[HF]_{init.}/[Ti]_{diss.}$). According to the authors, if $[HF]_{init.}/[Ti]_{diss.} \geq 6$, continuous and stable dissolution rate is achieved. However, as soon as the $[HF]_{init.}/[Ti]_{diss.} \approx 2–3$, the $HF/HNO_3$ acid solution loses its activity followed by formation of titanium oxo- and/or hydroxofluoro complexes. Interestingly, addition of new HF portion to the $HF/HNO_3$ solution recovers the activity of the acids, whereas for $HNO_3$ additions it was suggested that both passivation and dissolution are possible, but for total passivation a critical $HNO_3$ concentration is required [127].

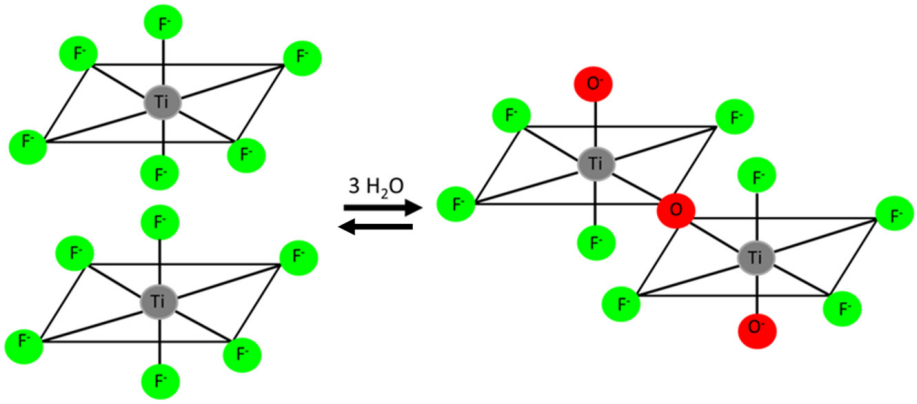


**Figure 3.9** Schematic presentation of the hydrolysis of $[TiF_6]^{2-}$ to titanium oxo- and/or hydroxofluoro complexes [127-129]

The main role of the chemical milling process using $HF/HNO_3$ acid solution is to remove the alpha-case layer formed during the various thermo-mechanical manufacturing processing steps of titanium and its alloys. Only few studies were found in the literature related to removal of the alpha-case using chemical milling solutions [125,126,135,136]. In most of the studies the effect of the $HF/HNO_3$ acid mixtures on the removal efficiency of the alpha-case layer formed during investment casting manufacturing method was examined. Say and Tsai [125] have investigated the chemical etching of the alpha-case layer in cast Ti-6Al-4V. The authors have proposed a mechanism for the chemical etching using $HF/HNO_3$ solution. The proposed mechanism involves etching by generating oxygen vacancies which are replaced by fluoride vacancies, resulting in formation of soluble titanium complexes. One of the notable studies on the corrosion behaviour of Ti-6Al-4V in $HF/HNO_3$ acid solutions is the work of Lin and Hong [124]. The authors have focussed on studying the effect of temperature and different volume ratios between HF and $HNO_3$ acids on the surface roughness of Ti-6Al-4V. Passivation of the alloy surface and finer surface roughness were observed in presence of $HNO_3$ acid. The authors observed continuous increase in corrosion rate of Ti-6Al-4V by up to 2.5 times, higher volume ratios of the $HNO_3$ acid compared to HF acid, whereas further increased $HNO_3$ acid resulted in slower corrosion rates. In the work of Gaiani et al. [136] the effect of chemical milling removal rate of the alpha-case layer for pure Ti and Ti-6Al-4V was investigated. The authors reported 10-15 % higher removal rate of pure titanium than of Ti-6Al-4V. Apparently, pure titanium and titanium alloys do not respond similarly in the $HF/HNO_3$ acid solutions.

Several reasons for the difference in the dissolution rates between pure titanium and alloys can be considered such as presence of two phases (α and β) in the titanium alloys as compared to pure titanium, the chemical composition, different crystallographic orientation of the grains, different microstructure and different dissolution mechanisms involved. In addition, one more

reason for the difference in dissolution rate might be different chemical composition of the oxide layer of the pure titanium metal and on an alloy. The study of Sittig [137] showed that the naturally formed oxide film on Ti-6Al-4V consists of mixture of $TiO_2$, $Ti_2O_3$ and TiO with contaminations of oxides such as $Al_2O_3$ and V oxides. An interesting observation is that treatment of the alloy in $HNO_3$ acid results in diminishing surface contaminations from $Al_2O_3$ and V oxides [137]. In addition, the study revealed selective and faster dissolution of the α-phase than of the β-phase in $HF/HNO_3$ acid solutions consisting of 0.18 M HF and 1.88 M $HNO_3$.

# 4 EXPERIMENTAL PART

In this chapter the investigated titanium alloys, the sample preparation methods and the experimental techniques used for analysing the samples are described.

## 4.1 Materials

In the present thesis two different forms of the Ti-6Al-2Sn-4Zr-2Mo and Ti-6Al-4V alloys were investigated.

### 4.1.1 Ti-6Al-4V

Ti-6Al-4V is an α+β alloy that possesses good combination of strength, corrosion resistance and fabrication ability. For the studies presented in **Papers I-IV**, Ti-6Al-4V was received in plate form in accordance with AMS 4911 L [138]. The microstructure of Ti-6Al-4V was equiaxed consisting of primary α grains and elongated α needles in transformed β matrix (see Figure 4.1 a). The chemical composition of the alloy is given in Table 4.1.

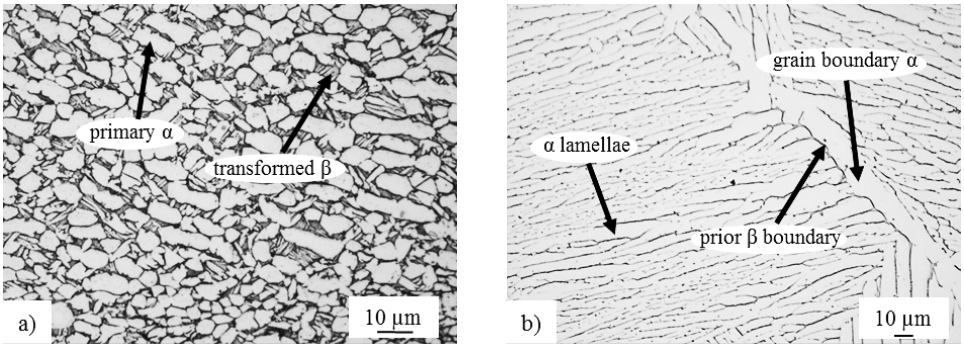


**Figure 4.1** Microstructure of Ti-6Al-4V a) plate form [used in **Papers I-IV**] and b) as-cast condition [used in **Papers V** and **VI**]

**Table 4.1** Chemical composition in wt. % of plate Ti-6Al-4V [138] [**Papers I-IV**]

| Element | Al | V | Fe | O | C | N | H | Y | Ti |
|---|---|---|---|---|---|---|---|---|---|
| **min** | 5.50 | 3.50 | -- | -- | -- | -- | -- | -- | Bal. |
| **max** | 6.75 | 4.50 | 0.3 | 0.20 | 0.08 | 0.05 | 0.015 | 0.005 | Bal. |

For the studies presented in **Papers V** and **VI,** Ti-6Al-4V in as-cast condition was used. The alloy had Widmanstätten microstructure consisting of coarse prior β grains composed of α-colonies of parallel α lamellae (see Figure 4.1 b). The chemical composition of this alloy was in the range of the plate form Ti-6Al-4V alloy, as shown in Table 4.1.

### 4.1.2 Ti-6Al-2Sn-4Zr-2Mo

Ti-6Al-2Sn-4Zr-2Mo is a near-α alloy that has high strength, high fracture toughness and good creep resistance. For the studies presented in **Papers I-III** wrought alloy was used, solution and precipitation heat treated according to AMS 4979 G [139]. The alloy had a bimodal microstructure consisting of equiaxed and/or elongated primary α grains in a transformed β matrix (see Figure 4.2 a). The chemical composition of the alloy in wt. % is shown in Table 4.2.

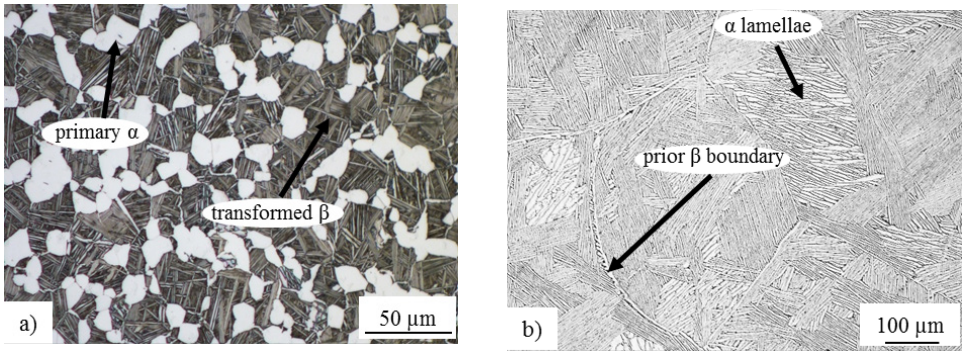


**Figure 4.2** Microstructure of Ti-6Al-2Sn-4Zr-2Mo a) wrought condition [used in **Papers I-III**] and b) as-cast condition [used in **Papers V** and **VI**]

**Table 4.2** Chemical composition in wt. % of wrought Ti-6Al-2Sn-4Zr-2Mo [139] [**Papers I-III**]

| Element | Al | Zr | Mo | Sn | Si | O | Fe | C | N | H | Y | Ti |
|---|---|---|---|---|---|---|---|---|---|---|---|---|
| **min** | 5.50 | 3.60 | 1.80 | 1.80 | 0.06 | -- | -- | -- | -- | -- | -- | Bal. |
| **max** | 6.50 | 4.40 | 2.20 | 2.20 | 0.10 | 0.15 | 0.10 | 0.05 | 0.05 | 0.0125 | 0.005 | Bal. |

For the studies presented in **Papers V** and **VI**, Ti-6Al-2Sn-4Zr-2Mo in as-cast condition was used. The alloy had Widmanstätten microstructure consisting of prior β grains composed of α-colonies of parallel α lamellae (see Figure 4.2 b). The chemical composition of the alloy investigated in the **Paper V** in wt. % is shown in Table 4.3, whereas the chemical composition of the alloy used in **Paper VI** was in the range of the wrought form Ti-6Al-2Sn-4Zr-2Mo alloy, as shown in Table 4.2.

**Table 4.3** Chemical composition in wt. % of as-cast Ti-6Al-2Sn-4Zr-2Mo [**Paper V**]

| Element | Al | Zr | Mo | Sn | Si | O | Fe | C | N | H | Y | Ti |
|---|---|---|---|---|---|---|---|---|---|---|---|---|
| **Wt. %** | 6.04 | 3.98 | 2.06 | 2.01 | 0.07 | 0.03 | 0.04 | 0.03 | 0.004 | 0.0014 | <0.001 | Bal. |

## 4.2 Sample preparation

The sample preparation for the studies presented in all the appended papers (**Papers I-VI**) involved cutting of the samples in specified geometrical shapes using electric discharge machining (EDM).

For **Papers I-III** the samples were cut into a square plate shape with dimensions 10 x 10 x 5 mm. After cutting, all samples were manually ground using silicon carbide polishing paper down to 2500P grit size (8.4 ± 0.5 μm) and cleaned with acetone in ultrasonic bath for 15 minutes. The samples were then rinsed with ethanol and dried in air. All samples were isothermally heat treated at three selected temperatures for heating times up to 500 hours. The heat treatment procedure is described in section 4.2.1.

For **Paper IV** cross-sectioned samples were mounted in Bakelite and prepared using standard metallographic procedure were used.

For **Paper V** the low cycle fatigue (LCF) samples were cut from the as-cast Ti-6Al-2Sn-4Zr-2Mo alloy using EDM. The geometry and dimensions are shown in **Paper V** (see Figure 2 in **Paper V**). All LCF samples were ground and polished to a final surface roughness of about 200 nm.

All samples used in **Paper VI** were cut into disk shapes with 3-4 mm height and 6.5 mm diameter using EDM. After cutting, one face of the samples was ground and polished using standard metallographic procedure. The last polishing step of all sample surfaces was performed using colloidal silica with particle size of 0.05 μm until mirror surface finish was achieved. The polishing of the samples was followed by ultrasonic cleaning in acetone for 15 minutes, rinsing with ethanol and drying in air.

### 4.2.1 Isothermal heat treatments

The isothermal heat treatments for the studies presented in **Papers I-III** were carried out in a box furnace (NABERtherm model N11/R) and a NABERtherm tube model furnace in air at atmospheric pressure. All square plate samples were placed on $Al_2O_3$ crucibles and inserted into the furnaces. Thermocouples positioned inside the furnaces were used to follow the actual temperature of the samples during testing. Every 24 hours the temperature of the furnace was checked. The deviation of the temperature inside the furnace was ± 5 ºC from the desired temperature. The samples were isothermally held at 500, 593 and 700 ºC for 5, 10, 50, 100, 200, 300, 400 and 500 hours.

All samples were weighted before and after each heat treatment using analytical microbalance SARTORIUS ANALYTICS with an accuracy of ± 0.0001 g.

In **Paper I** thermal gravimetric analysis (TGA) measurements on Ti-6Al-4V and Ti-6Al-2Sn-4Zr-2Mo were performed at 593 ºC in technical air for times up to 200 hours using thermal analysis instrument NETZSCH STA 446C. The samples for the TGA measurements were cut into size 17 x 2.5 x 10 mm.

### 4.2.2 Optical evaluation of alpha-case

The alpha-case thickness evaluation for **Papers I-IV** was performed after heat treatment of the samples and involved several steps. All samples were cut in halves and cleaned in acetone for 15 minutes using ultrasonic bath. The samples were then mounted in Bakelite (BUEHLER Simplimet model 1000). After mounting, the samples were polished with colloidal silica using a semiautomatic polishing machine (BUEHLER Phoenix 4000). The polished test samples were etched using a standard etching procedure for titanium alloys, which comprises two steps. First, the polished sample surfaces were swabbed with Kroll's reagent which consists of a mixture of 1-2 ml 40 % HF and 2-3 ml 65 % $HNO_3$ in 100 ml distilled water. This etching step was followed by etching in Weck's reagent which consists of 3 g dissolved $NH_4HF_2$ in 100 ml distilled water. The Weck's reagent etching was carried out for about 10 s, ceasing when bubbles started to appear. After etching, all the samples were rinsed with distilled water and ethanol followed by drying in air.

Figure 4.3 shows representative optical micrographs of Ti-6Al-4V and Ti-6Al-2Sn-4Zr-2Mo alloys which were used for optical evaluation of the alpha-case thickness. In total 40-60 measurements of the alpha-case thickness were performed on each sample. The measurements were performed along the entire perimeter of the cross-sectioned samples with approximately 500 μm spacing.

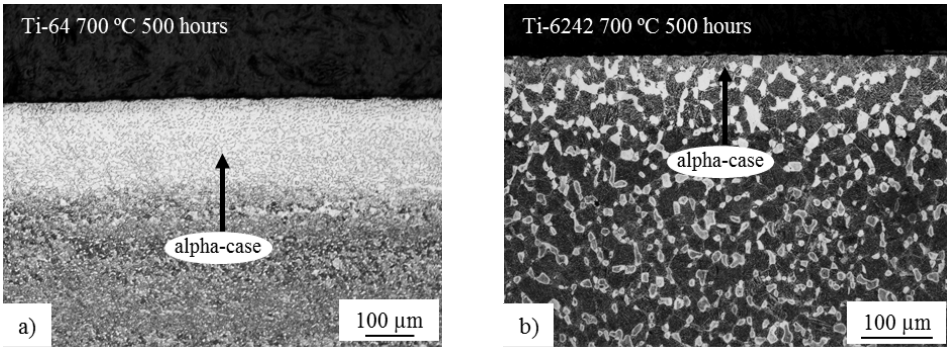


**Figure 4.3** Optical micrographs of alpha-case layer after two step etching of a) Ti-6Al-4V and b) Ti-6Al-2Sn-4Zr-2Mo

### 4.2.3 Chemical milling and etching

The LCF samples in **Paper V** were chemically treated prior to the LCF testing in solutions containing hydrofluoric (HF) and nitric acid ($HNO_3$) in mass concentration ratio 1:11. The LCF samples were treated for 5 and 60 minutes. The temperature of the milling solutions was controlled and kept in the range 40 ± 2 ºC.

In **Paper VI**, the disk samples were immersed into solutions containing HF and $HNO_3$ acids prior to imaging of the sample surfaces using atomic force microscopy (AFM). Two

concentration ratios, 1:3 (0.1 M HF + 0.3 M $HNO_3$) and 1:11 (0.1 M HF + 1.1 M $HNO_3$) of the acids, and three immersion times (1, 5 and 10 minutes) were used. The acid solutions were prepared by mixing appropriately calculated volumes of 40 % HF and 65 % $HNO_3$ acids in 50 ml distilled water.

## 4.3 Characterisation and mechanical testing techniques

In this section the experimental and the testing techniques used to investigate, analyse, and characterise the materials in the present thesis are described in a general manner.

### 4.3.1 Microstructural characterisation techniques

**Optical microscopy (OM)**

The microstructural characterisation of the materials used in the present thesis and the optical evaluation of the alpha-case thickness in **Papers I-IV** were performed using optical microscope NIKON ECLIPSE model MA200.

**Scanning electron microscopy (SEM)**

Scanning electron microscopes (SEM) model JEOL JSM-6460LV and high-resolution field emission scanning electron microscope (FE-SEM) model MERLIN from Carl Zeiss were used for characterisation of the oxide scales developed on the two studied alloys for the work presented in **Papers II** and **III**. The micrographs were obtained using secondary and back-scattered electrons mode, accelerating voltage of 3-25 kV, probe current of 84 μA for the JEOL and 1nA for FE-SEM. The chemical composition of the oxide scales was measured using Energy Dispersive Spectrometer (EDS) attached to the SEM microscopes.

In **Paper V**, the fractographic analysis of the fracture and lateral surfaces of the low cycle fatigue (LCF) samples was carried out using SEM JEOL JSM-6460LV and field emission (FE-SEM) JEOL JSM-7001F. The imaging was performed using secondary and back-scattered electrons with an accelerating voltage of 15-25 kV.

In **Paper VI**, scanning electron microscope (SEM, JEOL JSM-6460LV) was used to characterise the microstructure of the two investigated alloys. Imaging was performed using secondary electrons with an accelerating voltage of 20 kV and probe current of 84 μA. The chemical composition of the microstructural constituents, i.e. α-phase and β phase, in the two studied alloys was analysed by the EDS attached to the SEM.

**Electron Probe Micro Analyser (EPMA)**

Electron Probe Micro Analyser (EPMA) is a non-destructive instrumental technique and its principle of work is based on bombarding micro-volumes of the sample surface with focused electron beam and collection of the emitted X-ray photons. The elements present in the sample emit X-rays with characteristic wavelengths providing identification of the chemical composition

of the sample by recording the Wavelength Dispersive Spectroscopy (WDS) spectra. The WDS detector provides better spectral resolution and shorter detector dead time than SEM-EDS systems. This also provides better sensitivity for analysing light elements such as O, N and C. EPMA is considered as fully qualitative and quantitative method for elemental analysis of submicron-sized volumes at the sample surface with sensitivity in parts per million (ppm).

EPMA (JEOL JXA-8500F) was used to measure the concentrations of oxygen and the alloying elements along the oxygen enriched layer of Ti-6Al-4V and Ti-6Al-2Sn-4Zr-2Mo in the studies presented in **Papers II** and **III**. Accelerating voltage of 10 keV and probe current of 20 nA were used for the measurements. Line scans, with lengths between 100-400 μm, across the oxygen enriched layer thickness of cross-sectioned samples of the two studied alloys were performed. The measurements were carried out in point mode with step width in the range of 0.5-2 μm. The concentration of the measured elements was quantified by overlapping the intensities of the characteristic peaks from elements and standards with known concentrations. The following standards were used for calibration: titanium nitride (TiN) for measuring titanium (Ti) and nitrogen (N) concentrations, pure aluminium (Al), pure tin (Sn), pure zirconium (Zr), pure molybdenum (Mo), pure vanadium (V) for measuring Al, Sn, Zr, Mo, V and quartz ($SiO_2$) for measuring of O. The obtained intensity peaks were subjected to ZAF (Z-atomic weight, A-adsorption coefficient and F-fluorescence) correction [140].

**Focused Ion Beam Scanning Electron Microscopy (FIB-SEM)**

Focused ion beam (FIB) is an instrumental technique that is coupled with scanning electron microscope (SEM) and uses focused beam of ions instead of electrons to obtain an image of the sample. It finds broad applications in various scientific fields and is in materials science mainly used for deposition and ablation of materials. Different ion sources are available such as gold and iridium, but gallium ($Ga^+$) is the most typically used in FIB instruments because of its low melting temperature (30 ºC), low volatility and low vapour pressure. Low ion beam currents are used for imaging and high beam currents are used for sputtering or milling the sample surface [141].

A dual beam Focused Ion Beam FIB-SEM microscope, (Zeiss Neon 40 Crossbeam) was used in **Paper V** to mill the surface of the LCF sample that was chemically treated in $HF/HNO_3$ solution. The milling of the sample surface was performed by bombarding it with $Ga^+$ ions in order to form a trench to observe the subsurface morphology of the sample in cross-section view. Prior to the ion milling, a thin platinum layer with ~ 500 nm thickness was deposited onto the surface. A $Ga^+$ ion source was used to remove material from the surface in the following order: coarse milling with 10 nA, medium polishing with 2 nA and final polishing with 500 pA FIB current.

### 4.3.2 Phase and crystallographic characterisation techniques

**X-ray Diffraction (XRD)**

An X-ray Diffractometer (XRD model PANalytical Empyrean) equipped with a PIXcel3D detector was used in **Paper III** to record the XRD patterns of the oxide scales developed after heat treatment at 700 ºC for 500 hours. The X-ray tube was an Empyrean Cu LFF HR and scans were performed with 0.026º step size in the 2-theta range of 20º- 80º.

**Electron Back-Scattered Diffraction (EBSD)**

Electron back-scattered diffraction (EBSD) is a technique coupled with scanning electron microscope (SEM) providing quantitative information of the crystallographic nature of crystalline materials such as grain size, boundary character, grain orientation and identification of texture and phases [142]. EBSD works by placing a flat, highly polished sample at 70º angle to the incident electron beam as shown in Figure 4.4. The incident electron beam interacts with the sample surface and low energy backscattered electrons are diffracted. The diffracted electrons are detected on a phosphor screen and generate visible lines, called Kikuchi bands, or electron backscatter patterns (EBSP's). The EBSP's are projections of the geometry of the lattice planes in the crystal of the examined sample and provide information about the crystalline structure and crystallographic orientation of the grains.

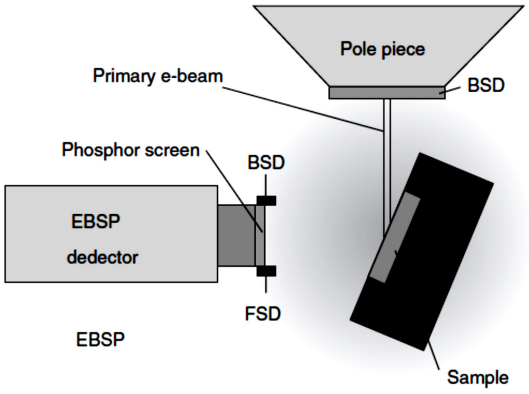


**Figure 4.4** Electron back-scattered diffraction setup and arrangement of the sample in the SEM [142]

In **Paper IV**, EBSD in FE-SEM (JEOL 7001F), equipped with an orientation imaging microscopy system was used for phase identification in the alpha-case layer and the in the bulk microstructure of Ti-6Al-4V in as-received condition and after heat treatment at 700 ºC for 500 hours. In addition, identification of the crystallographic orientation of the α-Ti grains in as-

received Ti-6Al-4V and in the alpha-case layer was performed in the regions where the nanoindentation measurements were carried out. The EBSD measurements were performed using two constant step sizes: 100 and 50 nm for obtaining the phase maps and crystallographic orientations, respectively. Acceleration voltage in the range of 15-20 kV and beam current of 1 nA were used.

### 4.3.3 Surface characterisation techniques

**X-ray Photoelectron Spectroscopy (XPS)**

X-ray photoelectron spectroscopy (XPS) is a technique that is used for surface characterisation of materials and provides identification of the chemical composition, the chemical state of the elements present in the material and the element distribution in depth. The working principle involves irradiation of the material surface with soft X-rays and measurements of the kinetic energy of the emitted photo electrons.

In **Paper III**, the oxide scales formed after heat treatment at 700 ºC for 500 hours in Ti-6Al-4V and Ti-6Al-2Sn-4Zr-2Mo were characterised using XPS on a SPECS system equipped with an Al anode XR50 source operating at 150 mW and a Phoibos 150 MCD-9 detector. The samples were mounted on a sample holder using double sided carbon adhesive. The area analysed was 3 x 3 mm. The surface of the samples was not cleaned by ion etching prior the XPS analysis. Spectra were recorded with pass energy of 25 eV at 0.1 eV steps at a pressure below $10^{-7}$ Pa and binding energies were referred to the C 1s peak at 284.45 eV. The following sequence of spectra was recorded: survey spectrum, C 1s, O 1s, Ti 2p, Al 2p, V 2p, Fe 2p, Sn 3d, Zr 3d and Mo 3d. Data were processed using CasaXPS program (Casa Software Ltd.,UK) [143] and the atomic fractions were calculated using peak areas normalised on the basis of acquisition parameters after background subtraction, experimental sensitivity factors and transmission factors provided by the manufacturer.

**Atomic Force Microscopy (AFM)**

In **Paper VI**, the AFM measurements were carried out in contact mode with a Solver AFM (NT-MDT) instrument equipped with 100 μm probe scanner. A PNP-DB type of cantilever (Nanosensors) was used with a length of 100 μm and a nominal force constant of 0.48 N/m with a specified tip radius of less than 10 nm. The measurements were performed in close-loop regime in x- and y-direction to reduce the non-linearity and cross-talk effect. Typical scan velocities of 20-50 μm/s were used depending on the surface roughness conditions. The topography data obtained for the mirror polished samples were used as reference for the two alloys before immersion in the $HF/HNO_3$ solutions.

**Kelvin Probe Force Microscopy (KPFM)**

In **Paper VI**, Scanning Kelvin Probe Force Microscopy (SKPFM) was used on mirror polished surface of the two alloys in air to identify possible galvanic elements between the α-

phase and the β-phase at microscopic scale. This technique is known as two-pass technique, where in the first pass the AFM tip scans the surface in contact mode and information of the topography of the sample surface is acquired. In the second pass the AFM tip follows exactly the trajectory of the first pass, but this time at fixed lift height position (100 nm) from the sample surface in order to detect the Volta-potential distribution across the metal surface. The AFM tip and the sample surface are electrically connected and once they are brought into close contact their Fermi levels will balance, which will form Volta-potential difference between the tip and the sample surface.

The SKPFM measurements were performed with an Ntegra Prima AFM (NT-MDT) with a 100 μm sample scanner in closed-loop operation mode. The tip was lifted to a 100 nm distance above the surface to minimize the effect of topography on the measured Volta-potential between the tip and the surface. The relative humidity was around 30-40 %. For the SKPFM measurements an n-type silicon cantilever NSG01 (produced by NT-MDT) with PtIr conductive coating with a nominal spring constant of 5.1 N/m and a nominal tip curvature radius of 35 nm was used. The work function (*WF*) of the probe was calibrated using freshly cleaved Highly Oriented Pyrolytic Graphite (HOPG) substrate and the *WF* was 4.67 eV. The same probe was used for each set of measurements. The typical scan velocity was about 48 μm/s.

### 4.3.4 Mechanical testing techniques

**Microhardness**

In **Paper I** and **II** the hardness of the investigated alloys in as-received condition and the hardness of the developed oxygen enriched, i.e. alpha-case layers were measured using MXT- α microhardness tester (MATSUZAWA) with a Vickers indenter. The applied load was 100 g and the indent size was approximately 20-25 μm.

**Nanoindentation**

In **Paper IV** the nanoindentation measurements were conducted with MTS NanoXP instrument using pyramidal Berkovich tip indenter. The indenter shape was calibrated using fused silica [144]. The obtained experimental data were analysed by Oliver and Pharr method [144,145]. Two sets of measurements were performed. The mechanical response of the α-Ti grains in the as-received alloy and in the alpha-case layer was evaluated as the average behaviour of 100 indentations arranged in 10 x 10 arrays at 200 nm of displacement depth. The distance between imprints was kept constant and equal to 5 μm, in order to avoid any overlapping effect of the plastically deformed zones. Additionally, the hardness profile along the alpha-case layer thickness was assessed by performing 3 x 60 arrays of imprints at 100 nm of maximum penetration depth with 4 μm of separation distance between each indent.

**Low Cycle Fatigue (LCF)**

In **Paper V**, the LCF tests were performed under strain control by uniaxial loading of the samples at a strain ratio R = 0 and a frequency f = 0.5 Hz, with triangular waveform, according to ASTM E606-04 [146]. The gauge length of the extensometer was 12.7 mm and all tests were carried out at room temperature using a closed loop servo controlled hydraulic system. Three different values of total strain range for performing the LCF tests were used, $\Delta\varepsilon_t$ = 0.5 %, 0.8 % and 1.2 %. In total, eight samples were tested in as-cast, i.e. as-machined condition, two at low, three at medium and three at high imposed strain. The rest of the samples were tested after either 5 or 60 minutes of chemical milling treatment in solution that consisted of HF and $HNO_3$ acids with 1:11 mass concentration ratio (four at $\Delta\varepsilon_t$ = 0.5 %, four at $\Delta\varepsilon_t$ = 0.8 % and three at $\Delta\varepsilon_t$ = 1.2 %, for both milling times).

### 4.3.5 Electrochemical measurements

In **Paper VI**, linear potentiodynamic polarisation (linear sweep voltammetry-LSV) was used to study the corrosion behaviour of the two alloys in pure HF acid with concentration 0.1 M and in HF/$HNO_3$ acid solutions with 1:3 and 1:11 molar concentration ratios between the two acids. The measurements were carried out on freshly polished sample surface in naturally-aerated solutions using potentiostat Autolab PG-STAT302N (Metrohm Autolab, Netherlands) controlled with Nova 2.0 software (Metrohm Autolab, Netherlands). The experimental setup consisted of polarisation and reference cells connected through salt bridge. Schematic drawing of the experimental setup is shown in Figure 1 in **Paper VI**. The two polarisation cells were fabricated from polytetrafluoroethylene (PTFE), Teflon material which is resistant to HF acid. A standard three-electrode system was used consisting of alloy sample as working electrode, a platinum wire as a counter electrode and Ag/AgCl (3 M KCl) as reference electrode. The alloy samples were embedded into fabricated PTFE rods with electrical contact. The electrolyte used in the reference cell was 1 M KCl, whereas the polarisation cell contained the HF/$HNO_3$ acid solution. Freshly prepared HF/$HNO_3$ acid solutions were used for each experiment. The scanning rate used for the polarisation measurements was 1 mV/s. All measurements were performed at room temperature.

Prior to potentiodynamic polarisation measurements the samples were immersed in the testing solutions for 5 minutes to stabilise. Then the open circuit potential ($E_{OCP}$) was monitored for 10 minutes. Finally, the linear potentiodynamic polarisation measurements were started.

# 5 SUMARRY OF APPENDED PAPERS

## 5.1 Paper I

**Study of alpha-case depth in Ti-6Al-2Sn-4Zr-2Mo and Ti-6Al-4V**

Raghuveer Gaddam, **Birhan Sefer**, Robert Pederson and Marta-Lena Antti

In **Paper I**, the alpha-case depths formed after isothermal heat treatments of Ti-6Al-2Sn-4Zr-2Mo at 500 and 593 ºC and of Ti-6Al-4V at 593 and 700 ºC in air for up to 500 hours were investigated. In addition, the isothermal oxidation behaviour of the two alloys using thermal gravimetric analysis (TGA) in technical air at 593 ºC for up to 200 hours was studied. The heat treatments resulted in formation of oxide scale on the surface of the two alloys and oxygen enriched layer below the oxide, i.e. alpha-case. The alpha-case depth was evaluated optically after etching the samples with two-step etching procedure. The etching revealed the alpha-case depth as bright continuous layer next to the edge of the samples. It was observed that the alpha-case depth is a function of temperature and time following approximately parabolic relationship for both alloys at all three temperatures. Similar alpha-case depth values (~ 30 μm) were measured optically for both alloys after treatment at 593 ºC for up to 500 hours. This indicated that there is no significant influence of the differences in chemical composition and microstructure between the alloys on the alpha-case depth. The 500 hours heat treatment of Ti-6Al-2Sn-4Zr-2Mo at 500 ºC and of Ti-6Al-4V at 700 ºC resulted in maximum alpha-case depths of 10 μm and 200 μm, respectively. The hardness of the alpha-case in Ti-6Al-2Sn-4Zr-2Mo and Ti-6Al-4V after treatment at 593 and 700 ºC for 500 hours was measured and compared with the bulk hardness. It was found that the alpha-case hardness is higher than the bulk hardness for both alloys. This is due to solid solution strengthening effect of the diffused oxygen into the bulk of the alloys. Additionally, the hardness along the alpha-case depth was measured for Ti-6Al-4V after treatment at 700 ºC for 500 hours. The obtained hardness profile showed that the hardness is gradually decreasing from the surface towards the bulk of the sample, where at depths of about 250 μm the bulk hardness value was reached. The TGA results for Ti-6Al-2Sn-4Zr-2Mo and Ti-6Al-4V showed continuous weight gain increase with respect to time. The obtained weight gain per surface area vs. time were analysed and found to obey approximately parabolic relationship. Larger weight gain was measured for Ti-6Al-4V than for Ti-6Al-2Sn-4Zr-2Mo. This was due to a thicker oxide scale formation in Ti-6Al-4V (~ 5 μm) compared with Ti-6Al-2Sn-4Zr-2Mo (< 1 μm).

***Author's contribution:*** The author performed all experimental work for Ti-6Al-4V, wrote the experimental section of the paper and presented the paper orally at the 7th EEIGM conference in Luleå, Sweden, March 2013.

## 5.2 Paper II

**Oxidation and alpha-case formation in Ti-6Al-2Sn-4Zr-2Mo alloy**

Raghuveer Gaddam, **Birhan Sefer**, Robert Pederson and Marta-Lena Antti

In **Paper II**, the oxidation and the alpha-case layer formation in Ti-6Al-2Sn-4Zr-2Mo after isothermal heat treatments in air at 500, 593 and 700 ºC for times up to 500 hours were studied. The isothermal heat treatments at all three temperatures resulted in formation of oxide scale and oxygen enriched layer, i.e. alpha-case below the oxide scale.

In general, it was observed that the weight gain and the alpha-case thickness are increasing with temperature and time. The weight gain analysis revealed that the oxidation mainly follows parabolic behaviour at all tested temperatures with some exceptions at 500 and 700 ºC where transitions in the oxidation kinetics at particular time intervals were observed. Cubic oxidation behaviour was observed at 500 ºC for times up to 200 hours which for prolonged times (≥ 200 hours) changed to parabolic. At 593 ºC the oxidation kinetics was parabolic for times up to 500 hours. At 700 ºC the oxidation kinetics followed parabolic behaviour up to 200 hours, which for longer times (≥ 200 hours) changed to linear. The activation energy for the parabolic oxidation in the temperature range of 500-700 ºC was estimated to be 157 kJ/mol.

The oxide scales formed after 500 hours exposure at all three tested temperatures were characterised by scanning electron microscope (SEM). The SEM micrographs of the oxides revealed both dense and porous morphology of the oxide scales depending on the temperature. At 500 ºC the oxide scale was compact and dense with thickness less than 1 μm, whereas at 593 ºC and 700 ºC higher thickness and porosity of the oxide scales were observed. The highest porosity of the oxide was observed in the sample heat-treated at 700 ºC for 500 hours. It is considered that the porous structure of the oxide scale at 700 ºC for times ≥ 200 hours is the main reason for the parabolic to linear change in the oxidation kinetics.

The alpha-case thickness formed in all samples after heat treatment up to 500 hours was evaluated optically and a parabolic relationship with respect to the exposure time at all three tested temperatures was observed. The optical alpha-case thickness measurements were used to estimate the oxygen diffusion parameters and the activation energy for oxygen diffusion. The activation energy for oxygen diffusion was estimated to be 153 kJ/mol.

Electron Probe Micro Analyser (EPMA) was used to measure the chemical composition and the oxygen content across the oxygen enriched layer thickness. The EPMA oxygen profiles revealed that the oxygen concentration in the alpha-case layer is highest at the surface, and decreasing gradually moving towards the bulk of the alloy. The oxygen profiles were used to estimate the oxygen enriched layer thickness. The values for the alpha-case thickness measured optically and the values for the oxygen enriched layer thickness estimated by the EPMA oxygen profiles were compared. Good agreement between both techniques in evaluation of the alpha-case thickness was observed for all samples, except for the samples heat-treated at 700 ºC for times ≥ 300 hours. The oxygen profiles for these samples revealed about 50 μm larger oxygen

enriched layer thicknesses in comparison to the ones measured optically. The hardness profile of the sample heat-treated at 700 ºC for 500 hours showed good agreement and similar alpha-case thickness as the one estimated by the oxygen profile. This shows that optical evaluation of the alpha-case thickness for the samples heat-treated at 700 ºC for times ≥ 300 hours underestimated the thickness of the oxygen enriched layer.

***Author's contribution:*** The author performed the optical evaluation of the alpha-case thickness and the microhardness measurements, analysed all experimental data and wrote the paper together with the first author and with suggestions from the other co-authors.

## 5.3 Paper III

**Oxidation behaviour of Ti-6Al-4V and Ti-6Al-2Sn-4Zr-2Mo alloys exposed to air at elevated temperatures**

**Birhan Sefer**, Raghuveer Gaddam, Robert Pederson, Antonio Mateo, Ragnar Tegman and Marta-Lena Antti

In **Paper III**, the isothermal oxidation behaviour in air at 500, 593 and 700 ºC for 500 hours of Ti-6Al-4V and Ti-6Al-2Sn-4Zr-2Mo was investigated and compared.

The oxidation of both alloys resulted in oxide scale formation and subsurface oxygen enriched layer, i.e. alpha-case. The weight gain results showed that the oxidation of two alloys is dependent on temperature and time. At 500 ºC the measured weight gain was small for both alloys and at 593 ºC and 700 ºC was higher for Ti-6Al-4V than for Ti-6Al-2Sn-4Zr-2Mo indicating that Ti-6Al-4V is less oxidation resistant than Ti-6Al-2Sn-4Zr-2Mo. The oxidation rates were analysed. It was found that both alloys obey approximately parabolic behaviour except at 700 ºC for times ≥ 200 hours where transition from parabolic to linear behaviour of the oxidation kinetics occurs. The parabolic rate constants and the activation energies for oxidation were estimated for alloys, 278 kJ/mol and 157 kJ/mol for Ti-6Al-4V and Ti-6Al-2Sn-4Zr-2Mo, respectively.

The X-ray diffraction (XRD) and X-ray photoelectron spectroscopy (XPS) analysis on the oxide scales revealed that the oxide scales consist of $TiO_2$ rutile type doped with the main alloying elements. In addition, scanning electron microscopy (SEM) showed a different morphology (i.e. dense and porous) of the oxides scales formed in the two alloys. Dense and well adherent oxide scales were observed for both alloys at all three temperatures, except at 700 ºC for oxidation times longer than 200 hours. The oxide scales were porous and spalled off. In addition, Ti-6Al-4V at 700 ºC after 500 hours formed multi-layered oxide structure consisting of rutile and alumina ($Al_2O_3$) layers. This type of oxide structure was absent for Ti-6Al-2Sn-4Zr-2Mo and only one double layer of $TiO_2$ and $Al_2O_3$ was observed.

The subsurface oxygen enriched layer, i.e. alpha-case developed as result of the oxidation was characterised and analysed using metallographic and microscopic techniques. The alpha-case layer thickness was measured optically after two-step etching, whereas the oxygen and other

elements present in the alloys were measured using electron probe micro analyser (EPMA). The EPMA oxygen profiles measured along the subsurface oxygen enriched layer showed that oxygen forms concentration gradient. The oxygen diffusion parameters and activation energy for oxygen diffusion in the alloys were estimated by using the optically measured values for the alpha-case thickness and the EPMA oxygen profiles. Microstructural change and element re-distribution in the bulk in Ti-6Al-4V after 500 hours at 700 ºC was observed. It was discerned that the alloying elements have tremendous importance of the oxidation behaviour of the alloys. In particular, V and Mo promoted increased oxidation kinetics after ≥ 200 hours oxidation at 700 ºC through formation of subsurface enriched β-phases and volatile oxides responsible for formation of porous oxides structure. The oxygen enriched layer showed significant Ti depletion for both alloys. A mechanism for alpha-case formation was proposed involving inward oxygen diffusion accompanied with outward diffusion of Ti.

***Author's contribution:*** The author performed all experimental work for Ti-6Al-4V and partially for Ti-6Al-2Sn-4Zr-2Mo, analysed all the experimental data and wrote the paper with suggestions from the co-authors.

## 5.4 Paper IV

**Evaluation of the bulk and alpha-case layer properties in Ti-6Al-4V at micro- and nano-metric length scale**

**Birhan Sefer**, Joan Josep Roa, Antonio Mateo, Robert Pederson, Marta-Lena Antti

In **Paper IV**, the hardness of the α-Ti grains in as-received Ti-6Al-4V and in the alpha-case layer developed after isothermal heat treatment at 700 ºC for 500 hours was measured and compared using nanoindentation. In addition, the crystallographic orientation using electron back-scattered diffraction (EBSD) of the α-Ti grains in the as-received Ti-6Al-4V alloy and in the alpha-case layer were analysed in order to evaluate the hardness anisotropy with respect to the grain orientations.

The measured average hardness of the α-Ti grains in the alpha-case layer was higher (9.4 ± 1.4 GPa) than the hardness of the α-Ti grains in the as-received alloy (6.7 ± 0.7 GPa). This is because of solid solution strengthening effect caused by the interstitial oxygen diffusion in the hexagonal close-packed (HCP) crystal structure of α-phase.

A correlation between the hardness and the crystallographic orientation of the grains was established. The results showed that the α-Ti grains of the as-received Ti-6Al-4V alloy exhibit hardness anisotropy with respect to their crystallographic orientation. The α-Ti grains orientated to the basal and/or close to the basal plane were harder than those with prismatic and close to prismatic plane. This is due to the different deformation mechanisms activated for each particular orientation. In the case of α-Ti grains with basal crystallographic orientation and/or close to the basal plane the dislocations glide parallel to the indentation surface, whereas for the α-Ti close to the prismatic and pyramidal orientation the dislocations pile up at the indentation surface. On the

other hand, the α-Ti grains in the alpha-case layer showed crystallographic texture, with the prismatic planes being the predominant orientation. Therefore, the hardness results across the alpha-case layer could not be correlated to the crystallographic orientation in terms of hardness anisotropy, but rather to the oxygen concentration present across the alpha-case layer.

***Author's contribution:*** The author planned the experimental work with help of the second co-author, performed most of the experiments, analysed the experimental data, wrote the paper with suggestions from the co-authors and presented the paper orally at the 13th World Conference on Titanium in San Diego, California, USA, August 2015.

## 5.5 Paper V

**Chemical milling effect on the low cycle fatigue properties of cast Ti-6Al-2Sn-4Zr-2Mo alloy**

**Birhan Sefer**, Raghuveer Gaddam, Joan Josep Roa, Antonio Mateo, Marta-Lena Antti, Robert Pederson

In **Paper V**, the influence of chemical milling treatment on the low cycle fatigue properties (LCF) was investigated. Short and long chemical milling times (i.e. 5 and 60 minutes) in $HF/HNO_3$ acid solution with 1:11 mass concentration ratio between the acids and three imposed total strain range values ($\Delta\varepsilon_t$ = 0.5 %, 0.8 % and 1.2 %) were tested. Additionally, for comparison a series of LCF samples in as-machined condition were also tested.

The LCF results showed significant drop of the fatigue life of the samples treated in the acid solution prior the LCF testing compared to the samples that were not chemically treated. In general, it was revealed that the fatigue life reduction is dependent on the milling time and imposed total strain range. The highest fatigue life reduction was observed for the samples tested at $\Delta\varepsilon_t$ = 0.5 %. Reduction of about 66 % after 5 minutes and 84 % after 60 minutes chemical milling were estimated.

Detailed fractographic analysis on the fracture surfaces of all tested samples was carried out by scanning electron microscopy (SEM). It was observed that the fatigue life reduction is in close correlation with the number of crack initiation sites for the samples chemically milled in the acid solution prior to the LCF tests. Only one main crack initiation site was identified in the non-milled LCF samples, but multiple crack initiation sites were discerned in the chemically milled samples. The SEM characterisation revealed that the substantial reduction of the LCF strength is because of selective and severely etched prior β grain boundaries and pit formation at the triple joints of the prior β grain boundaries with depth up to 100 μm. The surface defects caused by the chemical milling served as stress raisers which facilitated earlier fatigue crack initiation and thus significantly lowered the fatigue life.

***Author's contribution:*** The author performed the experimental work, but not the LCF testing, analysed the experimental data and wrote the paper with suggestions from the co-authors.

## 5.6 Paper VI

**Corrosion behaviour of cast Ti-6Al-4Vand Ti-6Al-2Sn-4Zr-2Mo alloys in hydrofluoric-nitric acid solutions**

**Birhan Sefer**, Illia Dobryden, Nils Almqvist, Robert Pederson, Marta-Lena Antti

In **Paper VI**, the influence of $HF/HNO_3$ acid solutions with molar concentration ratios 1:3 (0.1 M HF + 0.3 M $HNO_3$) and 1:11 (0.1 M HF + 1.1M $HNO_3$) on the corrosion behaviour of cast Ti-6Al-4V and Ti-6Al-2Sn-4Zr-2Mo alloys with Widmanstätten microstructure using electrochemical and atomic force microscopy (AFM) techniques was investigated.

Open circuit potential ($E_{OCP}$) and linear polarisation measurements were carried out for the two alloys when immersed in the $HF/HNO_3$ acid solutions. The $E_{OCP}$ changed towards nobler values with time for the alloys, indicating passivation through formation of $TiO_2$. The linear polarisation experiments showed that the corrosion behaviour of the alloys is dependent on the concentration ratio between the acids and the type of alloy. The corrosion rates were estimated for the two alloys using Tafel plot analysis. It was found that Ti-6Al-4V corrodes faster compared with Ti-6Al-2Sn-4Zr-2Mo in 1:3 $HF/HNO_3$ solutions, while in 1:11 ratio Ti-6Al-2Sn-4Zr-2Mo showed higher corrosion rate.

Scanning Kelvin Probe Force Microscopy (SKPFM) was used to measure the Volta-potential difference on mirror polished surface in air of the two alloys. The SKPFM maps revealed differences in the Volta-potential between the α-laths and the β-phase in the Widmanstätten microstructure of the two alloys. Nobler Volta-potential was measured for the β-phase as compared to the α-phase. Such difference in the Volta-potential between the two phases for the two alloys indicated possibility for formation and operation of micro-galvanic cells, where the α-phase would behave as local anode and the β-phase as local cathode. Moreover, the work function of the individual α-phase and β-phase was calculated for both alloys. The work function values for the individual phases were in agreement with the measured Volta-potentials.

AFM topography measurements were performed before and after immersion in 1:3 and 1:11 $HF/HNO_3$ solutions for up to 10 minutes. The AFM topography maps revealed selective and more pronounced attack of the α-phase compared to the β-phase in both alloys. In order to reveal the potential reasons for the faster corrosion of the α-phase, the chemical composition of the phases was measured using energy dispersive spectrometry (EDS). The EDS analysis showed significant difference in the content of the α- and β-stabilising alloying elements (Al and V for Ti-6Al-4V and Al and Mo for Ti-6Al-2Sn-4Zr-2Mo) between the phases. This difference is the main reason for the selective and faster corrosion of the α-phase as compared to the β-phase. Hence, all experimental facts confirmed the hypothesis for formation and operation of micro-galvanic cells between the two phases.

The height difference between the α-phase and the β-phase was measured and quantified as α/β height difference. It was observed that the α/β height difference is dependent on the concentration ratio between the acids and on the immersion time. The α/β height difference

measured for Ti-6Al-4V was larger in 1:3 $HF/HNO_3$ acid solution, whereas in 1:11 $HF/HNO_3$ solution a larger α/β height difference was measured for Ti-6Al-2Sn-4Zr-2Mo. A relationship between the corrosion behaviour in $HF/HNO_3$ acid solutions on macroscopic and microscopic scale of the two alloys was observed. The presented work is suggesting that the overall corrosion behaviour of both alloys studied in different concentration ratios of HF and $HNO_3$ is controlled by the microscopic corrosion behaviour of the individual micro constituents (i.e. α-phase and β-phase).

***Author's contribution:*** The author planned the experimental work and performed most of the experiments together with the second and third co-author, analysed the experimental data and wrote the paper with suggestions from the co-authors.

# 6 CONCLUSIONS AND FUTURE WORK

## 6.1 Conclusions

The work described in this thesis was aiming for investigating the oxidation and corrosion behaviour of the Ti-6Al-4V and Ti-6Al-2Sn-4Zr-2Mo alloys when exposed to elevated temperature in air and in $HF/HNO_3$ solution, respectively. Based on the experimental results and the observations presented in the **Papers I** to **VI** the following conclusions can be drawn:

*Oxidation*

- Ti-6Al-4V showed worse oxidation resistance than Ti-6Al-2Sn-4Zr-2Mo at 593 and 700 ºC, but there was no significant difference between the two alloys at 500 ºC.
- The oxidation resulted in formation of oxide scale and subsurface oxygen enriched layer (alpha-case) on both alloys. Oxide scale on both alloys was rutile, doped with the alloying elements. The hardness of the alpha-case layer was higher than the bulk for both alloys.
- The oxidation rate at 593 ºC followed parabolic relationship for both alloys. At 700 ºC there was a transition from parabolic to nearly linear oxidation behaviour for times ≥ 200 hours.
- Thicker oxide scales were formed on Ti-6Al-4V than on Ti-6Al-2Sn-4Zr-2Mo and with different morphology. Dense and well adhered oxide scales were formed at 500 and 593 ºC, whereas at 700 ºC the oxide structure was porous. There was a spallation of the oxide scales formed at 700 ºC for both alloys. For Ti-6Al-4V the oxide scale was multi-layered consisting of $TiO_2$ and $Al_2O_3$ layers after oxidation at 700 ºC. This type of oxide layered structure was absent in Ti-6Al-2Sn-4Zr-2Mo.
- For Ti-6Al-4V oxidation at the highest temperature and longest times resulted in notable re-distribution of the alloying elements and microstructural changes.
- The alloying elements played important role for the oxidation behaviour in both alloys. At 700 ºC for exposure times longer than 200 hours, V promoted faster oxidation by increase of the oxide growth rate and oxygen diffusion in Ti-6Al-4V, while Mo promoted faster oxygen diffusion into Ti-6Al-2Sn-4Zr-2Mo.

*Corrosion*

- Chemical milling of Ti-6Al-2Sn-4Zr-2Mo in $HF/HNO_3$ solution substantially reduced the low cycle fatigue (LCF) life as compared to non-milled specimens.
- Chemical milling treatment of Ti-6Al-2Sn-4Zr-2Mo resulted in attack of the prior beta grain boundaries, rendering in formation of ditches and corrosion pits.
- There was only one main crack initiation site in the non-milled samples, whereas multiple crack initiation sites were found on the chemically milled samples.
- Ti-6Al-4V corroded faster than Ti-6Al-2Sn-4Zr-2Mo in solution with 1:3 molar concentration ratio between HF and $HNO_3$ acids, while in 1:11 acid solution Ti-6Al-

2Sn-4Zr-2Mo corroded faster. At microscopic length scale the α-phase in both alloys was less noble than the β-phase and corroded faster.

- The variation in the chemical composition of the α- and β-stabilising elements in the α-phase and the β-phase of the two alloys rendered in formation of micro-galvanic cells between the micro constituents in the Widmanstätten microstructure.

## 6.2 Future work

The work described in the present thesis contributed to better understanding on the following aspects:

1. The oxidation behaviour (i.e. oxide scale and alpha-case formation) of Ti-6Al-4V and Ti-6Al-2Sn-4Zr-2Mo when exposed to air at elevated temperatures in the range 500-700 ºC.
2. The influence of the chemical milling treatment on the low cycle fatigue properties for Ti-6Al-2Sn-4Zr-2Mo.
3. The corrosion behaviour of Ti-6Al-4V and Ti-6Al-2Sn-4Zr-2Mo in different molar concentration ratios of $HF/HNO_3$ acid solutions.

However, the present work also raised new ideas for further research. The work in the **Papers I** to **III** suggested that the alloying elements present in Ti-6Al-4V and Ti-6Al-2Sn-4Zr-2Mo have significant influence on the oxidation behaviour and therefore it is considered that further work on investigating in-depth how different alloying elements influence the oxidation of Ti-6Al-4V and Ti-6Al-2Sn-4Zr-2Mo would be of interest. In particular, it would be a challenging task to determine the defect structure and identify the primary charge carriers of the oxide scales using XRD data in order to obtain detailed insight in the involved oxidation mechanisms. In **Paper III**, the formation of porous oxide structures in Ti-6Al-4V and Ti-6Al-2Sn-4Zr-2Mo when exposed at 700 ºC for 500 hours was related with formation of volatile oxides ($V_2O_5$ in Ti-6Al-4V and $MoO_3$ in Ti-6Al-2Sn-4Zr-2Mo) that evaporate. To substantiate this, thermogravimetric analysis coupled with mass spectroscopy (TGA-MS) may be helpful to detect and identify any evaporating oxide species.

For the aerospace industry it is of high importance to develop a universal reliable oxidation model that will predict the alpha-case layer thickness with high accuracy, applicable for different titanium alloys and oxidation conditions (temperature, time). Such an oxidation model would result in decreasing the costs for removal of the alpha-case either by machining or by chemical milling. To develop this type of model determination of the absolute oxygen concentration at the oxide/metal interface is required. One of the simplest ways to determine the oxygen content is by performing secondary ion mass spectrometry (SIMS) analysis.

Many studies in the literature are focused on investigating the influence of oxidation and the oxygen enriched layer (alpha-case) on the mechanical properties of titanium and its alloys, such as tensile properties, ductility, low cycle fatigue (LCF) properties, and fracture toughness. However, most of these studies are concerned with investigating the macroscopic mechanical behaviour and properties, taking into consideration the synergy effect on both phases. It is well

known that oxygen dissolves and mainly affects the α-phase and is therefore considered that more fundamental knowledge and understanding is required on how oxygen influences the deformation behaviour of single α and β grains enriched with oxygen. In context with the work performed in this thesis for Ti-6Al-4V and Ti-6Al-2Sn-4Zr-2Mo, the following set of experimental work is suggested for future work:

- Nanoindentation and EBSD characterisation of the primary α grains in the alpha-case layer of Ti-6Al-2Sn-4Zr-2Mo, similar as for Ti-6Al-4V in **Paper IV**. This work would provide insight on the effect of oxygen and hardness anisotropy of individual primary α grains.
- Macro and nano-scratch measurements on the alpha-case layer for both alloys. This would provide insight on the deformation behaviour of the oxygen enriched layers combining both phases as well as each phase individually.
- Nano-compression tests by means of Focussed Ion Beam (FIB) milled micro-pillars in individual oxygen enriched (alpha-case) α grains in Ti-6Al-4V and Ti-6Al-2Sn-4Zr-2Mo. This would provide the possibility to investigate the effect of oxygen dissolved in the α-phase in the alpha-case layer on the stress-strain response in order to determine the yield strength for each particular alpha case grain.
- Extracting TEM lamella from the parts of macro-scratch experiments in the alpha-case layer of both alloys. This would provide investigation of the deformation mechanisms of the oxygen enriched layer (alpha-case) as function of oxygen content.

Regarding the work related to the chemical milling and the corrosion behaviour of Ti-6Al-4V and Ti-6Al-2Sn-4Zr-2Mo some aspects need to be further investigated. As seen in **Paper VI**, the alloys behaved differently in $HF/HNO_3$ solutions exhibiting different final surface roughness after treatment. Since the surface condition reduced the LCF strength in Ti-6Al-2Sn-4Zr-2Mo, it is considered that further investigation is needed on optimizing what molar concentration ratio of the two acids would obtain the best surface status with minimum difference. The interaction of the acid solutions with the surface of the alloys at microscopic length scale is considered to be dependent on the orientation of the crystals. Therefore, as future work, it would be interesting to investigate the relationship between crystallographic orientations of α-phase and their susceptibility towards $HF/HNO_3$ acid solutions. The chemical milling process is dependent on the temperature and therefore further studies on how the temperature affects the corrosion behaviour of the two alloys are needed. In this thesis, only Widmanstätten type of microstructure of Ti-6Al-4V and Ti-6Al-2Sn-4Zr-2Mo was studied. It is suggested for future work to also investigate other types of microstructures of these two alloys. In context with these studies, it would be interesting to perform different types of heat treatments in order to reveal what effect different heat treatments would have on the corrosion behaviour of the alloys. This kind of study would require analysing the oxide film using spectroscopy techniques (XPS) in order to get insight into the chemical composition of the film and its influence on the corrosion behaviour in $HF/HNO_3$ acid solutions. Studying the corrosion process of the two alloys in-situ in $HF/HNO_3$

acids using electrochemical AFM would provide more detailed insight of the corrosion behaviour of the different phases at a microscopic length scale.

# REFERENCES


[1] M.J. Donachie, *Titanium a technical guide*, second ed., Materials Park-ASM International, Ohio, **2000**.

[2] C. Leyens, M. Peters, *Titanium and titanium alloys: Fundamentals and applications*, Wiley-VCH, Weinheim, **2003**.

[3] G. Lütjering, J. C. Williams, *Titanium*, second ed., Springer-Verlag, Berlin **2007**.

[4] R.R. Boyer, *An overview on the use of titanium in the aerospace industry*, Materials Science and Engineering A 213 (**1996**) 103-114.

[5] D. Eylon, S. Fujishiro, F.H. Froes, P.J. Postans, H*igh-temperature titanium alloys-A review*, Journal of Minerals Metals and Materials Society 1 (**1984**) 55-62.

[6] C.E. Shamblen, T.K. Redden, *Air contamination and embrittlement of titanium alloys*, in: R.I. Jaffe, N.E. Promisel (Eds.), The Science Technology and Application of Titanium, Pergamon Press, Oxford, (**1968**), pp. 199-208.

[7] R.N. Shenoy, J. Unnam, R.K. Clark, *Oxidation and embrittlement of Ti-6Al-2Sn-4Zr-2Mo alloy*, Oxidation of Metals 26 (**1986**) 105-124.

[8] C. Leyens, D. Weinem, M. Peters, W.A. Kaysser, *Influence of long term annealing on tensile properties and fracture of near- alpha titanium alloy Ti-6Al-2.75Sn-4Zr-0.4Mo-0.45Si*, Metallurgical and Materials Transactions 27A (**1996**) 1700-1708.

[9] R. Evans, R. Hull, B. Wilshire, *The effects of alpha-case formation on the creep fracture properties of the high-temperature titanium alloy IMI834*, Journal of Materials Processing Technolgy 56 (**1996**) 492-501.

[10] A.L. Pilchak, W.J. Porter, R. John, *Room temperature fracture processes of a near-α titanium alloy following elevated temperature exposure*, Journal of Materials Science 47 (**2012**) 7235-7253.

[11] R. Gaddam, M.-L. Antti, R. Pederson, I*nfluence of alpha-case layer on the low cycle fatigue properties of Ti-6Al-2Sn-4Zr-2Mo alloy*, Materials Science and Engeering A 599 (**2014**) 51-56.

[12] B. Sefer, *Oxidation and Alpha–Case Phenomena in Titanium Alloys used in Aerospace Industry: Ti–6Al–2Sn–4Zr–2Mo and Ti–6Al–4V*, Licentiate thesis, Luleå tekniska universitet, **2014**.

[13] P. Bridges, B. Magnus, *Manufacture of Titanium Alloy Components for Aerospace and Military Applications*, Research and Technology Organization, France, **2001**.

[14] F.C. Campbell, *Manufacturing Technology for Aerospace Structural Materials*, Elsevier, **2011**.

[15] J. Sieniawski, W. Ziaja, K. Kubiak, M. Motyka, *Microstructure and mechanical properties of high strength two-phase titanium alloys*, in: J. Sieniawski, W. Ziaja (Eds.), Titanium Alloys-Advances in Properties Control, InTech., China (**2013**), pp. 69-80.

[16] W.T. Harris, *Chemical Milling. The Technology of Cutting Materials by Etching*, Oxford University Press, New York, **1976**.

[17] AMS C-81769, *Chemical milling of metals*, **2008**.

[18] Y.L. Chen, *Chemical milling of titanium*, U.S. Patent No. 4900398A, Feb. 13, **1990**.

[19] M. Peters, J. Kumpfert, C.H. Ward, C. Leyens, *Titanium alloys for aerospace applications*, Advanced Engineering Materials 5 (**2003**) 419-427.

[20] C. Veiga, J. Davim, A. Loureiro, *Properties and applications of titanium alloys: a brief review*, Reviews of Advanced Materials Science 32 (**2012**) 133-148.

[21] P. Doorbar, M. Dixon, A. Chatterjee, *Aero-engine titanium from alloys to composites*, Materials Science Forum 618-619 (**2009**) 127-134.

[22] A.M.M. García, *Blisk Fabrication by Linear Friction Welding*, in: E. Benini (Eds.), Advances in Gas Turbine Technology, InTech., China (**2011**), pp. 411-434.

[23] P. Kofstad, *High temperature oxidation of metals*, John Wiley & Sons, Inc., New York, N.Y. **1966**.

[24] P. Kofstad, *High temperature corrosion*, Elsevier Applied Science Publishers, Crown House, Linton Road, Barking, Essex IG 11 8 JU, UK, **1988**.

[25] O. Kubaschewski, B.E. Hopkins, *Oxidation of Metals and Alloys*, second ed., Butterworths Scientific Publications, **1962**.

[26] K. Hauffe, *Oxidation of Metals*, Plenum Press, New York, **1965**.

[27] A. Fromhold, *Theory of Metal Oxidation*, North Holland Publishing, Amsterdam, **1976**.

[28] N. Cabrera, N. Mott, *Theory of the oxidation of metals*, Reports on Progress in Physics 12, Issue 1 (**1949**) 163-184.

[29] C. Wagner, W. Jost, *Diffusion in solids, liquids, gases*, W. Jost (Eds.), Academic Press, New York, **1952**.

[30] P. Kofstad, K. Hauffe, H. Kjollesdal, *Investigation on the oxidation mechanism of titanium*, Acta Chemica Scandinavica 12 (**1958**) 239-266.

[31] J. Unnam, R. Shenoy, R. Clark, *Oxidation of commercial purity titanium*, Oxidation of Metals 26 (**1986**) 231-252.

[32] H. Okamoto, *O-Ti (Oxygen-Titanium)*, Journal of Phase Equilibria 22 (**2011**) 515-515.

[33] P. Kofstad, *Nonstoichiometry, diffusion, and electrical conductivity in binary metal oxides*, Wiley-Interscience New York, **1972**.

[34] P. Kofstad, *Defects and transport properties of metal oxides*, Oxidation of Metals 44 (**1995**) 3-27.

[35] M. Kim, S. Baek, U. Paik, S. Nam, J. Byun, Electrical conductivity and oxygen diffusion in nonstoichiometric $TiO_{2-x}$, Journal of Korean Physical Society 32 (**1998**) 1127-1130.

[36] H. Conrad, *Effect of interstitial solutes on the strength and ductility of titanium*, Progress in Materials Science 26 (**1981**) 123-403.

[37] A. Kant, B. Strauss, *Dissociation energies of diatomic molecules of the transition elements. II. titanium, chromium, manganese, and cobalt*, Journal of Chemical Physics 41 (**1964**) 3806-3808.

[38] H.H. Wu, D.R. Trinkle, *Direct diffusion through interpenetrating networks: Oxygen in titanium*, Physical Review Letters 107 (**2011**) 0455041-0455044.

[39] Z. Liu, G. Welsch, *Literature survey on diffusivities of oxygen, aluminum, and vanadium in alpha titanium, beta titanium, and in rutile*, Metallurgical Transactions A 19 (**1988**) 1121-1125.

[40] Aerospace series–Test methods–Titanium and titanium alloys–Part 009–*Determination of surface contamination* (SS–EN 2003–009:2007), Swedish Standards Institute, (**2007**).

[41] C.J. Rosa, *Oxygen diffusion in alpha and beta titanium in the temperature range of 932 º to 1142 ºC*, Metallurgical Transactions 1 (**1970**) 2517-2522.

[42] J. Crank, *The Mathematics of Diffusion*, second ed., Oxford University Press, London, **1979**.

[43] W.P. Roe, H.R. Palmer, W.R. Opie, *Diffusion of oxygen in alpha and beta titanium*, ASM 52 (**1960**) 191-199.

[44] T. Wittberg, J.D. Wolf, R.G. Keil, P.S. Wang, *Low-temperature oxygen diffusion in alpha titanium characterized by Auger sputter profiling*, Journal of Vacuum Science and Technology A 1 (**1983**) 475-478.

[45] David, D., E. A. Garcia, and G. Béranger, *A comparative study of insertion and diffusion of oxygen and nitrogen in α-titanium*, in: H. Kimura, O. Izumi (Eds.), Titanium '80 Science and Technology, American Institute of Mining, Metallurgical and Petroleum Engineers Inc., Warrendale Pennsylvania (**1980**), pp. 537-543.

[46] M. Dechamps, P. Lehr, *Sur l'oxydation du titane α en atmosphère d'oxygène: rôle de la couche oxydée et mécanisme d'oxydation*, Journal of Less Common Metals 56 (**1977**) 193-207.

[47] D. David, G. Beranger, E. Garcia, *A study of the diffusion of oxygen in α-titanium oxidized in the temperature range 460-700 ºC*, Journal of Electrochemical Society 130 (**1983**) 1423-1426.

[48] F. Claisse, H.P. Koenig, *Thermal and forced diffusion of oxygen in β-titanium*, Acta Metallurgica 4 (**1956**) 650-654.

[49] L. F. Sokiryanskii, D. V. Ignatov, A. Ya. Shinyaev, I. V. Bogolyubova, V. V. Latsh, M. S. Model, *Titanovye Splavy Nov. Tekh., Mater. Nauch.-Tekh. Soveshch.*, in: N. P. Sazhin (Eds.), Izd. "Nauka": Moscow, USSR, Chemical Abstracts 71, no. 8 (**1969**), pp. 201–210.

[50] O. Carlson, F. Schmidt, R. Lichtenberg, *Investigation of reported anomalies in the electrotransport of interstitial solutes in titanium and iron*, Metallurgical Transactions A 6 (**1975**) 725-731.

[51] J. Stringer, *The oxidation of titanium in oxygen at high temperatures*, Acta Metallurgica 8 (**1960**) 758-766.

[52] P. Kofstad, P. Anderson, O. Krudtaa, *Oxidation of titanium in the temperature range 800-1200 ºC*, Journal of Less Common Metals 3 (**1961**) 89-97.

[53] P. Kofstad, *High-temperature oxidation of titanium*, Journal of Less Common Metals 12 (**1967**) 449-464.

[54] I. Kornilov, *Effect of oxygen on titanium and its alloys*, Metal Science and Heat Treatment 15 (**1973**) 826-829.

[55] J.L. Gomes, A. Huntz, *Correlation between the oxidation mechanism of titanium under a pure oxygen atmosphere, morphology of the oxide scale, and diffusional phenomena*, Oxidation of Metals 14 (**1980**) 249-261.

[56] E. Gemelli, N. Camargo, *Oxidation kinetics of commercially pure titanium*, Matéria 12 (**2007**) 525-531.

[57] S. Kumar, T.S. Narayanan, S.G.S. Raman, S. Seshadri, *Thermal oxidation of CP Ti-An electrochemical and structural characterization*, Materials Characterization 61 (**2010**) 589-597.

[58] S. Zabler, *Interstitial oxygen diffusion hardening-A practical route for the surface protection of titanium*, Materials Characterization 62 (**2011**) 1205-1213.

[59] H.L. Du, P.K. Datta, D.B. Lewis, J.S. Burnell-Gray, *Air oxidation behaviour of Ti6Al4V alloy between 650 and 850 ºC*, Corrosion Science 36 (**1994**) 631-642.

[60] S. Frangini, A. Mignone, F. de Riccardis, *Various aspects of the air oxidation behaviour of a Ti6Al4V alloy at temperatures in the range 600-700 ºC*, Journal of Materials Science 29 (**1994**) 714-720.

[61] H. Du, P. Datta, D. Lewis, J. Burnell-Gray, *High-temperature corrosion of Ti and Ti-6Al-4V alloy*, Oxidation of Metals 45 (**1996**) 507-527.

[62] H. Dong, X. Li, *Oxygen boost diffusion for the deep-case hardening of titanium alloys*, Materials Science and Engineering A 280 (**2000**) 303-310.

[63] M. Mungole, N. Singh, G. Mathur, *Oxidation behaviour of Ti6Al4V titanium alloy in oxygen*, Materials Science and Technology 18 (**2002**) 111-114.

[64] Y. Sugiura, *Growth behaviors of alpha cases in Ti-6Al-4V and Ti-10V-2Fe-Al alloys during high temperature heat treatment in air*, in: G. Lütjering, J. Albrech (Eds.), Titan-2003, Science and Technology IV, Wiley-VCH, Weinheim, (**2003**), pp. 2051-2057.

[65] F. Pitt, M. Ramulu, *Influence of grain size and microstructure on oxidation rates in titanium alloy Ti-6Al-4V under superplastic forming conditions*, Journal of Materials Engineering and Performance 13 (**2004**) 727-734.

[66] Z.X. Zhang, H. Dong, T. Bell, B. Xu, *The effect of treatment condition on boost diffusion of thermally oxidised titanium alloy*, Journal of Alloys and Compounds 431 (**2007**) 93-99.

[67] D. Jordan, *Study of alpha case formation heat treated Ti-6-4 alloy*, Heat Treating Progress 8 (**2008**) 45-47.

[68] H. Guleryuz, H. Cimenoglu, *Oxidation of Ti-6Al-4V alloy*, Journal of Alloys and Compounds 472 (**2009**) 241-246.

[69] A. Biswas, J.D. Majumdar, *Surface characterization and mechanical property evaluation of thermally oxidized Ti-6Al-4V*, Materials Characterization 60 (**2009**) 513-518.

[70] S. Kumar, T.S. Narayanan, S.G.S. Raman, S. Seshadri, T*hermal oxidation of Ti6Al4V alloy: Microstructural and electrochemical characterization*, Materials Chemistry and Physics 119 (**2010**) 337-346.

[71] R. Gaddam, B. Sefer, R. Pederson, M.-L. Antti, *Study of alpha-case depth in Ti-6Al-2Sn-4Zr-2Mo and Ti-6Al-4V*, IOP Conf. Series: Materials Science Engineering 48 (**2013**) 012002.

[72] D. Poquillon, C. Armand, J. Huez, *Oxidation and oxygen diffusion in Ti-6al-4V alloy: Improving measurements during SIMS analysis by rotating the sample*, Oxidation of Metals 79 (**2013**) 249-259.

[73] S. Zeng, A. Zhao, H. Jiang, X. Fan, X. Duan, X. Yan, *Cyclic oxidation behavior of the Ti-6Al-4V alloy*, Oxidation of Metals 81 (**2014**) 467-476.

[74] P.W.M. Peters, J. Hemptenmacher, C. Todd, O*xidation and stress enhanced oxidation of Ti-6-2-4-2*, in: G. Lütjering, J. Albrech (Eds.), Titan-2003, Science and Technology IV, Wiley-VCH, Weinheim, (**2003**), pp. 2067-2074.

[75] K.S. McReynolds, S. Tamirisakandala, *A study on alpha-case depth in Ti-6Al-2Sn-4Zr-2Mo*, Metallurgical Materials Transaction A 42 (**2011**) 1732-1736.

[76] J. Tiley, J. Shaffer, A. Shiveley, A. Pilchak, A. Salem, *The effect of lath orientations on oxygen ingress in titanium alloys*, Metallurgical Materials Transaction A 45 (**2014**) 1041-1048.

[77] R. Gaddam, B. Sefer, R. Pederson, M.-L. Antti, *Oxidation and alpha-case formation in Ti-6Al-2Sn-4Zr-2Mo alloy*, Materials Characterization 99 (**2015**) 166-174.

[78] I. Gurrappa, *On the mechanism of degradation of titanium alloy IMI 834 in an oxidizing atmosphere at elevated temperatures*, Corrosion Prevention and Control 49 (**2002**) 79-84.

[79] I. Gurappa, *Prediction of titanium alloy component life by developing an oxidation model*, Journal of Materials Science Letters 22 (**2003**) 771-774.

[80] K.S. Srinadh, V. Singh, *Oxidation behaviour of the near α-titanium alloy IMI 834*, Bulletin of Materials Science 27 (**2004**) 347-354.

[81] I. Gurrappa, *An oxidation model for predicting the life of titanium alloy components in gas turbine engines*, Journal of Alloys and Compounds 389 (**2005**) 190-197.

[82] W. Jia, W. Zeng, X. Zhang, Y. Zhou, J. Liu, Q. Wang, *Oxidation behavior and effect of oxidation on tensile properties of Ti60 alloy*, Journal of Materials Science 46 (**2011**) 1351-1358.

[83] M. Evans, A. Ward, *Corrosion resistance of Ti-6246 for high power aeroengine compressor discs and blades*, Materials Science and Technology 17 (**2001**) 945-953.

[84] R.W. Evans, R.J. Hull, B. Wilshire, *The effects of alpha-case formation on the creep fracture properties of the high-temperature titanium alloy IMI834*, Journal of Materials Processing Technolgy 56 (**1996**) 492-501.

[85] A.M. Chaze, C. Coddet, *Influence of aluminium on the oxidation of titanium between 550 and 750 ºC*, Journal of Less Common Metals 157 (**1990**) 55-70.

[86] S. Becker, A. Rahmel, M. Schorr, M. Schütze, *Mechanism of isothermal oxidation of the intermetallic TiAl and of TiAl alloys*, Oxidation of Metals 38 (**1992**) 425-464.

[87] R.A. Perkins, K.T. Chiang, G.H. Meier, *Formation of alumina on Ti-Al alloys*, Scripta Metallurgica 21 (**1987**) 1505-1510.

[88] Y. Shida, H. Anada, *The influence of ternary element addition on the oxidation behaviour of TiAl intermetallic compound in high temperature air*, Corrosion Science 35 (**1993**) 945-953.

[89] Y. Shida, H. Anada, *The effect of various ternary additives on the oxidation behavior of TiAl in high-temperature air*, Oxidation of Metals 45 (**1996**) 197-219.

[90] J. Lausmaa, *Surface spectroscopic characterization of titanium implant materials*, Journal of Electron Spectroscopy and Related Phenomena 81 (**1996**) 343-361.

[91] J.A. Van Orman, K.L. Crispin, *Diffusion in oxides*, Reviews in Mineralogy and Geochemistry 72 (**2010**) 757-825.

[92] J. Marucco, J. Gautron, P. Lemasson, *Thermogravimetric and electrical study of non-stoichiometric titanium dioxide $TiO_{2-x}$, between 800 and 1100 ºC*, Journal of Physics and Chemistry of Solids 42 (**1981**) 363-367.

[93] W.L. Finlay, J.A. Snyder, *Effects of three interstitial solutes (nitrogen, oxygen, and carbon) on the mechanical properties of high-purity, alpha titanium*, The American Institute of Mining, Metallurgical, and Petroleum Engineers 188 (**1950**) 1-10.

[94] H.R. Ogden, R.I. Jaffee, *The effects of carbon, oxygen and nitrogen on the mechanical properties of titanium and titanium alloys*, TML Report No. 20 (**1955**).

[95] A. Kahveci, G. Welsch, *Effect of oxygen on the hardness and alpha/beta phase ratio of Ti-6A1-4V alloy*, Scripta Metallurgica 20 (**1986**) 1287-1290.

[96] A. Kahveci, G. Welsch, *Hardness versus strength correlation for oxygen-strengthened Ti-6Al-4V alloy*, Scripta Metallurgica et Materialia 25 (**1991**) 1957-1962.

[97] J. Ruppen, P. Bhowal, D. Eylon, A.J. McEvily, *On the process of subsurface fatigue crack initiation in Ti-6Al-4V*, ASTM International Spec. Tech. Publ. (**1979**) 47-68.

[98] Z. Liu, G. Welsch, *Effects of oxygen and heat treatment on the mechanical properties of alpha and beta titanium alloys*, Metallurgical Transactions A 19 (**1988**) 527-542.

[99] A. Majorell, S. Srivatsa, R. Picu, *Mechanical behavior of Ti-6Al-4V at high and moderate temperatures-Part I: Experimental results*, Materials Science and Engineering A 326 (**2002**) 297-305.

[100] H. Fukai, H. Iizumi, K. Minakawa, C. Ouchi, *The effects of the oxygen-enriched surface layer on mechanical properties of α+β type titanium alloys*, ISIJ International 45 (**2005**) 133-141.

[101] A. Ebrahimi, F. Zarei, R. Khosroshahi, *Effect of thermal oxidation process on fatigue behavior of Ti-4Al-2V alloy*, Surface and Coatings Technology 203 (**2008**) 199-203.

[102] R. Dobeson, N. Petrazoller, M. Dargusch, S. McDonald, *Effect of thermal exposure on the room temperature tensile properties of Grade 2 titanium*, Materials Science and Engineering A 528 (**2011**) 3925-3929.

[103] W. Jia, W. Zeng, X. Zhang, Y. Zhou, J. Liu, Q. Wang, *Oxidation behavior and effect of oxidation on tensile properties of Ti60 alloy*, Journal of Materials Science 46 (**2011**) 1351-1358.

[104] D.P. Satko, J.B. Shaffer, J.S. Tiley, S.L. Semiatin, A.L. Pilchak, S.R. Kalidindi, Y. Kosaka, M.G. Glavicic, A.A. Salem, *Effect of microstructure on oxygen rich layer evolution and its impact on fatigue life during high-temperature application of α/β titanium*, Acta Materialia 107 (**2016**) 377-389.

[105] T. Horiya, T. Kishi, *Fracture Toughness of Titanium Alloys*, Nippon Steel Technical Reports 62, (**1994**) 85-91.

[106] J.R. Davis, *Corrosion: Understanding the Basics*, ASM International, **2000**.

[107] E. McCafferty, *Introduction to Corrosion Science*, Springer Science & Business Media, **2010**.

[108] M.G. Fontana, *Corrosion Engineering*, Tata McGraw-Hill Education, **2005**.

[109] J. Myers, H. Bomberger, F. Froes, *Corrosion behavior and use of titanium and its alloys*, Journal of Minerals Metals and Materials Society 36 (**1984**) 50-60.

[110] D. Shoesmith, J. Noël, *Corrosion of Titanium and its alloys*, in: T.J.A. Richardson (Eds.), Shreir's corrosion, Elsevier, (**2010**) pp. 2042-2052.

[111] G. Wranglén, *An introduction to corrosion and protection of metals*, Springer Netherlands, **1985**.

[112] M. Pourbaix, *Atlas of electrochemical equilibria in aqueous solutions*, second ed., National Association of Corrosion Engineers, **1974**.

[113] R. Schutz, 2003 FN Speller Award Lecture: *Platinum Group Metal Additions to Titanium: A Highly Effective Strategy for Enhancing Corrosion Resistance*, Corrosion 59 (**2003**) 1043-1057.

[114] T. Beck, R. Staehle, B. Brown, J. Kruger, A. Agrawal, *Localized corrosion*, NACE-3, TX: NACE, Houston. (**1974**) 644-672.

[115] J. Kelly, *The influence of fluoride ions on the passive dissolution of titanium*, Electrochimica Acta 24 (**1979**) 1273-1282.

[116] V. Raja, R. Angal, M. Suresh, *Effect of widmanstatten structure on protection potential of Ti-6Al-2Sn-4Zr-2Mo (0.1 Si) alloy in 1 M NaBr solution*, Corrosion 49 (**1993**) 2-7.

[117] I. Gurrappa, *Characterization of titanium alloy Ti-6Al-4V for chemical, marine and industrial applications*, Materials Characterization 51 (**2003**) 131-139.

[118] M. Atapour, A. Pilchak, G. Frankel, J. Williams, M. Fathi, M. Shamanian, *Corrosion behavior of Ti-6Al-4V with different thermomechanical treatments and microstructures*, Corrosion 66 (**2010**) 0650041-0650049.

[119] J. Chen, W. Tsai, I*n situ corrosion monitoring of Ti-6Al-4V alloy in $H_2SO_4$/HCl mixed solution using electrochemical AFM*, Electrochimica Acta 56 (**2011**) 1746-1751.

[120] A. Rodrigues, N. Oliveira, M. Dos Santos, A. Guastaldi, *Electrochemical behavior and corrosion resistance of Ti–15Mo alloy in naturally-aerated solutions, containing chloride and fluoride ions*, Journal of Materials Science, Materials in Medicine 26 (**2015**) 1-9.

[121] J.C. Souza, S.L. Barbosa, E.A. Ariza, M. Henriques, W. Teughels, P. Ponthiaux, J. Celis, L.A. Rocha, *How do titanium and Ti6Al4V corrode in fluoridated medium as found in the oral cavity? An in vitro study*, Materials Science and Engineering C 47 (**2015**) 384-393.

[122] D. Nakhaie, A. Davoodi, G.R. Ebrahimi, *The influence of cold plastic deformation on passivity of Ti-6Al-4V alloy studied by electrochemical and local probing techniques*, Corrosion 72 (**2015**) 110-118.

[123] P. Bijlmer, *Pickling titanium in hydrofluoric-nitric acid*, Metal Finish 68 (**1970**) 64-67.

[124] C. Lin, X. Hong, *Investigation of corrosion processing for Ti-6Al-4V in hydrofluoric-nitric acid system*, (**2011**) 349-355.

[125] W.C. Say, Y.Y. Tsai, *Surface characterization of cast Ti-6Al-4V in hydrofluoric-nitric pickling solutions*, Surface and Coatings Technology 176 (**2004**) 337-343.

[126] T. Schneiker, K. Forsberg, *Process chemistry and acid management for titanium pickling processes*, Titanium Europe (**2014**).

[127] E. Sutter, A. Cornet, G. Goetz, *Activity of the surface of titanium during pickling in nitric-hydrofluoric acid*, Corrosion (**1988**) 1923-1928.

[128] E. Sutter, G. Goetz-Grandmont, *The behaviour of titanium in nitric-hydrofluoric acid solutions*, Corrosion Science 30 (**1990**) 461-476.

[129] E. Sutter, F. Hlawka, A. Cornet, *Comparative behavior of titanium and zirconium in hydrofluoric-nitric acid pickling solutions*, Corrosion 46 (**1990**) 537-544.

[130] C.T. Blsen, NASA-TM-X53446, ORAD 634075, **1966**.

[131] C.N. Panagopoulos, *A surface study of chemically etched titanium*, Journal of Less Common Metals 134 (**1987**) 237-243.

[132] R. Matsuhashi, K. Takahashi, *The integral rate equation of pure titanium in nitric-hydrofluoric acid solutions*, Nippon Steel Technical Reports (**2002**) 59-63.

[133] K. Takahashi, R. Matsuhashi, I. Takayama, *Change of morphology of titanium surface by pickling in nitric-hydrofluoric acid solutions*, Nippon Steel Technical Reports (**2002**) 64-70.

[134] K. Takahashi, T. Yamazaki, T. Nishijima, H. Shimizu, *Effect of grain size and initial surface condition on glossiness and whiteness of the pickled titanium surface*, Nippon Steel Technical Reports (**2002**) 71-76.

[135] K. Mutombo, P. Russouw, G. Govender, *Chemically milled alpha-case layer from Ti-6Al-4V alloy investment cast*, Materials Science Forum 690 (**2011**) 477-480.

[136] S. Gaiani, E. Colombini, P. Veronesi, U. Rosa, *Optimization of the chemical milling of investment cast titanium alloys*, Titanium 2012 Conference, Atlanta USA, (**2012**).

[137] C. Sittig, M. Textor, N. Spencer, M. Wieland, P. Vallotton, *Surface characterization of implant materials c.p. Ti, Ti-6Al-7Nb and Ti-6Al-4V with different pretreatments*, Journal of Materials Science, Materials in Medicine 10 (**1999**) 35-46.

[138] AMS 4911 L, *Titanium alloy, sheet, strip, and plate 6Al-4V annealed* (SAE-AMS/MAM), (**2008**).

[139] AMS 4976 G, *Titanium alloy, forgings 6.0Al-2.0Sn-4.0Zr-2.0Mo solution and precipitation heat treated* (SAE-AMS/MAM), (**2008**).

[140] J. Goldstain, D. Newbury, D. Joy, C. Lyman, P. Echlin, E. Lifshin, I. Sawer, J. Michel, *Scanning electron microscopy and X-ray analysis*, Springer USA, **2003**.

[141] C.A. Volkert, A.M. Minor, *Focused ion beam microscopy and micromachining*, MRS Bulletin 32 (**2007**) 389-399.

[142] T. Maitland, S. Sitzman, *Electron backscatter diffraction (EBSD) technique and materials characterization examples*, Springer Berlin, **2007**.

[143] N. Fairley, *CasaXPS: Spectrum Processing Software for XPS, AES and SIMS*, Version 2.3.17, Casa Software Ltd., Cheshire, UK, 2016, <http://www.casaxps.com/>, (**2005**).

[144] W.C. Oliver, G.M. Pharr, *An improved technique for determining hardness and elastic modulus using load and displacement sensing indentation experiments*, Journal of Materials Research 7 (**1992**) 1564-1583.

[145] W.C. Oliver, G.M. Pharr, *Measurement of hardness and elastic modulus by instrumented indentation: Advances in understanding and refinements to methodology*, Journal of Materials Research 19 (**2004**) 3-20.

[146] ASTM Standards, ASTM E606, *Standard practice for strain-controlled fatigue testing*, The American Society for Testing and Materials, vol. 03.01 (**1998**).

# Part II

# *PAPER I*

*Study of alpha-case depth in Ti-6Al-2Sn-4Zr-2Mo and Ti-6Al-4V*

**Authors:**

Raghuveer Gaddam, **Birhan Sefer**, Robert Pederson, Marta-Lena Antti

**Published in:**

IOP Conf. Series: Materials Science and Engineering 48 (2013) 012002.

IOP Conf. Series: Materials Science and Engineering **48** (2013) 012002 doi:10.1088/1757-899X/48/1/012002

# Study of alpha-case depth in Ti-6Al-2Sn-4Zr-2Mo and Ti-6Al-4V

**R Gaddam[1], B Sefer[1], R Pederson[1,2] and M-L Antti[1]**
[1]Division of Materials Science, Luleå University of Technology, S-97187 Luleå, Sweden
[2]Research Centre, GKN Aerospace Engine Systems, S-46181 Trollhättan, Sweden

E-mail: raghuveer.gaddam@ltu.se

**Abstract.** At temperatures exceeding 480°C titanium alloys generally oxidises and forms a hard and brittle layer enriched with oxygen, which is called alpha case. This layer has negative effects on several mechanical properties and lowers the tensile ductility and the fatigue resistance. Therefore any alpha-case formed on titanium alloys during various manufacturing processes, such as heat treatment procedures, must be removed before the final part is mounted in an engine. In addition, long time exposure at elevated temperatures during operation of an engine could possibly also lead to formation of alpha-case on actual parts, therefore knowledge and understanding of the alpha-case formation and its effect on mechanical properties is important. Factors that contribute for growth of alpha-case are: presence of oxygen, exposure time, temperature and pressure. In the present study, isothermal oxidation experiments in air were performed on forged Ti-6Al-2Sn-4Zr-2Mo at 500°C and 593°C up to 500 hours. Similar studies were also performed on Ti-6Al-4V plate at 593°C and 700°C. Alpha-case depth for both alloys was quantified using metallography techniques and compared.

## 1. Introduction

The titanium alloys, Ti–6Al–2Sn–4Zr–2Mo (Ti-6242) and Ti-6Al-4V (Ti-64) are widely used for components in aeroengines because of their excellent combination of weight and strength [1-3]. The maximum service temperature for these alloys is limited to 450°C for Ti-6242 and 350°C for Ti-64 [2,3]. It is partly because of degradation of mechanical properties above these respective temperatures as at elevated temperatures (above 480°C), titanium alloys oxidises in oxygen containing environments; this results in simultaneous formation of an oxide ($TiO_2$) scale on the surface and an oxygen-rich layer beneath the scale, commonly referred to as alpha-case (α-case). Alpha-case is a continuous, hard, and brittle layer with higher oxygen content [1,2]. It forms because of higher solid solubility of oxygen in α-titanium (i.e.14.5 wt.% [4]) and higher affinity of titanium to absorb oxygen, which instantaneously reacts and stabilise the α phase. This brittle alpha-case degrades the mechanical properties such as tensile ductility and fatigue strength [5-10]. Therefore it is necessary to remove any alpha-case formed on parts manufactured from titanium alloys if they are subjected to high loads and/or dynamic loading conditions.

Environmental and economical requirements on future aero engines set higher demands on the efficiency and thereby pressure ratio. The increased pressure leads to higher temperatures, which could make it necessary to replace titanium alloys with nickel based super alloys in the front end of the engine. Unfortunately this increases the weight of the engine and leads to an increase of fuel consumption and is therefore undesirable. However, there is a possibility to increase the maximum working temperature of the currently used Ti-6242 alloy in compressor parts by developing a better understanding on how different mechanical properties and physical phenomena such as oxidation mechanisms are affected in the high temperature regimes. And since some aeroengine parts consists of a combination of both Ti-64 and Ti-6242. Hence both of these alloys are investigated in the current study. The objective of present study was to investigate the effect of heat treatment conditions on the

depth of alpha-case in two common aerospace grade titanium alloys; Ti-6242 and Ti-64. The heat treatment conditions investigated include the temperatures and times in ambient air that are of interest for heat treatment during manufacturing and for application in an aeroengine for both of these alloys.

## 2. Materials and Methods

The materials investigated are Ti-6242 and Ti-64 with the chemical compositions shown in table 1. Ti-6242 is a near- α alloy that has been solution and precipitation heat treated; and was obtained in forged condition according to AMS 4976G [11]. It consists of a bi-modal microstructure with primary α and transformed β (see figure 1(a)). Ti-64 is a α+β titanium alloy that has been obtained in plate form according to AMS 4911L [12], which consists of a microstructure with equiaxed primary α and elongated α in transformed β (see figure 1(b)).

**Table 1.** Chemical composition (wt.%) of the materials investigated.

| Material | Al | Sn | Zr | Mo | N | O | C | H | Fe | Si | V | Ti |
|---|---|---|---|---|---|---|---|---|---|---|---|---|
| Ti-6242 | 6.5 | 2.2 | 4.4 | 2.2 | 0.05 | 0.15 | 0.05 | 0.05 | 0.1 | 0.1 | - | Bal. |
| Ti-64 | 6.75 | - | - | - | 0.05 | 0.20 | 0.08 | 0.015 | 0.3 | - | 4.5 | Bal. |

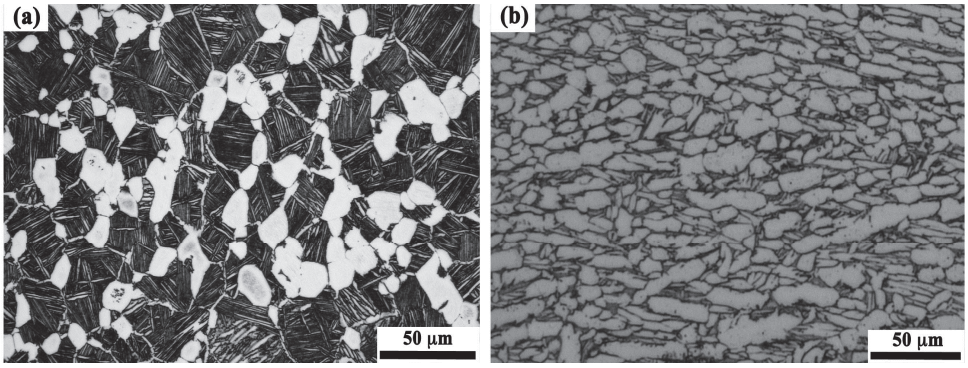


**Figure 1.** Optical micrographs showing the microstructure of as received materials, (a) forged Ti-6242 and (b) Ti-64 plate. In micrographs light or grey areas is α phase and dark areas is β.

### *2.1. Heat treatment*

The samples for heat treatments were cut using electric discharged machining (EDM) from the as received material in dimensions of 10 x 5 x 10 mm. Totally 64 samples were cut out, where two samples were used for each exposure time and temperature. All the sample surfaces were metallographically polished to remove the recast layer. Thereafter, the polished samples were ultrasonically cleaned in technical acetone for approximately 15 min and rinsed with ethanol. The cleaned samples were heat treated in ambient air using a Nabertherm box furnace (N11/R) and a Nabertherm tube furnace (RHTC 80-450/15) at atmospheric pressure. The temperature inside the furnace is calibrated using a reference sample with a thermocouple welded to it and positioned at the locations inside the furnace where the samples are placed. The temperature inside the furnace was about ± 5ºC of the desired temperature**.** The samples were placed onto an $Al_2O_3$ plate or crucible and then introduced into the furnaces at the desired temperature and isothermally held for selected exposure times as shown in table 2. All samples were weighed using a microbalance with an accuracy of ± 0.0001 g before and after each heat treatment. In addition, heat treatments were also performed on Ti-6242 and Ti-64 samples, with a cross section of 17 x 2.5 x 10 mm, in dry air (i.e. technical air)

using a simultaneous thermal analysis instrument (STA 449C from Netschz Gmbh). The samples were isothermally held at 593°C for 200 hours.

**Table 2.** Heat treatment conditions.

| Material | Temperature (ºC) | Exposure times (hour) |
|---|---|---|
| Ti-6242 forged | 500 | |
| | 593 | 5, 10, 50, |
| | | 100, 200, 300, |
| Ti-64 plate | 593 | 400 and 500 |
| | 700 | |

*2.2. Alpha-case evaluation*

Heat treated samples were cut into half, parallel to the face that is placed on the crucible (10 x 5 $mm^2$), thereafter ultrasonically cleaned in technical acetone for 15 min and rinsed with ethanol. Cleaned samples were mounted in bakelite using BUEHLER Simplimet model 1000 mounting machine and then metallographically prepared, which involves grinding and polishing the surface up to 0.05 μm with colloidal silica using a semiautomatic BUEHLER Phoenix 4000 polishing machine. The polished samples were etched in two steps to observe the alpha-case: first, swabbing the sample surface with Kroll's reagent (a mixture of 1-3 ml HF, 2-3 ml $HNO_3$ and distilled water) and second, immersing in Weck's reagent (1-3 g $NH_4HF_2$ and distilled water) for approximately 10 sec. Alpha-case layer was observed using a Nikon Eclipse optical microscope (model MA200) and the depth of alpha-case layer was quantitatively measured using NIS elements software. Totally 60 individual measurements of alpha-case depth on each sample were made along the entire perimeter at approximately 500 μm spacing on two samples of Ti-6242 and Ti-64 at each temperature and time combination, and the average values of alpha-case depth is then reported. The hardness measurements related to the alpha-case at the surface was obtained by applying a load of 100 g using MXT- α microhardness tester from Matsuzawa with a Vickers indenter (indent size is approximately 20 – 25 μm).

## 3. Results and Discussion

*3.1. Weight gain*

Figure 2(a) presents the amount of weight gain ($\Delta W$) per surface area ($A$) for Ti-6242 and Ti-64 when isothermally held at 593°C for 200 hours in dry air. It is calculated by dividing the weight gain values of the samples, measured using STA 449C, with their total surface areas. The unit is ($mg/cm^2$). From figure 2(a) it can be seen that the ($\Delta W/A$) increased with time and approximately followed a parabolic relationship for both the alloys. Similar behaviour for both the alloys was observed on samples that were isothermally held in a laboratory furnace at 593°C for up to 500 hours in ambient air, where the weight gain is calculated by weighing before and after the heat treatment. It was noted that in Ti-6242 samples held at 500°C for up to 500 hours the weight gain followed approximately a parabolic relationship, while deviating from parabolic below 100 hours. In contrast, Ti-64 samples held at 700°C showed deviation from parabolic relationship beyond 200 hours. The observation of weight gain in both the alloys is obtained by fitting and performing regression analysis of the weight gain data using the following equation [13]:

$$(\Delta W/A) = Kt^{1/n} \quad (1)$$

where $K$ is the rate constant and $n$ is the reaction index. At a constant temperature, the weight gain is assumed to be linear if $n$=1, parabolic if $n$=2. The weight gain in the Ti-6242 alloy at the tested temperatures is consistent with other investigators [8, 14]. On the other hand, the Ti-64 alloy that was

held at 700°C for up to 500 hours, indicated a transition from parabolic to linear weight gain at about 200 hours. This confirms with the results found by others [15-17]. In figure 2(a) it can be seen that weight gain is much higher in Ti-64 compared to Ti-6242 at the constant temperature and time. This could be due to the thicker oxide layer (≈ 5 μm) in Ti-64 than in Ti-6242 (< 1 μm), see figure 2(b) and figure 2(c).

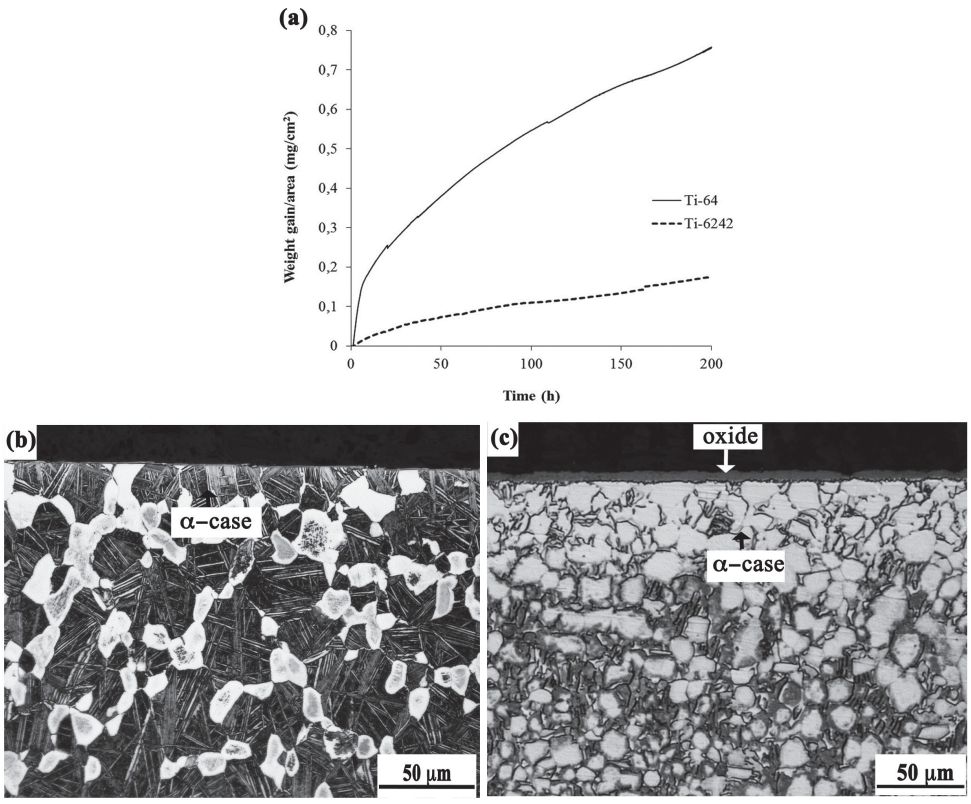


**Figure. 2** (a) Plot showing the weight gain per unit area (mg/cm$^2$) in Ti-6242 and Ti-64 held at 593°C for 200 hours in dry air, (b,c) optical micrographs of Ti-6242 and Ti-64, showing the oxide layer and alpha case.

*3.2. Alpha-case evaluation*

Figure 3 shows the representative optical micrographs of alpha-case (white layer) in Ti-6242 and Ti-64 after long exposure time (500 hours) at 593°C. It can be seen that alpha-case is formed beneath the surface simultaneously with the oxide (see Figure 3(b)). Figure 4 shows the plot of alpha-case depth versus exposure time for Ti-6242 and Ti-64 at the tested temperatures. Here, alpha-case is measured quantitatively using the optical micrographs. From figure 4, it can be seen that depth of alpha-case is increased with temperature and time in both the alloys and mainly follows a parabolic relationship at the selected heat treatment conditions. The maximum depth of alpha-case formed in Ti-6242 is approximately 30 μm when exposed at 593°C for 500 hours, and 10 μm at 500°C after 500 hours (see figure 4). The depth of alpha-case in Ti-64 when exposed to 593°C for 500 hours was about 30 μm. In addition, it is observed that a thick alpha-case layer of approximately 200 μm is formed in Ti-64 when exposed at 700°C for 500 hours.

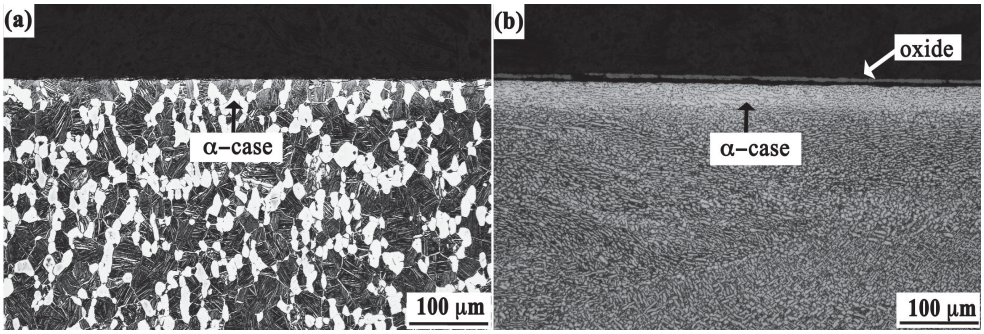


**Figure 3.** Optical micrographs showing alpha-case (white layer) in (a) Ti-6242 and (b) Ti-64 heated at 593°C up to 500 hours.

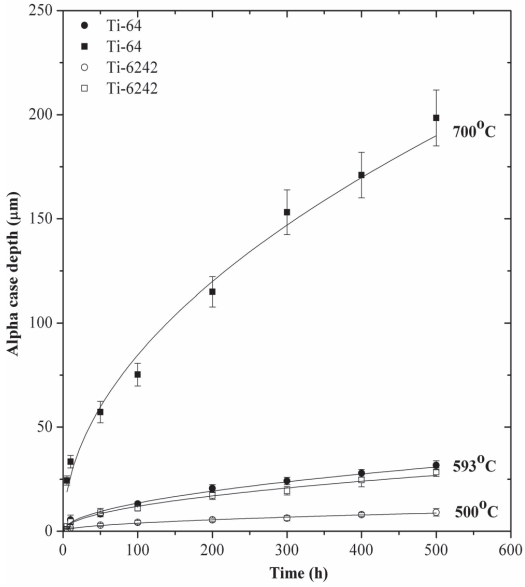


**Figure 4.** Variation of alpha-case depth in Ti-6242 and Ti-64 as a function of time at different temperatures. Empty data points correspond to Ti-6242 and filled data points are for Ti-64.

From figure 4, it can be seen that the growth of alpha-case in both Ti-6242 and Ti-64 alloys exposed at 593°C for 500 hours follows a parabolic relationship, which can be related to the bulk diffusion. The approximate solution that describe Fick's second law of diffusion is given by $x=\sqrt{(Dt)}$, where $x$ is alpha-case depth, $D$ is the diffusion coefficient ($m^2/s$), and $t$ is exposure time. Figure 5 shows a log-log plot of alpha-case depth versus exposure time. It shows a linear relationship with R-values 0.995. The exponents from the linear fits are nearly equal to 0.5. Hence, the values for $D$ are calculated from the slope obtained from the best-fit lines. The $D$ calculated here is found to be in the order of $10^{-16}$ $m^2/s$ for Ti-6242 and Ti-64. From the present study, it can be seen that there is no significant change in the depth of alpha-case and the diffusion of oxygen in Ti-6242 and Ti-64 when

exposed at 593°C up to 500 hours. This shows that there might be no substantial influence of the difference in chemical composition and the microstructure between the two alloys on alpha-case depth. Similar observations were also noted for both the alloys when exposed at 704°C for 24 hours in air [18].

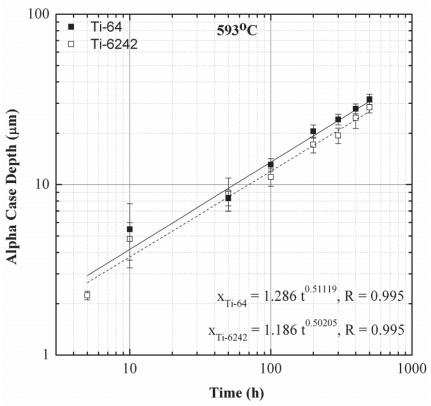


**Figure 5.** Plot showing the alpha-case depth vs exposure time for Ti-6242 (empty boxes) and Ti-64 (filled boxes) at 593°C up to 500 hours (log- log scale).

Alpha-case is commonly referred to a region enriched with oxygen. It is known that oxygen stabilizes the α phase and increases the strength of titanium by solid solution strengthening [2-3]. Therefore the alpha-case layer is harder than the bulk. Table 3 shows the results obtained from the microhardness measurements on Ti-6242 that are isothermally treated at 593°C; Ti-64 at 593 and 700°C for up to 500 hours. It was found that the hardness values in the alpha-case are higher in magnitude than in the bulk. Figure 6 shows the variation of hardness on the sample held at 700°C for 500 hours from the surface to the bulk. It can be seen that hardness values are gradually decreasing from the surface into the material to approximately 250 µm. From optical measurements on the samples held at 700°C for 500 hours, the depth of alpha-case is approximately measured to be 200 µm (see figure 4 and figure 6). The hardness values decrease with decreasing oxygen content. The difference in depth of alpha-case measured in optical microscope (OM) and indicated by the plateau in the hardness measurements suggests that there are uncertainties in identifying the border between the alpha-case layer and the bulk material in optical microscope after etching.

**Table 3.** Average hardness values (HV) for Ti-6242 and Ti-64 exposed at different temperatures.

| | Ti-6242 | Ti-64 | |
|---|---|---|---|
| | 593°C | 593°C | 700°C |
| Alpha case | 511 ± 40 | 412 ± 37 | 630 ± 34 |
| Bulk | 362 ± 23 | 332 ± 10 | 300 ± 2.88 |

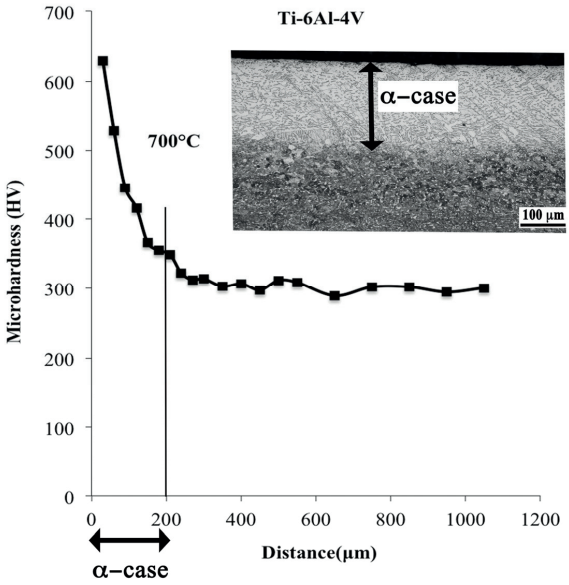


**Figure 6.** Variation of hardness from the surface to the bulk of the Ti-64 sample exposed to 700°C for 500 hours. An optical micrograph of the corresponding sample showing the alpha-case is also included (the white layer in the micrograph).

## 4. Conclusions

In the present work, isothermal heat treatments were performed on the Ti-6242 and Ti-64 titanium alloys in ambient air and at atmospheric pressure in order to study the depth of alpha-case. The conclusions are as follows:

1. Alpha-case depth in both alloys increases with temperature and time. Alpha-case growth mainly follows a parabolic relationship at 500 and 593°C in Ti-6242, and at 593°C and 700°C in Ti-64.

2. At 593°C after 500 hours Ti-6242 and Ti-64 have similar values of alpha-case depth (≈ 30 μm).

3. The alpha-case depth in Ti-6242 is 10 μm after 500 hours at 500°C.

4. The alpha-case depth in Ti-64 is 200 μm after 500 hours at 700°C.

5. The microhardness is higher in the alpha-case and decreases into the bulk.

6. A thicker oxide layer forms on Ti-64 then on Ti-6242 when isothermally held at 593$^{o}$C for 200 hours. This results in a higher weight gain/area for the Ti-64 alloy. The weight gain followed a parabolic relationship.

## 5. References

[1] Lutjering G and Williams J C 2007 *Titanium* 2nd ed (Berlin, Springer-Verlag)
[2] Leyens C and Peters M 2003 *Titanium and titanium alloys* (Wiley VCH Verlag GmbH, Weinheim) 187
[3] Boyer R R 1996 *Mater. Sci. Eng.* A **213(1-2)** 103
[4] Murray J L and Wriedt H A 1990 Binary alloy phase diagrams Massalski T B ed. (ASM International, Materials Park, Ohio) 2924
[5] Shamblen C E and Redden T K 1968 *Proc. of The Science, Technology, and Application of Titanium*, Jaffee R I and Promisel N E eds, (Pergamon Press, Oxford, United Kingdom) 199
[6] Ruppen J A and McEvily A J 1979 *Fatigue Engg. Mater. Struct.* **2** 63
[7] Bendersky L and Rosen A 1980 *Engg. Fract. Mech.* **13** 111
[8] Shenoy R N, Unnam J and Clark R K 1986 *Oxid. Met.* **26** 105
[9] Fukai H, Iizumi H, Minakawa K-N and Ouchi C 2005 *ISIJ Inter.* **45(1)** 133
[10] Chan K S, Koike M, Johnson B W and Okabe T 2008 *Metall. Mater. Trans.* **39A** 171
[11] AMS 4976 G 2008 Titanium alloy, forgings 6.0Al-2.0Sn-4.0Zr-2.0Mo solution and precipitation heat treated (SAE-AMS/MAM)
[12] AMS 4911 L 2008 Titanium alloy, sheet, strip, and plate 6Al-4V annealed (SAE-AMS/MAM)
[13] Kofstad P 1988 *High temperature corrosion* (Elseiver Applied Science, Essex)
[14] McReynolds K S and Tamirisakandala S 2011 *Metall. Mater. Trans.* A **42A** 1732
[15] Guleryuz H and Cimenoglu H 2009 *J. Alloys Compd.* **472** 241
[16] Frangini S, Mignone A and De Riccardis F 1994 *J. Mater. Sci.* **29** 714
[17] Du H L, Datta P K, Lewis D B and Burnell Gray J S 1994 *Corros. Sci.* **36(4)** 631
[18] Unnam J, Shenoy R N and Clark R K 1984 Effect of alloy chemistry and exposure conditions on the oxidation of titanium Report No. NASA TM-86295 (NASA Technical Memorandum)

**Acknowledgments**
The authors kindly acknowledge Graduate School of Space Technology and National Aviation Engineering Research Programme (NFFP) for funding the present work through research collaboration with GKN Aerospace Engine Systems, Sweden. We would also like to acknowledge Francois Mattera for assisting in the experiments.

## *PAPER II*

*Oxidation and alpha-case formation in Ti-6Al-2Sn-4Zr-2Mo alloy*

**Authors:**

Raghuveer Gaddam, **Birhan Sefer**, Robert Pederson, Marta-Lena Antti

**Published in:**

Materials Characterisation 99 (2015) 166-174.

Materials Characterization 99 (2015) 166-174

Contents lists available at ScienceDirect

Materials Characterization

journal homepage: www.elsevier.com/locate/matchar

# Oxidation and alpha-case formation in Ti–6Al–2Sn–4Zr–2Mo alloy

Raghuveer Gaddam [a,*], Birhan Sefer [a], Robert Pederson [a,b], Marta-Lena Antti [a]

[a] Division of Materials Science, Luleå University of Technology, S-97187 Luleå, Sweden
[b] Research and Technology Centre, GKN Aerospace Engine Systems, S-46181 Trollhättan, Sweden

article info

*Article history:*
Received 12 June 2014
Received in revised form 27 October 2014
Accepted 18 November 2014
Available online 18 November 2014

*Keywords:*
Titanium alloy
Oxidation
Oxygen diffusion
Optical metallography
SEM
EPMA

abstract

Isothermal heat treatments in ambient air were performed on wrought Ti–6Al–2Sn–4Zr–2Mo (Ti-6242) material at 500, 593 and 700°C for times up to 500 h. In the presence of oxygen at elevated temperatures simultaneous reactions occurred in Ti-6242 alloy, which resulted in the formation of an oxide scale and a layer with higher oxygen concentration (termed as alpha-case). Total weight gain analysis showed that there was a transition in the oxidation kinetics. At 500°C, the oxidation kinetics obeyed a cubic relationship up to 200 h and thereafter changed to parabolic at prolonged exposure times. At 593°C, it followed a parabolic relationship. After heat treatment at 700°C, the oxidation obeyed a parabolic relationship up to 200 h and thereafter changed to linear at prolonged exposure times. The observed transition is believed to be due to the differences observed in the oxide scale. The activation energy for parabolic oxidation was estimated to be 157 kJ/mol. In addition, alpha-case layer was evaluated using optical microscope, electron probe micro-analyser and microhardness tester. The thickness of the alpha-case layer was found to be a function of temperature and time, increasing proportionally, and following a parabolic relationship. The activation energy for the formation of alpha-case layer was estimated to be 153 kJ/mol.





* Corresponding author at: AB Sandvik Materials Technology, S-81181 Sandviken, Sweden.
*E-mail addresses:* raghuveer.gaddam@ltu.se, raghuveergaddam@gmail.com (R. Gaddam).

http://dx.doi.org/10.1016/j.matchar.2014.11.023 1044-5803/

## *PAPER III*

*Oxidation behaviour of Ti-6Al-4V and Ti-6Al-2Sn-4Zr-2Mo alloys exposed to air at elevated temperatures*

**Authors:**

**Birhan Sefer**, Raghuveer Gaddam, Robert Pederson, Antonio Mateo, Ragnar Tegman, Marta-Lena Antti

**Submitted to:**

Journal of Corrosion Science.

# Oxidation behaviour of Ti-6Al-4V and Ti-6Al-2Sn-4Zr-2Mo alloys exposed to air at elevated temperatures

Birhan Sefer[a,b*], Raghuveer Gaddam[a,c], Robert Pederson[a,d], Antonio Mateo[b], Ragnar Tegman[a], Marta-Lena Antti[a]

[a]Division of Materials Science, Luleå University of Technology, S-97187 Luleå, Sweden
[b]Department of Materials Science, Universitat Politècnica de Catalunya, Avda. Diagonal 647, 08028, Barcelona, Spain
[c]Sandvik Materials Technology, Sandviken, S-81181, Sweden
[d]Research and Technology Centre, GKN Aerospace Engine Systems, S-46181 Trollhättan, Sweden
*Corresponding author, e-mail: birhan.sefer@ltu.se ; Phone: +46(0)920492358, +46(0)735630494

**Abstract**

The isothermal oxidation of Ti-6Al-4V and Ti-6Al-2Sn-4Zr-2Mo alloys in air at 500, 593 and 700 ºC for up to 500 hours investigated. At 500 ºC for up to 500 hours the oxidation was slow for both alloys. At 593 ºC and 700 ºC Ti-6Al-2Sn-4Zr-2Mo exhibited better oxidation resistance than Ti-6Al-4V. The oxidation mainly followed parabolic rate at all temperatures for both alloys, except at 700 ºC for ≥ 200 hours where a transition to linear rate was noted. The activation energy values for oxidation, α-case formation and oxygen diffusion were estimated for both alloys. Moreover, microstructural changes and chemical re-distribution of the main alloying elements in Ti-6Al-4V after oxidation at 700 ºC for 500 hours were discerned. Finally, the role of the main alloying elements on the oxidation was discussed and an oxidation mechanism for oxide scale and oxygen enriched layer (α-case) growth was proposed.

**Keywords**: A. Titanium; B. EPMA; B. SEM; B. XPS; B. XRD; C. Oxidation.

## 1. Introduction

The titanium (Ti) alloys Ti-6Al-4V and Ti-6Al-2Sn-4Zr-2Mo are commonly used for manufacturing aero engine components in the fan and the compressor sections, mainly because of their high strength and low density properties compared to other engineering metal alloys [1-5]. The two alloys have different chemical compositions, which leads to different maximum service temperatures; 300 ºC for Ti-6Al-4V and 450 ºC for Ti-6Al-2Sn-4Zr-2Mo [6]. It is well established that when Ti alloys are exposed to temperatures above ~480 ºC in oxygen containing environments they start to oxidise. The oxidation includes formation of an n-type inward growing oxide scale ($TiO_2$) and oxygen diffusion into the Ti metal [7, 8]. The oxide scale formation occurs because of the high chemical reactivity of Ti with oxygen, whereas the oxygen diffusion is due to the relatively high solid solubility of oxygen in α-Ti (~33 at. %) [9]. In addition, oxygen also: (i) stabilises and hardens the α-Ti through interstitial solid solution strengthening mechanism, (ii) increases the β transus temperature and (iii) stimulates increase of the α/β phase ratio [10].

The oxygen diffusion into the Ti metal is responsible for oxygen embrittlement, i.e. formation of an oxygen enriched layer beneath $TiO_2$ commonly known as "alpha-case" (α-case) [1, 2, 4]. Alpha-case normally forms as result of various manufacturing processes of Ti alloy components such as different forming and thermo-mechanical operations [11, 12], but it might also form locally on parts in aero engines during operation. Alpha-case is known as a continuous, hard and brittle layer that has detrimental effect on the ductility, fracture toughness and fatigue life [7, 13-17]. Therefore, α-case

formation is either prevented using high temperature coatings [18, 19], or removed by machining or chemical milling [4].

Many authors have been investigating the oxidation of different Ti alloys used in aerospace applications in air at elevated temperatures [7, 8, 12, 20-36]. In most of the published work, the oxidation was investigated using thermogravimetric, microscopic and metallographic techniques. The α-case layer thickness, developed after isothermal oxidation in air and atmospheric pressure, was measured optically after using appropriate etchants on Ti-6Al-4V by Sugiura [26], Pitt and Ramulu [28] and on Ti-6Al-2Sn-4Zr-2Mo by McReynolds and Tamirisakandala [33]. The authors used the α-case thickness values to estimate the oxygen diffusion parameters. Another method widely used for estimation of the α-case thickness is micro-hardness measurements [37]. This methodology was applied on Ti-6Al-4V by Frangini and Mignone [20], Zhang *et al.* [30], Guleryuz and Cimenoglu [31] and Kumar *et al.* [32], whereas on Ti-6Al-2Sn-4Zr-2Mo by Shenoy *et al.* [7] and Shamblen *et al.* [13].

A survey of the relevant literature reveals that although many authors have investigated the oxidation of Ti-6Al-4V and Ti-6Al-2Sn-4Zr-2Mo [7, 11-13, 21, 22, 25, 26, 28, 31-33, 35, 36], there is still lack of studies comparing the oxidation behaviour of the two alloys. In particular, there is scarcity of understanding the growth mechanisms of the oxide scale and the α-case layer as well as the influence of alloying elements on the growth mechanisms. The present work will address this gap by investigating and comparing the oxidation behaviour of the two alloys and highlight the growth mechanisms of the oxide scale and α-case layer.

## 2. Material and methods

### *2.1 Materials*

The materials investigated were Ti-6Al-4V and Ti-6Al-2Sn-4Zr-2Mo alloys. Ti-6Al-4V is an $\alpha+\beta$ alloy received in plate form according to AMS 4911L [38] consisting of an equiaxed microstructure with primary $\alpha$ grains and elongated $\alpha$ needles in transformed $\beta$ (Fig. 1a). Ti-6Al-2Sn-4Zr-2Mo is a near-$\alpha$ alloy received in wrought condition, solution and precipitation heat-treated according to AMS 4976G [39]. Ti-6Al-2Sn-4Zr-2Mo has a bi-modal microstructure, composed of primary $\alpha$ grains and transformed $\beta$, where the transformed $\beta$ consists of $\alpha$ and $\beta$ lamellas (Fig. 1b).

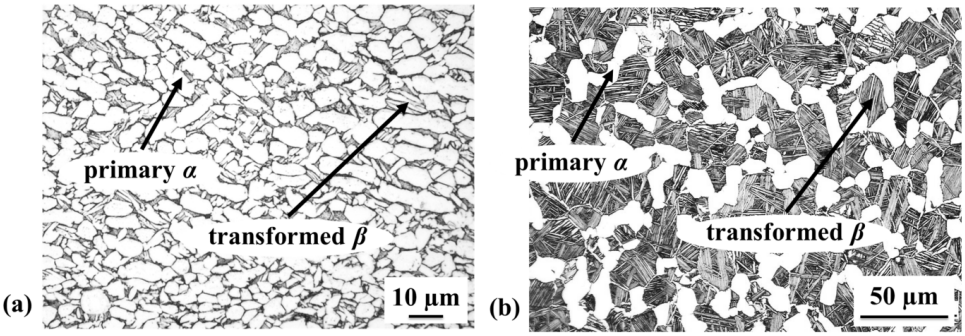


**Figure 1.** Optical micrographs of the microstructure of as-received (a) Ti-6Al-4V and (b) Ti-6Al-2Sn-4Zr-2Mo [35].

Table 1 shows the chemical composition in weight percentage for the two alloys according their material specifications [38, 39].

**Table 1**
Chemical compositions in wt. % of as-received Ti-6Al-4V and Ti-6Al-2Sn-4Zr-2Mo alloys.

| | Al | V | Sn | Zr | Mo | N | O | C | H | Fe | Si | Y | Ti |
|---|---|---|---|---|---|---|---|---|---|---|---|---|---|
| **Ti-64** | 6.75 | 4.5 | - | - | - | 0.05 | 0.20 | 0.08 | 0.015 | 0.3 | - | - | Bal. |
| **Ti-6242** | 6.14 | - | 2.02 | 4.06 | 1.97 | 0.003 | 0.14 | 0.008 | 0.0049 | 0.02 | 0.08 | <0.0004 | Bal. |

*2.2 Specimen preparation and isothermal oxidation*

In total 96 specimens (48 Ti-6Al-4V and 48 Ti-6Al-2Sn-4Zr-2Mo) were cut by electric discharge machining (EDM) to dimensions of 10 x 5 x 10 mm. After cutting, the specimens were ground to remove the recast layer from the EDM process. The specimens were cleaned in acetone for 15 minutes using ultrasonic bath, rinsed with ethanol and dried. After cleaning, the specimens were isothermally oxidised at 500, 593 and 700 ºC for 5, 10, 50, 100, 200, 300, 400 and 500 hours in air using a NABERTHERM box furnace (N11/R). Two specimens were used for each isothermal oxidation treatment. A thermocouple positioned at a specific location inside the furnace was used to follow and control the actual temperature of the specimens, and the accuracy was ± 5 ºC. All oxidised specimens were cooled in air to room temperature. Before and after each isothermal oxidation all specimens were weighed using an analytical microbalance scale (SARTORIUS ANALYTICS) with an accuracy of ± 0.0001 g.

*2.3 Oxide scale analysis*

An X-ray diffractometer (XRD) equipped with a PIXcel3D detector was used to record the XRD patterns of the oxide scale. The X-ray tube was an Empyrean Cu LFF HR and scans were performed with 0.026° step size in the 2-θ range of 20°-80°.

Scanning electron microscopes (SEM, JEOL JSM-6460LV and FEG-SEM, Merlin© from Carl Zeiss), were used to analyse the oxide scales formed on the specimens. Imaging was performed using secondary and back-scattered electrons with an accelerating voltage of 3-25 kV and probe current of 1 nA-84 μA.

The oxide scales were also analysed using XPS on a SPECS system equipped with an Al anode XR50 source operating at 150 mW and a Phoibos 150 MCD-9 detector. The specimens were mounted on a sample holder using double sided carbon adhesive. Note that the surface of the specimens was not cleaned by ion etching prior to the XPS analysis and that a surface area of 3 x 3 mm was analysed. Spectra were recorded with pass energy of 25 eV at 0.1 eV steps at a pressure below $10^{-7}$ Pa and binding energies were referred to the C 1s peak at 284.4 eV. The following sequence of spectra was recorded: survey spectrum, C 1s, O 1s, Ti 2p, Al 2p, V 2p, Fe 2p, Sn 3d, Zr 3d and Mo 3d. The XPS spectra were processed using CasaXPS program (Casa Software Ltd., UK) [40] and the atomic fractions (%) were calculated using peak areas normalised on the basis of acquisition parameters after background subtraction (experimental sensitivity factors and transmission factors provided by the manufacturer). Note that due to C contamination of the oxide surfaces, probably hydro-carbons from air exposure and handling of the specimens, the atomic concentration of the elements was additionally adjusted to maximum 100 at. % by considering C (wt.%) = 0.

*2.4 Oxygen enriched layer analysis*

For optical evaluation of the oxygen enriched layer (α-case), the specimens were prepared by conventional metallographic procedure including grinding and polishing of the specimen surfaces and

etching using a two-step etching procedure. The etching was performed as follows; swabbing the specimen surface with Kroll's reagent (1-3 ml HF, 2-3 ml $HNO_3$ in 100 ml $H_2O$) in the first step and in the second step immersion of the specimen in Weck's reagent (1-3 g $NH_4HF_2$ in 100 ml distilled water). The two-step etching revealed the α-case layer as a continuous white layer at the edge of the specimens. Such white layer was observed along the entire periphery of the cross-section of all specimens. The average α-case layer thickness was measured by an optical microscope NIKON Eclipse MA200 and in total 40-60 measurements were conducted on each specimen, along the entire perimeter with approximately 500 μm spacing.

The chemical composition of the oxygen enriched layer was analysed using a JEOL JXA-8500F Electron Probe Micro Analyser (EPMA), with an accelerating voltage of 10 keV and a beam current of 20 nA probe. The EPMA measurements were performed with a step width of approximately 0.5-2 μm. The EPMA measurements were performed in point mode (50-300 points) from the edge to the bulk with 0.5 μm probe diameter and 0.5-2 μm between each point.

## 3. Results and Discussion

### *3.1 Weight gain*

Fig. 2 shows the weight gain per surface area ($\Delta W/A$) *vs.* oxidation time at 500, 593 and 700 ºC for Ti-6Al-4V (Fig. 2a) and Ti-6Al-2Sn-4Zr-2Mo (Fig. 2b). The $\Delta W/A$ was calculated by dividing the weight difference of the specimens measured before and after oxidation ($\Delta W$) with the total surface area of the specimens ($A$).

From Fig. 2 is seen that the ΔW/A for both alloys is a function of temperature and oxidation time. At 500 ºC the weight gain for both alloys is very small, while at 593 and 700 ºC it is significantly higher for Ti-6Al-4V than for Ti-6Al-2Sn-4Zr-2Mo, indicating that Ti-6Al-4V is oxidising faster at these temperatures. In addition, a notable increase in the weight gain at 700 ºC after 200 hours oxidation times is observed for Ti-6Al-4V (see Fig.2a).

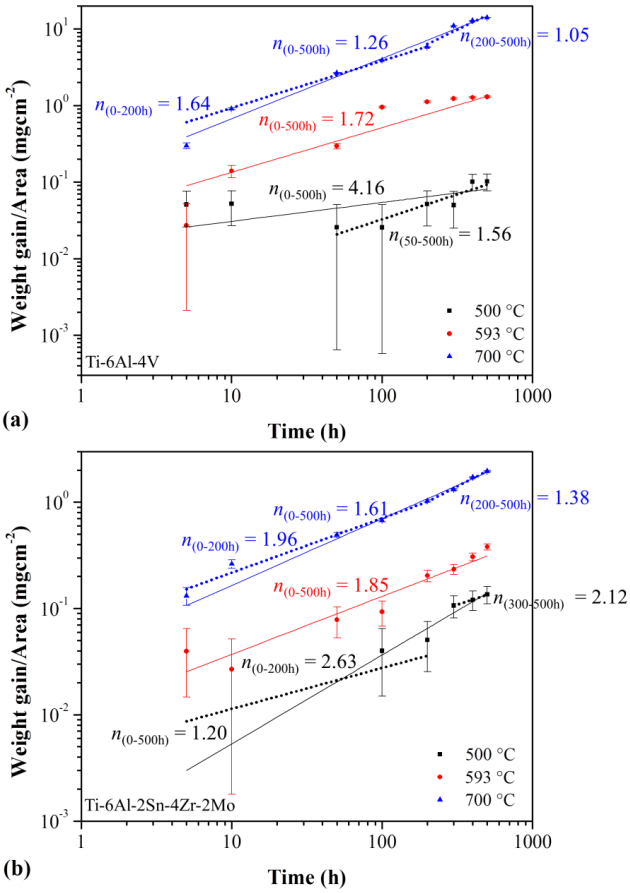


**Figure 2.** Log-log plots of the weight gain per surface area *vs.* time for (a) Ti-6Al-4V and (b) Ti-6Al-2Sn-4Zr-2Mo alloys at 500 ºC, 593 ºC and 700 ºC for up to 500 hours.

The oxidation rates were analysed from the log-log plots using the following equation [41]:

$$\left(\frac{\Delta W}{A}\right)^n = k_n t \qquad (1)$$

where $k_n$ is the rate constant, $t$ is the oxidation time and $n$ is the reaction index. At a constant temperature, the weight gain per surface area is linear if $n = 1$, parabolic if $n = 2$, cubic if $n = 3$ and quartic if $n = 4$ [41]. The statistical parameters obtained by the regression analysis are shown in Table 2.

**Table 2**
Statistical parameters for Ti-6Al-4V and Ti-6Al-2Sn-4Zr-2Mo obtained by regression analysis of ($\Delta W/A$) *vs*. *t* log-log plots from Fig. 2.

| **Ti-6Al-4V** | | | | |
|---|---|---|---|---|
| **Temperature (ºC)** | **Time (h)** | $\Delta W/A = k_n t^n$ | $n$ | $\sigma (k_n)$ |
| 500 | 50-500 | $y = 0.0016x^{0.64}$, $R^2 = 0.89$ | 1.56 | 0.0016 |
| 593 | 0-500 | $y = 0.0350x^{0.58}$, $R^2 = 0.83$ | 1.72 | 0.0403 |
| 700 | 0-200 | $y = 0.2252x^{0.61}$, $R^2 = 0.99$ | 1.64 | 0.0429 |
| | 200-500 | $y = 0.0416x^{0.94}$, $R^2 = 0.91$ | 1.05 | 0.0608 |
| **Ti-6Al-2Sn-4Zr-2Mo** | | | | |
| 500 | 300-500 | $y = 0.0071x^{0.47}$, $R^2 = 0.99$ | 2.12 | 0.0012 |
| 593 | 0-500 | $y = 0.0105x^{0.54}$, $R^2 = 0.97$ | 1.85 | 0.0036 |
| 700 | 0-200 | $y = 0.0668x^{0.51}$, $R^2 = 0.99$ | 1.96 | 0.0114 |
| | 200-500 | $y = 0.0216x^{0.72}$, $R^2 = 0.99$ | 1.38 | 0.0061 |

At 500 ºC it is difficult to draw any conclusion on the oxidation rates from the $n$ values due to the very low weight gain at this temperature. However, a parabolic behaviour is indicated for oxidation time interval 50-500 hours for Ti-6Al-4V and for Ti-6Al-2Sn-4Zr-2Mo for times longer than 300 hours. At 593 ºC the oxidation rate for both alloys follows parabolic relationship for the entire oxidation time. At 700 ºC, for Ti-6Al-4V an approximately parabolic rate for 0-200 hours is noticed, whereas for the time interval 200-500 hours a transition from parabolic to linear oxidation behaviour occurs ($n$~1). Similar behaviour can be seen for Ti-6Al-2Sn-4Zr-2Mo at 700 ºC even though the weight gain for this alloy is much lower than for Ti-6Al-4V and no obvious change in the weight gain is observed for times longer than 200 hours as seen for Ti-6Al-4V.

The parabolic rate constants, $k_p$ values, were calculated for the parabolic regions from Table 2 by fitting the experimental points from Fig. 2 by the following equation [42]:

$$\left(\frac{\Delta W}{A}\right) = \sqrt{k_p t} + C \qquad (2)$$

where $k_p$ is the parabolic rate constant in $g^2cm^{-4}s^{-1}$ and $C$ is a constant. Even though the statistical parameters obtained from the oxidation rate analysis at 500 ºC for the two alloys contained large errors (see Table 2, $R^2$ fits and σ ($a$) values), they were still used to calculate the parabolic rate constants in order to compare the two alloys. The $k_p$ values along with the standard errors $\sigma (k_p)$ for both alloys and all three temperatures are listed in Table 3. The estimated $k_p$ values show that the oxidation of Ti-6Al-4V is two orders of magnitude faster at 593 ºC and one order of magnitude faster at 700 ºC as compared to Ti-6Al-2Sn-4Zr-2Mo.

**Table 3**
Parabolic rate constants ($k_p$) and their standard errors σ ($k_p$) for Ti-6Al-4V and Ti-6Al-2Sn-4Zr-2Mo alloys.

| | **Ti-6Al-4V** | | **Ti-6Al-2Sn-4Zr-2Mo** | |
|---|---|---|---|---|
| **Temperature (ºC)** | $k_p$ ($g^2cm^{-4}s^{-1}$) | σ ($k_p$) | $k_p$ ($g^2cm^{-4}s^{-1}$) | σ ($k_p$) |
| 500 | $8.16 \times 10^{-15}$ | $3.36 \times 10^{-16}$ | $9.31 \times 10^{-15}$ | $3.14 \times 10^{-17}$ |
| 593 | $1.34 \times 10^{-12}$ | $2.33 \times 10^{-14}$ | $7.84 \times 10^{-14}$ | $5.76 \times 10^{-16}$ |
| 700 | $5.73 \times 10^{-11}$ | $2.22 \times 10^{-14}$ | $1.42 \times 10^{-12}$ | $3.68 \times 10^{-15}$ |

The temperature dependence of $k_p$ was estimated by the Arrhenius equation [41]:

$$k = k_0 \cdot \exp\left(-\frac{Q_{ox}}{RT}\right) \qquad (3)$$

where $k_0$ is the frequency factor, $Q_{ox}$ is the activation energy for parabolic oxidation, $R$ is the universal gas constant (8.3143 J/(mol K)) and $T$ is the reaction temperature (K). The $Q_{ox}$ values for Ti-6Al-4V and Ti-6Al-2Sn-4Zr-2Mo alloys were estimated to 278 kJ/mol and 157 kJ/mol, respectively.

Fig. 3 shows Arrhenius plots for Ti-6Al-4V and Ti-6Al-2Sn-4Zr-2Mo from the present work and from literature. The $Q_{ox}$ values estimated for Ti-6Al-4V are similar to those reported in the literature by Unnam et al. [8], Frangini and Mignone [20], Du et al. [21], Guleryuz and Cimenoglu [31] and Poquillon et al. [43], and for Ti-6Al-2Sn-4Zr-2Mo similar to those reported by Shenoy *et al.* [7].

Table 4 shows the regression fits, the estimated $Q_{ox}$ values and corresponding standard errors estimated for Ti-6Al-4V and Ti-6Al-2Sn-4Zr-2Mo from the present work and from literature. As seen, the estimated $Q_{ox}$ values for both alloys lie in the range of those reported in literature.

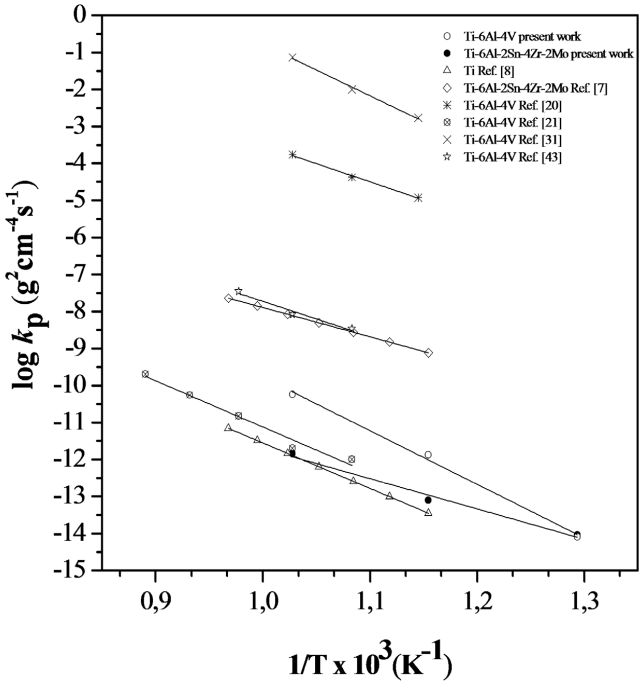


**Figure 3.** Arrhenius plots for oxidation of Ti-6Al-4V and Ti-6Al-2Sn-4Zr-2Mo from the present work and from other authors.

**Table 4**
Regression fits, $Q_{ox}$ values and corresponding standard errors for Ti-6Al-4V and Ti-6Al-2Sn-4Zr-2Mo estimated in the present work and from literature.

| | $y = a + bx$ | $Q_{ox}$ (kJ/mol) |
|---|---|---|
| **Ti-6Al-4V present work** | $y = 4.7235 - 14.4939x$, $R^2=0.99$ | 278 ± 17 |
| **Ti-6Al-2Sn-4Zr-2Mo present work** | $y = -3.5070 - 8.1895x$, $R^2=0.98$ | 157 ± 18 |
| **Ti-6Al-2Sn-4Zr-2Mo, Ref. [7]** | $y = -0.007 - 7.8877x$, $R^2=1$ | 151 |
| **Commercially pure Ti, Ref. [8]** | $y = 0.7275 - 12.2802x$, $R^2=1$ | 235 |
| **Ti-6Al-4V, Ref. [20]** | $y = 6.3482 - 9.8582x$, $R^2=0.99$ | 192 ± 12 |
| **Ti-6Al-4V, Ref. [21]** | $y = 1.3591 - 12.4791x$, $R^2=0.97$ | 267 ± 21 |
| **Ti-6Al-4V, Ref. [31]** | $y = 13.1267 - 13.9062x$, $R^2=0.99$ | 276 ± 18 |
| **Ti-6Al-4V, Ref. [43]** | $y = 1.7883 - 9.5139x$, $R^2=0.94$ | 182 ± 32 |

*3.2 Oxide scale*

Fig. 4 shows SEM micrographs of the oxide scales on Ti-6Al-4V and Ti-6Al-2Sn-4Zr-2Mo after oxidation at 593 and 700 ºC for 5 and 500 hours. The thickness of the oxide scale in Ti-6Al-4V is larger than in Ti-6Al-2Sn-4Zr-2Mo for all three tested temperatures and times. The thicknesses range from less than 500 nm to 85 µm for Ti-6Al-4V and to 5 µm for Ti-6Al-2Sn-4Zr-2Mo. This corroborates the larger weight gain measured for Ti-6Al-4V compared to Ti-6Al-2Sn-4Zr-2Mo (see Fig. 2). The oxidation at 500 ºC resulted in very thin (< 1 µm), dense, adherent and uniform oxide scales for both alloys even after 500 hours oxidation time. Similar morphology of the oxide scales is also observed at 593 ºC for all oxidation times (see Fig. 4a to 4d). However, at 700 ºC only specimens oxidised until 100 hours show dense, well adherent and uniform oxide scales, whereas the oxide scale becomes porous for times ≥ 200 hours both alloys (see Fig. 4g and 4h).

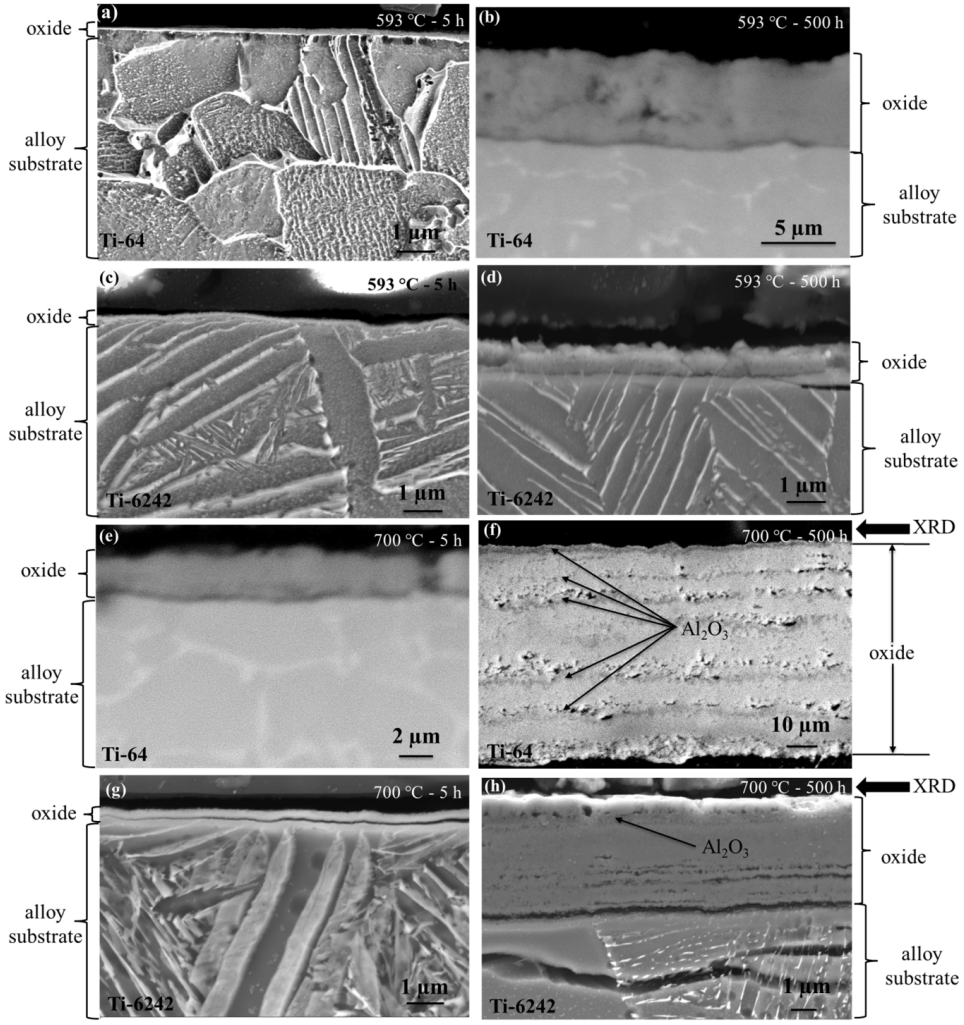


**Figure 4.** SEM micrographs of the oxide scales after 5 and 500 hours at 593 and 700 ºC on Ti-6Al-4V (a), (b), (e) and (f) and on Ti-6Al-2Sn-4Zr-2Mo (c), (d), (g) and (h). The black arrows in (f) and (h) indicate the surface on which XRD measurements were carried out.

Spallation of the oxide scales was observed for both alloys at 700 ºC as seen in the SEM micrographs in Fig. 5. The spallation was more severe in Ti-6Al-4V than in Ti-6Al-2Sn-4Zr-2Mo. The oxide scales on Ti-6Al-4V spalled off from the metal substrate as thin and brittle flakes (see Fig. 5a and 5b) with average thickness of ~90 µm for the longest oxidation time. Such flaking of the oxide scales was not observed on Ti-6Al-2Sn-4Zr-2Mo, where the spallation manifested more like a loss of small particles or fragments (see Fig. 5c). It is considered that the spallation of the oxide scales is due to thermally induced stresses developed during the relatively fast air cooling and the differences in thermal expansion coefficients between the oxide scale and the alloys [44, 45].

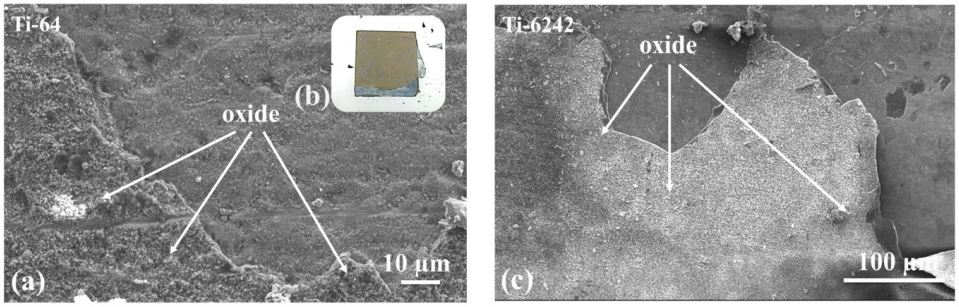


**Figure 5.** SEM micrographs of the oxide after 500 hours at 700 ºC for (a) Ti-6Al-4V, (b) representative digital image of oxide spallation in Ti-6Al-4V alloy and (c) Ti-6Al-2Sn-4Zr-2Mo.

Fig. 6 shows EDS (energy dispersive spectrometry) element mappings of the oxide scales formed after 500 hours oxidation at 700 ºC on Ti-6Al-4V and Ti-6Al-2Sn-4Zr-2Mo, and the corresponding chemical composition is shown in Table 5. The EDS maps for Ti-6Al-4V revealed a multi-layered structure of the oxide scale consisting of Ti and aluminium (Al) layers arranged in ordered patterns at certain distances. Additionally, vanadium (V) and iron (Fe) were probed in the oxide scale of Ti-6Al-4V (see Table 5). Such morphology was absent in Ti-6Al-2Sn-4Zr-2Mo where the oxide scale mainly consisted of Ti doped with tin (Sn), zirconium (Zr), molybdenum (Mo) and silicon (Si) together with a uniform layer of Al at the top surface of the scale. This difference in morphology indicates that the two alloys, even though exposed to the same testing conditions (temperature, time and environment), exhibit different oxidation behaviour.

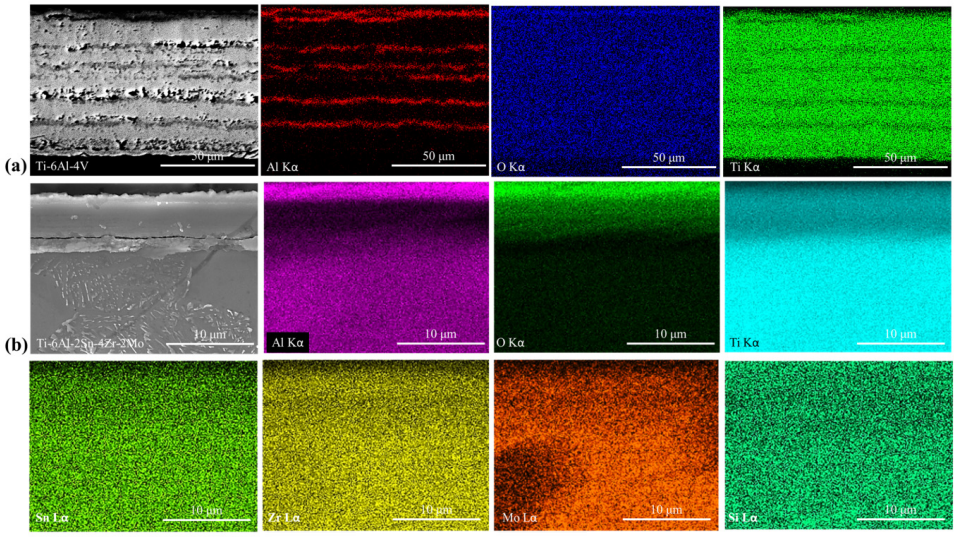


**Figure 6.** SEM-EDS element maps of the oxide scales formed at the surface after 500 hours oxidation at 700 ºC on (a) Ti-6Al-4V and (b) Ti-6Al-2Sn-4Zr-2Mo.

**Table 5**
EDS chemical composition of the oxide scales formed on Ti-6Al-4V and Ti-6Al-2Sn-4Zr-2Mo after 500 hours oxidation at 700 ºC.

| | Ti | O | Al | V | Sn | Zr | Mo | Fe | Si |
|---|---|---|---|---|---|---|---|---|---|
| **Ti-6Al-4V** | 55.95 | 38.53 | 2.91 | 2.38 | - | - | - | 0.33 | - |
| **Ti-6Al-2Sn-4Zr-2Mo** | 50.16 | 18.50 | 3.33 | - | 1.31 | 2.36 | 1.14 | - | 0.08 |

In order to identify the phases present in the oxide scales X-ray diffraction (XRD) was carried out. Fig. 7 shows XRD patterns of the oxide scales formed on Ti-6Al-4V and Ti-6Al-2Sn-4Zr-2Mo after 500 hours at 700 ºC. The XRD measurements were made on the top of the oxide scales (i.e. plane view). The black arrows in Fig. 4f and 4h point at the side of the oxide scale where the XRD measurements were carried out. Note that the oxide scale formed on Ti-6Al-4V was detached from the metal substrate; while the oxide scale on Ti-6Al-2Sn-4Zr-2Mo remained attached (see Fig. 4h). Analysis of the XRD patterns reveals that the oxides in both alloys consist of rutile type of $TiO_2$, which is in agreement with results reported elsewhere [7, 20-22, 31]. Peaks for $\alpha$- and $\beta$-Ti phases were also identified in Ti-6Al-2Sn-4Zr-2Mo (Fig. 7b), which is due to penetration of the X-rays through the oxide scale (<5 μm) into the alloy substrate. In previous works on Ti-6Al-4V [20-22], presence of $Al_2O_3$ phase in the oxide scale was reported. In the current work, weak diffraction signals that might correspond to $Al_2O_3$ phase in the two XRD patterns were discerned, but they were not possible to identify due to low intensity. Therefore, no presence of $Al_2O_3$ phase was identified, even though the EDS maps clearly evidenced presence of Al layers. Possible and reasonable explanations for not identifying $Al_2O_3$ phase are penetration of the X-rays through the thin Al surface layer (3-5 μm) and overlapping of the strongest peaks of $Al_2O_3$ with those from $TiO_2$.

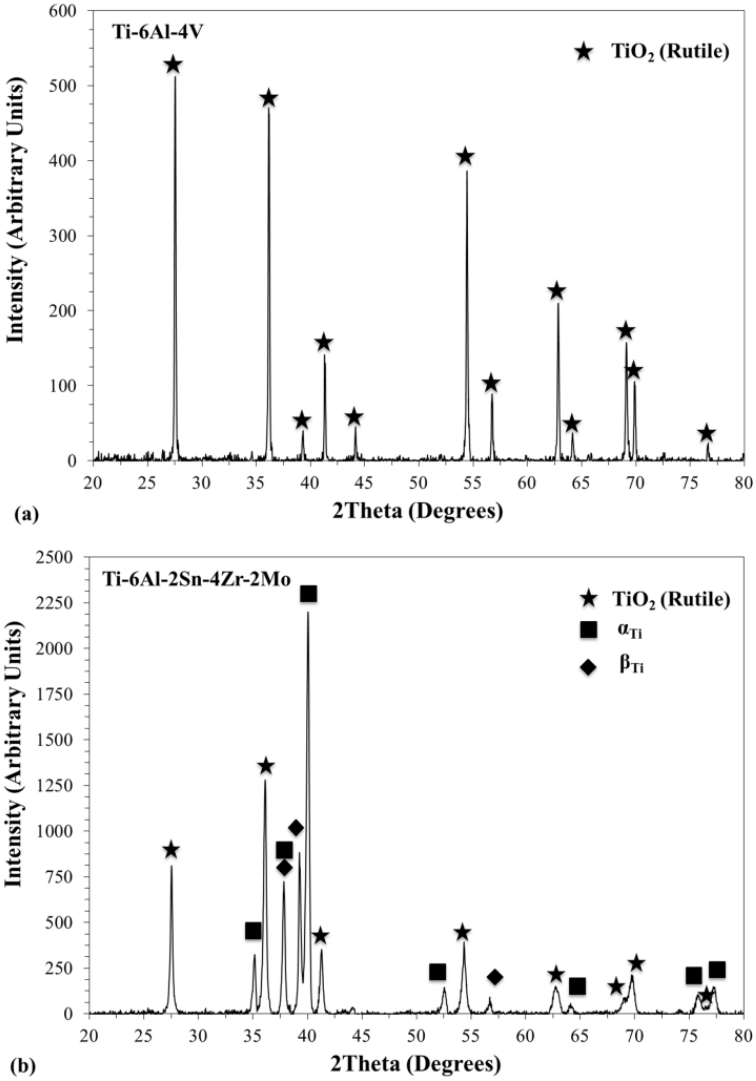


**Figure 7.** XRD patterns of the oxide scales formed after 500 hours at 700 ºC on (a) Ti-6Al-4V detached oxide flake (see Fig. 4f) and (b) Ti-6Al-2Sn-4Zr-2Mo oxide scale formed on top of the alloy surface (see Fig. 4h). Powder Diffraction File (PDF) numbers used for phase identification of $TiO_2$ rutile, $\alpha$-Ti and $\beta$-Ti were as follow: 01-089-4920, 00-005-0682 and 00-044-1288.

To verify the presence or absence of $Al_2O_3$ on the surface of the oxide scales in Ti-6Al-4V and Ti-6Al-2Sn-4Zr-2Mo, XPS was also used. Analysis of the XPS spectra recorded on the oxide scales formed after 500 hours at 700 ºC (oxides shown in Fig. 4f and 4h) revealed that the dominant lines are Ti and O, with weaker contributions from the main alloying elements such as Al and V in Ti-6Al-4V and Al, Sn, Zr and Mo in Ti-6Al-2Mo-4Zr-2Mo. In the Ti-6Al-4V oxide a signal of Fe was also detected. The dominant Ti and O signals of the XPS spectra indicate that the oxide scales in both alloys mainly consist of $TiO_2$ [46], which is in agreement with the XRD results. Table 6 shows the normalised atomic concentrations for all elements, calculated from the high-resolution XPS spectra.

**Table 6**
Normalised chemical composition of the oxide scales in at. % formed on Ti-6Al-4V and Ti-6Al-2Mo-4Zr-2Mo after 500 hours at 700 ºC.

| Element | Ti-64 | Ti-6242 |
|---|---|---|
| O | 78.87 | 78.99 |
| Ti | 13.87 | 14.06 |
| Al | 4.85 | 4.46 |
| Fe | 1.78 | - |
| V | 0.61 | - |
| Zr | - | 1.95 |
| Mo | - | 0.34 |
| Sn | - | 0.17 |

Fig. 8 shows the XPS spectra and the measured binding energies for Ti 2p, O 1s, Al 2p Fe 2p and V 2p recorded on the oxide scale formed on Ti-6Al-4V after 500 hours at 700 ºC (Fig. 4f). The shape and the positions of the Ti peaks in the Ti 2p region (Fig. 8a) show that Ti is present as $Ti^{4+}$. However, contributions to the Ti 2p peak are also seen in the region where $Ti^{3+}$ and $Ti^{2+}$ are expected, indicating that the oxide also contains fractions of $Ti_2O_3$ and TiO owing to oxygen vacancies present at or in the vicinity of the surface . The O 1s spectrum in Fig. 8b shows asymmetry on the higher energy side, which can be attributed to surface defects, low coordinated oxygen or plasmon excitations [47, 48]. High-resolution spectral analysis was used for deconvolution of the O 1s envelopes into three subpeaks often assigned to oxygen in $TiO_2$ and hydrogen-bonded oxygen, such as hydroxides and chemisorbed water [49]. The Al spectrum shown in Fig. 8c indicates that Al is present as $Al^{3+}$ or $Al_2O_3$, without any contribution of metallic Al. This result confirms that the Al multi-layered structure observed by EDS in Fig. 6a consists of $Al_2O_3$. The shape and the positions of the Fe peaks (Fig. 8d) reveal that the Fe is present in form of oxide, i.e. as $Fe^{3+}$ or $Fe^{2+}$ and/or a mixture of both. V was also detected on the surface (Fig. 8e), but its concentration (see Table 6) and signal were weak. It is common not to, or only weakly, detect V on the oxide surface on Ti-6Al-4V [50]. V is more evident inside the oxide (see Table 5). The measured binding energy for V $2p_{3/2}$ (516.4 eV) indicates that V is present in the oxidized states $V^{5+}$, $V^{4+}$ or $V^{3+}$ most likely as $V_2O_5$, $V_2O_4$, $VO_2$ or $V_2O_3$. It is important to point out that the reduced species such as $V^{4+}$ and $V^{3+}$ can form as result of experimental artefacts such as $V_2O_5$ degradation under the X-ray beam during measurement.

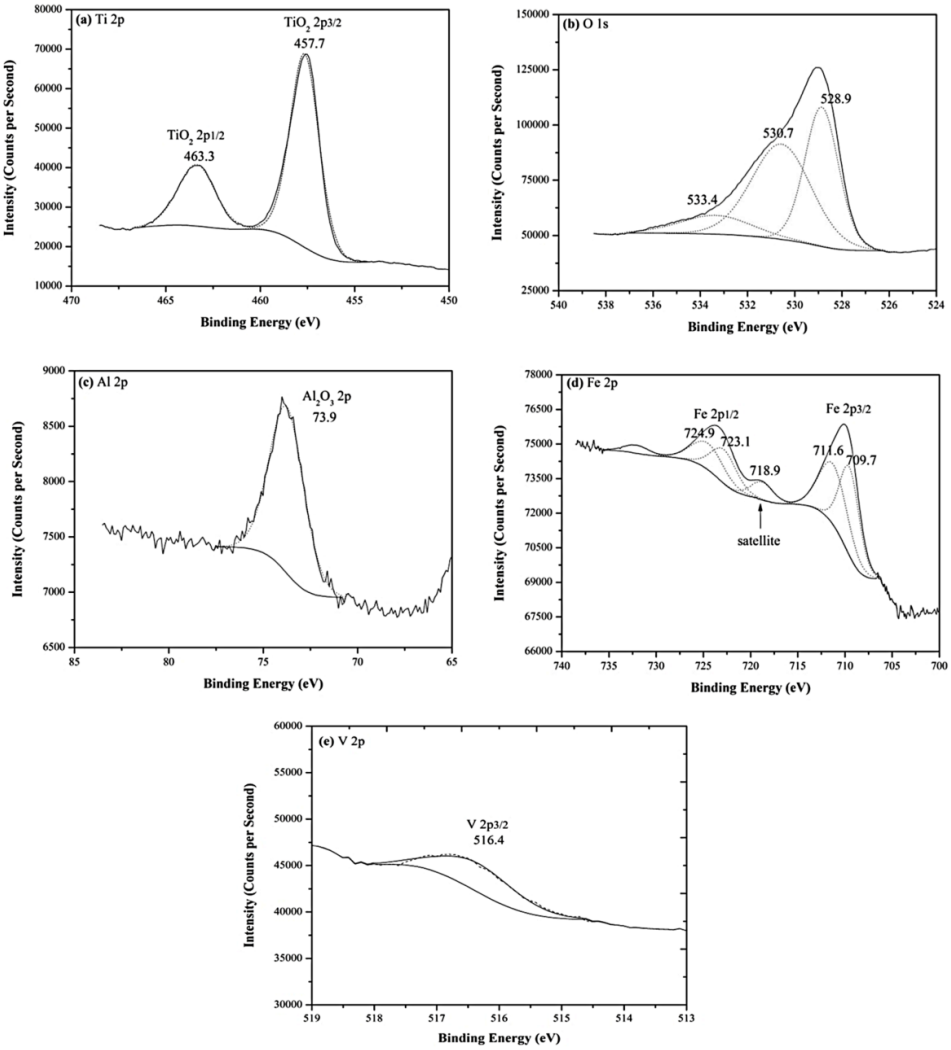


**Figure 8.** XPS spectra of the oxide scale formed on Ti-6Al-4V after 500 hours at 700 ºC (a) Ti 2p, (b) O 1s, (c) Al 2p, (d) Fe 2p and (e) V 2p.

Fig. 9 shows the XPS spectra along with the binding energies for Ti 2p, O 1s, Al 2p, Sn 3d, Zr 3d and Mo 3d recorded on the oxide scale on Ti-6Al-2Sn-4Zr-2Mo formed after 500 hours at 700 ºC (Fig. 4h). Similar as for Ti-6Al-4V, the oxide surface mainly consists of $TiO_2$ and small fractions of $Ti_2O_3$ and TiO (Fig. 9a). The slight difference in the binding energies for the Ti $2p_{1/2}$ and Ti $2p_{3/2}$ between Ti-6Al-4V and Ti-6Al-2Sn-4Zr-2Mo is considered to be because of the dissimilarity in chemical composition of the alloys. However, the peak separation energy between the first subpeak in O 1s and Ti $2p_{3/2}$, results in identical values for both alloys, 71.2 eV, which is in good agreement for $TiO_2$ reported in the literature [47-49]. The shape of the O 1s spectrum in the oxide scale of Ti-6Al-2Sn-4Zr-2Mo (Fig. 9b) is identical with the shape for the Ti-6Al-4V oxide scale and shows asymmetry on the higher energy side because of the above mentioned reasons. However, the deconvolution of the O 1s envelopes results in two subpeaks instead of three as for Ti-6Al-4V. The Al spectrum (Fig. 9c) for

Ti-6Al-2Sn-4Zr-2Mo is identical with Ti-6Al-4V and indicates that Al is present as $Al_2O_3$, without contribution of metallic Al. This result confirms that the Al layer is $Al_2O_3$ also in Ti-6Al-2Sn-4Zr-2Mo. The shape and the position of the Sn peak in the Sn 3d region (Fig. 9d) show that Sn is present in $Sn^{4+}$ oxidizing state (i.e. $SnO_2$) or metallic Sn. The spectrum for Zr and the measured binding energies shown in Fig. 9e indicate that Zr is present in $Zr^{4+}$ and $Zr^0$ oxidizing state in form of $ZrO_2$ or metallic Zr. Fig. 9f shows the spectrum for Mo along with the measured binding energies for Mo $3d_{5/2}$ and Mo $3d_{3/2}$ and indicates that Mo is present in $Mo^{6+}$, $Mo^{5+}$, $Mo^{4+}$ or $Mo^0$ oxidizing state in the form of $MoO_3$, $Mo_4O_{11}$, $MoO_2$ or metallic Mo. However, similarly as for $V^{5+}$, $Mo^{6+}$ could possibly degrade over time under the X-ray beam, which would result in reduced species, i.e. species with lower valence state than 6+.

The XPS analysis on the oxide scales formed in the two alloys after 500 hours at 700 ºC revealed that the oxides consist of a $TiO_2$ matrix doped with the main alloying elements Al, V and Fe for Ti-6Al-4V and Al, Sn, Zr and Mo for Ti-6Al-2Sn-4Zr-2Mo.

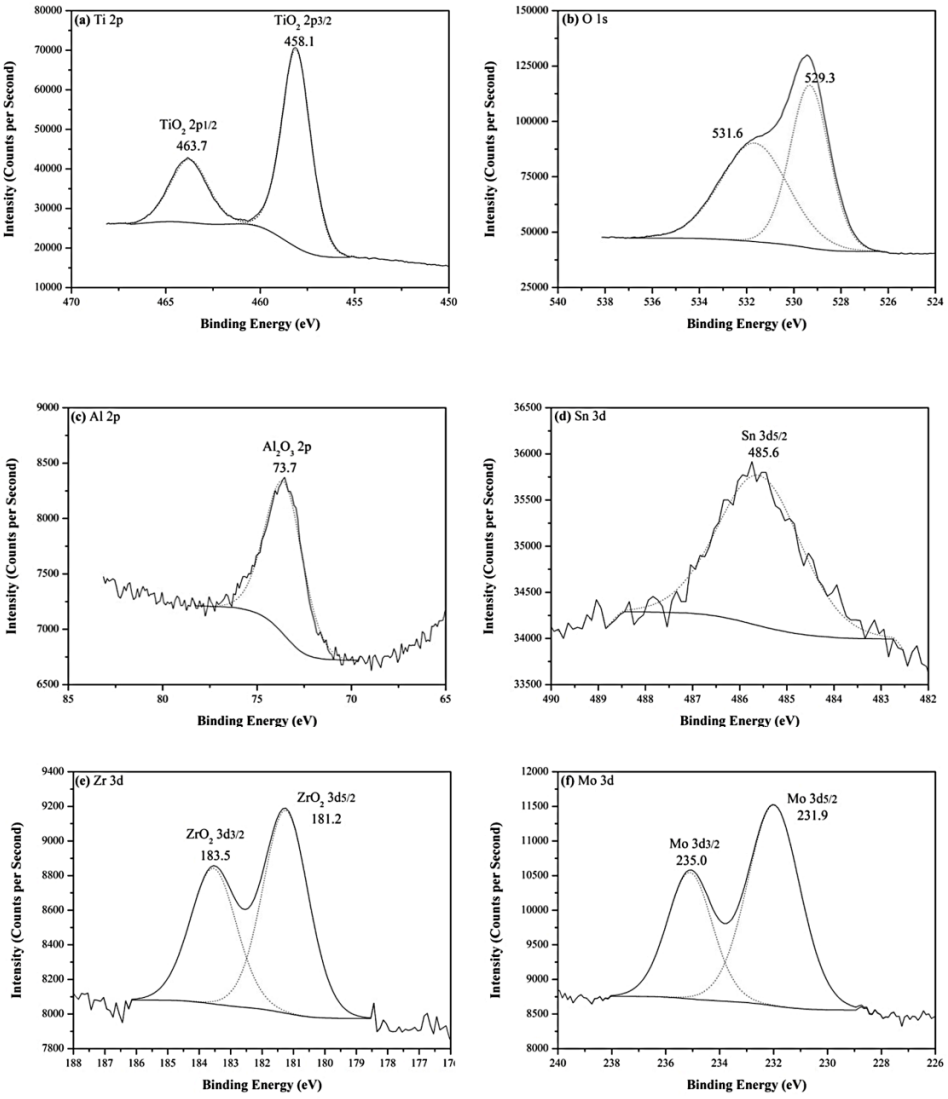


**Figure 9.** XPS spectra of the oxide scale formed in Ti-6Al-2Sn-4Zr-2Mo after 500 hours at 700 ºC (a) Ti 2p, (b) O 1s, (c) Al 2p, (d) Sn 3d, (e) Zr 3d, (f) Mo 3d.

*3.3 Oxygen enriched layer*

Fig. 10 shows representative optical micrographs of the oxygen enriched layer (α-case) formed in Ti-6Al-4V and Ti-6Al-2Sn-4Zr-2Mo after oxidation at 700 ºC for 5 and 500 hours. The thickness of the layer was evaluated from optical micrographs for all sets of specimens for both alloys after two-step etching.

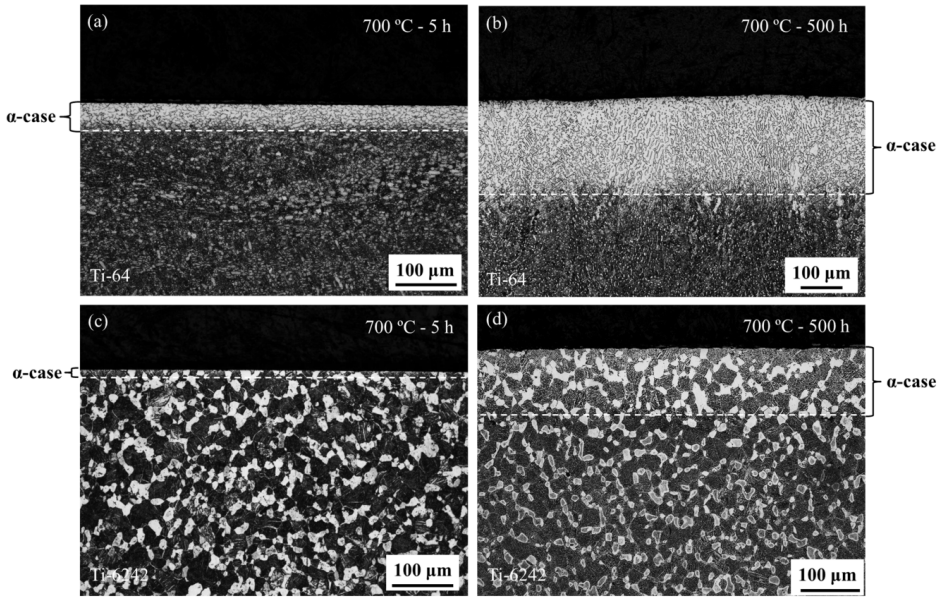


**Figure 10.** Representative optical micrographs of Ti-6Al-4V and Ti-6Al-2Sn-4Zr-2Mo specimens showing the oxygen enriched layer (α-case) formed after oxidation at 700 ºC for 5 and 500 hours. The white dashed lines indicate the oxygen enriched layer boundary.

Fig. 11 shows log-log plots of the optically measured α-case thicknesses as a function of oxidation time, for both Ti-6Al-4V and Ti-6Al-2Sn-4Zr-2Mo. Each data point represents 40-60 individual measurements of the α-case layer thickness along the entire periphery of the specimens. The thickness of the α-case layer is larger by increasing temperature and time for both alloys. After 500 hours at 500, 593 and 700 ºC the average α-case layer thickness measured in Ti-6Al-4V was 6.5, 32 and 198 µm, whereas for Ti-6Al-2Sn-4Zr-2Mo it was 9, 28 and 108 µm.

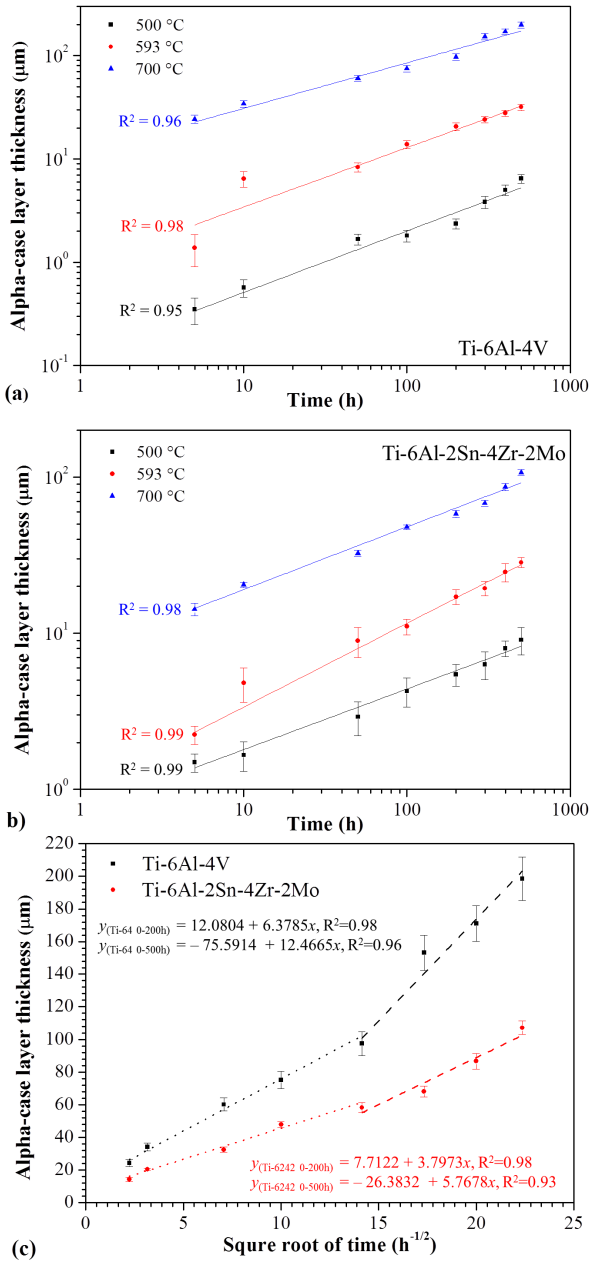


**Figure 11.** Optically measured α-case layer thickness *vs.* time after oxidation at 500, 593 and 700 ºC for (a) Ti-6Al-4V and (b) Ti-6Al-2Sn-4Zr-2Mo alloys and (c) change of the slope for both alloys at 700 ºC above 200 hours oxidation time.

The oxygen diffusion coefficients ($D$) in the two alloys were estimated from the optically measured α-case layer thicknesses by applying Fick's second law:

$$x = \sqrt{Dt} \qquad (4)$$

where $x$ is the α-case layer thickness in μm, $D$ is the diffusion coefficient in $m^2/s$ and $t$ is the oxidation time in seconds.

Alpha-case layer thickness *vs*. square root of time plots were used to derive the $D$ values from the slopes of the fitted linear regression straight lines and the statistical parameters are listed in Table 7. A slight increase in the slope of the straight lines after 200 hours oxidation at 700 ºC was seen for both alloys (see Fig. 11c), similar as for the weight gain.

**Table 7**
Regression analysis statistical parameters of α-case thickness *vs.* square root time from Fig. 11 for Ti-6Al-4V and Ti-6Al-2Sn-4Zr-2Mo

| **Ti-6Al-4V** | | | |
|---|---|---|---|
| **Temperature (ºC)** | **Time (h)** | ***y = a + bx*** | ***σ (b)*** |
| 500 | 0-500 | $y = -0.1648 + 0.22642x$, $R^2 = 0.93$ | 0.0241 |
| 593 | | $y = -1.4965 + 1.4887x$, $R^2 = 0.98$ | 0.0833 |
| 700 | | $y = 7.7842 + 7.5702x$, $R^2 = 0.97$ | 0.5007 |
| **Ti-6Al-2Sn-4Zr-2Mo** | | | |
| 500 | 0-500 | $y = 0.6525 + 0.3528x$, $R^2 = 0.99$ | 0.0113 |
| 593 | | $y = -0.4541 + 1.2325x$, $R^2 = 0.99$ | 0.0448 |
| 700 | | $y = 7.0595 + 3.9426x$, $R^2 = 0.98$ | 0.2235 |

The oxygen enriched layer was also analysed with EPMA, which resulted in chemical composition profiles of the elements present in the alloys. Fig. 12 shows SEM micrographs with corresponding EPMA composition profiles for Ti-6Al-4V and Ti-6Al-2Sn-4Zr-2Mo specimens that were subjected to oxidation for 500 hours at 593 ºC and 700 ºC, respectively. As seen from the profiles, each line represents the concentration and corresponds to the distribution of a particular element. Analysis of the profiles allows clear distinction between the oxide scale and the subsurface oxygen enriched layer thickness (see Fig. 12a and 12b). Variations of the element concentrations were discerned and these are related to the different element contents present in different microstructural constituents in the alloys.

The main purpose of using EPMA was to accurately measure the oxygen distribution along the thickness of the oxygen enriched layer. However, because of difficulties to quantify the absolute oxygen concentration by EPMA, the measured oxygen concentration values were normalised with respect to the bulk oxygen concentrations, 0.2 wt. % and 0.14 wt. % for Ti-6Al-4V and Ti-6Al-2Sn-4Zr-2Mo, respectively (see Table 1). More extensive description of the normalisation of the oxygen concentration can be found elsewhere [36]. Fig. 12c shows a representative normalised oxygen profile for Ti-6Al-2Sn-4Zr-2Mo, as a function of the distance, after oxidation at 593 ºC for 500 hours. The oxygen profile shows existence of an oxygen gradient with the highest oxygen concentration at the surface of the specimen. The oxygen profile shows the distribution of oxygen along the thickness of the specimen and can therefore be used to estimate the oxygen diffusion parameters. Thus, the EPMA oxygen profiles were fitted with the following equation of Fick's second law:

$$\frac{c - c_0}{c_s - c_0} = 1 - erf\left(\frac{x}{2\sqrt{Dt}}\right) \qquad (5)$$

where $c_0$ is the bulk oxygen concentration, $c_s$ is the oxygen concentration at the oxide/metal interface, $x$ is the distance from this interface, $t$ is the time and $D$ is the diffusion coefficient in $m^2/s$. Equation (5) was used to fit only the oxygen enriched layer thickness by excluding the thickness of the oxide scale.

The oxide/metal interface in the oxygen concentration profiles was identified by comparing the chemical composition profiles of O and N as shown in Fig. 12d. As soon as the EPMA probe reaches the alloy substrate sudden decline of the N concentration to 0 wt. % occurs. As shown in previous work [36], the N concentration in the alloys was below the detection limit of the EPMA instrument, and therefore the N profiles were used to identify the oxide/metal interface. Table 8 summarises the calculated $D$ values and their corresponding standard errors for oxygen diffusion using the experimental results from the optical evaluation of the α-case layer thickness and from the fittings of the normalised oxygen profiles. Note that the oxygen diffusion coefficients estimated via the fitting method are average values obtained using the fitting of the oxygen profiles of 5, 50 and 500 hours oxidation times.

**Table 8**
Diffusion coefficients and standard errors for oxygen diffusion calculated using the optical α-case layer thickness measurements and the fitting of the EPMA normalised oxygen profiles.

| | | Ti-6Al-4V | | Ti-6Al-2Sn-4Zr-2Mo | |
|---|---|---|---|---|---|
| | **Temperature (ºC)** | ***D*** **($m^2s^{-1}$)** | **σ (*D*)** | ***D*** **($m^2s^{-1}$)** | **σ (*D*)** |
| optical measurements | 500 | $1.42 \times 10^{-17}$ | $1.61 \times 10^{-19}$ | $3.46 \times 10^{-17}$ | $3.58 \times 10^{-20}$ |
| | 593 | $6.16 \times 10^{-16}$ | $1.93 \times 10^{-18}$ | $4.22 \times 10^{-16}$ | $5.58 \times 10^{-19}$ |
| | 700 | $1.59 \times 10^{-14}$ | $6.96 \times 10^{-17}$ | $4.32 \times 10^{-15}$ | $1.39 \times 10^{-17}$ |
| fitting of the oxygen profiles | 500 | $5.79 \times 10^{-19}$ | $1.16 \times 10^{-19}$ | $2.89 \times 10^{-18}$ | $5.01 \times 10^{-19}$ |
| | 593 | $3.19 \times 10^{-17}$ | $8.65 \times 10^{-18}$ | $4.01 \times 10^{-17}$ | $4.81 \times 10^{-18}$ |
| | 700 | $7.13 \times 10^{-16}$ | $5.83 \times 10^{-17}$ | $6.82 \times 10^{-16}$ | $3.59 \times 10^{-17}$ |

The temperature dependence of $D$ was estimated by an Arrhenius type of equation:

$$D = D_0 \exp\left(-\frac{Q}{RT}\right) \qquad (6)$$

where $D_0$ is the pre-exponent factor, $Q$ is the activation energy for diffusion of oxygen, $R$ is the universal gas constant (8.3143 J/(mol K)) and $T$ is the temperature (K). The average activation energy has been calculated by plotting log $D$ *vs.* $1/T$ where the slope of the best fit line is equal to $-Q/2.303R$. The average $Q$ value calculated for Ti-6Al-4V by optically evaluated α-case layer thickness data was 220 kJ/mol and by using the fitting data 223 kJ/mol. For Ti-6Al-2Sn-4Zr-2Mo an activation energy ($Q$) of 151 kJ/mol was calculated using the optical results and 171 kJ/mol by using the fitting results.

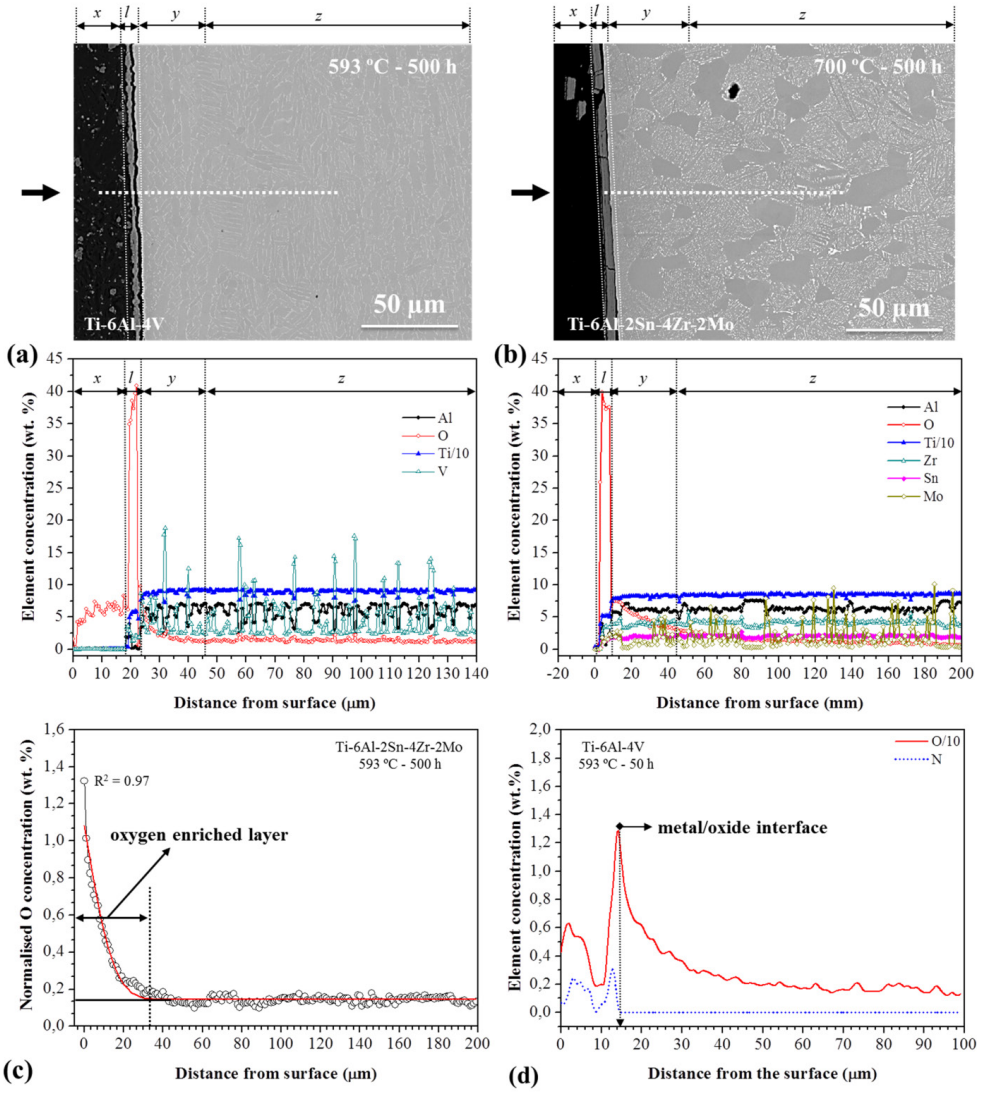


**Figure 12.** SEM micrographs and corresponding EPMA chemical composition profiles after oxidation at (a) 593 ºC for 500 hours in Ti-6Al-4V; (b) 700 ºC for 500 hours in Ti-6Al-2Sn-4Zr-2Mo; *x*, *l*, *y* and *z* refer to the thickness of mount (Bakelite), the oxide scale, the oxygen enriched layer and alloy substrate, respectively; (c) representative normalised oxygen profile after 500 hours at 593 ºC for Ti-6Al-2Sn-4Zr-2Mo, the fitting line refers to the best fit obtained with equation (5); (d) representative profile used for identification of the oxide/metal interface. The black arrows in (a) and (b) indicate the direction of the measurements.

To validate the calculated oxygen diffusion parameters and activation energies, comparison of the oxygen diffusion results from other work was performed. Fig. 13 shows Arrhenius plots for oxygen diffusion in Ti-6Al-4V and Ti-6Al-2Sn-4Zr-2Mo from the present work obtained from the optical and fitting methods and from different methods used in literature for Ti, rutile, Ti-6Al-4V and Ti-6Al-2Sn-4Zr-2Mo.

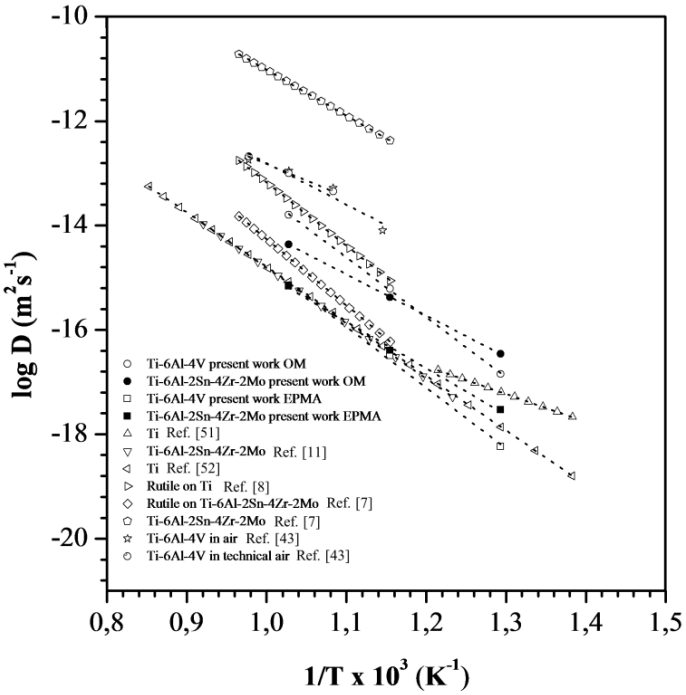


**Figure 13.** Arrhenius plots for oxygen diffusion in Ti-6Al-4V and Ti-6Al-2Sn-4Zr-2Mo alloys from the present work and from literature.

The estimated *Q* values, their respective standard errors and the pre-exponent factors for Ti-6Al-4V and Ti-6Al-2Sn-4Zr-2Mo calculated in the present work and those collected from literature are shown in Table 9. As seen, the estimated *Q* values for oxygen diffusion in the two alloys from the present work are similar to those reported in the literature.

**Table 9**
*Q* values with corresponding standard errors and pre-exponent factors calculated for Ti-6Al-4V and Ti-6Al-2Sn-4Zr-2Mo in the present work and from literature.

| | $Q_{ox}$ (kJ/mol) | $Do$ ($m_2$/s) |
|---|---|---|
| **Ti-6Al-4V** present work[1] | 220 ± 4 | $1.01 \times 10^{-2}$ |
| **Ti-6Al-2Sn-4Zr-2Mo** present work[1] | 151 ± 1 | $5.43 \times 10^{-7}$ |
| **Ti-6Al-4V** present work[2] | 223 ± 11 | $7.23 \times 10^{-4}$ |
| **Ti-6Al-2Sn-4Zr-2Mo** present work[2] | 171 ± 8 | $9.11 \times 10^{-7}$ |
| **Ti,** Ref. [51][3] | 102 | $4.97 \times 10^{-11}$ |
| **Ti-6Al-2Sn-4Zr-2Mo,** Ref. [13][4] | 203 | $6.19 \times 10^{-5}$ |
| **Ti,** Ref. [52][5] | 200 | $4.49 \times 10^{-5}$ |
| **Rutile on Ti,** Ref. [8][6] | 232 | $8.70 \times 10^{-2}$ |
| **Rutile on Ti-6Al-2Sn-4Zr-2Mo,** Ref. [7][7] | 243 | $2.68 \times 10^{-2}$ |
| **Ti-6Al-2Sn-4Zr-2Mo,** Ref. [7] | 167 | $5.19 \times 10^{-3}$ |
| **Ti-6Al-4V in air,** Ref. [43][8] | 152 ± 29 | $1.32 \times 10^{-5}$ |
| **Ti-6Al-4V in technical air,** Ref. [43] | 121 ± 1 | $3.12 \times 10^{-7}$ |

*Methods used to estimate oxygen diffusion: [1]optical evaluation of the α-case layer thickness, [2]fitting of EPMA oxygen profiles, [3]oxygen concentration gradient Auger electron spectroscopy, [4,6,7]thermogravimetry, [5]thermogravimetry, stress-strain aging, [8]oxygen concentration gradient secondary ion mass spectrometry.

*3.4 Mechanisms of oxide scale and oxygen enriched layer formation*

Oxidation of titanium comprises of two physical phenomena running simultaneously and if these phenomena are analysed and assessed separately, the resulting outcome could improve the understanding of the oxidation mechanisms for oxide scale and oxygen enriched (α-case) layer growth.

***a. Oxide scale growth mechanism.*** To describe the oxidation mechanism of a given metal, the primary charge carriers and the predominant diffusion mechanism in the oxide scale should be identified. In the present work, the oxidation of Ti-6Al-4V and Ti-6Al-2Sn-4Zr-2Mo resulted in formation or rutile type of oxide scale. It is well established that rutile is an n-type oxide exhibiting significant non-stoichiometry $TiO_{2-x}$, where $x$ could vary up to ~0.008 depending on temperature and oxygen partial pressure. The oxygen deficiency of rutile is compensated with oxygen vacancies and Ti interstitials in the oxide structure, which are the primary charge carriers [53, 54]. In general, it has been concluded that titanium interstitials predominate at low oxygen activities and high temperatures, whereas oxygen vacancies are important at high oxygen activities and low temperatures [41]. Based on this, it is reasonable to deduce that the mechanism of oxide growth takes place within the rutile scale through outward migration of titanium interstitials and inward diffusion of oxygen vacancies from an outer part of the scale, where the rate determining process is the transport properties of the oxide scale [40]. It is important to highlight that the direction of oxide scale growth is downward, i.e. the oxide/metal interface is constantly moving towards the bulk of the metal as the oxide scale growth proceeds. This particular oxide scale growth mechanism encounters for parabolic oxidation rate, where dense, continuous and well adherent oxide scale is formed. Such oxide morphology is observed for the two alloys after oxidation at 500, 593 and 700 ºC, where parabolic oxidation rate is obeyed (see Table 2 and Fig. 4).

In particular oxidation time intervals there are transitions in the oxidation rates. For oxidation times ≥ 200 hours at 700 ºC the alloys exhibit transition in the oxidation rate from parabolic to linear (para-linear) relationship. This is evidenced by the weight gain *vs*. time plots shown in Fig. 2. In the work of Kofstad et al. [55] it was reported that para-linear oxidation of titanium typically takes place at a critical total weight gain in the range of 2-5 mg/cm$^2$. This is in agreement with the results for Ti-6Al-4V, where the measured total weight gain for ≥ 200 hours was 5.8 mg/cm$^2$. Even though the total weight gain measured for Ti-6Al-2Sn-4Zr-2Mo at 700 ºC was much lower than for Ti-6Al-4V and no obvious change in the weight gain rate was observed, the estimated $n$ value ($n$ = 1.38) for 200-500 hours oxidation time interval indicates that para-linear oxidation regime takes place also in this alloy [30]. The lamellar oxide scale structure (see Fig. 4f) on Ti-6Al-4V for oxidation times ≥ 200 hours is an additional evidence for para-linear oxidation rate at 700 ºC. It is well established that linear oxidation rate mainly reflects through increased oxide scale growth rate, where the oxygen diffusion proceeds at rates determined by the oxygen gradient and the oxygen diffusion coefficient in titanium [41]. The transition from parabolic to linear oxidation observed at 700 ºC for the two alloys in this work can be explained as breakdown of the protective behaviour of the oxide scale due to high stresses developed as result of nucleation and growth of the oxide grains and formation of porous oxide structure. This breakdown results in increased oxygen activity at the oxide/metal interface and consequently increases the concentration of the diffused oxygen in the metal substrate. In fact, this correlates well with the observed microstructures of the oxide scales developed after 500 hours at 593 ºC and 200 hours at 700 ºC. Fig. 14 shows SEM micrographs comparing the oxide scale microstructures developed on Ti-6Al-4V and Ti-6Al-2Sn-4Zr-2Mo after oxidation at 593 ºC for 500 hours and 700 ºC for 200 hours. Comparison of the SEM micrographs clearly evidences that the increase in oxidation temperature from 593 ºC to 700 ºC results in formation of porous oxide structure and larger crystal size of the oxides. In addition, it has been proposed that the para-linear transition can

be associated to oxygen diffusion in the metal, which at $TiO_{0.35}$ generates significant changes in the lattice parameters of the crystal structure [41]. This may then lead to significant internal stresses in the metal which could initiate cracking, delamination of the outer layer and subsequent increased oxidation rate [41].

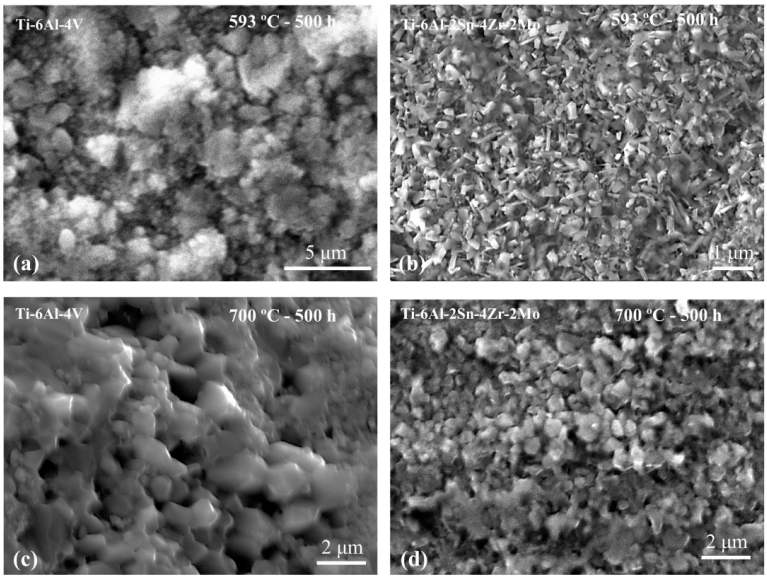


**Figure 14.** SEM micrographs of oxide scale microstructures on (a) and (c): Ti-6Al-4V and (b) and (d): Ti-6Al-2Sn-4Zr-2Mo after oxidation at 593 ºC for 500 hours and at 700 ºC for 200 hours.

Comparison of the oxidation rates for both alloys leads to the conclusion that Ti-6Al-2Sn-4Zr-2Mo exhibits higher oxidation resistance than Ti-6Al-4V in the temperature range 500-700 ºC for up to 500 hours oxidation time. This is evidenced by the estimated parabolic rate constants and oxidation activation energies for Ti-6Al-4V and Ti-6Al-2Sn-4Zr-2Mo (see Table 2, 3 and 4). The significant difference in oxidation behaviour between the two alloys, when subjected to the same conditions (temperature and time), is due to diversity in chemical composition and the individual influence of each alloying element on the oxidation. The XRD and XPS oxide scale characterisation showed that the oxide mainly consists of rutile doped with the main alloying elements present in each alloy; Al, and V in Ti-6Al-4V and Al, Sn, Zr and Mo in Ti-6Al-2Sn-4Zr-2Mo. In continuation, the influence of alloying elements will be discussed.

***Influence of Al on the oxidation behaviour.*** Aluminium is an important $\alpha$-stabilising alloying element in Ti alloys, improving the strength properties and high temperature resistance [1, 2, 4]. The work of Chaze and Coddet [56] showed that Al additions reduce the oxygen dissolution in Ti-Al alloys when oxidized up to 700 ºC by forming $Al_2O_3$ layer on top of the oxide scale. It is well known that Al has higher activity compared to Ti and that $Al_2O_3$ is thermodynamically more stable than $TiO_2$ at lower oxygen partial pressures. Therefore, one could expect it thermodynamically impossible to form $Al_2O_3$ on top of $TiO_2$. However, Du *et al.* [21] have shown that a compact $Al_2O_3$ layer is always formed on top of the $TiO_2$ during air oxidation of Ti-6Al-4V at elevated temperatures. The authors based their conclusions on thermodynamic calculations and experimental facts. Moreover, they claimed that the presence of V suppress the Al activity to the extent that $Al_2O_3$ is unlikely to develop at the oxide/metal interface, but must be formed on the top of the oxide. In the present work, Al takes

part in the oxidation process of the two alloys through formation of $Al_2O_3$ multi-layers in Ti-6Al-4V and single $Al_2O_3$ layer on top of the oxide scale in Ti-6Al-2Sn-4Zr-2Mo. The presence of $Al_2O_3$ in the oxides of both alloys was evidenced by SEM-EDS mapping (Fig. 6) and XPS (Fig. 8 and Fig. 9). The main role of a dense $Al_2O_3$ layer on top of the oxide scale is to inhibit oxygen diffusion into the alloy substrate. However, although $Al_2O_3$ was present in the oxide scales of both alloys it did not completely inhibit the oxygen diffusion into the alloy substrates as shown in Section 3.3. The observation of different morphology of the $Al_2O_3$ layer in the two alloys gives an indication that Al takes part in the oxidation via different mechanisms. It is suggested that the other main alloying elements of the two alloys have effect on the $Al_2O_3$ layer formation mechanism and more detailed discussion will be provided later in this section.

***Influence of V and Mo on the oxidation behaviour.*** Vanadium and molybdenum are important *β*-stabilising elements for Ti alloys [1, 2, 4], having influence on the oxidation resistance. Previous studies [57-60] suggested that V has detrimental effect on the oxidation behaviour in Ti-Al system alloys through suppression of the formation of protective $Al_2O_3$ layer on top of the oxide scale, thereby stimulating faster oxidation kinetics. This effect has been observed for V concentration of 1.4 wt. % [58] and it was more evident the higher V concentrations present in the Ti alloy [57]. Molybdenum alone has limiting effect on improving the high temperature oxidation resistance in titanium aluminides. It has been suggested that its main role is inhibition of oxygen diffusion into the metal substrate via promoting dense $Al_2O_3$ layer formation [61]. In the present work, V and Mo are identified in the rutile scale after oxidation of Ti-6Al-4V and Ti-6Al-2Sn-4Zr-2Mo, respectively. The XPS results indicate that V and Mo are present as oxides with different valence states. For V this is expected, because at 700 ºC different Ti-V-O phases are forming [62]. The influence of V and Mo on the oxidation behaviour is complex and for clarification, in-depth analysis of the phenomena taking place in the subsurface oxygen enriched layer is required.

Analysis of the EPMA chemical composition profiles for the alloys reveals significant re-distribution of the main α- and *β*-stabilising elements, Al and V in Ti-6Al-4V and Al and Mo in Ti-6Al-2Sn-4Zr-2Mo as compared to as-received material. Most notable element re-distribution is noted after oxidation at 700 ºC for 500 hours. Fig. 15 compares the chemical composition profiles of *α*- and *β*-stabilising elements in Ti-6Al-4V (Fig. 15a for V and 15b for Al) and Ti-6Al-2Sn-4Zr-2Mo (Fig. 15c for Mo and 15d for Al) before and after oxidation at 700 ºC for 500 hours, for a defined distance from the surface. The profiles reveal information about the size and distribution of *α* and *β* phases. For example, the amount of *β*-stabilising elements increases when *β* phase is probed, but drops to minimum when *α* phase is probed and vice versa. These maximum and minimum amounts of the *β*-stabilising elements result in peaks that represent *β* phase (see Fig. 15a, designation *β*), whereas each plateau between peaks depicts *α* phase, where the amount of the *β* stabilising elements is low (see Fig. 15a, designation *α*). Similar peaks and plateaus in the profiles of *α*-stabilising element are observed (see Al profiles in Fig. 15b and 15d). The height of a peak corresponds to the measured concentration of the *α*- or *β*-stabilising elements, whereas the widths of a peak and a plateau correspond to the phase size and its distribution.

In Ti-6Al-4V, a significant rise of V concentration occurs, ranging from maximum 8 wt. % in the as-received specimen to about 42 wt. % at maximum after 500 hours at 700 ºC.

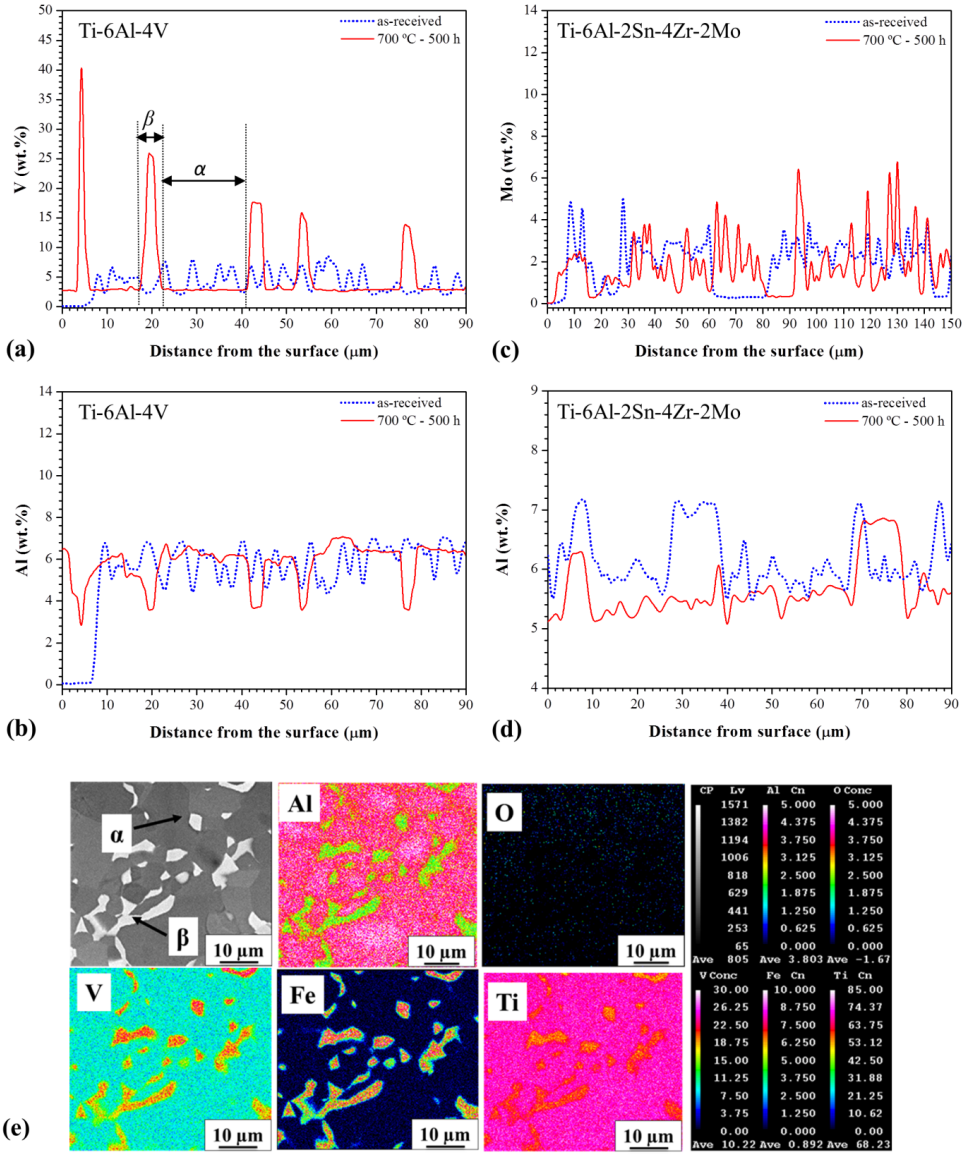


**Figure 15.** (a)-(d) EPMA chemical composition profiles before and after isothermal oxidation at 700 ºC for 500 hours for vanadium (a) and aluminium (b) in Ti-6Al-4V, and molybdenum (c) and aluminium (d) in Ti-6Al-2Sn-4Zr-2Mo; (e) EPMA element mapping of the oxygen enriched layer in Ti-6Al-4V showing the element re-distribution after 500 hours at 700 ºC.

The highest V concentration (42 wt. %) is measured at a distance of 5-7 μm from the alloy surface (Fig. 15a), gradually decreasing moving towards the bulk of the specimen until the average bulk V concentration is reached (4.5 wt. %). It is observed that V is diffusing into the $\beta$ phase during the long oxidation of 500 hours. It is anticipated that during the 500 hours at 700 ºC equilibrium is reached.

The relatively fast cooling to room temperature, i.e. air cooling, does not dramatically change the chemical composition in the $\beta$ phase with regard to V content. The peak height and plateau width increase in the V concentration profile compared to as-received specimen indicating microstructural changes. The $\beta$ phases in the as-received alloy become enriched with V after oxidation. Moreover, an increased Fe content in $\beta$ phase is noted, ranging from 2-10 wt. %. It is well known that Fe contents larger than 0.1 wt. % stabilise $\beta$ phase at temperatures above 590 ºC [63]. Fe is a $\beta$-eutectoid element, with a eutectoid temperature of 590 ºC, below which $\beta$-Ti decomposes into $\alpha$-Ti and intermetallic FeTi. However, if the cooling rate is fast enough, such as air cooling in this case, the decomposition does not take place and $\beta$-Ti remains at the grain boundaries forming precipitates, which suppress the grain coarsening [63]. Such $\beta$ phase, rich in V and Fe, is found in the oxygen enriched layer in Ti-6Al-4V after oxidation at 700 ºC (see Fig. 15e). Ti and V form solid solution at 700 ºC according to the Ti-V phase diagram [9]. Analysis of the width of the plateau in the V and Al concentration profiles (Fig. 15a and Fig. 15b) shows that the sharp peaks in the as-received specimen become broader after oxidation. This indicates that coarsening of the microstructure in Ti-6Al-4V occurs as a result of 500 hours oxidation. The primary $\alpha$ grain coarsening in Ti-6Al-4V confirms the hypothesis that oxygen dissolution in the metal leads to significant internal stresses that cause cracking and delamination of the oxide scale and subsequent increase of the oxidation rate. The grain coarsening effect in Ti-6Al-4V substantiates the para-linear transition of the oxidation rate observed at 700 ºC for times $\geq$ 200 hours.

The microstructure of Ti-6Al-2Sn-4Zr-2Mo is more complex and the interpretation of the Mo and Al concentration profiles is more difficult (Fig. 15c and 15d). No obvious trend between the as-received and the oxidised specimen in terms of variation of the Mo concentration is observed. Instead, only an increase in Mo concentration in the $\beta$ phase with respect to temperature is observed (Fig. 15c). This indicates that Mo prefers the BCC lattice sites of the $\beta$ phase, which is expected. In addition, depletion of the Al content in Ti-6Al-2Sn-4Zr-2Mo after oxidation is discerned (see Fig. 15d). This indicates that Al diffuses outward from the subsurface inner layer and contributes to the oxidation resistance of Ti-6Al-2Sn-4Zr-2Mo by forming dense $Al_2O_3$ layer on top of the oxide scale (see Fig. 4h and Fig. 6b). In contrast, such subsurface Al depletion in Ti-6Al-4V is not observed (see Fig. 15 b).

Vanadium and molybdenum tend to diffuse and segregate into the $\beta$ phase during the long oxidation (see Fig. 15a and 15c). However, the self-diffusion of Mo is not pronounced such as for V, which is not surprising since Mo exhibits several orders in magnitude lower diffusivity compared to V [64]. Vanadium and molybdenum take part in the oxidation through outward diffusion and doping of the $TiO_2$ matrix, as shown with the XPS results. It is suggested that the doping of the rutile oxide with V and Mo enables stable oxide growth that results in formation of compact and well adherent oxide scales on the top of Ti-6Al-4V and Ti-6Al-2Sn-4Zr-2Mo, respectively. However, this mechanism is valid only during parabolic oxidation when dense and well adherent oxide scales are formed (i.e. at 500 and 593 ºC for oxidation times up to 500 hours and at 700 ºC for oxidation times up to 200 hours). As seen, the oxidation of both alloys at 700 ºC for times longer than 200 hours results in formation of porous oxide structure (see Fig. 14c and 14d). It is believed that V and Mo significantly influence the oxidation behaviour of Ti-6Al-4V and Ti-6Al-2Sn-4Zr-2Mo when oxidised at 700 ºC for times $\geq$ 200 hours. Hence, it is suggested that the influence of V and Mo is related to their ability to form volatile oxide species such as $V_2O_5$ and $MoO_3$. In fact, the XPS analysis of the oxide scales formed on both alloys indicates possible presence of these volatile oxide species. $V_2O_5$ and $MoO_3$ exhibit low melting points, 674 ºC for $V_2O_5$ and 795 ºC for $MoO_3$ [41] indicating high possibility for evaporation from the rutile oxide. It is considered that the evaporation of $V_2O_5$ and $MoO_3$ could cause physical defects in

the oxide scale and thereby it is reasonable to associate this phenomenon to the formation of porous oxide scale in the two alloys when subjected to oxidation at 700 ºC for longer oxidation times. In addition, the relatively high vapour pressure of $MoO_3$ at 700 ºC ($4.69 \cdot 10^{-4}$ atm) [65] supports our hypothesis for the ability of $MoO_3$ to evaporate from the rutile oxide scale. To clarify the influence of V and Mo on the oxidation behaviour at 700 ºC for oxidation time $\geq$ 200 hours it is important to highlight the oxide scale growth direction and the oxygen partial pressure across the oxide scale thickness. During oxidation, the oxide scale grows downward and thereby it is reasonable to consider that the oxide/metal interface is constantly moving towards the alloy substrate. In addition, it is well known that the oxygen partial pressure varies across the oxide scale thickness being highest at the air/oxide interface and lowest at the oxide/metal interface. Considering the oxide growth direction, the variation of the oxygen partial pressure in the oxide scale and the pronounced self-diffusion of V and Mo into the alloy substrate forming enriched V or Mo $\beta$ phases just below the oxide scale, it is reasonable to conclude that when the enriched V and Mo $\beta$ phases reach suitable oxygen partial pressure in the oxide scale they will be oxidised to their most stable oxide form. With high certainty even volatile oxides (i.e. $V_2O_5$ and $MoO_3$) that could easily evaporate from the oxide structure are formed. In the case of Ti-6Al-4V, it is considered that the V oxidation substantially supresses the Al activity for oxygen due to the high V concentration in the $\beta$ phases (up to 42 wt. %, see Fig 15a). This confirms the detrimental influence of V on the high temperature oxidation resistance of Ti-6Al-4V. To support our hypothesis for $V_2O_5$ formation and evaporation from the oxide scale leading to formation of pores, a microstructural characterisation of the oxide scale and the subsurface oxygen enriched layer was performed. Fig. 16 shows SEM micrograph of the oxide scale (Fig. 16 a) and corresponding optical micrograph of the oxygen enriched layer (Fig. 16 b) close to the surface of Ti-6Al-4V specimen after 500 hours at 700 ºC. The size and distribution of pores in the oxide scale (mainly in between the multi-layers of $TiO_2$ and $Al_2O_3$) are similar to the size and distribution of the V enriched $\beta$ phases present in the subsurface oxygen enriched layer. An interesting observation is that just below the large pores a sufficiently dense layer of $TiO_2$ is formed. Thus, it is considered that the porous oxide structure in combination with stresses developed in the oxide scale, cracking and delamination will allow elevated oxygen activity at the oxide/metal interface and consequently lead to suitable conditions for forming another dense layer of rutile. This will compromise the oxidation kinetics for both the oxide scale and oxygen enriched layer growth.

For Ti-6Al-2Sn-4Zr-2Mo, similar influence of Mo as of V in Ti-6Al-4V on the oxidation behaviour of Ti-6Al-2Sn-4Zr-2Mo is suggested. However, it is considered that due to the presence of more alloying elements (Sn, Zr, Si) that influence the oxidation behaviour, the phenomenon of $MoO_3$ formation and evaporation from the oxide scale responsible for the porous oxide structure is not as pronounced as in Ti-6Al-4V. More detailed description on the influence of these elements is provided later in this section.

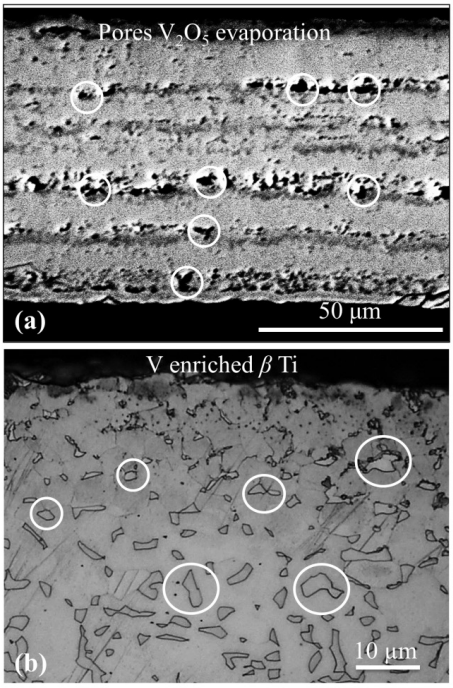


**Figure 16.** (a) SEM micrograph of the oxide scale and (b) optical micrograph of the subsurface oxygen enriched layer of Ti-6Al-4V after oxidation at 700 ºC for 500 hours. Note that the size and distribution of the pores is similar to the size and distribution of the V enriched $\beta$ phases present in the subsurface oxygen enriched layer.

***Influence of Fe on the oxidation behaviour.*** In the oxide scale formed on Ti-6Al-4V after oxidation at 700 ºC, the presence of Fe was identified. The XPS analysis reveals that Fe is present in the oxide scale either as $Fe^{3+}$ or $Fe^{2+}$ and/or a mixture of both. In earlier works by Shida *et al.* [59, 60], Fe was classified as a neutral element that does not significantly affect the oxidation resistance of Ti-Al alloys. However, since the effective ionic radii of six coordinated $Fe^{3+}$ (78 pm) and $Fe^{2+}$ (64 pm) are slightly lower than the six coordinated $Ti^{2+}$ (86 pm) and similar to $Ti^{3+}$ (67 pm) and $Ti^{4+}$ (61 pm), Fe preferably takes place in the substitutional sites of the rutile $TiO_2$ matrix [66]. Thus, it is considered that the doping of the rutile structure would result in lowering the oxygen diffusion through the oxide structure. Support for such belief of the effect of Fe on the oxygen diffusivity in rutile is the work of Sasaki *et al.* [67]. Based on theoretical calculations the authors showed that there is a significant drop of the oxygen diffusivity when Fe is present in the rutile structure at concentrations $\geq$ 0.35 at. %. In addition, they also suggested that Fe doping causes instability of the rutile oxide which results in formation of shear planes that obstruct the ion movements.

***Influence of Sn, Zr, and Si on the oxidation behaviour.*** Tin and zirconium are neutral alloying elements that provide better strength and creep resistance to the Ti alloys [1, 2, 4]. Si is also an important alloying element providing creep and oxidation resistance [1, 2, 4]. As shown in [61] the addition of third elements to Ti alloys enhances the oxidation resistance mainly via three mechanisms: (i) valence controlling mechanism, that includes inhibition of $TiO_2$ growth and promotion of $Al_2O_3$ formation and growth, (ii) diffusion barrier formation mechanism, that involves forming of a physical

barrier, i.e. layer on the substrate surface, that hinders oxygen diffusion and substrate elements, and (iii) modification mechanism, that involves promotion of $Al_2O_3$ formation in the initial stages of the oxide scale formation. In the present work, Sn, Zr and Si were also identified beside Al and Mo in oxide scale of Ti-6Al-2Sn-4Zr-2Mo. The XPS analysis of the oxide scale reveals that Sn, and Zr are present in the oxide scale of Ti-6Al-2Sn-4Zr-2Mo either in oxide or in metallic form. Comparison of the effective radii of six coordinated $Sn^{4+}$ (69 pm) and $Zr^{4+}$ (72 pm) with the six coordinated $Ti^{2+}$ (86 pm), $Ti^{3+}$ (67 pm) and $Ti^{4+}$ (61 pm) [66] clearly indicates that these elements have influence on the oxidation behaviour of Ti-6Al-2Sn-4Zr-2Mo via valence controlling mechanism that involves inhibition of the oxide scale growth and promoting dense $Al_2O_3$ protective layer formation, i.e. barrier for oxygen diffusion. Comparison of the thicknesses of the oxide scales formed on Ti-6Al-4V and Ti-6Al-2Sn-4Zr-2Mo subjected to the same oxidation conditions clearly evidence that the oxide growth in Ti-6Al-2Sn-4Zr-2Mo is hindered compared to Ti-6Al-4V (see Fig. 4f and Fig. 4h). In addition, from the SEM-EDS maps shown in Fig. 6 it can be clearly discerned that the $Al_2O_3$ layer formed is denser for Ti-6Al-2Sn-4Zr-2Mo than for Ti-6Al-4V. Thus, it may be concluded that the presence of Sn and Zr in the Ti-6Al-2Sn-4Zr-2Mo alloy promotes stable oxide growth and formation of compact $Al_2O_3$ protective layer which serves as barrier for oxygen diffusion. As mentioned before, it is suspected that Sn and Zr in combination with the observed self-diffusion of V and Mo have different influence on the mechanism for $Al_2O_3$ formation. It is considered that the formation of more compact and uniform $Al_2O_3$ layer in Ti-6Al-2Sn-4Zr-2Mo owes to the outward diffusion of Al from an inner layer of the alloy substrate, which is not the case for Ti-6Al-4V. Supportive results that clarify our belief for the different mechanism of $Al_2O_3$ formation between the alloys are the Al concentration profiles shown in Fig. 15. The Al concentration profiles clearly evidence that Al depletion occurs along the oxygen enriched layer of Ti-6Al-2Sn-4Zr-2Mo in contrast to the as-received material. Such depletion of the Al content in the oxygen enriched layer of Ti-6Al-4V has not been observed.

With regard to the oxide scale growth, it is considered that Sn and Zr might have the effect of oxide grain size refinement. Such influence on the oxide grain size would involve oxide grain nucleation that impedes the oxygen diffusion through the oxide scale. In fact, the grain size refinement can be clearly seen by comparing the oxide scale micrographs for Ti-6Al-4V and Ti-6Al-2Sn-4Zr-2Mo shown in Fig. 14. The oxide grain size of the Ti-6Al-2Sn-4Zr-2Mo is finer compared to Ti-6Al-4V. The influence of Si on the oxidation resistance of Ti-6Al-2Sn-4Zr-2Mo is considered to be tremendously important. It is considered that Si involves similar mechanisms as Sn and Zr. In particular, as shown in [61], Si promotes diffusion of Al in the oxide scale, stabilises Ti through reducing its activity and hinders outward diffusion of Ti, and improves adherence of the oxide scale to the alloy substrate. All of these mechanisms can be assigned to Si in the oxidation behaviour of Ti-6Al-2Sn-4Zr-2Mo. In fact, the effect of Si on the improved adherence of the oxide scale could explain the less pronounced spallation of the oxide scale as compared to Ti-6Al-4V (see Fig. 5). Based on all experimental facts it may be concluded that the more diverse chemical composition of Ti-6Al-2Sn-4Zr-2Mo enables higher oxidation resistance compared to Ti-6Al-4V.

***Oxygen enriched layer and alpha-case growth mechanism.*** During isothermal oxidation of titanium and its alloys at temperatures above 480 ºC oxygen dissolves into the free interstitial positions of the α-Ti hexagonal-closed packed (hcp) crystal structure and is thereby stabilising and hardening the $\alpha$ phase by solid solution strengthening mechanism.

Based on the oxidation study of the alloys in the present work, a mechanism for α-case growth is proposed. It has been discerned that at 700 ºC the α-case layer thickness follow similar trend as the weight gain results (see Fig. 2 and Fig. 11). Taking into account that the majority of the weight gain is due to oxide scale formation and growth, it is reasonable to consider that the subsurface layer must have had significant Ti depletion. Therefore, plausible hypothesis for the predominant mechanism for α-case layer growth would be inward interstitial diffusion of oxygen in the hcp crystal structure of α-

Ti followed by outward diffusion of Ti at the oxide/metal interface to form $TiO_2$. Fig. 17 shows comparison of the oxygen and Ti concentration profiles measured after oxidation at 700 ºC for 500 hours. The profiles show notable Ti depletion in the subsurface of the alloys. These results evidence our hypothesis for the growth mechanism.

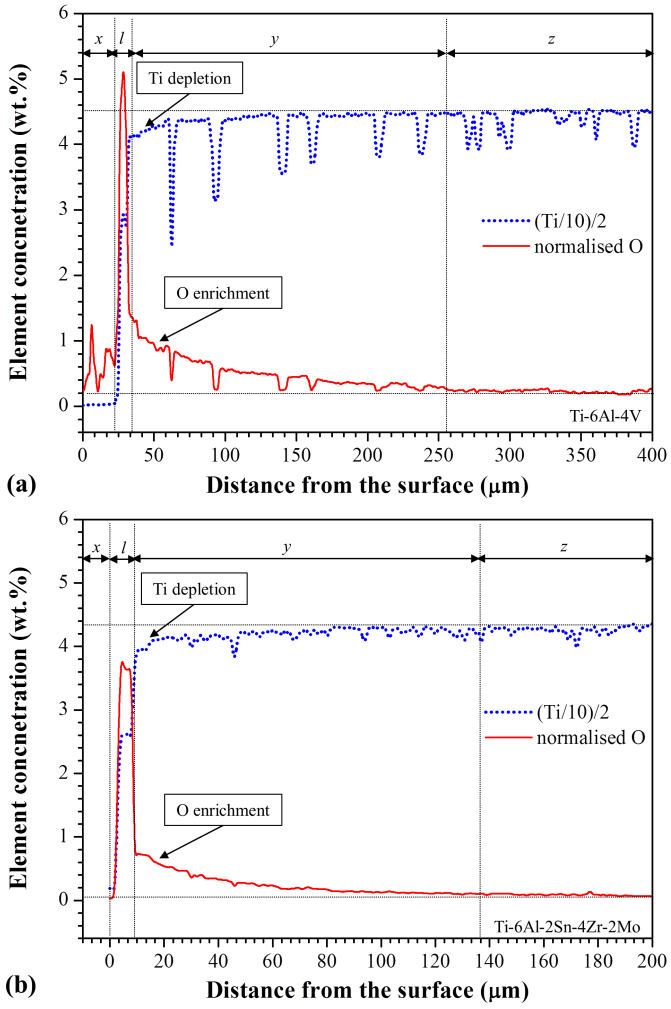


**Figure 17.** Comparison of the oxygen and titanium concentration profiles measured along the oxygen enriched layer thickness after oxidation at 700 ºC for 500 hours in (a) Ti-6Al-4V and (b) Ti-6Al-2Sn-4Zr-2Mo; *x*, *l*, *y* and *z* refer to the thickness of mount (Bakelite), the oxide scale, the oxygen enriched layer and alloy substrate, respectively.

## 4. Conclusions

In the present work the isothermal oxidation behaviour of Ti-6Al-4V and Ti-6Al-2Sn-4Zr-2Mo in the temperature range of 500-700 ºC in air was investigated and the following conclusions are made:

1. The Ti-6Al-2Sn-4Zr-2Mo alloy exhibits stronger oxidation resistance than Ti-6Al-4V.
2. The isothermal oxidation of the two alloys resulted in simultaneous formation of an oxide scale and an oxygen enriched layer.
3. The oxidation for both alloys mainly followed parabolic relationship, except at 700 ºC for oxidation times longer than 200 hours where transition from parabolic to linear oxidation rate occurred.
4. The activation energy for oxidation was calculated to be 278 kJ/mol for Ti-6Al-4V and 157 kJ/mol for Ti-6Al-2Sn-4Zr-2Mo.
5. The oxide scale on both alloys consisted of $TiO_2$ rutile type. The oxidation at 700 ºC resulted in porous oxide structure in both alloys. Multi-layered oxide scale structure consisting of $TiO_2$ and $Al_2O_3$ layers was observed in Ti-6Al-4V, whereas such multi-layered morphology of the oxide scale was absent in Ti-6Al-2Sn-4Zr-2Mo and only one double layer of $TiO_2$ and $Al_2O_3$ was observed.
6. The oxide scales formed at 700 ºC after 500 hours were doped with all main alloying elements present in respective alloy, i.e. Al and V for Ti-6Al-4V and Al, Sn, Zr and Mo for Ti-6Al-2Sn-4Zr-2Mo.
7. A re-distribution of the alloying elements in the microstructure occurred in both alloys. The $\beta$ phase became enriched with V and Fe in Ti-6Al-4V, and Mo in Ti-6Al-2Sn-4Zr-2Mo.
8. The alloying elements in Ti-6Al-4V (Al, V and Fe) and in Ti-6Al-2Sn-4Zr-2Mo (Al, Sn, Zr and Mo) played important roles for the oxidation behaviour. At 700 ºC for exposure times longer than 200 hours, V and Mo had strong impact on the oxidation behaviour of the alloys. Both elements were promoting faster oxidation kinetics (i.e. change from parabolic to linear behaviour) by enhancing the internal oxygen diffusion.

**Acknowledgments**

The authors kindly acknowledge the Erasmus Mundus Program through the European Joint Doctoral Program in Materials Science and Engineering (DocMASE, Grant number 512225-1-2010-1-DE-ERA MUNDUS-EMJD), the Swedish Foundation for Strategic Research (SSF), the Graduate School of Space Technology and the Aeronautical Research Engineering Programme (NFFP) for financial support. The authors would like to acknowledge GKN Aerospace Engine Systems, Sweden for its support during the research work and Francois Mattera for assisting in performing the oxidation experiments for Ti-6Al-2Sn-4Zr-2Mo. We would like to acknowledge Morten Raanes at Norwegian University of Science and Technology, Norway for performing the EPMA measurements and for fruitful discussions in evaluating the results. The assistance of the PhD student Daniel Hedman from Luleå University of Technology in mathematical modelling and fitting of the EPMA oxygen profiles is gratefully appreciated. We kindly acknowledge Montserrat Domínguez Escalante from the Centre for Research in NanoEngineering (CRNE) at the "Universitat Politècnica de Catalunya", Barcelona, Spain for performing the XPS measurements and for fruitful discussions in evaluating the results.

## References


[1] G. Lütjering, Titanium, second ed., Springer, Berlin 2007.

[2] C. Leyens, M. Peters, Titanium and titanium alloys fundamentals and applications, Wiley-VCH, Weinheim, 2003.

[3] R.R. Boyer, An overview on the use of titanium in the aerospace industry, Mater. Sci. Eng. A 213 (1996) 103-114.

[4] M.J. Donachie, Titanium a technical guide, second ed., Materials Park-ASM International, Ohio, 2000.

[5] A.M.M. García, Blisk Fabrication by Linear Friction Welding, in: E. Benini (Eds.), Advances in Gas Turbine Technology, InTech., China 2011, pp. 411-434.

[6] D. Eylon, S. Fujishiro, F.H. Froes, P.J. Postans, High-temperature titanium alloys-A review, J. Met. 1 (1984) 55-62.

[7] R.N. Shenoy, J. Unnam, R.K. Clark, Oxidation and embrittlement of Ti-6Al-2Sn-4Zr-2Mo alloy, Oxid. Met. 26 (1986) 105-124.

[8] J. Unnam, R. Shenoy, R. Clark, Oxidation of commercial purity titanium, Oxid. Met. 26 (1986) 231-252.

[9] J.L. Murray, Phase diagrams of binary titanium alloys, Materials Park-ASM International, Ohio, 1987.

[10] A.I. Kahveci, G.E. Welsch, Effect of oxygen on the hardness and alpha/beta phase ratio of Ti6A14V alloy, Scr. Metall. 20 (1986) 1287-1290.

[11] S. Sung, Y. Kim, Alpha-case formation mechanism on titanium investment castings, Mater. Sci. Eng. A 405 (2005) 173-177.

[12] D. Jordan, Study of alpha case formation heat treated Ti-6-4 alloy, Heat Treating Progr. 8 (2008) 45-47.

[13] C.E. Shamblen, T.K. Redden, Air contamination and embrittlement of titanium alloys, in: R.I. Jaffe, N.E. Promisel (Eds.), The Science, Technology and Application of Titanium, Pergamon Press, Oxford, 1968, pp. 199-208.

[14] C. Leyens, D. Weinem, M. Peters, W.A. Kaysser, Influence of long term annealing on tensile properties and fracture of near- alpha titanium alloy Ti-6Al-2.75Sn-4Zr-0.4Mo-0.45Si, Metall. Mater. Trans. 27A (1996) 1700-1708.

[15] R. Evans, R. Hull, B. Wilshire, The effects of alpha-case formation on the creep fracture properties of the high-temperature titanium alloy IMI834, J. Mater. Process. Technol. 56 (1996) 492-501.

[16] A.L. Pilchak, W.J. Porter, R. John, Room temperature fracture processes of a near-α titanium alloy following elevated temperature exposure, J. Mater. Sci. 47 (2012) 7235-7253.

[17] R. Gaddam, M.-L. Antti, R. Pederson, Influence of alpha-case layer on the low cycle fatigue properties of Ti-6Al-2Sn-4Zr-2Mo alloy, Mater. Sci. Eng. A 599 (2014) 51-56.

[18] C. Leyens, M. Peters, W.A. Kaysser, Intermetallic Ti-Al coatings for protection of titanium alloys: Oxidation and mechanical behavior, Surf. Coat. Technol. 94-95 (1997) 34-40.

[19] I. Gurrappa, A. Gogia, High performance coatings for titanium alloys to protect against oxidation, Surf. Coat. Technol. 139 (2001) 216-221.

[20] S. Frangini, A. Mignone, F. de Riccardis, Various aspects of the air oxidation behaviour of a Ti6Al4V alloy at temperatures in the range 600-700 °C, J. Mater. Sci. 29 (1994) 714-720.

[21] H.L. Du, P.K. Datta, D.B. Lewis, J.S. Burnell-Gray, Air Oxidation Behavior of Ti-6Al-4V Alloy Between 650 and 850 °C, Corros. Sci. 36 (1994) 631-642.

[22] H.L. Du, P.K. Datta, D.B. Lewis, J.S. Burnell-Gray, High temperature corrosion of titanium and Ti-6Al-4V alloy, Oxid. Met. 45 (1996) 507-527.

[23] M. Evans, A. Ward, Corrosion resistance of Ti-6246 for high power aeroengine compressor discs and blades, Mater. Sci. Technol. 17 (2001) 945-953.

[24] I. Gurrappa, On the mechanism of degradation of titanium alloy IMI 834 in an oxidizing atmosphere at elevated temperatures, Corros. Prev. Control. 49 (2002) 79-84.

[25] P.W.M. Peters, J. Hemptenmacher, C. Todd, Oxidation and stress enhanced oxidation of Ti-6-2-4-2, in: G. Lütjering, J. Albrech (Eds.), Titan-2003, Science and Technology IV, Wiley-VCH, Weinheim, 2003, pp. 2067-2074.

[26] Y. Sugiura, Growth behaviors of alpha cases in Ti-6Al-4V and Ti-10V-2Fe-Al alloys during high temperature heat treatment in air, in: G. Lütjering, J. Albrech (Eds.), Titan-2003, Science and Technology IV, Wiley-VCH, Weinheim, 2003, pp. 2051-2057.

[27] K.V.S. Srinadh, V. Singh, Oxidation behaviour of the near α-titanium alloy IMI 834, Bull. Mater. Sci. 27 (2004) 347-354.

[28] F. Pitt, M. Ramulu, Influence of grain size and microstructure on oxidation rates in titanium alloy Ti-6Al-4V under superplastic forming conditions, J. Mat. Eng. and Perform. 13 (2004) 727-734.

[29] I. Gurrappa, An oxidation model for predicting the life of titanium alloy components in gas turbine engines, J. Alloys Compd. 389 (2005) 190-197.

[30] Z.X. Zhang, H. Dong, T. Bell, B. Xu, The effect of treatment condition on boost diffusion of thermally oxidised titanium alloy, J. Alloys Compd. 431 (2007) 93-99.

[31] H. Guleryuz, H. Cimenoglu, Oxidation of Ti-6Al-4V alloy, J. Alloys Compd. 472 (2009) 241-246.

[32] S. Kumar, T.S. Narayanan, S.G.S. Raman, S. Seshadri, Thermal oxidation of Ti6Al4V alloy: Microstructural and electrochemical characterization, Mater. Chem. Phys. 119 (2010) 337-346.

[33] K.S. McReynolds, S. Tamirisakandala, A study on alpha-case depth in Ti-6Al-2Sn-4Zr-2Mo, Metall. Mat. Trans. A 42 (2011) 1732-1736.

[34] W. Jia, W. Zeng, X. Zhang, Y. Zhou, J. Liu, Q. Wang, Oxidation behavior and effect of oxidation on tensile properties of Ti60 alloy, J. Mater. Sci. 46 (2011) 1351-1358.

[35] R. Gaddam, B. Sefer, R. Pederson, M.-L. Antti, Study of alpha-case depth in Ti-6Al-2Sn-4Zr-2Mo and Ti-6Al-4V, IOP Conf. Series: Mater. Sci. Eng. 48 (2013) 012002.

[36] R. Gaddam, B. Sefer, R. Pederson, M.-L. Antti, Oxidation and alpha-case formation in Ti-6Al-2Sn-4Zr-2Mo alloy, Mater. Charact. 99 (2015) 166-174.

[37] Aerospace series-Test methods-Titanium and titanium alloys-Part 009-Determination of surface contamination (SS-EN 2003-009:2007), Swedish Standards Institute (2007).

[38] AMS 4911 L, Titanium alloy, sheet, strip, and plate 6Al-4V annealed (SAE-AMS/MAM) (2008).

[39] AMS 4976 G, Titanium alloy, forgings 6.0Al-2.0Sn-4.0Zr-2.0Mo solution and precipitation heat treated (SAE-AMS/MAM) (2008).

[40] N. Fairley, CasaXPS: Spectrum Processing Software for XPS, AES and SIMS, Version 2.3.17, Casa Software Ltd., Cheshire, UK, 2016, <http://www.casaxps.com/> (2005).

[41] P. Kofstad, High temperature corrosion, Elsevier Applied Science Publishers, Crown House, Linton Road, Barking, Essex IG 11 8 JU, UK, 1988.

[42] B. Pieraggi, Calculations of parabolic reaction rate constants, Oxid. Met. 27 (1987) 177-185.

[43] D. Poquillon, C. Armand, J. Huez, Oxidation and oxygen diffusion in Ti-6al-4V alloy: Improving measurements during SIMS analysis by rotating the sample, Oxid. Met. 79 (2013) 249-259.

[44] S.S. Jiang, K.F. Zhang, Study on controlling thermal expansion coefficient of ZrO2-TiO2 ceramic die for superplastic blow-forming high accuracy Ti-6Al-4V component, Materials and Design. 30 (2009) 3904-3907.

[45] G. Welsch, R. Boyer, E.W. Collings, Materials Properties Handbook: Titanium alloys, Materials Park-ASM International, Ohio, 1994.

[46] J. Chastain, R.C. King, J. Moulder, Handbook of X-ray photoelectron spectroscopy: a reference book of standard spectra for identification and interpretation of XPS data, Physical Electronics Eden Prairie, MN, 1995.

[47] W. Göpel, J. Anderson, D. Frankel, M. Jaehnig, K. Phillips, J. Schäfer, G. Rocker, Surface defects of TiO2 (110): A combined XPS, XAES AND ELS study, Surf. Sci. 139 (1984) 333-346.

[48] G. Rocker, W. Göpel, Titanium overlayers on TiO2 (110), Surf. Sci. 181 (1987) 530-558.

[49] T. Sham, M. Lazarus, X-ray photoelectron spectroscopy (XPS) studies of clean and hydrated TiO 2 (rutile) surfaces, Chem. Phy. Lett. 68 (1979) 426-432.

[50] J. Lausmaa, Surface spectroscopic characterization of titanium implant materials, J. Electron. Spectrosc. Relat. Phenom. 81 (1996) 343-361.

[51] T. Wittberg, J.D. Wolf, R.G. Keil, P.S. Wang, Low-temperature oxygen diffusion in alpha titanium characterized by Auger sputter profiling, J. Vac. Sci. Technol. A 1 (1983) 475-478.

[52] D. Gupta, S. Weinig, Interactions between interstitial and substitutional solutes in an HCP lattice, Acta Metall. 10 (1962) 292-298.

[53] P. Kofstad, Note on the defect structure of rutile (TiO2), J. Less Comm. Met. 13 (1967) 635-638.

[54] P. Kofstad, Nonstoichiometry, diffusion, and electrical conductivity in binary metal oxides, Wiley-Interscience New York, 1972.

[55] P. Kofstad, P. Anderson, O. Krudtaa, Oxidation of titanium in the temperature range 800-1200 °C, J. Less Common Met. 3 (1961) 89-97.

[56] A.M. Chaze, C. Coddet, Influence of aluminium on the oxidation of titanium between 550 and 750 °C, J. Less Common Met. 157 (1990) 55-70.

[57] R. Perkins, K. Chiang, G. Meier, Formation of alumina on Ti-Al alloys, Scripta Metall. 21 (1987) 1505-1510.

[58] S. Becker, A. Rahmel, M. Schorr, M. Schütze, Mechanism of isothermal oxidation of the intermetallic Ti-Al and of Ti-Al alloys, Oxid. Met. 38 (1992) 425-464.

[59] Y. Shida, H. Anada, The influence of ternary element addition on the oxidation behaviour of TiAl intermetallic compound in high temperature air, Corros. Sci. 35 (1993) 945-953.

[60] Y. Shida, H. Anada, The effect of various ternary additives on the oxidation behavior of TiAl in high-temperature air, Oxid. Met. 45 (1996) 197-219.

[61] J. Dai, J. Zhu, C. Chen, F. Weng, High temperature oxidation behavior and research status of modifications on improving high temperature oxidation resistance of titanium alloys and titanium aluminides: A review, J. Alloys Compd. 685 (2016) 784-798.

[62] M. Enomoto, The O-Ti-V system (oxygen-titanium-vanadium), J. Phase Equilib. 17 (1996) 539-545.

[63] D.J. Simbi, J.C. Scully, The effect of residual interstitial elements and iron on mechanical properties of commercially pure titanium, Mater Lett. 26 (1996) 35-39.

[64] R.P. Elliott, Diffusion in titanium and titanium alloys, 1962.

[65] E. Gulbransen, K. Andrew, F. Brassart, Vapor pressure of molybdenum trioxide, J. Electrochem. Soc. 110 (1963) 242-243.

[66] R.D. Shannon, Revised effective ionic radii and systematic studies of interatomic distances in halides and chalcogenides, Acta Cryst. 32 (1976) 751-767.

[67] J. Sasaki, N. Peterson, L. De Jonghe, Fast diffusion of iron in single-crystal rutile and iron doped rutile, Mater. Res. Soc. Symp. Ptoc. 24 (1983) 39.

## *PAPER IV*

*Evaluation of the bulk and alpha-case layer properties in Ti-6Al-4V at micro- and nano-metric length scale*

**Authors:**

**Birhan Sefer**, Joan Josep Roa, Antonio Mateo, Robert Pederson, Marta-Lena Antti

**Published in:**

Proceedings of the 13th World Conference on Titanium, John Wiley & Sons Inc., Hoboken, New Jersey, 2016, pp. 1619-1624.

**Proceedings of the 13th World Conference on Titanium**
*Edited by: Vasisht Venkatesh, Adam L. Pilchak, John E. Allison, Sreeramamurthy Ankem, Rodney Boyer, Julie Christodoulou, Hamish L. Fraser, M. Ashraf Imam, Yoji Kosaka, Henry J. Rack, Amit Chatterjee, and Andy Woodfield*
***TMS (The Minerals, Metals & Materials Society), 2016***

# EVALUATION OF THE BULK AND ALPHA-CASE LAYER PROPERTIES IN Ti-6Al-4V AT MICRO- AND NANO-METRIC LENGTH SCALE

Birhan Sefer[1,2], Joan Josep Roa[2], Antonio Mateo[2], Robert Pederson[1,3], Marta-Lena Antti[1]
[1]Division of Materials Science, Luleå University of Technology, S-97187 Luleå, Sweden
[2]Department of Materials Science, Universitat Politècnica de Catalunya, Avda. Diagonal 647, 08028 Barcelona, Spain
[3]Research and Technology Centre, GKN Aerospace Engine Systems, S-46181 Trollhättan, Sweden

Keywords: Titanium alloy, Heat treatment, Alpha-case layer, Hardness, Nanoindentation, Electron Back-scattered diffraction, Phase transformation.

**Abstract**

In the present study the hardness of individual alpha ( )-Ti grains in Ti-6Al-4V was measured by nanoindentation using Berkovich tip indenter. Additionally, alpha-case layer was induced by performing isothermal heat treatment at 700 °C in air for 500 hours. The average hardness of the -Ti grains found in the bulk material and in the alpha-case layer were 6.7 ± 0.7 GPa and 9.4 ± 1.4 GPa, respectively. The high hardness of the -Ti grains in the alpha-case layer is due to solid solution strengthening caused by interstitial oxygen diffusion. The thickness of the developed alpha-case layer was estimated metallographically and compared with that measured from a hardness profile performed along the layer. Moreover, electron back-scattered diffraction was used to determine the local crystallographic orientation, the texture of the alloy microstructure, as well as phase fraction changes where the nanoindentation measurements were performed.

## *PAPER V*

*Chemical milling effect on the low cycle fatigue properties of cast Ti-6Al-2Sn-4Zr-2Mo alloy*

**Authors:**

**Birhan Sefer**, Raghuveer Gaddam, Joan Josep Roa, Antonio Mateo, Marta-Lena Antti, Robert Pederson

**Published in:**

International Journal of Fatigue 92 (2016) 193-202.

International Journal of Fatigue 92 (2016) 193–202

Contents lists available at ScienceDirect

International Journal of Fatigue

journal homepage: www.elsevier.com/locate/ijfatigue

# Chemical milling effect on the low cycle fatigue properties of cast Ti–6Al–2Sn–4Zr–2Mo alloy

Birhan Sefer [a,b,⇑], Raghuveer Gaddam [a,c], Joan Josep Roa [b], Antonio Mateo [b], Marta-Lena Antti [a], Robert Pederson [a]

[a] Division of Materials Science, Luleå University of Technology, S-97187 Luleå, Sweden
[b] Department of Materials Science, Universitat Politècnica de Catalunya, Av. Diagonal 647, Barcelona, Spain
[c] Sandvik Materials Technology, Sandviken, S-81181, Sweden

article info

*Article history:*
Received 23 February 2016
Received in revised form 3 July 2016
Accepted 4 July 2016
Available online 5 July 2016

*Keywords:*
Titanium alloy
Chemical milling
Pitting corrosion
Low cycle fatigue
Fractography

abstract

The current research work presents the chemical milling effect on the low cycle fatigue properties of cast Ti–6Al–2Sn–4Zr–2Mo alloy. Chemical milling treatment is one of the final steps in manufacturing titanium alloy components that removes the brittle alpha-case layer formed during various thermal processes. The treatment includes immersion of the components in solutions containing hydrofluoric (HF) and nitric ($HNO_3$) acids in relevant molar ratios. Although this treatment demonstrates advantages in handling components with complex net geometries, it may have detrimental effects on the surface, by introducing pitting and/or intergranular corrosion and thereby adversely affecting in particular the fatigue strength. The first series of specimens were tested in as-machined condition. Two more series were, prior to fatigue testing, subjected to 5 and 60 min chemical milling treatment. It was found that the fatigue lives were substantially decreased for the chemically treated specimens. The fractographic investigation of all mechanically tested samples revealed multiple fatigue crack initiation sites in the chemically milled samples. These cracks were located either at the prior beta grain boundary or the prior beta grain boundary triple joints. The prior beta grain boundaries were found to have deep ditch-like appearance which depth increased with increasing milling time. These ditch-like grain boundaries acts as stress raisers and thereby promote early fatigue crack initiation and thus lower fatigue life.





⇑ Corresponding author at: Division of Materials Science, Luleå University of Technology, S-97187 Luleå, Sweden.
*E-mail address:* birhan.sefer@ltu.se (B. Sefer).
http://dx.doi.org/10.1016/j.ijfatigue.2016.07.003
0142-1123/

## *PAPER VI*

*Corrosion behaviour of cast Ti-6Al-4V and Ti-6Al-2Sn-4Zr-2Mo alloys in hydrofluoric-nitric acid solutions*

**Authors:**

**Birhan Sefer**, Illia Dobryden, Nils Almqvist, Robert Pederson, Marta-Lena Antti

**Submitted for publication.**

# Corrosion behaviour of cast Ti-6Al-4V and Ti-6Al-2Sn-4Zr-2Mo alloys in hydrofluoric-nitric acid solutions

Birhan Sefer [a,b*], Illia Dobryden [a,c], Nils Almqvist [a], Robert Pederson [a,d], Marta-Lena Antti [a]

[a]Division of Materials Science, Luleå University of Technology, S-97187 Luleå, Sweden
[b]Department of Materials Science and Metallurgical Engineering, Universitat Politècnica de Catalunya, Av. Diagonal 647, 08028 Barcelona, Spain
[c]Division of Surface and Corrosion Science, KTH Royal Institute of Technology, S-100 44 Stockholm, Sweden
[d]Research and Technology Centre, GKN Aerospace Engine Systems, S-46181 Trollhättan, Sweden
*Corresponding author, e-mail: birhan.sefer@ltu.se; phone: +46(0)920492358; +46(0)735630494

**Abstract**

The corrosion behaviour of cast Ti-6Al-4V and Ti-6Al-2Sn-4Zr-2Mo in hydrofluoric-nitric solutions with 1:3 and 1:11 molar ratios was investigated using electrochemical and atomic force microscopy (AFM). Faster corrosion rate in 1:3 solution was measured for Ti-6Al-4V than for Ti-6Al-2Sn-4Zr-2Mo, whereas in 1:11 solution Ti-6Al-2Sn-4Zr-2Mo exhibited higher corrosion rate. Scanning kelvin probe force microscopy (SKPFM) measurements revealed difference in the Volta-potential between the α-laths and the β-Ti phase in the Widmansttäten microstructure indicating operation of micro-galvanic cells between the micro constituents. The AFM topography measurements demonstrated faster corrosion of the α-Ti phase compared to the β-Ti phase, in both alloys. In 1:3 solution higher α/β height difference was measured in Ti-6Al-4V, whereas in 1:11 solution the difference was higher in Ti-6Al-2Sn-4Zr-2Mo. The results revealed that the corrosion behaviour is controlled by the microscopic corrosion behaviour of the individual micro constituents.

**Keywords:** Titanium alloys; Hydrofluoric-nitric solution; Micro-galvanic corrosion; Potentiodynamic polarisation; AFM; SKPFM.

## 1. Introduction

Ti-6Al-4V (Ti-64) and Ti-6Al-2Sn-4Zr-2Mo (Ti-6242) are two important titanium alloys used in the aerospace industry for manufacturing of aero-engine components. Both alloys have high specific strength and excellent corrosion resistance [1]. These alloys are commonly employed for manufacturing aero-engine components for sections in the engine where the temperature during service does not exceed 300 ºC and 450 ºC for Ti-64 and Ti-6242, respectively [2]. The manufacturing process of titanium alloy components for aerospace applications normally involves different thermo-mechanical treatments that are carried out at elevated temperatures and in oxygen containing environments [3]. In such conditions, the titanium alloys are highly reactive with oxygen and it results in formation of oxide on the metal surface and oxygen enriched subsurface layer commonly referred as “alpha-case” [4-7]. Alpha-case is a continuous hard and brittle layer that has detrimental effect on important mechanical properties of titanium alloys such as ductility, fracture toughness and fatigue strength [8-11]. Therefore, it is of high importance to eliminate this layer, especially on components that are subjected to dynamic loading conditions during service. One of the conventional industrial methods used to remove alpha-case is processing of the components in corrosive solutions that contain mixtures of hydrofluoric (HF) and nitric

($HNO_3$) acids. This method is also known as pickling or chemical milling [12]. The treatment involves immersion of the component in the acidic solution under closely controlled conditions. The component is kept in the solution for a specified time, which is long enough to dissolve the entire alpha-case layer, but short enough to maintain the tolerance of the final component geometry within specification. Normal processing time for chemical milling is between 5-60 minutes and during this time typically 5-40 µm material from the surface of the components is removed.

The chemical milling of the oxide and the alpha-case layer is complicated and involves a combination of chemical and electrochemical reactions occurring at the metal/solution interface. The processes taking place on the metal surface can be described trough the following reactions [13]:

$$TiO_2(s) + 6HF(aq) \rightarrow H_2TiF_6(aq) + 2H_2O(l) \quad (1)$$

$$Ti(s) + 6HF(aq) \rightarrow H_2TiF_6(aq) + 2H_2(g) \quad (2)$$

$$3H_2(g) + 2HNO_3(aq) \rightarrow 4H_2O(l) + 2NO(g) \quad (3)$$

$$3Ti(s) + 18HF(aq) + 4HNO_3(aq) \rightarrow 3H_2TiF_6(aq) + 8H_2O + 4NO(g) \quad (2 + 3)$$

$$3Ti(s) + 10HNO_3(aq) \rightarrow 3TiO(NO_3)_2(s) + 5H_2O(l) + 4NO(g) \quad (4)$$

Reaction (1) results in dissolution of oxide scale and leads to formation of soluble titanium hexa fluoro complexes. Once the oxide is entirely dissolved, the bare titanium metal is exposed to the hydrofluoric acid. In such condition, the metal will start reacting with the acid according reaction (2). Similar as in reaction (1), the reaction (2) results in formation of titanium hexa fluoro complexes and hydrogen gas [14]. The hydrogen gas may cause hydride formation which could lead to hydrogen embrittlement that dramatically deteriorates important mechanical properties of the component during service. Therefore, in order to hinder the hydrogen gas formation a strong oxidising acid, $HNO_3$ is used in combination with the HF acid. The role of $HNO_3$ acid is to prevent hydrogen gas formation. The mixture of HF-HNO3 acid solution results in formation of hexa fluoro complexes without hydrogen gas formation (*see reaction (2 + 3)*). Moreover, $NO_x$ gas (i.e. mixture of NO and $NO_2$) is also formed. The $HNO_3$ acid also oxidises the alloy surface, which results in formation of a passive film of $TiO_2$. The process of oxidising the titanium alloy surfaces by $HNO_3$ acid and formation of passive $TiO_2$ film is represented by reaction (4). The formed passive film is dissolved by HF and this leads to formation of soluble titanium hexa fluoro complexes. The reaction (2 + 3) is taking place continuously on the metal surface and this provides continuous material dissolution from the component surface.

The reaction between the titanium alloy surface and the HF-$HNO_3$ solution depends on many parameters such as concentration ratio between the HF and $HNO_3$ acids, temperature, processing time, stirring rate and aging of the solution. Through maintaining a precise control of all these parameters, a uniform and constant removal rate of material from the surface can be achieved. However, occasionally undesired consequences such as localised corrosion in form of crevice, pitting and/or intergranular corrosion on the components surface may occur [15]. Surface defects formed as a result of localised corrosion phenomena may be detrimental to the fatigue strength of the titanium alloys. In fact, our recent work [16] showed that chemical milling treatment induces localised corrosion, which significantly reduced the low cycle fatigue strength of the investigated Ti-6Al-2Sn-4Zr-2Mo alloy. Therefore, it is important to understand and address these corrosion phenomena at a microscopic scale for titanium alloys.

The corrosion behaviour of titanium and Ti-6Al-4V alloy in HF-$HNO_3$ solution have been studied by several authors [13,14,17-20]. Studies for Ti-6Al-4V alloy in other solutions than HF-$HNO_3$ acids can be also found [21-23]. However, studies on Ti-6Al-2Sn-4Zr-2Mo alloy are limited [24]. Among the most notable corrosion studies of titanium in HF-$HNO_3$ solutions are the works of Lin et al.[13], Say et al. [14] and Sutter et al. [17-19]. The authors used conventional electrochemical methods in combination with spectrometry and spectroscopy to reveal the corrosion behaviour and the corrosion products in different ratios of the HF-$HNO_3$ solution. However, these conventional electrochemical methods are lacking detailed insight on the corrosion phenomena at microscopic scale, which is crucial for resolving the corrosion behaviour of different micro constituents and/or phases in alloys that consist of two and more micro constituents and/or phases. It is therefore necessary to apply other methods to improve the understanding of the corrosion phenomena at microscopic scale.

Atomic force microscopy (AFM) is one useful technique [25]. AFM can perform accurate in situ or ex situ measurements of the metal surface roughness and height changes due to the interaction of the metal surface with corrosive solutions [23]. Moreover, the AFM method known as Scanning Kelvin Probe Force Microscopy (SKPFM) provides accurate mapping of the Volta-potential distribution across the passive metal surface [25,26] and also accurate measure of the local work function (*WF*), i.e. the minimum required work for electron extraction from within the sample to a distance just outside the sample. The possibility to map the Volta-potential with high resolution and on a well-controlled small scale, less than submicron size (0.1 μm), was shown to be highly useful to investigate localised corrosion phenomena of Al and Mg alloys [25-27] and also on Ti-6Al-4V alloy [28].

The main objective of the present work was to study the corrosion behaviour of Ti-6Al-4V and Ti-6Al-2Sn-4Zr-2Mo alloys in HF-$HNO_3$ solutions with different concentration ratios using electrochemical and AFM techniques. The chemical composition of HF and $HNO_3$ selected in this work, i.e. their respective molar concentration ratios (1:3 and 1:11), simulates the industrial conditions for chemical milling treatment that is normally applied during the manufacturing of titanium alloy components for different applications.

## 2. Material and methods

### *2.1 Material and sample preparation*

Two titanium alloys were investigated, the α+β alloy Ti-6Al-4V (Ti-64) and the near-α alloy Ti-6Al-2Sn-4Zr-2Mo (Ti-6242), both in cast condition. The chemical compositions of the alloys were analysed using inductively coupled plasma mass spectrometry (ICP-MS) and the values are given in Table 1. All test samples were cut out into disk shape with 3-4 mm height and 6.5 mm diameter using electric discharge machining. After cutting, one face of the sample was ground and polished using colloidal silica with particle size of 0.05 μm until mirror surface finish was achieved. The surface area of the polished face of the samples was 0.33 $cm^2$. The polishing of the samples was followed by ultrasonic cleaning for 15 minutes in acetone, rinsing with ethanol and drying in air.

**Table 1**
Chemical composition in wt. % of the two titanium alloys investigated in the present work.

| | Al | V | Sn | Zr | Mo | N | O | C | H | Fe | Si | Y | Ti |
|---|---|---|---|---|---|---|---|---|---|---|---|---|---|
| Ti-64 | 6.75 | 4.34 | - | - | - | 0.05 | 0.20 | 0.08 | 0.015 | 0.185 | - | - | Bal. |
| Ti-6242 | 6.50 | - | 2.20 | 4.40 | 2.10 | 0.05 | 0.15 | 0.05 | 0.0125 | 0.055 | 0.10 | <0.0001 | Bal. |

*2.2 Microscopy*

The samples were prepared by conventional etching procedure including swabbing the surface of mirror polished samples for 10 seconds with Kroll's reagent (1 ml HF (40 %) + 2 ml $HNO_3$ (65 %) in 100 ml distilled water). Optical microscope (Nikon Eclipse model MA200) and scanning electron microscope (SEM JEOL JSM-6460LV) were used to characterise the microstructure of the two investigated alloys.

SEM imaging was performed using secondary electrons with an accelerating voltage of 20 kV and probe current of 84 μA. The chemical composition of the microstructural constituents was analysed by energy dispersive spectrometer (EDS).

*2.3 Preparation of the hydrofluoric-nitric acid solutions*

The HF-$HNO_3$ solutions were prepared from per analysis, hydrofluoric acid (HF = 40 %) and nitric acid ($HNO_3$ = 65 %) and distilled water. Two HF-$HNO_3$ solutions with different molar concentration ratios acids were used; 1:3 ratio consisting of 0.1 M HF and 0.3 M $HNO_3$ and 1:11 consisting of 0.1 M HF and 1.1 M $HNO_3$.

*2.4 Electrochemical measurements*

Potentiodynamic polarisation was used to study the behaviour in HF with concentration 0.1 M and in HF-$HNO_3$ solutions with 1:3 and 1:11 concentration ratios. The measurements were carried out on freshly polished sample surfaces in naturally-aerated HF-$HNO_3$ acid solutions using potentiostat Autolab PG-STAT302N controlled with Nova 2.0 software (Metrohm Autolab, Netherlands). Fig. 1 shows the experimental setup for the potentiodynamic polarisation measurements consisted of polarisation and reference cell connected through salt bridge (Teflon U-tube with diameter of 4 mm field with agar that contains dissolved $KNO_3$) and potentiostat.

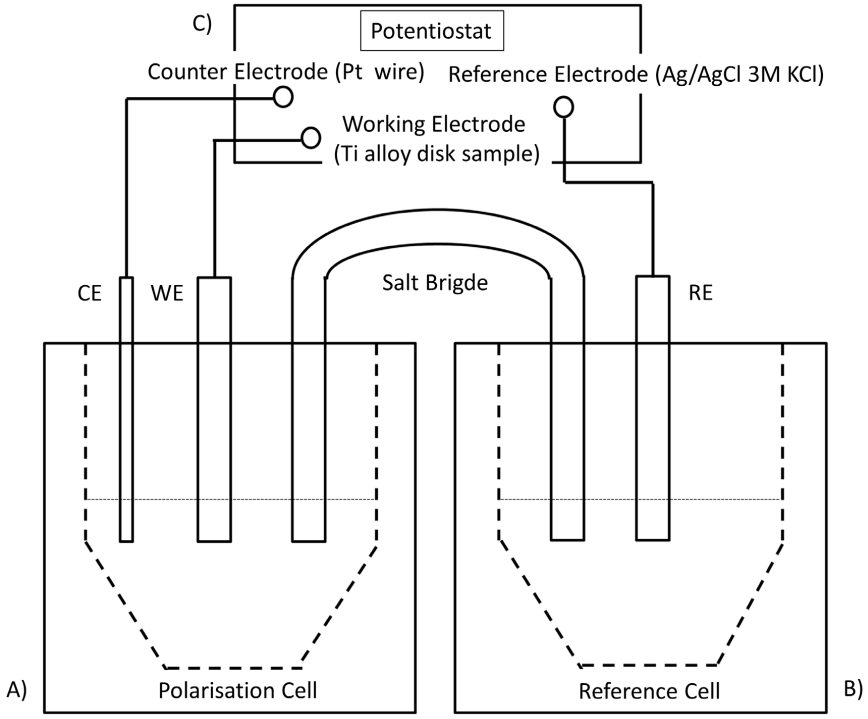


**Figure 1.** Experimental setup for the potentiodynamic polarisation measurements: A) polarisation cell B) reference cell connected through salt bridge and C) potentiostat.

The cells were fabricated from polytetrafluoroethylene (PTFE), Teflon material resistant to HF acid. A standard three-electrode system consisting of titanium alloy disk sample as working electrode (WE), platinum wire as a counter electrode (CE), and Ag/AgCl (3 M KCl) as reference electrode (RE). The titanium alloy disk samples were embedded into fabricated PTFE rods with electrical contact. The electrolyte used in the reference cell was 1 M KCl, whereas the polarisation cell contained the HF-$HNO_3$ testing solutions. Freshly prepared HF-$HNO_3$ acid solutions were used for each measurement. The scanning rate used for the polarisation measurments was 1 mV/s. All measurements were performed at temperature of 22-23 ºC.

The samples were left for 5 minutes in the testing solutions to stabilise before the polarisation measurements were conducted. Prior to the polarisation measurements, the open circuit potential ($E_{OCP}$) was monitored for 10 minutes. Note that a fixed derivative limit (dE/dt = $1 \cdot 10^{-6}$ V/s) was set for recording the $E_{OCP}$. The derivative limit determines the time when the potentiostat will automatically stop recording the potential.

*2.5 Atomic Force Microscopy (AFM)*

Contact mode AFM (Solver AFM, NT-MDT) equipped with a 100 µm probe scanner with capacitive position sensors in all three directions was used to study the topography of the surfaces after immersion in

$HF\text{-}HNO_3$ solutions with 1:3 and 1:11 molar concentration ratios for 0, 1, 5 and 10 minutes, respectively. A selected surface area of each sample was imaged in order to obtain information of the topography before and after each immersion. A protocol for performing the AFM measurements was developed consisting of the following steps:

1. *Marking the sample surfaces.* On each sample a surface area of interest was selected and marked by four indentions using a Vickers microhardness testing machine. The indents were used as orientation tool in order to distinguish and keep track of the surface area at microscopic scale after immersing the samples for different times into the $HF\text{-}HNO_3$ solutions. The typical distance between the indents was around 300-400 μm.
2. *AFM imaging.* The AFM height measurements were performed on mirror polished samples and surface areas of 40 x 40 μm at 512 x 512 pixel resolution prior to immersing the samples into the $HF\text{-}HNO_3$ solutions. A PNP-DB type of cantilever (Nanosensors) was used with a length of 100 μm and a nominal force constant of 0.48 N/m with a specified tip radius of less than 10 nm. The measurements were performed in close-loop regime in x- and y-direction to reduce the non-linearity and cross-talk effect. Typical scan velocities of 20-50 μm/s were used depending on the surface roughness conditions. The topography data obtained for the mirror polished samples were used as reference for the two alloys before immersion in the acid solutions.
3. *Immersion of the samples in the $HF\text{-}HNO_3$ solutions.* The samples were immersed into freshly prepared 15 ml $HF\text{-}HNO_3$ solutions for the above specified time intervals. The immersion of the samples into the testing solutions was followed by standard cleaning procedure involving rinsing with distilled water, ultrasonic cleaning for 15 minutes in acetone, rinsing the samples with ethanol and drying in air.
4. *Post immersion AFM imaging.* After immersion of the samples the area of interest was identified with help of the optical microscope equipped in the AFM instrument followed by AFM imaging. The post immersion AFM measurements were also conducted on areas of 40 x 40 μm.

Steps 3 and 4 were repeated consequently on each Ti-64 and Ti-6242 sample after immersion in $HF\text{-}HNO_3$ solutions for 1, 5 and 10 minutes, respectively.

To determine the height differences between the α- and β-Ti phases, raw AFM images were first subjected to a line fit in the fast scan direction followed by a second order plane fit to remove any influence from the scanner bow. The height difference was then evaluated as the difference in height between the two peaks appearing in the image height histogram.

*2.6 Scanning Kelvin Probe Force Microscopy (SKPFM)*

The SKPFM measurements were performed with an Ntegra Prima AFM (NT-MDT) in a two-pass technique and a 100 μm sample scanner in closed-loop operation at ambient humidity of about 30-40 %. The tip was lifted to a 100 nm distance above the surface to minimize the effect of topography on the measured Volta-potential between the tip and surface. For the SKPFM measurements, an n-type silicon cantilever NSG01 (NT-MDT) with PtIr conductive coating was used with a nominal spring constant of 5.1 N/m and a nominal tip curvature radius of 35 nm. The work function (*WF*) of the probe was calibrated using freshly cleaved highly oriented pyrolytic graphite (HOPG) substrate and it was found to be 4.67 eV. The typical scan velocity was about 50 μm/s. The same probe was used for each set of measurement and its work function was calibrated on the HOPG substrate. The typical scan velocity was about 48 μm/s. The SKPFM Volta-potential difference images in this study were not inverted and are shown as were measured (i.e. as raw data), similar as presented previously in [29]. Thus, in the non-inverted data, the

lower measured Volta-potential corresponds to nobler material [29]. The Volta-potentials were determined from the non-inverted and raw SKPFM data maps by applying the histogram tool (Nova, NT-MDT software) on the selected areas corresponding to the α- and β-Ti phases. The histogram tool provides an accurate determination of the mean value for the Volta-potential.

## 3. Results and Discussion

### *3.1 Microstructure*

Fig. 2 shows optical and SEM micrographs of the microstructure of Ti-64 (Fig. 2a and Fig. 2b) and Ti-6242 (Fig. 2c and Fig. 2d). Both alloys have completely transformed beta structures consisting of large prior β grains with α-colonies inside, well known for high fracture toughness but lower tensile and fatigue strengths. This type of microstructure is known as lamellar and is normally referred to as Widmanstätten type of microstructure. Moreover, the α-colonies consist of parallel *α*-laths separated with thin β-Ti phase interfaces. Note that in the optical micrographs the bright laths represent the *α*-Ti phase with hexagonal close packed (HCP) crystal structure, whereas the dark interfaces between the laths are representing the β-Ti phase with body centred cubic-(BCC) crystal structure. On the SEM micrographs (Fig. 2b and 2d) α-Ti and β-Ti phases are marked and show opposite contrast with respect to the optical micrographs.

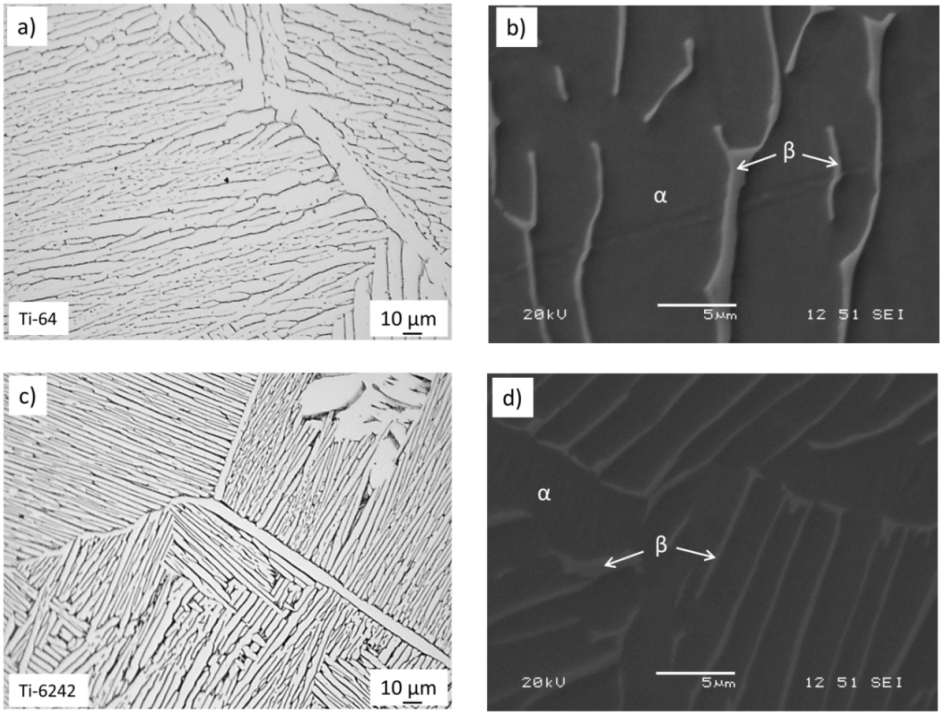


**Figure 2.** Widmanstätten microstructure in cast Ti-64 a) optical micrograph b) SEM micrograph and in cast Ti-6242 c) optical micrograph d) SEM micrograph.

*3.2 Electrochemical study*

Recording the open circuit potential ($E_{OCP}$) allows studying metal stability in various corrosive solutions. This type of experiment provides measurement of the time during which the metal will form a stable passive oxide film on the surface protecting the metal against corrosion [30]. In principle, a change of the measured potential with time to positive direction (nobler potential) indicates formation of a passive film on the metal surface, whereas a steady potential indicates that the passive film remains unimpaired and protective. Furthermore, if the potential change to negative direction after some time then the passive film has lost its protective nature and corrosion takes place [21].

Fig. 3 shows the evolution of $E_{OCP}$ as a function of immersion time recorded for Ti-64 and Ti-6242 when immersed in 0.1 M HF and in HF-$HNO_3$ solutions with 1:3 and 1:11 molar concentration ratios. In all solutions tested and for both alloys the $E_{OCP}$ changed to nobler values with respect to time with exception for Ti-64 in 1:11 concentration ratio of the HF-$HNO_3$ solution, where a drop of the potential was recorded during the first 60-80 seconds. However, after prolonged time the $E_{OCP}$ changed to positive direction (*see Fig. 3e*). The change of the $E_{OCP}$ to more positive values indicates formation of passive films of $TiO_2$ on the surface of the samples, which protects the alloys against corrosion and promotes improved corrosion resistance. In all three solutions different immersion times were required to obtain stable potentials. The recorded $E_{OCP}$ values and the respective immersion times to obtain stable potential for Ti-64 and Ti-6242 in all testing solutions are shown in Table 2.

**Table 2**

Open circuit potentials ($E_{OCP}$) and respective immersion times recorded for Ti-64 and Ti-6242 alloys in HF and in HF-$HNO_3$ solutions with 1:3 (0.1 M HF + 0.3 M $HNO_3$) and 1:11 (0.1 M HF + 1.1 M $HNO_3$) molar concentration ratios.

| | Ti-64 | | Ti-6242 | |
|---|---|---|---|---|
| Solution | $E_{OCP}$ (mV) | $t$ (s) | $E_{OCP}$ (mV) | $t$ (s) |
| HF | - 975 | 600 | - 782 | 600 |
| HF-$HNO_3$ (1:3) | - 216 | 250 | - 147 | 390 |
| HF-$HNO_3$ (1:11) | - 135 | 470 | - 252 | 220 |

In 0.1 M HF solution, the measured $E_{OCP}$ did not reach stable potential even after 600 seconds immersion time for any of the alloys. However, in 1:3 and 1:11 HF-$HNO_3$ solutions stable potentials were measured for both the alloys at times shorter than the maximum measuring time of 600 seconds (*see Table 2*). The nobler potential recorded for Ti-6242 in 0.1 M HF solution reveals that a stable passive surface film of $TiO_2$ is formed easier than on Ti-64.

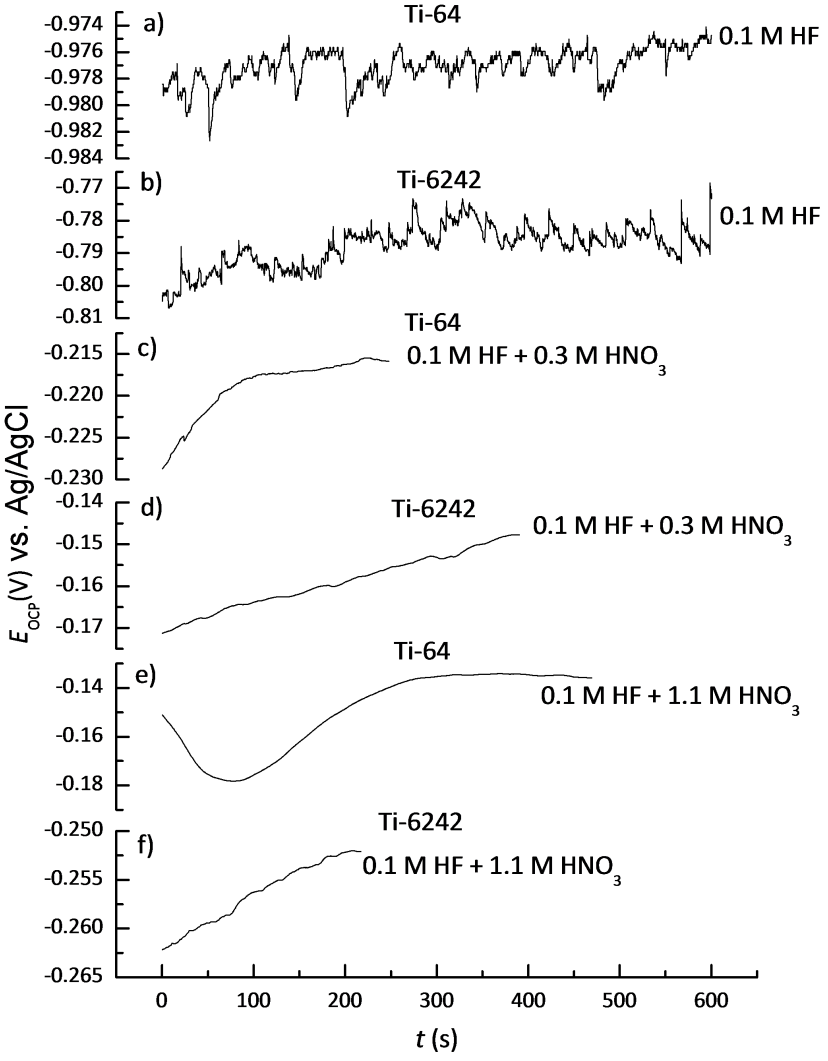


**Figure 3.** Open circuit potential values ($E_{OCP}$) versus time for Ti-64 and Ti-6242 recorded after 5 minutes stabilisation of the samples in the testing HF-$HNO_3$ acid solutions, a) and b) 0.1 M HF; c) and d) 0.1 M HF + 0.3 M $HNO_3$ and e) and f) 0.1 M HF + 1.1 M $HNO_3$ solutions.

In 1:3 HF-$HNO_3$ solution the $E_{OCP}$ for the two alloys changed to significantly more positive values compared to the 0.1 M HF solution (*see Table 2*). This is considered to be due to the strong oxidising capacity of the $HNO_3$ acid, promoting the formation of a passive surface film of $TiO_2$ (*see reaction (4) in Introduction*). Similar as in the HF solution, the recorded $E_{OCP}$ for Ti-6242 was nobler compared to the Ti-64 alloy. This indicates that in this HF-$HNO_3$ solution (1:3 molar concentration ratio) the passivation of Ti-6242 is easier compared with the Ti-64 alloy. The immersion time required to obtain stable potential was shorter than 600 seconds for both alloys (*see Table 2*).

In 1:11 HF-$HNO_3$ solution the $E_{OCP}$ for Ti-64 was nobler than for Ti-6242, in contrast to the observations made in only HF solution and in HF-$HNO_3$ solution with molar concentration ratio of 1:3. This indicates that Ti-64 more easily forms passive surface film of $TiO_2$ than the Ti-6242 alloy. Apparently, the increase of $HNO_3$ concentration from 0.3 M to 1.1 M resulted in modification of the kinetics for the formation of passive film of $TiO_2$ and consequently the corrosion behaviour of the two studied alloys.

Moreover, the effect of $HNO_3$ acid on hindering the hydrogen gas formation can be observed in the $E_{OCP}$ results (*see reaction (3) in Introduction*). The plots shown in Fig. 3a and 3b show noise, i.e. fluctuations of the recorded potential for both Ti-64 and Ti-6242 alloys in only HF solutions. It is considered that the instability of the recorded potential is due to hydrogen gas formation on the surface (*see reaction (2) in Introduction*). In contrast, as soon as the $HNO_3$ acid is in combination with HF the $E_{OCP}$ noise signal vanished (*see Fig. 3c-3f*).

Fig. 4 shows polarisation curves obtained for Ti-64 (Fig. 4a) and Ti-6242 (Fig. 4b) alloys in the three different solutions (0.1 M HF, 1:3 and 1:11 HF-$HNO_3$ solutions). The logarithmic values of the current density are plotted as function of the applied potential. The polarisation curves recorded for both alloys show typical shape for metal that goes from active to passive behaviour. At potentials below the corrosion potential ($E_{CORR}$), the cathodic reaction, i.e. reduction, takes place, whereas at potentials above $E_{CORR}$ the anodic reaction, i.e. the oxidation, occurs. In the active potential range the alloys exhibit uniform dissolution, i.e. corrosion, under passive film-free conditions. Further increase of the potential to positive values results in passivation of the alloy surfaces. The passivation potentials ($E_{PP}$) for two alloys isolated by the polarisation curves from Fig. 4 were $E_{PP}$ (Ti-64 in 0.1 M HF) = 33 mV, $E_{PP}$ (Ti-64 in 0.1 M HF + 0.3 M $HNO_3$) = 168 mV, $E_{PP}$ (Ti-64 in 0.1 M HF + 1.1 M $HNO_3$) = 92 mV, $E_{PP}$ (Ti-6242 in 0.1 M HF) = 28 mV, $E_{PP}$ (Ti-6242 in 0.1 M HF + 0.3 M $HNO_3$) = 139 mV, $E_{PP}$ (Ti-6242 in 0.1 M HF + 1.1 M $HNO_3$) = 92 mV.

The polarisation curves from Fig. 4 were analysed using the corrosion rate analysis tool in Nova 2.0 Autolab Metrohm software and were fitted using the Butler-Volmer equation:

$$I = I_{CORR}\left( e^{\frac{2.303(E - E_{CORR})}{\beta_a}} - e^{\frac{2.303(E - E_{CORR})}{\beta_c}} \right) \qquad (1)$$

where $I$ is the measured current, $I_{CORR}$ is the corrosion exchange current, $E$ is the applied potential, $E_{CORR}$ is the corrosion potential and $\beta_a$ and $\beta_c$ are the Tafel slopes for the anodic and cathodic branches.

The values calculated for $E_{CORR}$ (mV), $I_{CORR}$ (μA), $i_{CORR}$ (corrosion current density/$\mu Acm^{-2}$), $\beta_a$ and $\beta_c$ (V/decade) and the corrosion rates in mm/year are presented in Table 3.

**Table 3**

$E_{CORR}$, $I_{CORR}$, $i_{CORR}$, $\beta_a$, $\beta_c$ and corrosion rate for Ti-64 and Ti-6242 alloys in different solutions.

| | Ti-64 | | | Ti-6242 | | |
|---|---|---|---|---|---|---|
| | HF | $HF-HNO_3$ (1:3) | $HF-HNO_3$ (1:11) | HF | $HF-HNO_3$ (1:3) | $HF-HNO_3$ (1:11) |
| $E_{CORR}$ (mV) | − 973 | − 165 | − 85 | − 769 | − 82 | − 204 |
| $I_{CORR}$ (μA) | 2.367 | 11.222 | 13.425 | 1.655 | 6.741 | 17.069 |
| $i_{CORR}$ (μA/cm$^2$) | 7.174 | 34.006 | 40.682 | 5.015 | 20.428 | 51.724 |
| $\beta_a$ (V/decade) | 2.0136 | 0.4091 | 0.2618 | 1.2043 | 0.2837 | 0.2223 |
| $\beta_c$ (V/decade) | 1.763 | − 0.606 | − 0.444 | 1.292 | − 0.452 | − 0.319 |
| Corrosion rate (mm/year) | 63.6 | 301.5 | 360.6 | 43.3 | 176.3 | 446.4 |

The corrosion rate (*CR*) for both alloys in all testing solutions was calculated based on the obtained values from the analysis and by applying the following equation [31]:

$$CR = K \frac{i_{CORR}}{\rho A} EW \qquad (2)$$

where $K$ is constant that defines the units for the corrosion rate ($K$ = 3.27 x 10$^{-3}$, mm g/μA cm yr), $i_{CORR}$ is corrosion current density (μAcm$^{-2}$), $\rho$ is density of the alloy (g/cm$^3$), $A$ is sample surface area (cm$^2$) and $EW$ is equivalent weight a dimensionless unit (i.e. mass of metal in grams that will be oxidised by the passage of one Faraday electric charge i.e. 96489 ± 2 C). For the calculation of the corrosion rate the following values were used: density of 4.42 g/cm$^3$ and 4.54 g/cm$^3$ for Ti-64 and Ti-6242, respectively; surface area of the samples 0.33 cm$^2$ and equivalent weight of 11.98 grams for Ti in valence state +4.

The data in Table 3 reveals that the corrosion rate of the two alloys is not only dependent on the composition of the $HF-HNO_3$ acid solutions, but is also dependent of the type of alloy i.e. chemical composition of the alloys. In general, increased concentration of $HNO_3$ resulted in increased corrosion rate for both alloys (*see Table 3*). The corrosion rate was almost twice as high for Ti-64 than for Ti-6242 in 1:3 $HF-HNO_3$ acids solution, whereas in 1:11 ratio the corrosion rate of Ti-64 was 1.23 times slower than that of Ti-6242. Increase of the corrosion rate by increasing the $HNO_3$ concentration is expected behaviour. As shown in [32] for destroying the passivity of titanium (i.e. $TiO_2$ passive film) except presence of $F^-$ ions, a low pH condition is also required. In principle, high acidic environment (i.e. solution with low pH values) would result in easier dissolution of the passive $TiO_2$ film, thus faster corrosion rates. The pH of HF (0.1 M), $HF-HNO_3$ (0.1 M + 0.3 M) and $HF-HNO_3$ (0.1 M + 0.3 M) acids solutions were estimated theoretically. HF is weak acid with $Ka$ = 7.2 x 10$^{-4}$ (p$Ka$ 3.14) [33]. It was estimated that 0.1 M HF aqueous solution would result in pH = 2. In contrast, $HNO_3$ is a strong acid that completely dissociates in aqueous solution into hydronium ions ($H_3O^+$) and nitrate ions ($NO_3^-$) resulting in highly acidic environment i.e. low pH values. Correspondingly, for 1:3 and 1:11 $HF-HNO_3$ acid solutions was estimated to result in pH = 0.52 and pH = 0.04, respectively.

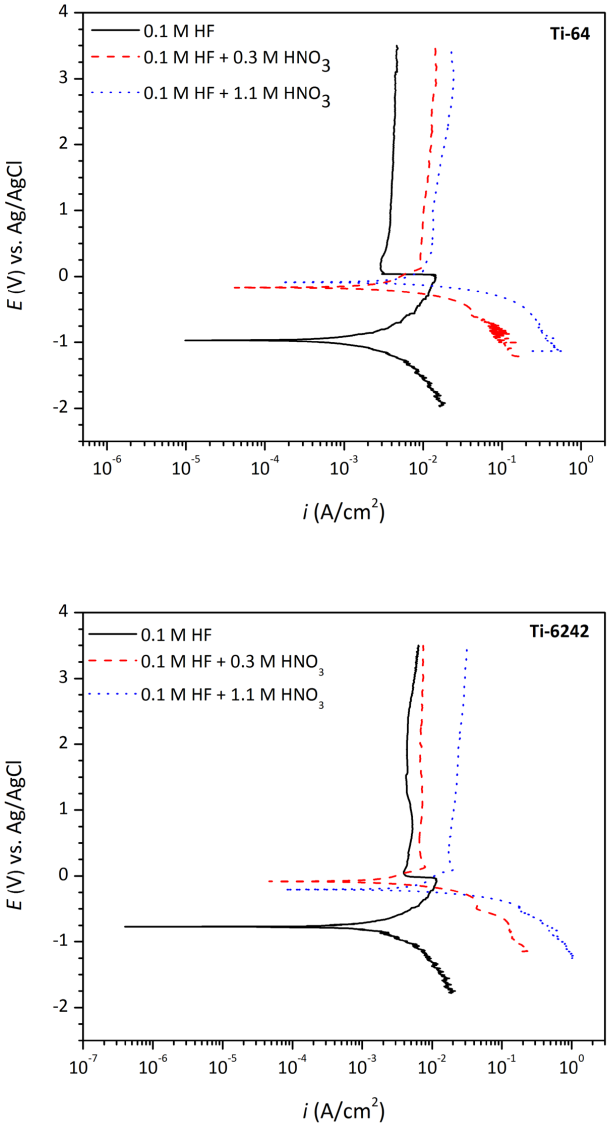


**Figure 4.** Polarisation curves recorded in 0.1 M HF ($E_{START\ vs.\ Ag/AgCl}$ = -2 V; $E_{END\ vs.\ Ag/AgCl}$ = 3.5 V; $\upsilon$ = 1 mV/s), 0.1 M HF + 0.3 M $HNO_3$ and 0.1 M HF + 1.1 M $HNO_3$ ($E_{START\ vs.\ Ag/AgCl}$ = -1.25 V; $E_{END\ vs.\ Ag/AgCl}$ = 3.5 V; $\upsilon$ = 1 mV/s) for a) Ti-64 and b) Ti-6242.

At potentials above $E_{PP}$ both alloys in all three solutions exhibit passive behaviour through formation of $TiO_2$ passive film. Increase of the current density due to transpassive dissolution and oxygen evolution was not discerned in any of the testing conditions. In reducing conditions, as in HF, the predominant cathodic reaction is hydrogen gas evolution (*see reaction (2) in Introduction*). In presence of $HNO_3$, which is the strong oxidising agent, the two alloys spontaneously passivate and thus do not exhibit active anodic region in the polarisation curve. This can be seen in Fig. 4 by comparing the polarisation curves recorded in only HF and 1:3 and 1:11 molar concentration ratio of HF and $HNO_3$ acids. Under these conditions the open circuit corrosion rate is expected to be controlled by the passivation current density ($i_{PASS}$/Acm$^{-2}$) [34]. Fig. 5 compares the passivation current densities isolated from the polarisation curves of the two alloys in all three solutions. As seen, the two alloys exhibit different behaviour, which is dependent on the concentration ratio between the acids. In 1:3 molar concentration ratio, $i_{PASS}$ was larger for Ti-64, whereas in 1:11 ratio $i_{PASS}$ was higher for Ti-6242. The $i_{PASS}$ values are in good agreement with the recorded $E_{OCP}$ values (*see Table 2*) and the calculated corrosion rates (*see Table 3*) for the two alloys in 1:3 and 1:11 solutions.

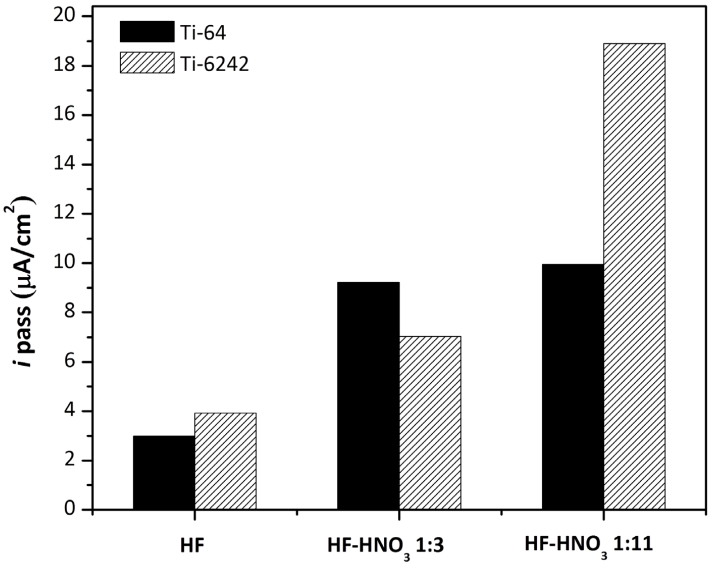


**Figure 5.** Passivation current densities ($i_{PASS}$/Acm$^{-2}$) for Ti-64 and Ti-6242 in 0.1 M HF, 0.1 M HF + 0.3 M $HNO_3$ (1:3) and 0.1 M HF + 1.1 M $HNO_3$ (1:11) isolated from the polarisation curves in Fig. 4.

*3.3 AFM study*

Fig. 6 shows the topography and the Volta-potential difference maps measured in air on mirror polished surface samples of Ti-64 (Fig. 6a) and Ti-6242 (Fig. 6b). The parallel α-laths and the thin β-Ti phase layers between the α-laths are clearly discerned. The Volta-potential difference maps indicate that there is a local potential difference between α- and β-Ti phases at microscopic scale. Thus, it is assumed that there

is formation and operation of local micro-galvanic cells between the two micro constituents (in both alloys) when they are in contact with HF-$HNO_3$ solution.

In the case of Ti-64, the β-Ti phase has lower Volta-potential compared to the α-Ti phase (*see right SKPFM Volta-potential map on Fig. 6a*). It should be recalled that the SKPFM data are raw data and not inverted, and in this convention, lower Volta-potential corresponds to nobler micro constituent, whereas higher Volta-potential corresponds to less noble one. The same applies for the Volta-potential map of Ti-6242 (*see right SKPFM Volta-potential map on Fig. 6b*). Thus, the Volta-potential maps demonstrate that the phases having higher Volta-potential are more active and thus the α-Ti phases are acting as the anode while the nobler β-Ti phases are acting as local cathodes. This correlates well with the results and trends observed in [28] for Ti-64. It is considered that such scenario would result in profound faster corrosion i.e. dissolution of the α-Ti phase compared to the β-Ti phase in both alloys when they are in contact with HF-$HNO_3$ solutions.

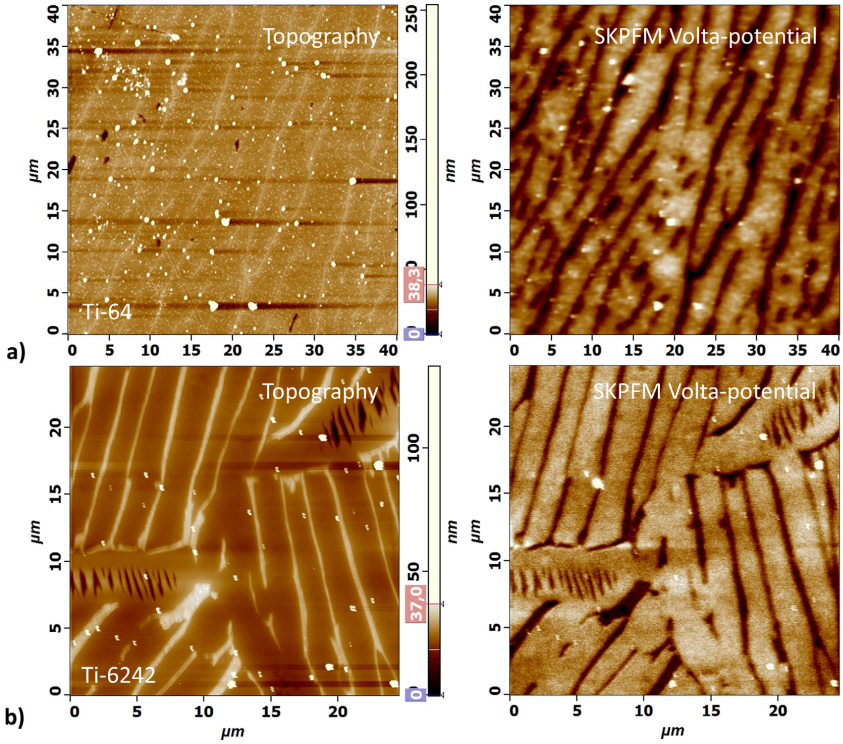


**Figure 6.** Topography (left) and Volta-potential difference maps (right) measured in air with SKPFM for a) Ti-64 and b) Ti-6242. The darker areas correspond to lower Volta-potential, while the brigther areas correspond to the higher Volta-potential on the SKPFM maps. The color bar is not shown for the SKPFM images due to applied filtering operations to clearly present the contrast between α- and β-Ti phases.

The Volta-potential difference and the work function (*WF*) of the individual α- and β-Ti phases for both alloys were calculated and the obtained values are shown in Table 4.

**Table 4**
Volta-potential difference ($V_{PD}$) measured with SKPFM on mirror polished Ti-64 and Ti-6242 samples and corresponding calculated work functions (*WF*) using the work function of the cantilever ($WF_{tip}$ = 4.67 eV).

| | Ti-64 | | Ti-6242 | |
|---|---|---|---|---|
| | $V_{PD}$ (V) | *WF* (eV) | $V_{PD}$ (V) | *WF* (eV) |
| *Experiment 1* | | | | |
| α-Ti phase | 0.21 | 4.46 | 0.72 | 3.95 |
| β-Ti phase | 0.19 | 4.48 | 0.69 | 3.98 |
| *Experiment 2* | | | | |
| α-Ti phase | 0.13 | 4.54 | 0.44 | 4.23 |
| β-Ti phase | 0.06 | 4.61 | 0.39 | 4.28 |

The Volta-potential difference in terms of nobility between the phases in the two alloys corresponds well to the calculated *WF* for the two phases in Ti-64 and Ti-6242, showing lower *WF* for the α-Ti phase than for the β-Ti phase (*see Table 4*). As follows from the definition of the *WF*, in the case of β-Ti phase higher energy is required to remove an electron from the Fermi level to the position just outside the sample. Also, the Volta-potentials for the α- and β-Ti phase were higher for Ti-6242 than for Ti-64 and correspondingly the *WF*s showed the same trends. The lower *WF* for Ti-6242, and a less required energy to remove electron in comparison to Ti-64, can be due to the different and more complicated chemical composition as compared to Ti-64 and other properties such as different atom packing, different amount of defects, crystalline edges and more. As shown in [28,35] the increased density of crystal defects leads to a decrease of the *WF* for metals, due to the increased probability for the electron to escape from the surface. In alignment to the discerned trends for the values of Volta-potential difference and *WF*s between the both alloys, we have performed two SKPFM measurements to confirm the trends between the Volta-potential difference and *WF* between the phases in each alloy. The second measurement was performed long time after the first measurement. It was found that the absolute Volta-potentials differed, as expected, due to influence from humidity, temperature and surface conditions on the measured potentials. However, the observed trends, such as larger Volta-potential for α-Ti phase than for β-Ti phase in both alloys, larger *WF* for β-Ti phase than for α-Ti phase also in both alloys and the larger *WF* for α-Ti phase and β-Ti phase for Ti-64 than for Ti-6242, were reproducible.

Fig. 7 and 8 shows virtually illuminated 3-dimensional (3D) AFM height images and corresponding representative AFM cross-section profiles measured for Ti-64 and Ti-6242 samples after immersion for 0, 1, 5 and 10 minutes in solutions composed of 1:3 and 1:11 molar concentration ratios between HF and $HNO_3$. From the profiles the effect of HF-$HNO_3$ solutions on the micro constituents (i.e. α- and β-Ti phases) can be observed. The α-Ti phase in both the alloys dissolved faster than the β-Ti phase. This behaviour has been observed previously in the work of Chen and Tsai [19] in $H_2SO_4$/HCl and Nakhaie et al. [28] in HF/$HNO_3$ for Ti-64 and Raja et al. [16] for Ti-6242 in 1 M NaBr solution. The effect of local difference in dissolution in HF-$HNO_3$ solutions of the micro constituents of the two alloys confirms the hypothesis of formation and operation of local micro-galvanic cells between the α- and β-Ti phases.

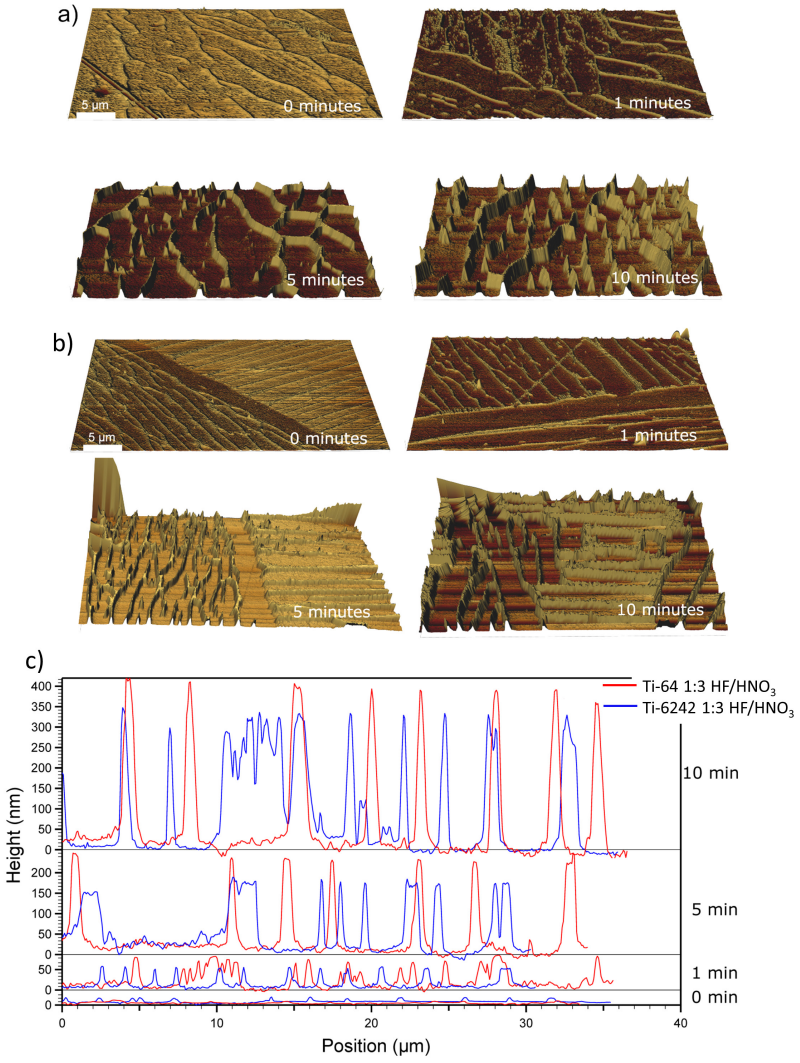


**Figure 7.** Virtually illuminated 3D AFM height images of a) Ti-64, b) Ti-6242 and c) representative AFM cross-section profiles of Ti-64 (red) and Ti-6242 (blue) after immersion in 1:3 molar concentration ratio of $HF/HNO_3$ solutions for 0, 1, 5 and 10 minutes (all profiles are displayed with the same vertical and lateral scaling and all surface plots are 40 µm in size, have the same vertical z-scaling but with different color coding to outline surface features).

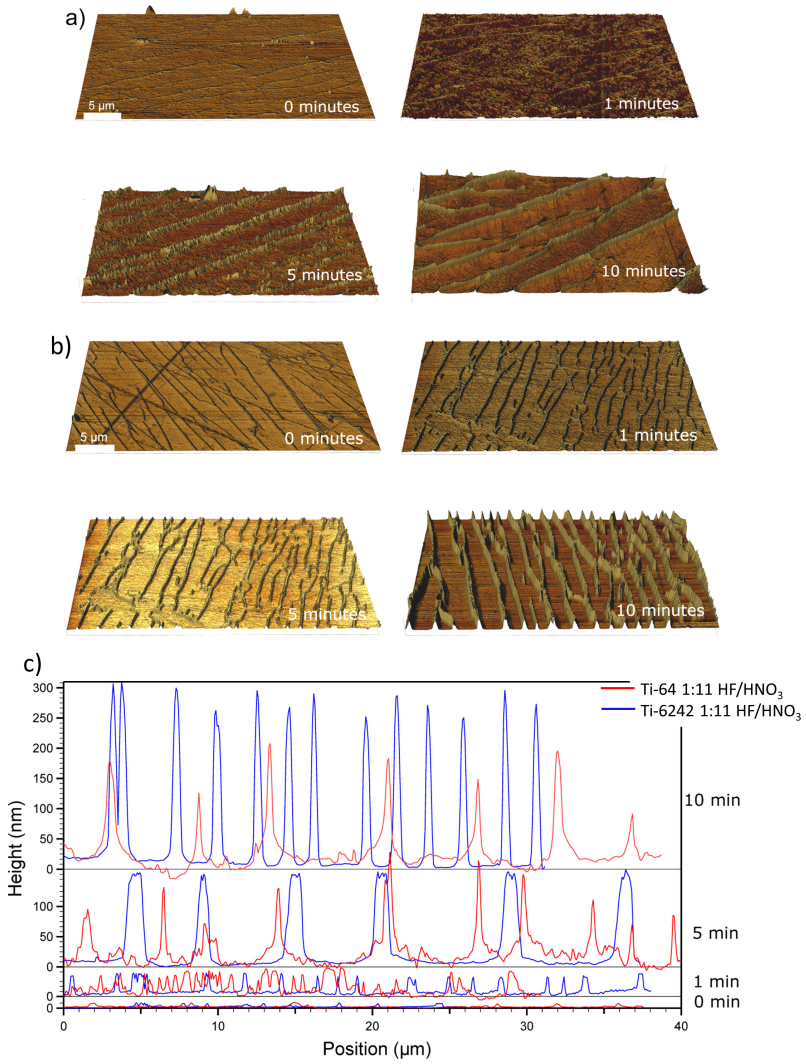


**Figure 8.** Virtually illuminated 3D AFM height images of a) Ti-64, b) Ti-6242 and c) representative AFM cross-section profiles of Ti-64 (red) and Ti-6242 (blue) after immersion in 1:11 molar concentration ratios of $HF/HNO_3$ solutions for 0, 1, 5 and 10 minutes (all profiles are displayed with the same vertical and lateral scaling and all surface plots are 40 µm in size, have the same vertical z-scaling but with different color coding to outline surface features).

It is well established that one of the common reasons for localised corrosion (i.e. corrosion on micron and submicron length scale) are inhomogeneity of the chemical composition. Therefore, the chemical compositions of α- and β-Ti phases in the Ti-64 and Ti-6242 alloys were measured using energy

dispersive spectrometry (EDS). The measured mean concentrations in wt. % from 15 individual measurements on randomly selected positions on the samples surface (i.e. α- and β-Ti phases) and the corresponding standard deviations are shown in Table 5.

**Table 5**
Chemical composition in wt. % of the main alloying elements in α- and β-Ti phases measured by EDS for Ti-64 and Ti-6242 alloys in as-cast condition.

| Ti-64 | | | Ti-6242 | | |
|---|---|---|---|---|---|
| Element (wt.%) | α-Ti phase | β-Ti phase | Element (wt.%) | α-Ti phase | β-Ti phase |
| Al | 4.77 ± 0.03 | 2.76 ± 0.63 | Al | 4.59 ± 0.05 | 3.28 ± 0.33 |
| V | 2.49 ± 0.06 | 12.00 ± 3.77 | Sn | 2.06 ± 0.10 | 2.25 ± 0.02 |
| Fe | - | 1.01 ± 0.52 | Zr | 3.23 ± 0.10 | 4.37 ± 0.45 |
| Ti | 92.73 ± 0.09 | 84.23 ± 3.63 | Mo | 0.23 ± 0.09 | 4.98 ± 1.00 |
| | | | Si | 0.07 ± 0.03 | 0.09 ± 0.03 |
| | | | Ti | 89.81 ± 0.16 | 84.68 ± 1.27 |

Comparison between the chemical compositions of the individual micro constituents revealed notable variations of the main α- and β-stabilising elements. As expected, in Ti-64 a difference in the content of Al (α-stabilising element) and V (β-stabilising element) between α- and β-Ti micro constituents was observed. Moreover, there was notable difference of Fe content between the constituents in the Ti-64 alloy. In Ti-6242, as for Ti-64, the measured composition of the Al (α-stabilising element) and Mo (β-stabilising element) content in α- and β- constituents varied notably. It is considered that the partitioning of the α- and β-stabilising elements in these two alloys is the key factor controlling the corrosion behaviour at microscopic scale. It is well known that additions of V and Mo results in improved resistance to localised corrosion of titanium alloys, whereas additions of Al was noted to be detrimental [15]. Since notable variation of the α- and β-stabilising elements was measured, it is reasonable to consider that the α- and β-Ti phases in both alloys would exhibit different electrochemical potential when are in contact with HF-$HNO_3$ solutions. This was substantiated by the SKPFM experiments for the two alloys (*see SKPFM Volta-potential maps in Fig. 6*). The different chemical composition and different potential of the two phases in both alloys results in formation and operation of local micro-galvanic cells between the phases. Thus, one of the phases behaves as anode dissolving faster compared to the other phase that behaves as cathode and dissolves at slower rate. In the present work, the α-Ti phase that is enriched in Al and deficient in V for Ti-64 and enriched in Al and deficient in Mo for Ti-6242 operates as local anode and dissolves faster as compared to the β-Ti phase. Thus the β-Ti phase in the two alloys operates as local cathode. This was corroborated with the AFM experiments performed before and after immersion of the alloys into the HF-$HNO_3$ solutions for various immersion times (*see Fig. 7 and Fig. 8*). Another parameter that could be important for the faster corrosion of the α-Ti phase in HF-$HNO_3$ solutions is the crystallographic orientation of the α-colonies. Hence, further studies of the crystallographic orientation effect on the corrosion behaviour are encouraged.

In order to better understand how different concentration ratios of the acids influence the corrosion (i.e. dissolution) of the individual micro constituents in the two alloys the AFM topography was measured before and after immersion in 1:3 and 1:11 molar concentration ratios of the HF-$HNO_3$ solutions for various immersion times. These topography data were used to estimate and quantify the α-Ti phase versus β-Ti phase height difference, i.e. α/β height difference.

Fig. 9 shows the plot of the estimated α/β height difference for both alloys as a function of immersion time in 1:3 and 1:11 molar concentration ratios of the HF-$HNO_3$ solutions. A tendency of increasing α/β height difference as a result of prolonged immersion times in the HF-$HNO_3$ solutions can be observed. Additionally, an effect of the concentration ratio of the acid solutions on the α-Ti phase corrosion rate was observed. In 1:3 molar concentration ratio of the acids the α/β height difference was larger in Ti-64, whereas in the solution with 1:11 ratio the estimated α/β height difference was larger in Ti-6242. This indicates that, although both alloys exhibited faster corrosion of α- than the β-Ti phase, their corrosion rate is also affected strongly by the concentration ratio of the acids.

This corrosion behaviour at microscopic length scale of the micro constituents (i.e. α/β height difference) for Ti-64 and Ti-6242 as function of the HF and $HNO_3$ concentration ratio is in correlation with the corrosion behaviour observed by the electrochemical study in the present work. The corrosion rate estimated for both alloys was dependent on the concentration ratio of the two acids, showing higher corrosion rates for Ti-64 in 1:3 and lower in 1:11 HF-$HNO_3$ solutions, compared with Ti-6242. In addition, the α/β height difference measured for both alloys and its dependence on the concentration ratio of the acids correlates well with the change of the passivation current densities as a function of the concentration ratio of HF and $HNO_3$. Higher passivation current density was observed for Ti-64 in 1:3 HF-$HNO_3$ solution than for Ti-6242, whereas in 1:11 HF-$HNO_3$ solution the passivation current density was higher for Ti-6242.

Hence, as a summary based on the experimental facts observed in the present work, it is considered that the corrosion behaviour at a microscopic scale of the individual micro constituents controls and defines the overall corrosion behaviour of both alloys. This is dependent on the concentration ratio of the HF and $HNO_3$ acids, on the type of alloy and their chemical composition. In principle, change of the concentration ratio from 1:3 to 1:11 of the acids influenced significantly the corrosion behaviour of Ti-64 and Ti-6242. Additionally, both alloys have different chemical composition of the main α- and β-stabilising elements in their respective micro constituents (i.e. α- and β-Ti phase). This difference leads to formation of micro-galvanic cells between the two main micro constituents, where the α-Ti phase behaves as local anode and the β-Ti phase behaves as local cathode. The formation of micro-galvanic cells between the two micro constituents in the two alloys was substantiated by the SKPFM and AFM measurements. Both the Volta-potential distribution and the calculated work functions indicated difference in the nobility of the individual micro constituents.

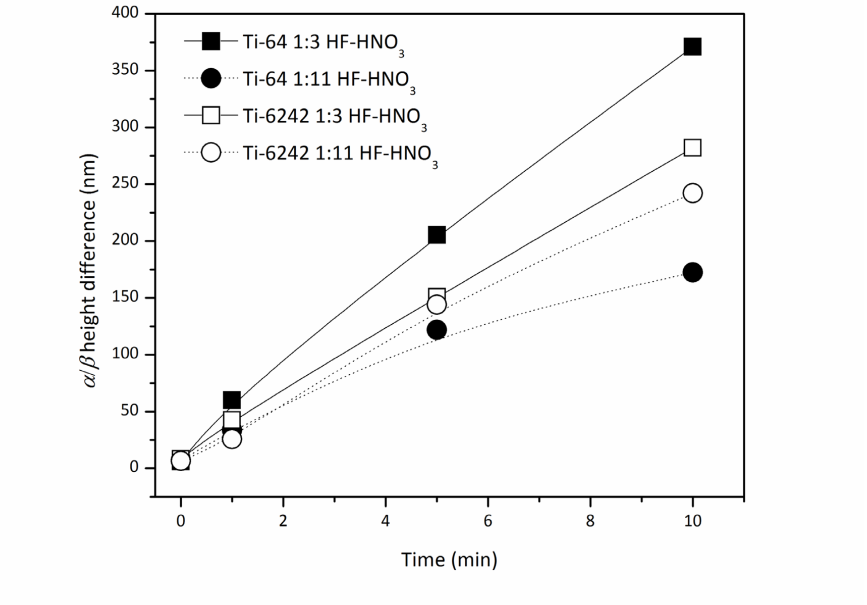


**Figure 9.** Diagram of the measured α/β height difference from the AFM topography data (Fig. 7 and 8) for Ti-64 and Ti-6242 alloys after immersion in 1:3 and 1:11 HF-$HNO_3$ solutions for 0, 1, 5 and 10 minutes.

## 4. Conclusions

The corrosion behaviour of cast Ti-6Al-4V and Ti-6Al-2Sn-4Zr-2Mo at macroscopic and microscopic scale in HF-$HNO_3$ solutions with two molar concentration ratios (1:3 and 1:11) was investigated by means of electrochemical and Atomic Force Microscopy (AFM) techniques. The main findings and conclusions are as follows:

1. The corrosion behaviour of Ti-64 and Ti-6242 alloys in HF-$HNO_3$ solutions is complex and dependent on time, the molar concentration ratio of the HF and $HNO_3$ acids (1:3 and 1:11), the type of titanium alloy and its chemical composition.
2. The Ti-64 alloy corrodes faster in 1:3 and slower in 1:11 HF-$HNO_3$ solutions compared to Ti-6242.
3. The α-Ti phase is less noble than the β-Ti phase in both alloys and dissolves faster in HF/$HNO_3$ solutions.
4. Micro-galvanic cells form and operate in the two alloys between the α- and β-Ti phases when the alloys are in contact with HF-$HNO_3$ solution and this is because of chemical compositional differences of the α- and β-stabilising elements in each phase.

5. The overall corrosion behaviour of the two alloys is defined and controlled by the individual corrosion behaviour of the α-Ti phase.

**Acknowledgments**

The authors kindly acknowledge Erasmus Mundus Programme through the European Joint Doctoral Programme in Materials Science and Engineering Programme (DocMASE, Grant number 512225-1-2010-1-DE-ERA MUNDUS-EMJD), the Swedish Foundation for Strategic Research (SSF)-Sweden for providing the financial assistance and the Kempe Foundations grant SMK-2546 for funding the AFM equipment. We kindly acknowledge Assoc. Prof. Nazanin Emami from Luleå University of Technology for providing us with the potentiostat Autolab PG-STAT302N for the electrochemical measurements and we are grateful to Clémence Luc for performing the measurements. We would like also to acknowledge Professor Ragnar Tegman from Luleå University of Technology for his valuable contribution in discussion of the results and revising this paper.

**References**

[1] R.R. Boyer, An overview on the use of titanium in the aerospace industry, Mater. Sci. Eng. A 213 (1996) 103-114.

[2] D. Eylon, S. Fujishiro, F.H. Froes, P.J. Postans, High-temperature titanium alloys-A review, J. Met. 1 (1984) 55-62.

[3] M.J. Donachie, Titanium a technical guide, second ed., ASM International, Materials Park, OH, 2000.

[4] R. Gaddam, B. Sefer, R. Pederson, M.-L. Antti, Study of alpha-case depth in Ti-6Al-2Sn-4Zr-2Mo and Ti-6Al-4V, IOP Conf. Series: Mater. Sci. Eng. 48 (2013) 012002.

[5] R. Gaddam, B. Sefer, R. Pederson, M.-L. Antti, Oxidation and alpha-case formation in Ti-6Al-2Sn-4Zr-2Mo alloy, Mater. Charact. 99 (2015) 166-174.

[6] B. Sefer, J.J. Roa, A. Mateo, R. Pederson, M.-L. Antti, Evaluation of the bulk and alpha-case layer properties in Ti-6Al-4V at micro- and nano-metric length scale, in: V. Venkatesh, A.L. Pilchak, J.E. Allison, S. Ankem, R. Boyer, J. Christodoulou, H.L. Fraser, M.A. Imam, J. Kosaka, H.J. Rack, A. Chaterjee, A. Woodfield (Eds.), Proceedings of the 13th World Conference on Titanium, John Wiley & Sons Inc., Hoboken, New Jersey, 2016, pp. 1619-1624.

[7] B. Sefer, R. Gaddam, R. Pederson, A. Mateo, R. Tegman, M.-L. Annti, Oxidation behaviour of Ti-6Al-4V and Ti-6Al-2Sn-4Zr-2Mo alloys exposed to air at elevated temperatures, Corros. Sci. (2016) under revision.

[8] K.S. Chan, M. Koike, B.W. Johnson, T. Okabe, Modeling of alpha-case formation and its effects on the mechanical properties of titanium alloy castings, Metall. Mat. Trans. A 39 (2008) 171-180.

[9] C. Leyens, M. Peters, D. Weinem, W.A. Kaysser, Influence of long-term annealing on tensile properties and fracture of near-α titanium alloy Ti-6Al-2.75Sn-4Zr-0.4Mo-0.45Si, Metall. Mat. Trans. A 27 (1996) 1709-1717.

[10] A. Pilchak, W. Porter, R. John, Room temperature fracture processes of a near-α titanium alloy following elevated temperature exposure, J. Mater. Sci. 47 (2012) 7235-7253.

[11] R. Gaddam, M.-L. Antti, R. Pederson, Influence of alpha-case layer on the low cycle fatigue properties of Ti-6Al-2Sn-4Zr-2Mo alloy, Mater. Sci. Eng. A 599 (2014) 51-56.

[12] G. Lütjering, J.C. Williams, Titanium, Springer, 2003.

[13] C. Lin, X. Hong, Investigation of corrosion processing for Ti-6Al-4V in hydrofluoric-nitric acid system, ASME International Manufacturing Science and Engineering Conference, Volume 1, Corvallis, Oregon, USA, June 13–17, (2011) 349-355.

[14] W.C. Say, Y.Y. Tsai, Surface characterization of cast Ti-6Al-4V in hydrofluoric-nitric pickling solutions, Surf. Coat. Technol. 176 (2004) 337-343.

[15] T. Beck, R. Staehle, B. Brown, J. Kruger, A. Agrawal, Localized corrosion, NACE-3, TX: NACE, Houston. (1974) 644-672.

[16] B. Sefer, R. Gaddam, J.J. Roa, A. Mateo, M.-L. Antti, R. Pederson, Chemical milling effect on the low cycle fatigue properties of cast Ti–6Al–2Sn–4Zr–2Mo alloy, Int. J. Fatigue 92 (2016) 193-202.

[17] E. Sutter, F. Hlawka, A. Cornet, Comparative behavior of titanium and zirconium in hydrofluoric-nitric acid pickling solutions, Corrosion 46 (1990) 537-544.

[18] E. Sutter, A. Cornet, G. Goetz, Activity of the surface of titanium during pickling in nitric-hydrofluoric acid, 6th World Conference on Titanium (1988) 1923-1928.

[19] E. Sutter, G. Goetz-Grandmont, The behaviour of titanium in nitric-hydrofluoric acid solutions, Corros. Sci. 30 (1990) 461-476.

[20] P. Bijlmer, Pickling titanium in hydrofluoric-nitric acid, Metal Finish 68 (1970) 64-67.

[21] I. Gurrappa, Characterization of titanium alloy Ti-6Al-4V for chemical, marine and industrial applications, Mater. Charact. 51 (2003) 131-139.

[22] M. Atapour, A. Pilchak, G. Frankel, J. Williams, M. Fathi, M. Shamanian, Corrosion behavior of Ti-6Al-4V with different thermomechanical treatments and microstructures, Corrosion. 66 (2010) 065004-065004-9.

[23] J. Chen, W. Tsai, In situ corrosion monitoring of Ti–6Al–4V alloy in $H_2SO_4$/HCl mixed solution using electrochemical AFM, Electrochim. Acta. 56 (2011) 1746-1751.

[24] V. Raja, R. Angal, M. Suresh, Effect of widmanstatten structure on protection potential of Ti-6Al-2Sn-4Zr-2Mo (0.1 Si) alloy in 1 M NaBr solution, Corrosion. 49 (1993) 2-7.

[25] P. Schmutz, G. Frankel, Corrosion study of AA2024-T3 by scanning Kelvin probe force microscopy and in situ atomic force microscopy scratching, J. Electrochem. Soc. 145 (1998) 2295-2306.

[26] V. Guillaumin, P. Schmutz, G. Frankel, Characterization of corrosion interfaces by the scanning Kelvin probe force microscopy technique, J. Electrochem. Soc. 148 (2001) B163-B173.

[27] M. Jönsson, D. Thierry, N. LeBozec, The influence of microstructure on the corrosion behaviour of AZ91D studied by scanning Kelvin probe force microscopy and scanning Kelvin probe, Corros. Sci. 48 (2006) 1193-1208.

[28] D. Nakhaie, A. Davoodi, G.R. Ebrahimi, The Influence of cold plastic deformation on passivity of Ti-6Al-4V alloy studied by electrochemical and local probing techniques, Corrosion 72 (2015) 110-118.

[29] L. Lacroix, L. Ressier, C. Blanc, G. Mankowski, Combination of AFM, SKPFM, and SIMS to study the corrosion behavior of S-phase particles in AA2024-T351, J. Electrochem. Soc. 155 (2008) C131-C137.

[30] A. Rodrigues, N. Oliveira, M. Dos Santos, A. Guastaldi, Electrochemical behavior and corrosion resistance of Ti–15Mo alloy in naturally-aerated solutions, containing chloride and fluoride ions, J. Mater. Sci. Mater. Med. 26 (2015) 1-9.

[31] ASTM G102-89, Standard practice for calculation of corrosion rates and related information from electrochemical measurements, 1999.

[32] Y. Fovet, J. Gal, F. Toumelin-Chemla, Influence of pH and fluoride concentration on titanium passivating layer: stability of titanium dioxide, Talanta. 53 (2001) 1053-1063.

[33] S.S. Zumdahl, S.A. Zumdahl, Chemistry–6 th Edition Houghton Mifflin, Boston, Massachusetts. (2006).

[34] R.G. Kelly, J.R. Scully, D. Shoesmith, R.G. Buchheit, Electrochemical Techniques in Corrosion Science and Engineering, CRC Press, 2002.

[35] A. Nazarov, D. Thierry, Application of Volta potential mapping to determine metal surface defects, Electrochim. Acta. 52 (2007) 7689-7696.